NASA CR-135092
BBN Report No. 3332

ANALYSIS AND DESIGN OF A HIGH TIP SPEED, LOW SOURCE NOISE AIRCRAFT FAN INCORPORATING SWEPT LEADING EDGE ROTOR AND STATOR BLADES

Richard E. Hayden
Donald B. Bliss
Bruce S. Murray
K.L. Chandiramani
Joseph I. Smullin
with
Pierre G. Schwaar (AVCO Lycoming Division)

NASA Contract No. NAS3-18512

December 1977

Submitted to:
NASA Lewis Research Center
21000 Brookpark Road
Cleveland, Ohio 44135

1. Report No.	2. Government Accession No.	3. Recipient's Catalog No.
NASA CR-135092		

4. Title and Subtitle

Analysis and Design of a High Tip Speed, Low Source Noise Aircraft Fan Incorporating Swept Leading Edge Rotor and Stator Blades

5. Report Date

December 1977

6. Performing Organization Code

7. Author(s)

Richard E. Hayden, Donald B. Bliss, Bruce S. Murray, K.L. Chandiramani, Joseph I. Smullin, and Pierre G. Schwaar

8. Performing Organization Report No.

3332

9. Performing Organization Name and Address

Bolt Beranek and Newman Inc.
50 Moulton Street
Cambridge, Massachusetts 02138

10. Work Unit No.

505-03-12

11. Contract or Grant No.

NAS3-18512

12. Sponsoring Agency Name and Address

National Aeronautics and Space Administration
Langley Research Center
Hampton, VA 23665

13. Type of Report and Period Covered

Contract Report 1974-1977

14. Sponsoring Agency Code

15. Supplementary Notes

Project Manager, James G. Lucas, V/STOL and Noise Division
NASA Lewis Research Center
Cleveland, OH 44135

16. Abstract

In modern high bypass ratio turbofans, the fan thrust is achieved in a single fan stage, which usually requires supersonic tip speeds of the fan rotor to produce the necessary pressure rise. In such fans, the predominant sources of noise are shocks radiated from the supersonically-moving rotor blades (called multiple-pure-tone [MPT] noise), and tones radiated from the rotor wake interaction with stator vanes.

In this program, two advanced noise reduction concepts were applied to the design of a 1.6 pressure ratio single stage fan. The goal of the design was to reduce the following acoustic sources: multiple pure tone noise, rotor-wake/stator-blade interaction noise, and noise due to operating the rotor in distorted or turbulent inflow. Unique nonradial blading of the rotor and stator was used to achieve these goals. The rotor blade leading edges were swept so that the *normal* component of flow to the edge is *subsonic* at all points along the blade span, thus preventing the occurrence of leading edge shockwaves. The stator vanes were designed to minimize noise generated by rotor wakes incident on the blades by progressively sweeping the vanes from root to tip in order to produce subsonic trace speeds for the unsteady loads along the span. Special aerodynamic and structural design considerations were required to assure the performance and integrity of this unusual blade and vane design.

This report summarizes the physical rationale for the swept blade concepts, the detailed aerodynamic, acoustic, and structural design, and the mechanical assembly of the rig fan.

17. Key Words (Suggested by Author(s))	18. Distribution Statement
Aeroacoustics; Fan and Compressor Noise Reduction; Low Source Noise Fan; Subsonic Leading Edge Rotor Blades; Swept Blades; Turbofan.	

19. Security Classif. (of this report)	20. Security Classif. (of this page)	21. No. of Pages	22. Price*
Unclassified	Unclassified	227	

* For sale by the National Technical Information Service, Springfield, Virginia 22161

FOREWORD

The purpose of this report is to describe a recently completed program to design and manufacture an experimental transonic fan model featuring novel methods for noise reduction at the source. The program was conducted between 1974 - 1976 under contract NAS3-18512 issued by NASA Lewis Research Center, with Bolt Beranek and Newman Inc. (BBN) as the prime contractor and AVCO Lycoming as a subcontractor. The contract resulted from a NASA request for proposals (RFP) concerning CTOL aircraft engine fan source reduction concepts. The intent of the RFP was to identify advanced design concepts for reducing both rotor and stator sources which could be implemented with existing aerodynamic and structural design capabilities. The RFP encouraged proposals to reduce noise from high speed single stage fans.

BBN proposed the use of "subsonic leading edge" rotor blades and variably swept stator vanes as the concepts to be investigated. The study and engineering work culminated in the fabrication of a 20-inch diameter fan stage to be tested for acoustic and aerodynamic performance at the Lewis Research Center, National Aeronautics and Space Administration, Cleveland, Ohio.

Bolt Beranek and Newman Inc. (BBN), Cambridge, Massachusetts, served as the prime contractor with overall program responsiblity, as well as prime technical responsibility for the fan acoustic design, and other areas. The Lycoming Division of AVCO Corporation, Stratford, Connecticut, was a major subcontractor to BBN, with responsibilities in aerodynamic and mechanical design, and manufacture of the fan hardware. Rotor blades and stator vanes were manufactured under subcontract by New England Aircraft Products, Farmington, Connecticut.

Also included in the program were efforts to develop a 3-dimensional compressible flow computer program to analyze the flow through the rotor, especially in the vicinity of the leading edge, and the investigation of the feasibility of using porous trailing edges on the stators to reduce broadband noise. The 3-D flow program was discontinued at the time the rotor design was finalized, and the porous edge concept was not used because of the difficulties perceived in manufacture of small vanes from available porous metal materials.

Numerous individuals at BBN and AVCO made significant contributions to this project. Mr. Richard Hayden served as project manager, and contributed to the acoustic design of the fan as well as other areas. Dr. Donald Bliss served as an associate project manager and had responsibility for the concept of the rotor blade, the rotor acoustic design, and the coordination of the aerodynamic design with AVCO. Mr. Bruce Murray also served as an associate project manager and supervised the mechanical design and manufacturing aspects of the fan. The stator acoustic design was carried out by Dr. K.L. Chandiramani, and Mr. Joseph Smullin. Drs. John McElman and John O'Callahan performed finite element stress analysis of the rotor blades, and Dr. O'Callahan contributed to numerical fluid mechanical analysis of the rotor flow field.

At AVCO Lycoming, Mr. Pierre Schwaar served as the principal investigator and has primary program responsibility for the fan aerothermodynamical design, and for implementing the subsonic rotor leading edge concept and the acoustic design of the stator blades within operational structural constraints. Mr. Herbert Kaehler led AVCO's work on structural analysis and Mr. John Banks supervised mechanical design and manufacturing activities there.

Mr. James G. Lucas of the NASA Lewis Research Center's V/STOL and Noise Division was the NASA Program Manager, and contributed valuable assistance in the mechanical design and manufacturing areas, and in the integration of the fan into NASA's test facilities.

This report has been designated as Bolt Beranek and Newman (BBN) Report No. 3332.

TABLE OF CONTENTS

TABLE OF CONTENTS *(Cont.)*

TABLE OF CONTENTS *(Cont.)*

LIST OF FIGURES AND TABLES

Figure page

LIST OF FIGURES AND TABLES *(Cont.)*

LIST OF FIGURES AND TABLES *(Cont.)*

Figure page

LIST OF FIGURES AND TABLES *(Cont.)*

Figure page

Table

LIST OF FIGURES AND TABLES *(Cont.)*

SUMMARY

On current generation high bypass ratio turbofan engines, the fan is a predominant noise source which must be controlled to meet future aircraft noise goals. Of the various approaches to turbofan engine noise reduction, the most attractive is reducing the strength of the noise-producing elements at the source, thus avoiding weight and performance penalties associated with various sound suppression approaches.

In modern high bypass ratio turbofans, the fan thrust is achieved in a single fan stage, which usually requires supersonic tip speeds of the fan rotor to produce the necessary pressure rise. In such fans, the predominant sources of noise are shocks radiated from the supersonically-moving rotor blades (called multiple-pure-tone [MPT] noise), and tones radiated from the rotor wake interaction with stator vanes.

In this program, two advanced noise reduction concepts were applied to the design of a 1.6 pressure ratio single stage fan. The goal of the design was to reduce the following acoustic sources: multiple pure tone noise, rotor-wake/stator-blade interaction noise, and noise due to operating the rotor in distorted or turbulent inflow. Unique nonradial blading of the rotor and stator was used to achieve these goals. The rotor blade leading edges were swept so that the *normal* component of flow to the edge is *subsonic* at all points along the blade span, thus preventing the occurrence of leading edge shockwaves. The stator vanes were designed to minimize noise generated by rotor wakes incident on the blades by progressivly sweeping the vanes from root to tip in order to produce subsonic trace speeds for the unsteady loads along the span. Special aerodynamic and structural design considerations were required to assure the performance and integrity of this unusual blade and vane design.

The rotor design using a blade concept with shock-free leading edges (except at points of inflection where weak conical shocks occur) is highly flexible in that a large family of blade shapes and leading edge contours may, in general, be used to achieve the noise reduction goal. The swept rotor design is also attractive since it should perform equally well at off-design conditions if it has been designed to perform properly at the highest envisioned rotor speed. The swept edges also are compatible with reducing noise generation due to inflow distortion.

In the final design of the particular rotor ultimately constructed, a reversal of the sweep direction was required near mid-span to minimize stress levels in the blade. Once this was done, aeroacoustical-structural design iterations led to a blade with acceptable stress levels and no additional compromise in acoustic performance beyond the expected weak conical shock at the sweep reversal point.

The aerodynamics of subsonic leading edge rotor cascades with supersonic absolute inflow velocities are not well known, and will clearly require further study.

The concept of forcing the trace speeds of moving load distributions on stator vanes to be subsonic was introduced for the first time in this program. The design of a stator which uses this concept requires a controlled rate of axial sweep-back (or circumferential skew), the details of which depend heavily on the rotor wake field which varies with distance from the rotor. The selection of a stator vane number for a given rotor design is done with the familiar cutoff condition in mind; however, supersonic rotor tip speeds make it impossible to completely cut off the radiation at the tips of the stator vanes. No serious aerodynamic or structural problems were associated with the swept stator. The stator acoustic design procedure is now well-defined in terms of flow parameters needed as inputs, but the ability to predict the necessary flow parameters of the rotor wake field is presently limited.

SECTION 1

INTRODUCTION

With the advent of high bypass ratio turbofan engines, and the associated decrease in exhaust velocity, the fan stage has become the dominant aircraft engine noise source. Therefore, fan noise reduction is a problem of primary importance in the ongoing effort to evolve quieter aircraft. Furthermore, it is increasingly important that any penalty in operating efficiency incurred by noise reduction methods be minimized.

In general, noise reduction can be achieved in two ways: (1) reduction through the attenuation of propagating sound fields; and (2) reduction of the strength of the noise sources themselves. The first approach typically involves the use of absorptive duct liners and splitters, and possibly basic modifications to the inlet duct geometry. Because add-on features are required, and the duct length may be increased, the penalties associated with this approach are added weight and some direct reduction in aerodynamic efficiency. Furthermore, there may be a degree of noise generation associated with some treatment modifications, such as in-duct splitters, particularly if the inflow to the fan is disturbed.

The second approach, which is the reduction of noise at the source, can be pursued in many ways. The basic fan design parameters can be chosen to give more favorable acoustic behavior. For instance, the tip speed can be reduced, the spacing between the rotor and stator can be increased, and the number of blades and vanes can be altered to prevent the propagation of certain duct modes. Whether these options can be exercised in a given case depends on the design constraints on the performance and size of the system.

Because, in most circumstances, acoustic considerations cannot dictate the choice of basic fan design parameters, other means of noise source reduction are worthy of consideration. These other means of source reduction necessarily involve changes in the aerodynamic design of the blades and vanes. The design changes may occur either within the framework of conventional design practice, such as the use of optimized blade section properties, or may involve the exploration of novel concepts. Although development of all the design data needed for implementing novel concepts for noise source reduction may be initially difficult, the noise reduction potential of a successful concept may greatly exceed the reduction obtained by more conventional means. Of course, the final test of an acoustically successful concept must always be whether any associated penalties in performance, complexity, and system integration can be overcome or, at least, justified in relation to the benefits.

The subsonic leading edge rotor is implemented by tailoring (sweeping) the rotor leading edge to the mean inflow such that subsonic Mach number flow is achieved normal to the leading edge along the entire span, thus preventing shock generation. Previous use of partially-swept transonic rotors was done in an effort to reduce transonic drag rise and thus improve stage efficiency. Swept stators have been previously used to reduce noise, but the design concept implemented here involves tailoring the leading edge shape to a detailed estimate of the rotor wake field incident upon the stator.

The remainder of this report is organized to describe in detail the rationale for selection of the particular concepts (Sections 2 and 3), details of the design procedure used on the swept rotor blades (Section 5) and stator vanes (Section 6), residual noise sources (Section 7), and facility integration (Section 8). Appendices contain a listing of aerothermodynamic design parameters (App. A), a discussion of geometric considerations for subsonic leading edge rotor blades (App. B), a detailed discussion of acoustical considerations in the stator design (App. C), discussion of empirical estimates of fan noise levels (App. D), and a useful algorithm for estimating trace speeds of rotor wakes on stator vane leading edges (App. E).

* * * * *

SECTION 2

TRANSONIC FAN NOISE SOURCES

This section summarizes the major noise sources and mechanisms encounted with transonic fans. Typical design characteristics of single stage transonic fans are summarized in Table 1.

TABLE 1. TYPICAL CHARACTERISTICS OF SINGLE STAGE TRANSONIC FANS.

Pressure Ratio Range	1.4 - 1.8
Tip Speed	300 to 600 m/s (1000-2000 ft/sec)
Relative Rotor Tip Mach No.	1.1 - 1.8
Rotor Inlet Hub/Tip Ratio	.35 - .50
Stator Hub Mach No.	.8

The most important noise sources, which involve both the rotor and stator, are:

Shockwave noise from the supersonic portion of the rotor blades, often called multiple pure tone (MPT) noise.

Rotor/stator interaction noise caused by unsteady loading due to aerodynamic interaction (tonal and broadband noise).

Noise caused by unsteady loading on rotor blades interacting with inflow distortions and turbulence (tonal and broadband noise).

A brief elaboration on each of these sources is now provided.

2.1 Shockwave Noise

When the relative flow past the rotor becomes supersonic, the propagation of shock waves out of the inlet duct becomes an important noise source. The upstream propagation of waves from blade rows with detached and attached shock wave patterns is shown in Fig. 1 (from Ref. 1). Because the pressure field must satisfy a periodicity condition, expansion waves occur in the regions between the shock waves.

Several investigations (Refs. 2 through 7) have shown that nonlinear effects are an important factor in the upstream shock propagation process. Because nonlinear attenuation occurs more rapidly for higher initial levels, an increase or reduction of the

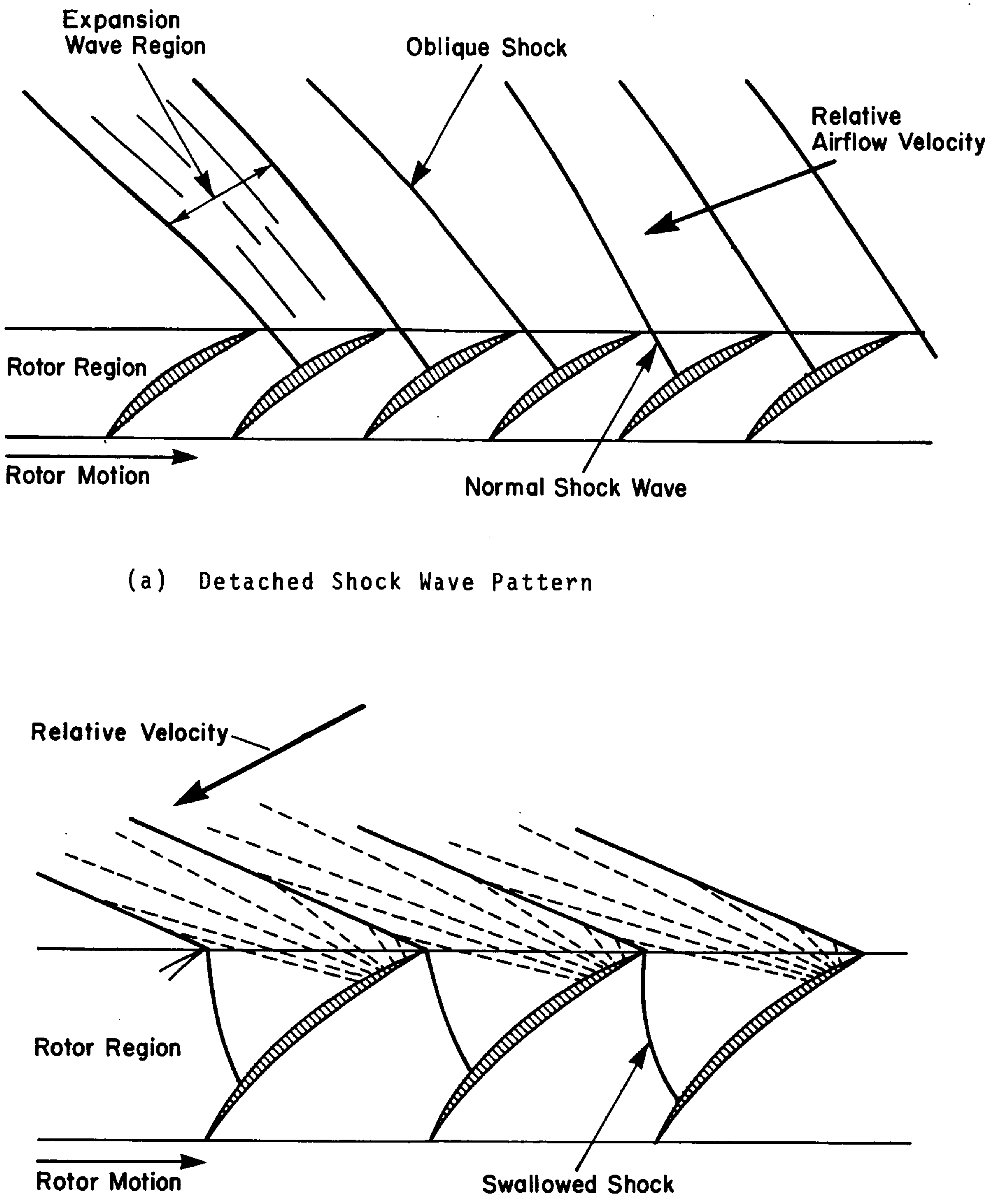

(a) Detached Shock Wave Pattern

(b) Attached Shock Wave Pattern

FIG. 1. POSSIBLE SHOCK WAVE CONFIGURATIONS FOR ROTORS IN SUPERSONIC FLOW.

shock strength at the blades does not produce a comparable increase or reduction of levels at the end of the inlet duct, or in the far field. This effect is strongest when the wave train in the duct is well ordered and can be considered nearly one-dimensional in character. The important consequence of this effect is that very substantial levels of source reduction must be achieved to guarantee a worthwhile reduction in level in the far field.

Another important consequence of nonlinear propagation is the redistribution of the shock noise spectrum from blade passage frequency and its harmonics to the rotor shaft rotation frequency and its harmonics. This redistribution occurs because of blade-to-blade differences in the initial strength and position of the shock waves. These blade-to-blade differences are caused by variations in manufacturing tolerances that may affect the circumferential location, setting angle, thickness, and camber of the blades. Because the shock train structure is inherently unstable to perturbations in strength and position, these initial disturbances need not be large. As an example, when periodic variations in shock strength occur, the stronger shocks tend to overtake and dominate the weaker shocks because of nonlinear effects. Because the variations in strength are caused by blade-to-blade differences, they are periodic in the shaft rotation speed. Thus, as the wave train propagates, the harmonics of shaft speed become increasingly important relative to the harmonics of blade passage frequency. Fig. 2 shows the redistribution of energy from blade passage frequency to shaft rotation frequency as the result of an initial amplitude perturbation to one shock in a wave train. Figure 3 shows sketches of typical noise spectra for a subsonic fan, which has no shock noise, and for a supersonic fan, where the tones at the harmonics of shaft speed are clearly present. Clearly the multiple pure tone noise due to shock wave propagation is a major noise problem.

2.2 Rotor/Stator Interaction Noise

Unsteady aerodynamic loads on rotor blades or stator vanes produced by the aerodynamic interaction between the rotor and stator are an important source of both tonal and broadband noise. The main causes of the aerodynamic interaction are the interference with the potential flow pressure and velocity fields and the interaction with the viscous and turbulent wakes from upstream blades. The potential field interaction that produces tonal noise at the harmonics of the blade passage frequency can be virtually

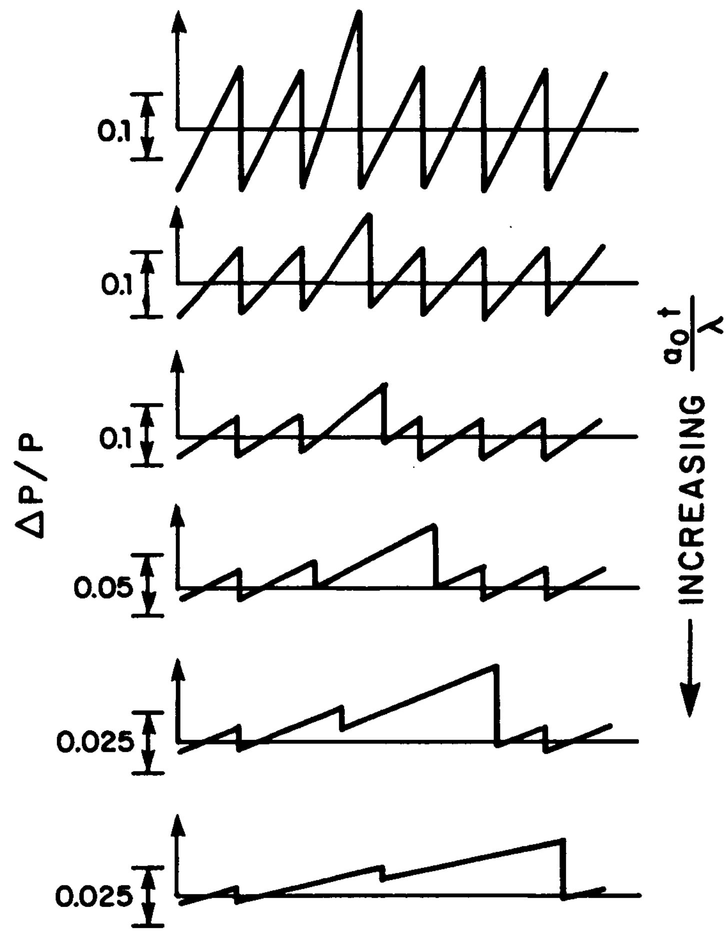

FIG. 2. DEVELOPMENT OF A SHOCK TRAIN WITH AN INITIAL DISTURBANCE (from Ref. 5).

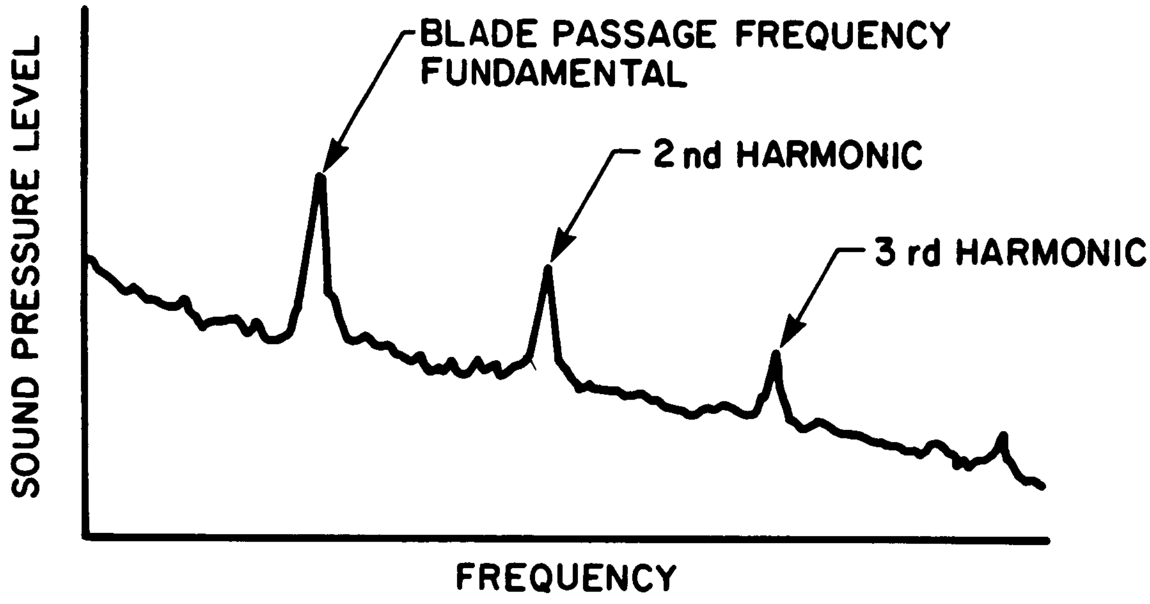

a) TYPICAL NOISE SPECTRUM FOR A SUBSONIC TIP SPEED FAN

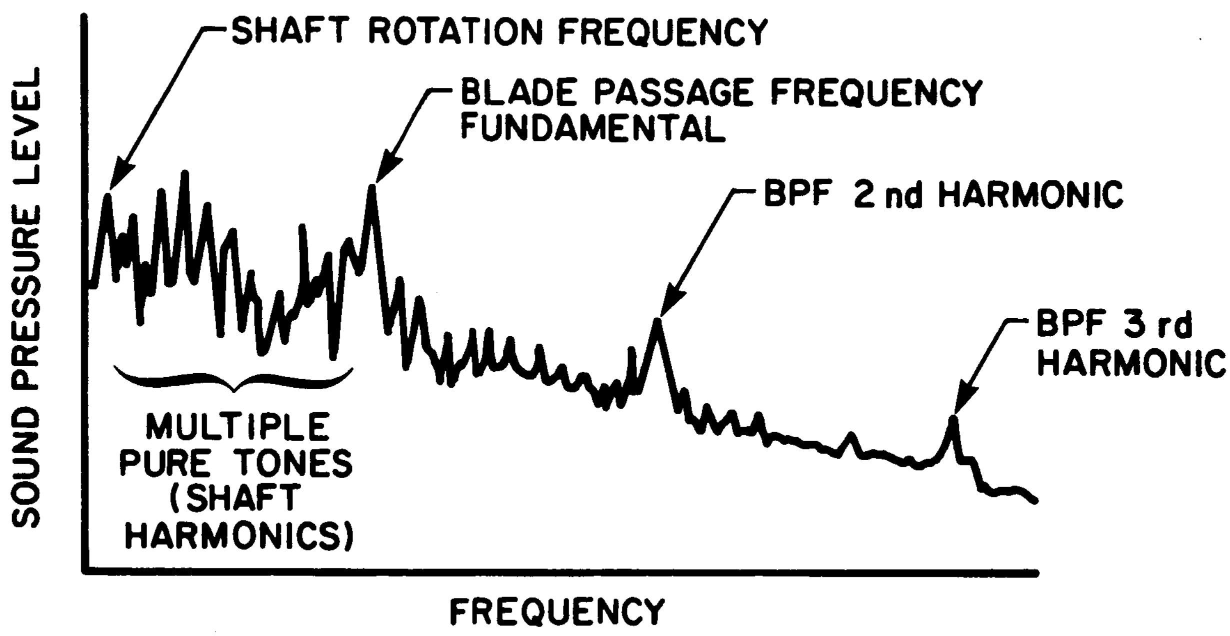

b) TYPICAL NOISE SPECTRUM FOR A SUPERSONIC TIP SPEED FAN

FIG. 3. TYPICAL FAN NOISE SPECTRA FOR SUBSONIC AND SUPERSONIC TIP SPEEDS.

eliminated by providing adequate spacing between the rotor and stator. Increasing the spacing on a high by-pass ratio fan stage is usually practical and does not involve a severe aerodynamic penalty. The interaction of the stator vanes with the "mean component"(steady velocity deficit) of the rotor wakes produces tonal noise at the harmonics of blade passage frequency, while the interaction with the wake turbulence produces broadband noise. Increasing the spacing between the rotor and stator also reduces - but does not necessarily eliminate - this noise source.

2.3 Inflow Distortion Noise

The inflow to the fan rotor typically exhibits a degree of spatial nonuniformity and a certain amount of turbulence. Sound is produced by unsteady loads on the rotor blades operating in this disturbed inflow. Steady spatial nonuniformity causes tonal noise to be produced at the harmonics of blade passage frequency, and the presence of turbulence produces broadband noise. However, if the turbulence scales are sufficiently long in the streamwise direction, then many blades will interact with a given disturbance in a similar manner, producing peaks in the noise spectrum at the harmonics of blade passage frequency. Because the basis for this noise source is a random process, the amplitude of these peaks will vary in time in a random manner. Inflow distortions have been shown to be a potentially important noise source in static fan test facilities. Their importance in an actual flight environment is less certain, since the effect of forward motion is usually to reduce certain types of inflow distortion.

SECTION 3

NOISE SOURCE REDUCTION CONCEPTS

In this section, the concepts for the reduction of rotor and stator noise sources are described. A review of the detailed analysis and design procedures associated with the implementation of these concepts in the present program is postponed to the sections later in the report dealing with detailed design.

3.1 Rotor Noise Reduction

As discussed in the previous section, two noise sources associated with the rotor are multiple pure tone noise due to shock waves and inflow distortion noise. This section describes a concept which has the potential to substantially reduce multiple pure tone noise. As an additional advantage, this concept will also help reduce the problem of inflow distortion noise.

In principle, upstream-propagating shockwave noise can be reduced by designing for careful alignment of the relative velocity, w, with the suction surface near the rotor blade leading edge, as shown in Fig. 4a. However, completely shockfree entry into the blade row cannot be achieved in conventional blading because of the finite thickness of the blade leading edge. The effect of thickness is illustrated in Fig. 4b. Moreover, since the relative inflow direction varies with the operating conditions, the proper alignment cannot be maintained in off-design operation, nor in the presence of inflow distortions. Thus, this concept presents several practical difficulties for application to aircraft fans which do not operate at a single design point.

A different approach to obtain shockfree entry into a blade row is now described. It is believed that this approach does not suffer from the shortcoming of the more conventional approach just described. Consider a blade whose leading edge is swept relative to the local inflow velcocity vector. The leading edge would in general appear swept when viewed from the side and skewed when viewed from the front. If the leading edge is swept such that the Mach number of the relative flow component normal to the leading edge is everywhere subsonic, a shockless leading edge results. In wing theory, this is referred to as a "subsonic leading edge in supersonic flow" (See, for instance, Ref. 8). In rotating applications, the radial variation in relative Mach number makes it possible, in principle, to completely avoid upstream shock wave propagation by using leading edge and surface generating line sweep which varies from hub to tip. In practice, structural constrains force some design compromises. In the present design, the structural

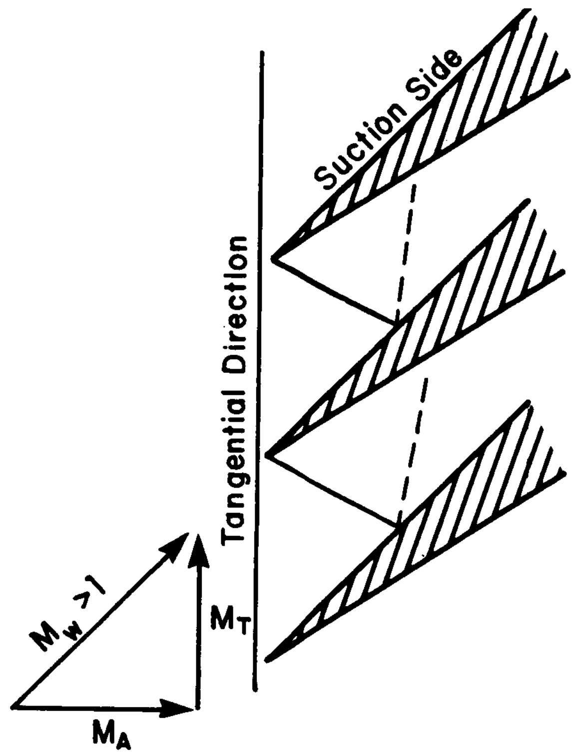

(a) Two-Dimensional Leading Edge Design Without Upstream Waves

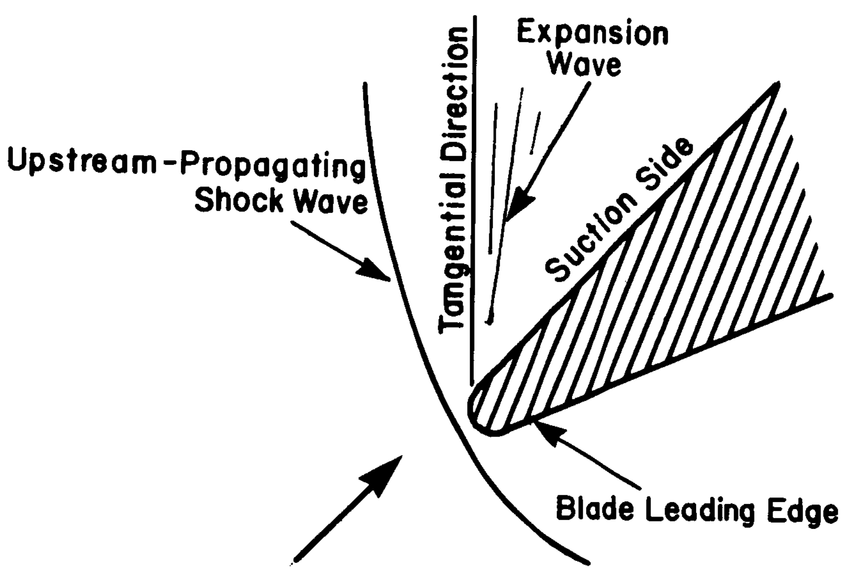

(b) The Effect of Leading Edge Thickness

FIG. 4. SHOCKLESS LEADING EDGE DESIGN AND THE EFFECT OF THICKNESS.

compromise entails the presence of a train of conical shocks upstream of the rotor associated with a sweep discontinuity in the leading edge. From the standpoint of preventing shock noise, the design can be made insensitive to operating conditions, relative flow alignment, and inlet distortions by designing the sweep distribution for the highest relative inflow Mach number to be expected; thus ensuring a lower subsonic normal Mach number component for off-design conditions. This insensitivity is considered to be a major asset.

The underlying aerodynamic idea is now reviewed. Figure 5a shows a swept wing of infinite extent subject to an incident supersonic flow. Since there is no spanwise variation in the wing geometry, the axial component has no effect. The aerodynamic forces are determined entirely by the component of the flow normal to the wingspan. If the component normal to the span is subsonic, then there are no shock waves associated with the flow over this wing. Of course, to be completely shockless, the normal component must be sufficiently subsonic that transonic flow effects do not occur in the normal flow plane. The only effect of the axial component is in the structure of the viscous boundary layer on the wing surface, but this is not related to the presence or absence of shock waves. The same ideas are applicable, of course, to an infinite span sweptback cascade. Fig. 5b shows a finite span wing sweptback to have subsonic leading edges. The aerodynamic behavior is now considerably more complicated. In particular, the presence of conical shocks at the front and rear of the wing root and at the rear of the tips is unavoidable. These isolated points on the wing are discontinuities in the otherwise subsonic edges. The conical shocks are, however, weaker than their two-dimensional counterparts and, because of their three-dimensional nature, decrease in strength with distance from their point of origin.

The application of a subsonic leading edge to a fan blade is illustrated in Fig. 5c. This illustration is simplified to its essential form, showing only the radial change in Mach number. The actual process is nonplanar because of the change in direction of the inflow with radial location. The particular case illustrated applies to a transonic fan, since part of the incident flow is subsonic. Then the leading edge can be made completely shockless even though the blade is of finite extent assuming that one is able to predict and accommodate the effects of spanwise flows (Ref. 9).

The local leading edge sweep at each radial station is chosen to be greater than the Mach angle of the local flow, i.e., the swept edge must lie within the local Mach cone. This assumes that the normal flow to the leading edge is everywhere subsonic. Because of the gradient in Mach number, the incident flow is subsonic at the base of the blade so a shock cannot emanate from this point (unlike the wing root in Fig. 3b). Hence, the blade leading edge can be entirely shockless, except for the effects of aerodynamic interference between the blade tip and the shroud which produce conical shocks. If the fan were completely supersonic, a conical shock should also occur at the root of the blade. By designing the leading edge and the other generating lines of the forward portion of the blade surface to be subsonic for the situation that produces maximum relative flow Mach number, the edge will remain subsonic under all other operating conditions. The blade leading edge would usually be designed to have a constant normal velocity (Mach number) component at all points along the span at radii (from the hub) greater than that at which the critical normal Mach number, $M_{W_{crit}}$, is reached. The critical Mach number is that normal Mach number (<1) at which thickness effects would cause the flow to become transonic.

In addition to sweepback, Figs. 6a, 6b, and 6c show swept forward and compound sweep blades that are also possible configurations. All of the blade configurations must have a conical shock at the tips caused by aerodynamic interference with the shroud. The compound sweep blade will also have a weak conical shock at the discontinuity in sweep, which is positioned somewhere along the leading edge (assuming the discontinuity lies in the region of supersonic relative inflow). Although the compound sweep blade has the acoustic penalty of introducing a weak conical shock, it offers other definite advantages. Structural considerations provide the most severe constraint to the design of high speed fans with swept blades. Fairly large excursions of the leading edge are required to implement this concept. It should be noted that the family of three-dimensional curves that satisfies the subsonic leading edge condition is not unique and therefore considerable latitude exists to determine structurally optimum shapes. Figure 7 shows the type of conical shock wave pattern for a compound sweep blade. The blade in the sketch closely resembles the design developed during the course of the project being described.

Figure 8 compares the operation of a moderately loaded blade row with and without subsonic leading edges in supersonic flow. As explained above, the subsonic edge region allows shock-free entry into the blade row. The blade rows are identical except for the addition of a subsonic leading edge region in one case. The front surface of the blade must be designed so that any shocks generated on the suction surface of

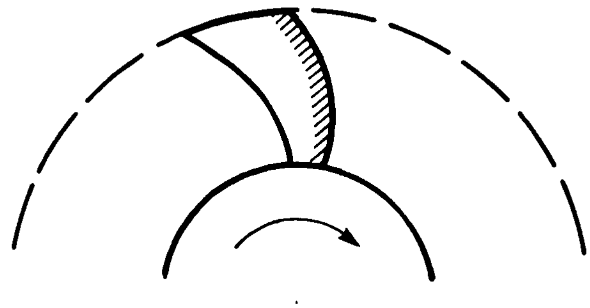

A. Swept Back

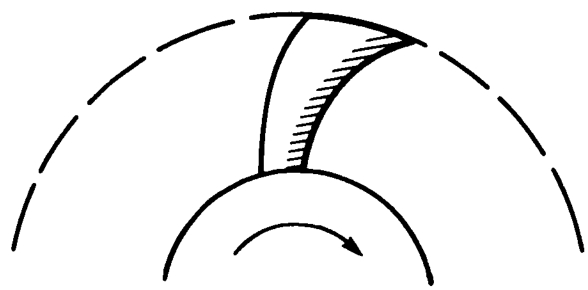

B. Swept Forward

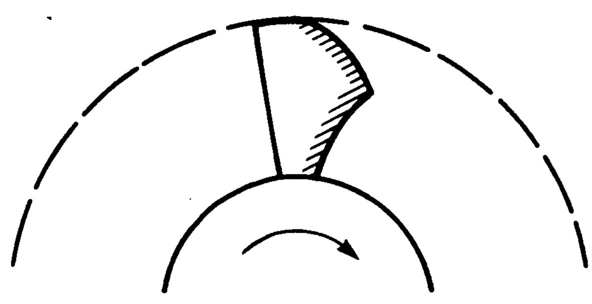

C. Compound Sweep

FIG. 6. FRONT VIEW OF SOME POSSIBLE BLADE CONFIGURATIONS WITH SUBSONIC LEADING EDGES.

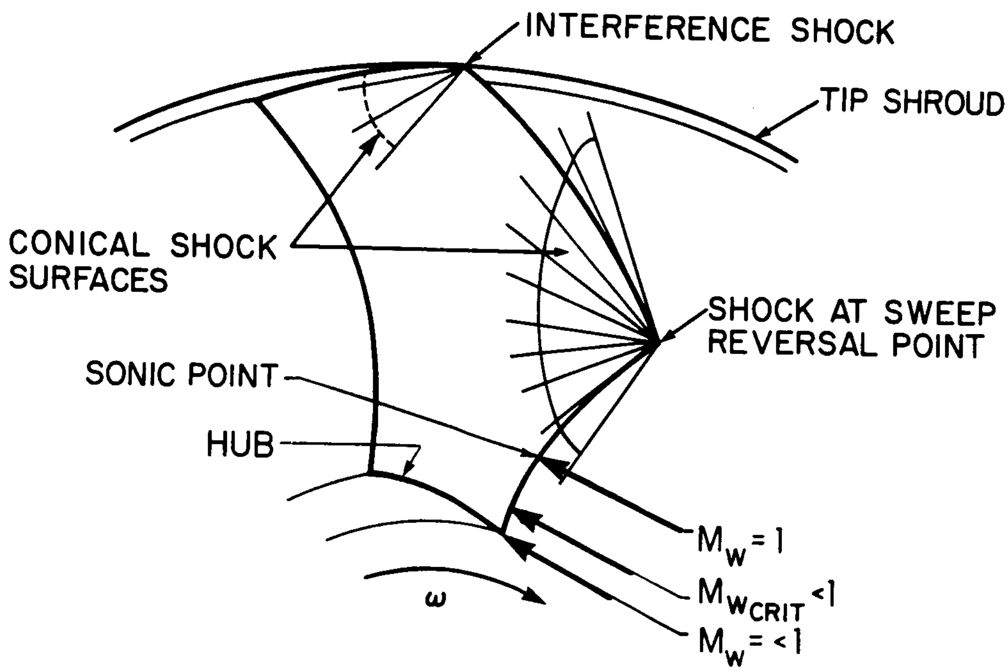

FIG. 7. CONICAL SHOCK FIELD FROM A ROTOR BLADE WITH A COMPOUND SWEEP LEADING EDGE.

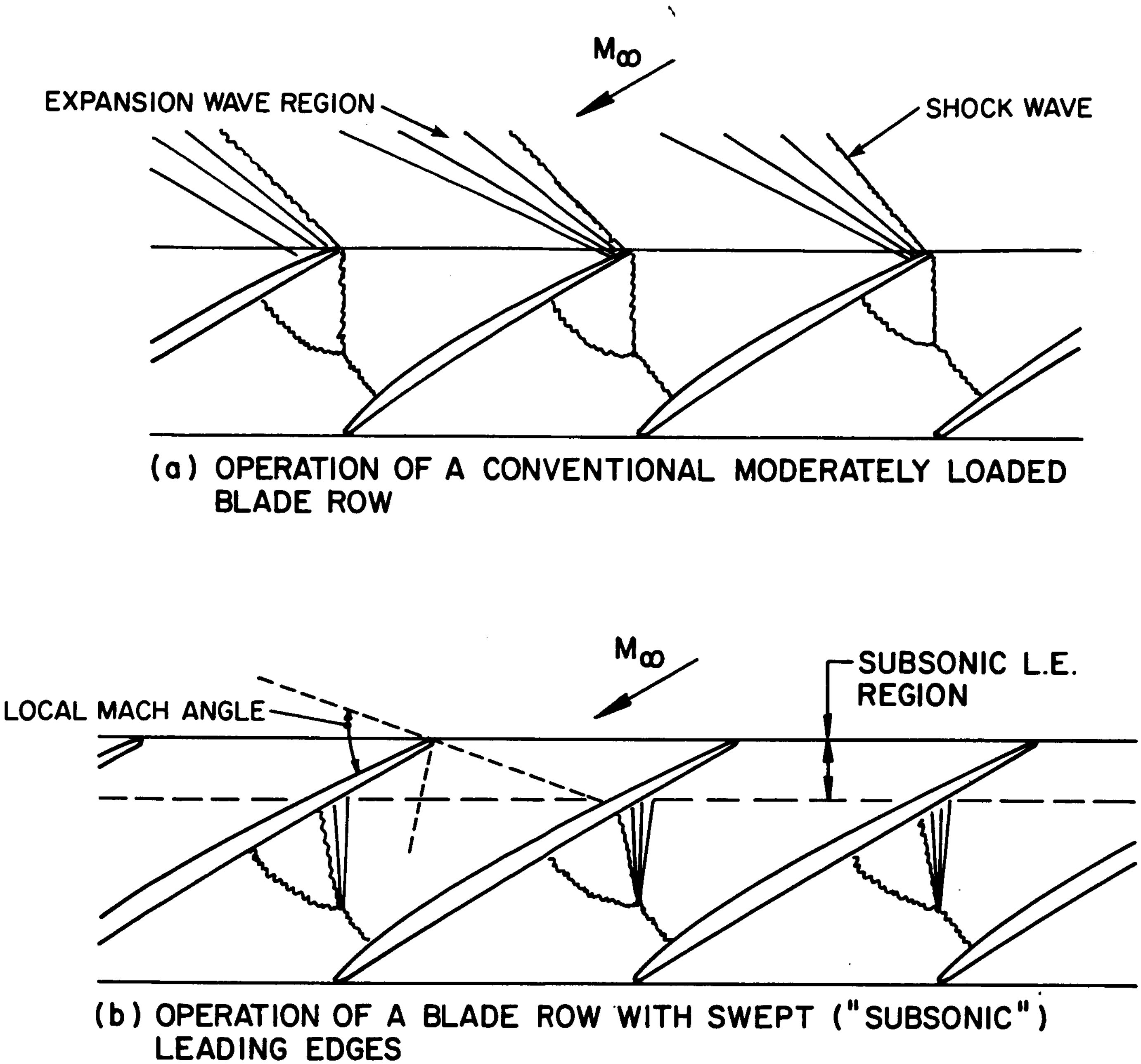

FIG. 8. COMPARISON OF THE OPERATION OF A MODERATELY LOADED BLADE ROW WITH AND WITHOUT SUBSONIC LEADING EDGES.

the blade are formed sufficiently far back that the disturbance is entirely contained in the blade row, even during off-design operation.

Using a swept leading edge also helps reduce the response of the rotor to inflow distortions, because the magnitude of the response is largely determined by the velocity component normal to the leading edge (Ref. 10). The effect of inflow distortion is most important near the tip of the rotor where the relative velocity is highest. Fortunately, the concept for sweeping the blades requires the most sweep near the tip.

3.2 Stator Noise Reduction by Leading Edge Sweeping and Blade/Vane Number Selection

Although increasing the spacing between the rotor and stator leads to some noise reduction, the aerodynamic interaction between the rotor wakes and stator vanes remains an important noise source. Further reduction by conventional means can be achieved by choosing the proper number of blades and vanes to cut off many of the acoustic spinning modes in the duct (Ref. 11). When the rotor tip speed is subsonic, the blade and vane numbers can be chosen so that all the spinning modes at blade passage frequency, and at least some of the modes at higher harmonics, are cut off. However, if the rotor tip speed is supersonic, at least one spinning mode at blade passage frequency cannot be cut off, regardless of the choice of blade and vane numbers. Since supersonic spinning speeds often occur on transonic fan designs, other means of stator noise reduction are of considerable interest.

Figure 9a illustrates the interaction of a row of stator vanes with rotor wakes when viewed on a surface of constant radius from the fan axis. The wakes can be described as flow regions with an average velocity $\overline{W}$ lower than the velocity of the adjacent fluid, upon which a turbulent perturbation velocity field Δw is superimposed.

Figure 9b shows a sketch of a three-dimensional wake/vane interaction in a fan. The structure of the viscous, usually turbulent, wakes that trail each rotor blade is complex. However, on the average, these wakes can be considered as being convected with the mean flow in which they are imbedded. The nature of the downstream mean flow is such that the convection process will distort the wakes from their original shape; namely, the downstream flow is distorted both axially and circumferentially across a given radial path, leaving the downstream pattern of the wake disturbance very much altered from the pattern at the rotor trailing edge. Suppose, for instance, the rotor is designed to give a mean flow that has a uniform axial velocity distribution and a free vortex tangential velocity distribution. Assuming

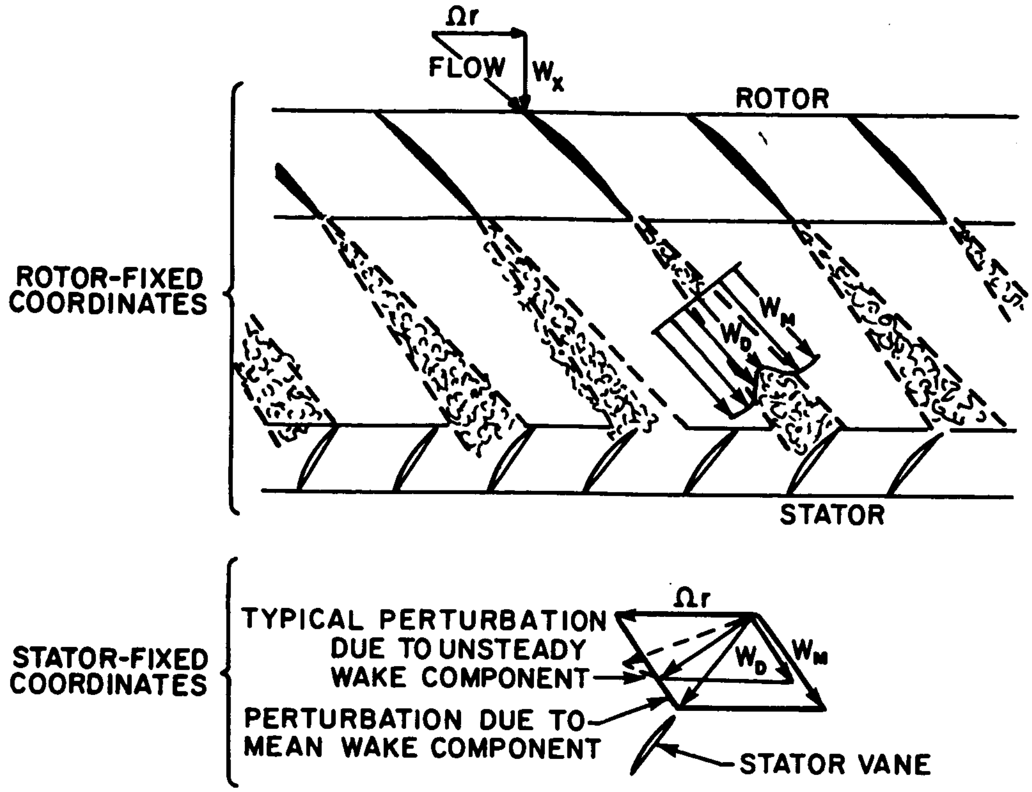

(a) The Interaction of the Stator Vane Row with the Mean and Unsteady Rotor Wake Components as Seen on a Constant Radius Surface.

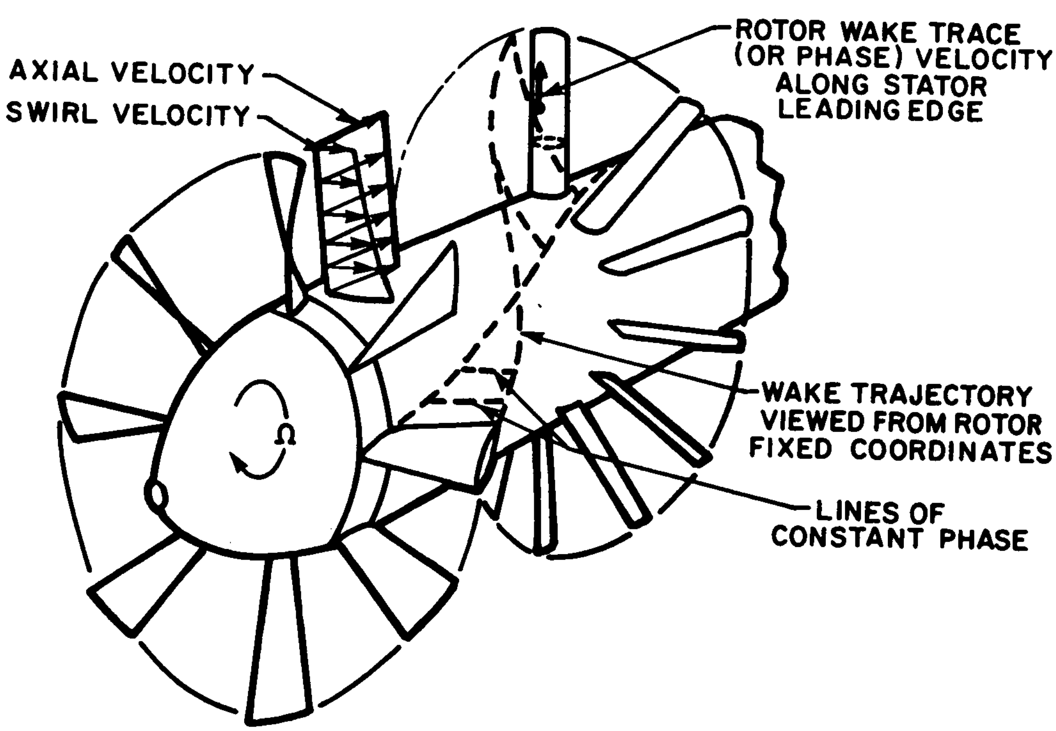

(b) A Sketch Showing the Three-Dimensional Nature of the Rotor-Wake/Stator-Vane Interaction.

FIG. 9. THE CHARACTERISTICS OF ROTOR-WAKE/STATOR-VANE INTERACTION.

the wakes are radial at the rotor trailing edge, it is clear that the tangential velocity component will act to skew the wakes over, with the hub region leading the tip region. This situation is illustrated in Fig. 9b. In this case, the interaction of a given wake with a given stator vane does not occur simultaneously all along the stator vane span. Instead, the instantaneous spanwise interaction region of a single rotor wake will extend over only a portion of any one vane and will sweep along the vane leading edge, beginning at the hub and ending at the tip. The skewing of a wake due to convection by the downstream mean flow can be sufficient to involve simultaneously portions of several stator vanes.

The shape of wake and the magnitude of its velocity components vary from hub to tip. To complete this picture of the downstream flow field, one must consider the unsteady velocity components which account for the turbulent structure of the wakes and for any other sources of inhomogenieties in the flow, e.g., inlet flow distortions, large-scale flow instabilities, and blading errors. In general, the statistical properties of these unsteady components can be expected to vary axially, circumferentially, and radially.

Both the mean and unsteady velocity components of the wake flow induce unsteady loads on the stator vanes. The mean component will produce a load distribution that travels from hub to tip, changing shape and amplitude in accordance with the radial variation of the mean flow properties and wake strength, width, and skew. Imposed on this traveling load distribution will be the unsteady effect of the turbulent structure of the wake. The end result of all sources of unsteady loading on the stator vanes is to produce tonal and broadband noise. The tonal noise is usually considered to be the more important noise source. The speed at which the point of interaction of the flow disturbance with the vane travels along the span is called the *trace speed*.

A particular source of unsteady loading will produce no significant acoustic radiation if it satisfies a subsonic and non-accelerating trace speed criterion along the vane span. The trace speed concept has been previously recognized for the problem of helicopter-blade/vortex interaction by Widnall (Ref. 12) although it has not been generally recognized in the study of fan noise.

The interaction of the wake with the vane produces a load distribution that travels along the vane. Suppose the vane is much longer than an acoustic wavelength. Following the trace of a phase front of this load distribution, acoustic radiation can occur along the vane span if the magnitude of the load changes, the phase speed changes with time, or if the phase speed is supersonic. For instance, in fan noise analyses the rotor-wake/stator-vane interaction is usually assumed to be two-dimensional (corresponding to infinite spanwise trace speed). The conditions mentioned above are *necessary* for radiation but not *sufficient*. The interaction with the acoustic field produced by the other vanes must also be considered before the actual occurrence of acoustic radiation can be established. Therefore, regions along the stator vane span can be expected to be poor radiators if the phase speeds are subsonic, nearly constant, and local levels do not vary rapidly. Other regions may or may not be efficient radiators depending on the behavior of the distribution of sources elsewhere on the stator. Furthermore, end effects at the hub and tip (within approximately one half an acoustic wavelength of the ends) makes these regions potential radiators. These considerations are discussed in Appendix C, and justified in detail in Bliss, *et al.*, (Ref. 13).

Understanding the rotor-wake/stator-vane interaction and the criteria for radiation from the span of a single vane suggests ways in which the vane configuration can be altered to achieve noise reduction. The vane should be shaped so that loads traveling along the span move at a constant subsonic speed. Assuming that the amplitude of the load distribution, moving with a phase front, is essentially constant, then radiation from the vane span will not occur (except for end-effects). The condition of a constant subsonic spanwise trace speed can be achieved by sweeping or skewing the stator vanes, as illustrated in Fig. 10. In this illustration, the lines of constant phase can be considered to be the intersection of the rotor wakes with the plane of observation (e.g., the r-θ plane in Fig. 10a, and the r-z plane in Fig. 10b). Except for the effect of shape changes, these lines travel at constant speed (rotational in the r-θ plane and rectilinear in the r-z plane) because of the rotation of the rotor. The speed at which a phase front traces the leading edge of the stator vane depends on the shape of the leading edge and the shape of the phase front. Clearly the trace speed can be controlled by either sweeping or skewing the stator vane. With this approach, radiation from the stator span can be prevented, leaving only acoustic radiation from end effects at the hub and tip of the vane. Radiation from the hub region can be cut off by the proper choice of blade and vane numbers, provided that the rotation speed of wakes at the hub is subsonic. Since the rotation speed of wakes at the stator tip will usually be supersonic for a transonic fan, the radiation from tip end effects can never be entirely cut off. Note that the rotor

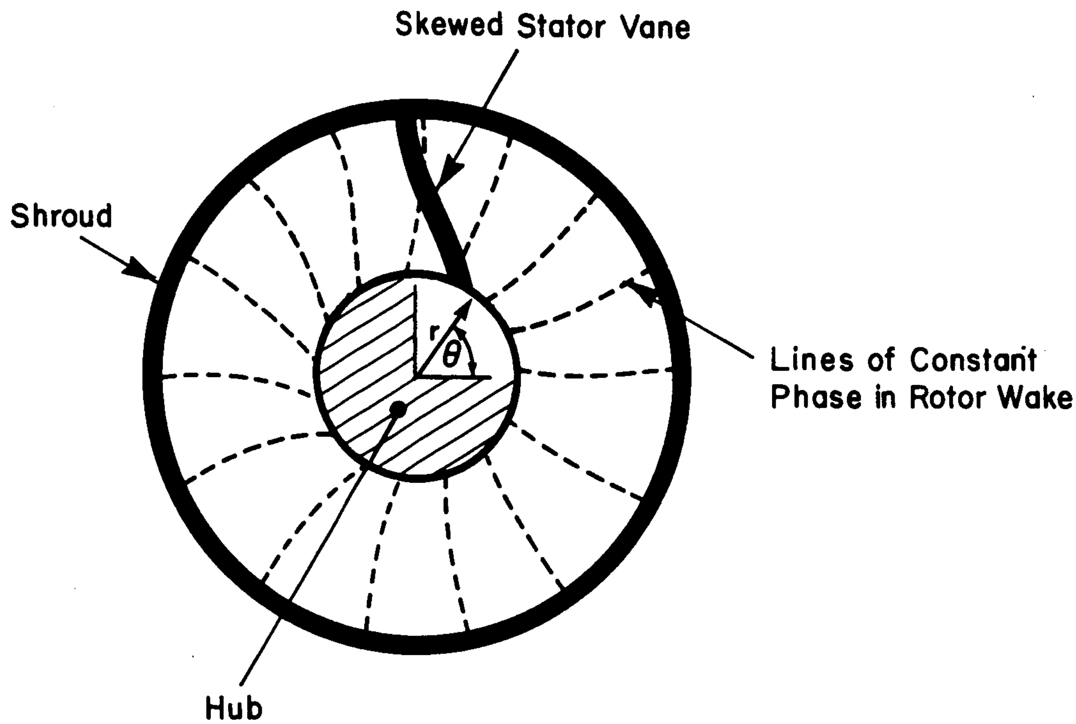

(a) Schematic Axial View (r-θ plane)-Skewed Vane

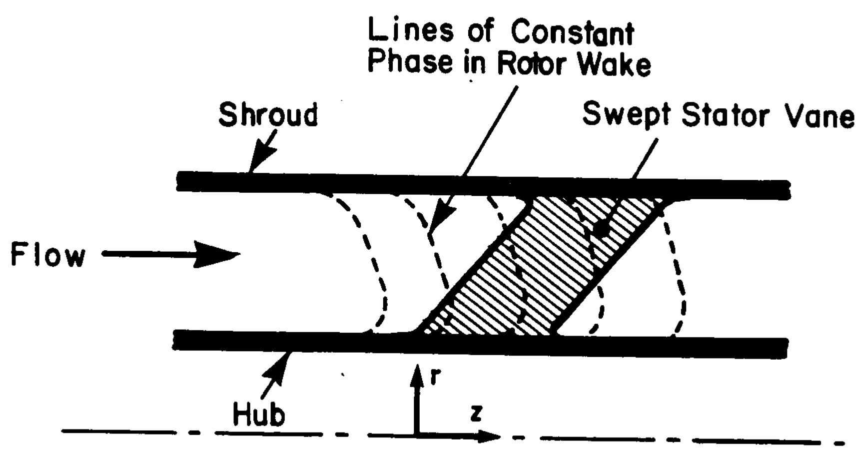

(b) Longitudinal Section (r-z Plane)-Swept Vane

FIG. 10. SCHEMATIC OF PHASE SHIFTS BETWEEN ROTOR WAKES AND SKEWED/SWEPT STATOR VANE.

wake pattern rotates with the same angular velocity Ω as the rotor. Thus, at any given radius at any downstream location between the rotor and stator, the rotation speed of the wake pattern is simply, Ωr, which is different than the swirl velocity component. This can be best visualized from rotor fixed coordinates from which the wake pattern appears "frozen."

Another, but related, way to view the effect of sweeping or skewing the stator vanes is as follows. Tyler and Sofrin (1962) have shown that for a given circumferential mode number, m, and hub-to-tip ratio, ν, the radial structure of an acoustic spinning mode can be described by an infinite series of characteristic functions. The functions in this series differ according to their radial order, μ, i.e., each function has a different number of nodes in the interval between the hub and tip. The spinning speed at which each of these functions begins to radiate is always supersonic and increases with increasing radial order. Therefore, at a given supersonic spinning speed and fixed m and σ, only a certain number of the functions corresponding to the lowest radial order will not be cut off. Vanes can be skewed or swept so that the number of wakes on a given vane is increased, raising the radial order of the load distribution on the vanes. The acoustic energy is thereby redistributed to higher radial orders, some of which will be cut off. The relationship between duct mode cut off and the constant subsonic trace criterion is discussed by Bliss, *et al.*, (Ref. 13), and in Appendix C.

SECTION 4

FAN STAGE DESIGN SUMMARY

An experimental transonic fan stage was designed and constructed using the noise reduction concepts explained in the two preceding sections. The fan uses compound sweep rotor blades designed to have "subsonic leading edges" in the region of supersonic relative inflow. The stator vanes were swept back to achieve a constant subsonic trace speed of rotor wakes along the vane span. Figures 11a, b and c show photographs of the actual fan stage. A cross-sectional view of the fan as it will appear when installed in the test facility of NASA Lewis is shown in Fig. 12. As indicated in the illustration, the fan will be tested in both forward and reverse installation arrangements in order to measure both the fore and aft noise characteristics. The design data for the fan stage is summarized in Table 2. In the remainder of the report, the detailed design procedures used in the development of the fan stage are described.

TABLE 2. FAN STAGE DESIGN SUMMARY

Stage Characteristics:

Stage Pressure Ratio, P_4/P_1 = 1.6
Mass Flow Rate, W = 31.2 kg/s (68.8 lb/sec)
Specific Mass Flow Rate: (referred to annular area at rotor inlet)

W_{as} = 199.03 kg/s·m² (40.76 lb/sec·ft²)

Polytropic Stage Efficiency, η = 0.86

Rotor:

28 Compound Sweep Blades
Leading Edge Normal Mach Number = 0.91
Tip Speed = 480 m/s (1575 ft/sec)
Relative Tip Inlet Mach Number = 1.593
Rotor Inlet Tip Radius = 249 mm (9.803 in)
Rotor Inlet Hub-Tip Ratio = 0.442
Rotor Pressure Ratio, P_2/P_1 = 1.64

Stator:

59 Swept Back Vanes
Sweep Angle = 25° At Root, 40° At Tip
Stator Inlet Mach Number = 0.80
Stator Pressure Loss $\Delta P_{3-4}/P_3$ = .025

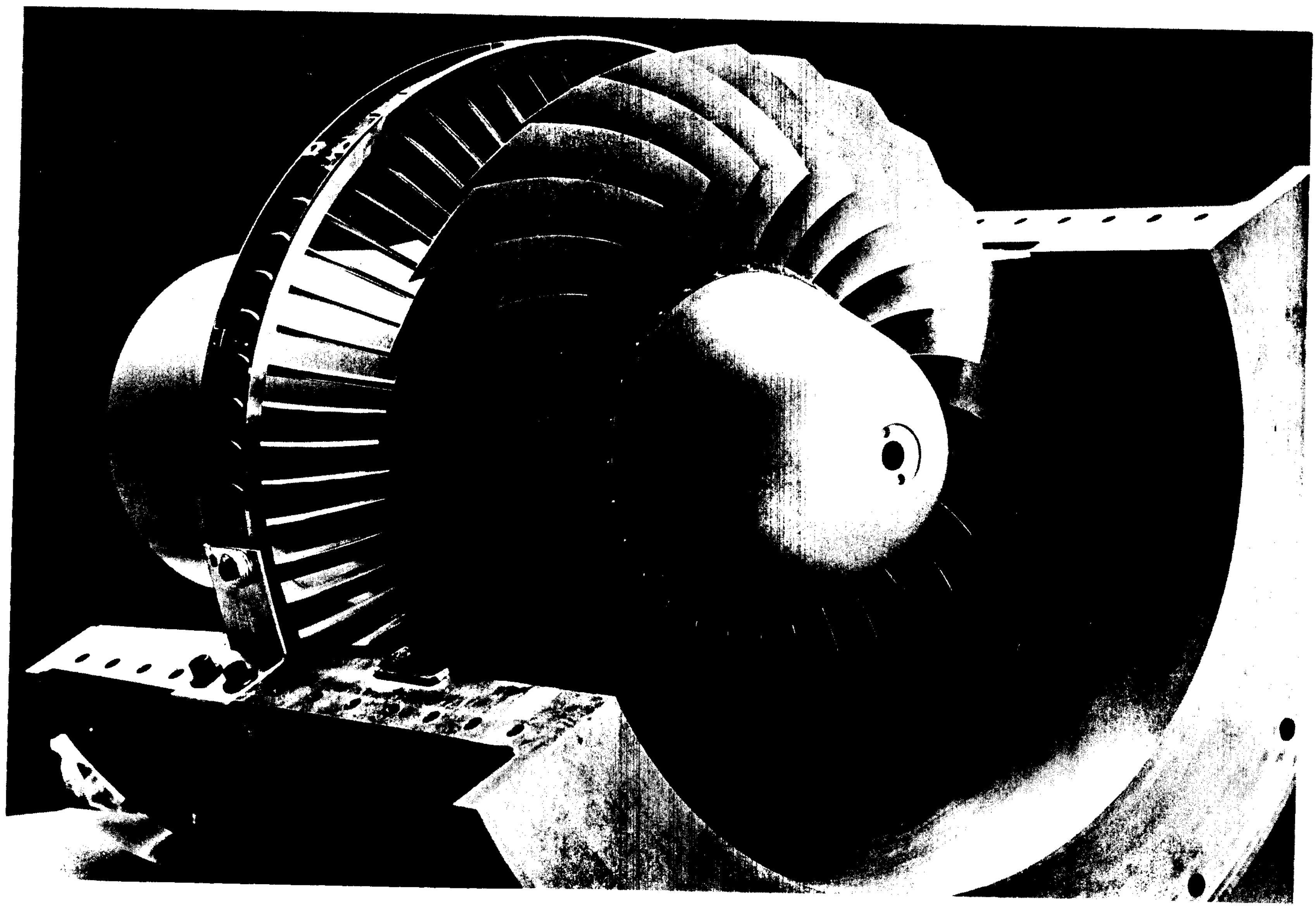

(a) 45° VIEW OF ROTOR AND STATOR ASSEMBLY FROM FRONT OF FAN

FIG. 11. PHOTOGRAPHS OF THE EXPERIMENTAL FAN STAGE

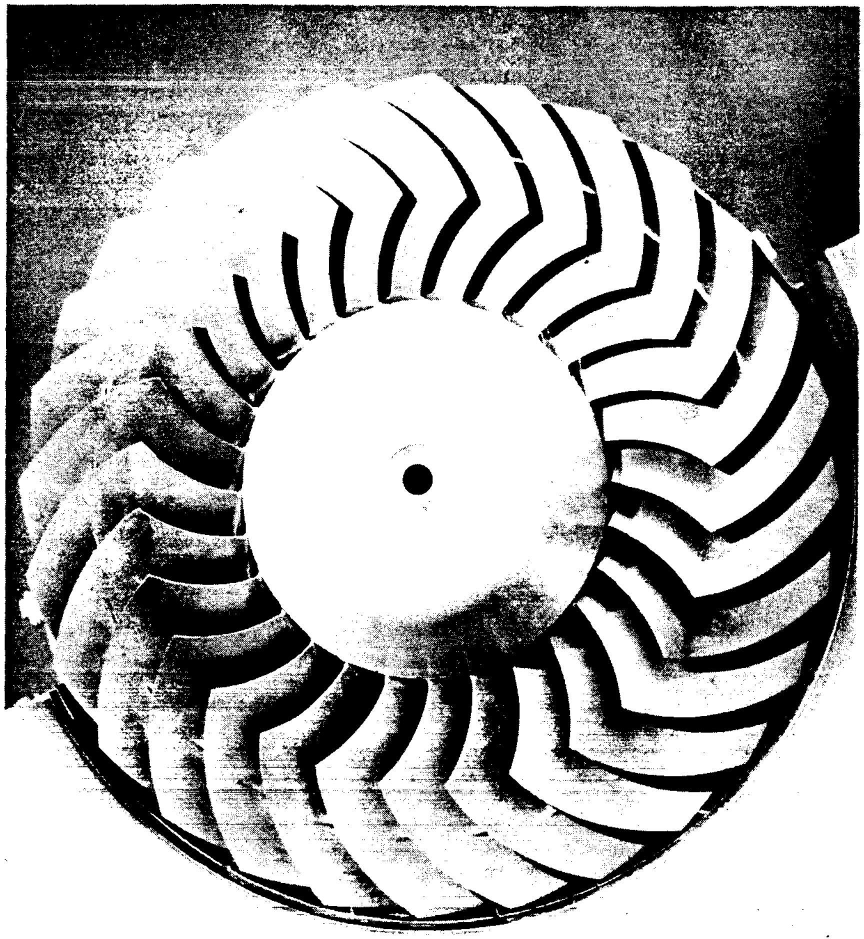

(b) Front View

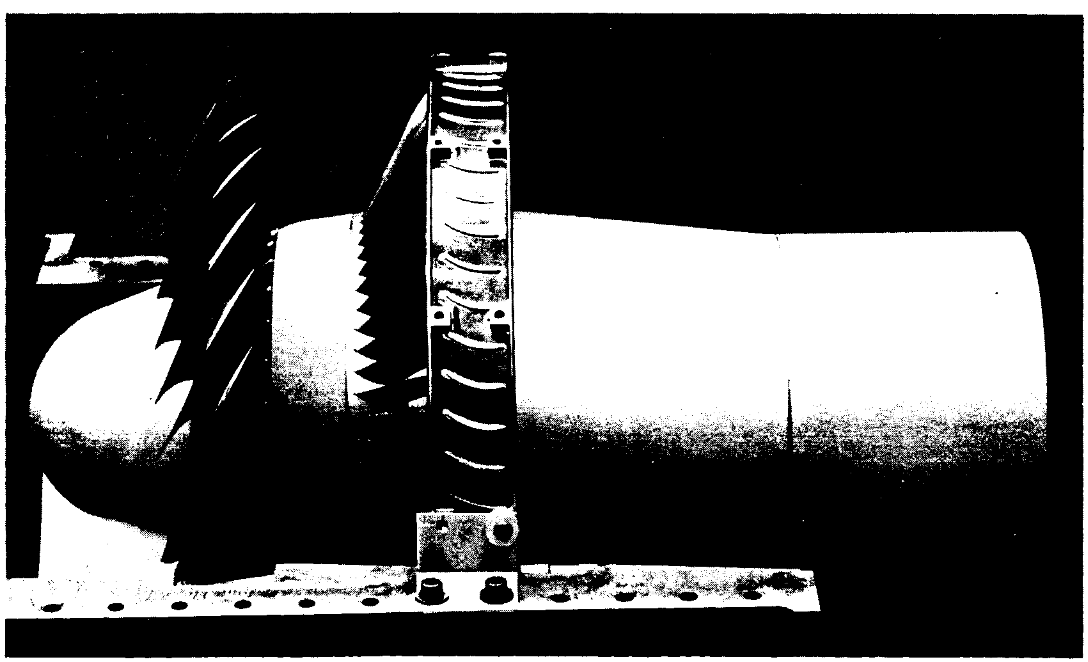

(c) Side View

FIG. 11 concluded PHOTOGRAPHS OF THE EXPERIMENTAL FAN STAGE.

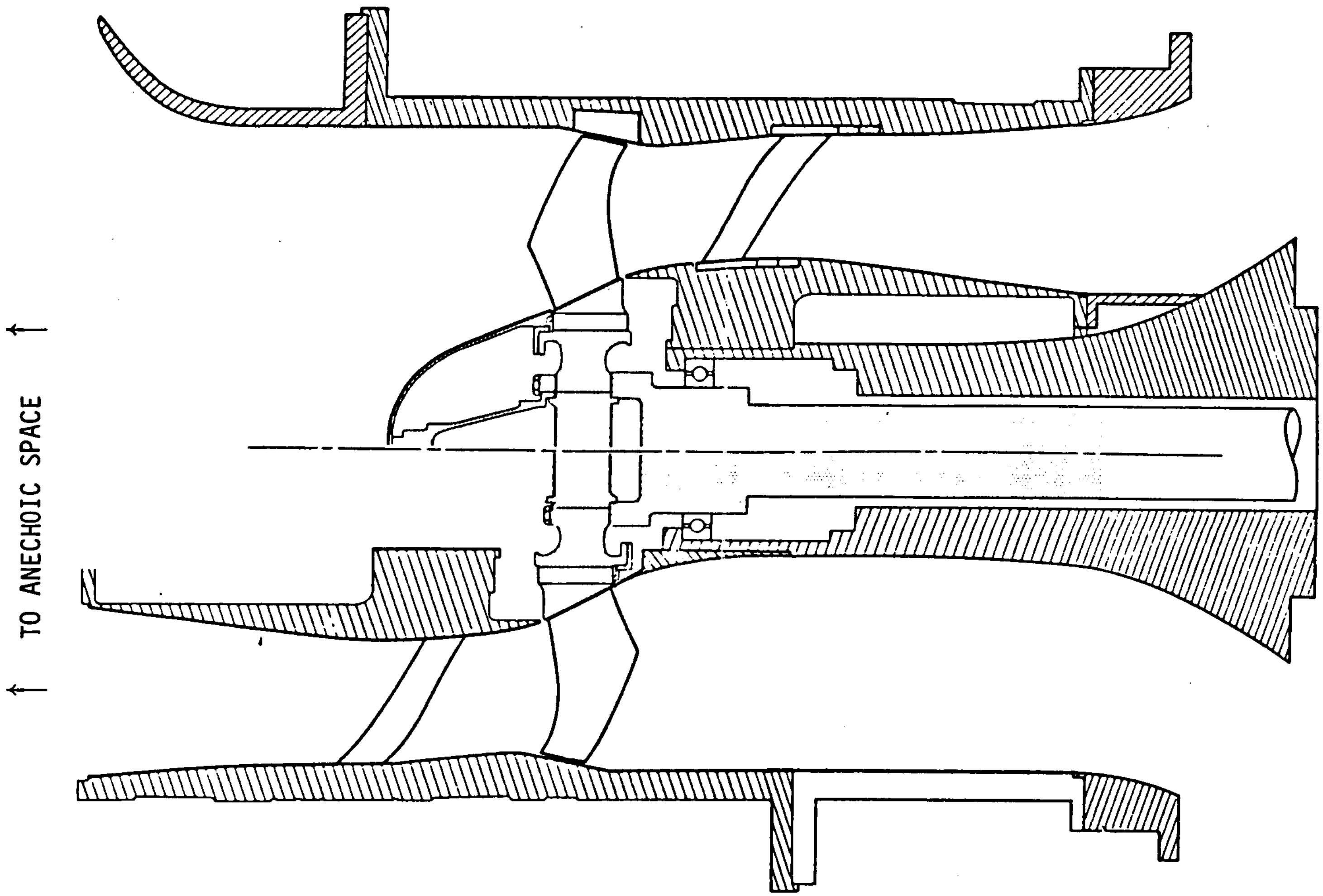

FIG. 12. FORWARD AND REVERSE INSTALLATION IN THE W2 FAN NOISE TEST FACILITY AT NASA LEWIS.

SECTION 5

DETAILED ROTOR DESIGN

This section deals with all aspects of the detailed analysis and design procedures associated with the fan rotor. The aerodynamic design of a transonic rotor having blades with "subsonic" leading edges differs significantly from conventional design practice because the acoustic, aerodynamic, and structural requirements interact strongly with each other from the very beginning of the preliminary design phase. Therefore it was necessary to conduct numerous aerodynamic-acoustic-structural design iterations to optimize and finalize a rotor configuration satisfying all the design requirements.

The overall design point data for the rotor are listed in Table 2 of the previous section.

5.1 Aerodynamic Design

Certain differences are to be expected in the aerodynamic behavior of a rotor with subsonic leading edges. Since the entry into the blade row is shock free, any shocks that occur must remain within the blade row under all operating conditions because the edge region cannot support a shock system. Furthermore, the effects of sweep may introduce other three-dimensional flow phenomena which are not present in a conventional blade design. Given these facts, the rotor aerodynamic design was undertaken using the best conventional design practice combined with an anticipation of the most important effects of swept edges. The design was carried out primarily with the use of an axisymmetric flow computer program. Conventional (two-dimensional) methods for analyzing the flow behavior within the blade row are not really adequate for the three-dimensional case of blades with swept "subsonic" edges. To handle this problem analytically requires a more general approach. Some work was done to adapt a new fully three-dimensional computer code to the analysis of flow through the blades with swept edges, but was discontinued due to schedule requirements.

An important question in the design of a rotor with "subsonic" edges is related to its surge margin. Because the edge region cannot support a shock system it was felt that the surge margin might be reduced. Such a reduction would occur, if the effective rotor operating range were limited by the condition that the shock system remain within the covered cascade region. The flow configuration in which the shock system must remain within the covered cascade, however, does not yield the maximum static pressure rise achievable in a conventional transonic-supersonic rotor. Consequently, in a stage where surge is not triggered prematurely by the stator flow conditions, a rotor with subsonic leading edges might result in a decrease of the surge margin as compared to a conventional design.

Since the rotor aerodynamic loading essentially depends upon the rotor static pressure rise, the selection of the meridional flow path was the main design step taken to achieve the desired loading levels. Meridional channel conicity and curvature through the rotor section were traded off in several preliminary design attempts. The flow calculations were performed by means of a code which solves the general equation of radial equilibrium on straight axial or slanted stations for the axisymmetric flow case taking into account the radial variation of the blade efficiency. The polytropic efficiency η assumed for the rotor blading is shown in Fig. 13, where η is derived from

$$\frac{P_2}{P_1} = \left(\frac{T_2}{T_1}\right)^{(\eta)\left(\frac{\gamma}{\gamma-1}\right)}$$

It was found that the comparatively large channel conicity across the rotor section required by the high design pressure ratio $P_4/P_1 = 1.6$ and the wall curvature needed at rotor exit to prevent excessive channel contraction in the free space between rotor and stator, combine to shift the maximum rotor static pressure rise from the tip towards the midspan location, where the shock system has the greatest tendency to move upstream into the uncovered cascade region because of the lower relative inlet Mach number. The main preliminary design effort consequently was directed toward minimizing the static pressure rise at the critical midspan location.

The optimum channel configuration is shown in Fig. 14. The flow conditions are summarized on the Aero design program (R-121) input and output printout attached in Appendix A.

Figure 15a shows the distribution of the rotor static pressure ratio P_2/P_1 over the channel height, together with the relative inlet Mach number M_{w_1} and the corresponding normal shock pressure ratio $\hat{P}_1/P_1$, which is roughly equivalent to the static pressure ratio obtained in the front portion of a conventional cascade with a normal shock attached to the leading edge.

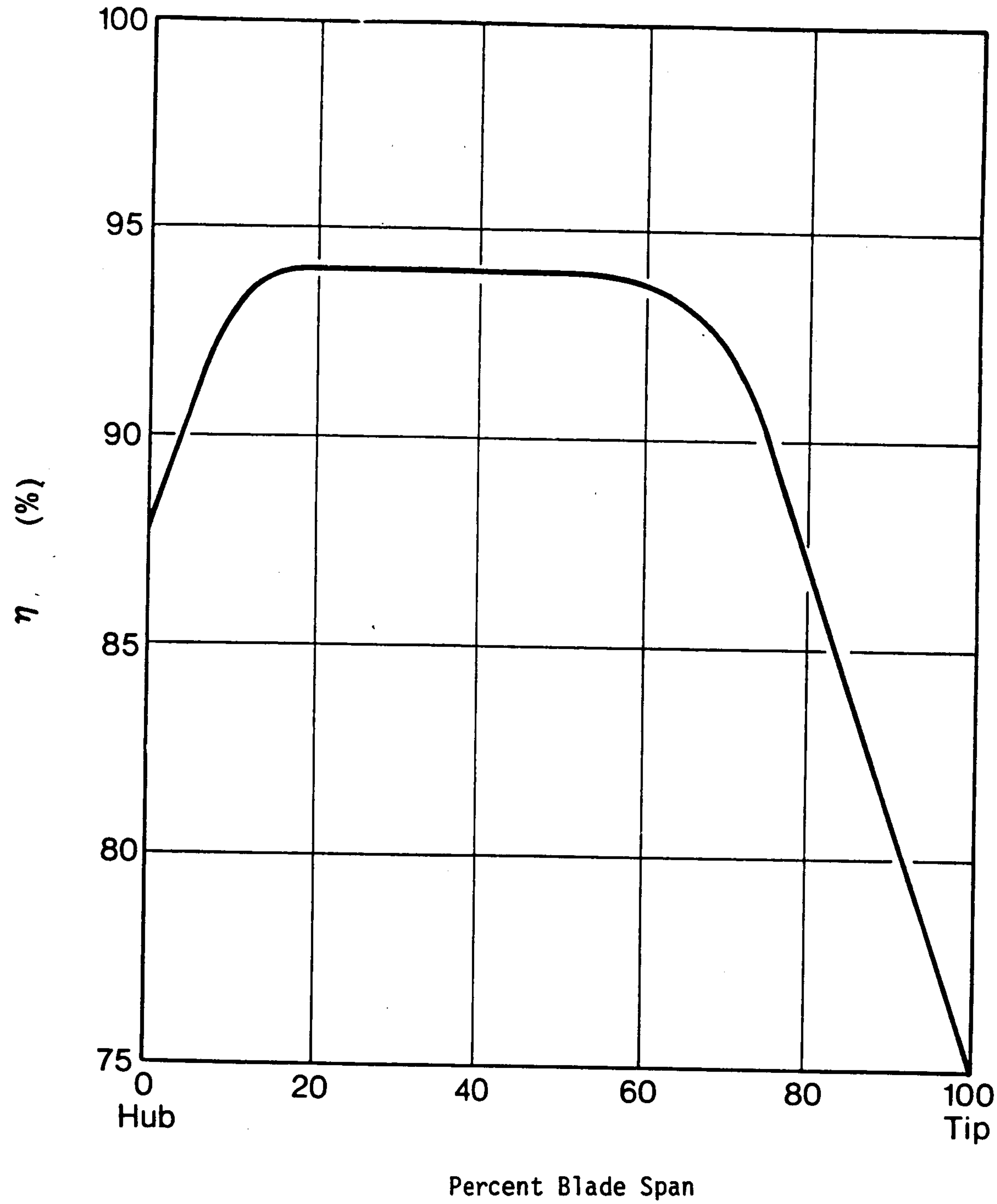

FIG. 13. ROTOR POLYTROPIC EFFICIENCY η

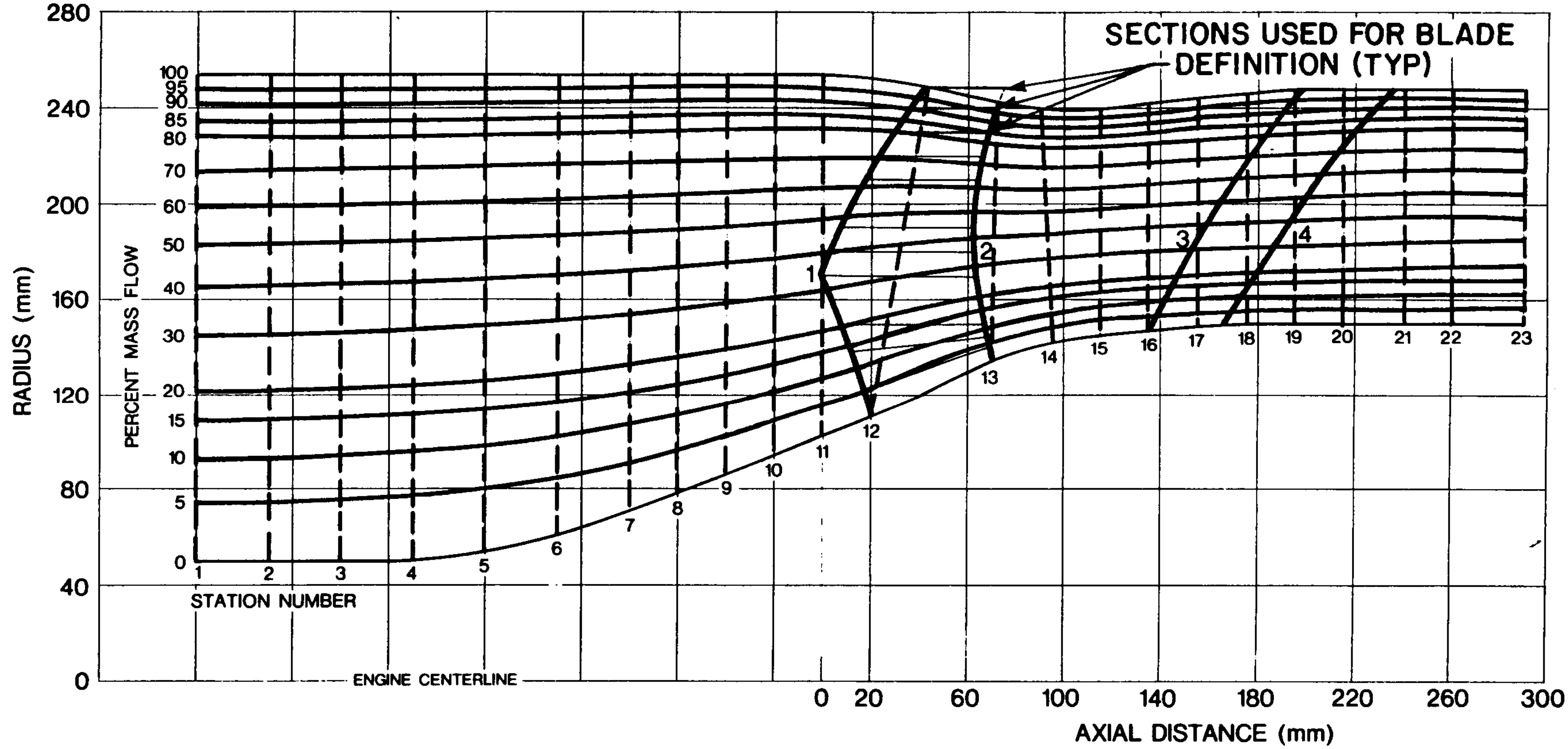

FIG. 14. MERIDIONAL FLOW PATH.

Three types of operating conditions can be distinguished along the rotor blade span.

(a) From the hub to the sonic radius $r_{1(M_{W_1} = 1)}$, the rotor static pressure rise is achieved essentially by subsonic relative flow deceleration and centrifugation.

(b) From $r_{1(M_{W_1} = 1)}$, to $r_{1(P_2/P_1=\hat{P}_1/P_1)}$ the rotor static pressure rise must be achieved through a channel-contained normal shock or a pseudoshock system followed by subsonic relative flow deceleration. The radial distribution of the rotor static pressure ratio P_2/P_1 determined how far this operating condition extends beyond the sonic radius. In the present case, it extends roughly from the 12% to the 40% mass flow streamline, or from 20% to 53% of the span, i.e., slightly beyond the point of sweep reversal. The maximum inlet Mach number in this blade section remains below the 1.3 level at which the interaction of normal shock with a turbulent boundary layer produces extensive flow separation ($\hat{P}/P = 1.8$). If minor flow separation does occur in the upper portion of this region, the flow will reattach to the blade because of the large solidity provided in the vicinity of the point of sweep reversal. Consequently, it is expected that the design flow conditions will be obtained over this critical span section by a shock configuration located in the forward, yet still covered portion, of the cascade.

(c) In the upper blade section, P_2/P_1 is smaller than $\hat{P}_1/P_1$, and the shock system consequently moves progressively toward the rear portion of the cascade. Since no shock is attached to the leading edge, the flow conditions are essentially similar to those in the diverging section of a converging-diverging nozzle in the supersonic off-design operating range.

Figure 15b schematically shows the meridional projection of the rotor blade and the anticipated shock/pseudoshock interception area on its pressure and suction sides. The main question pertains to the rotor surge margin, i.e. the extent to which the tip region will be allowed to increase its pressure ratio beyond the design value by forward shifting of the shock configuration before (i) flow separation occurs at the hub, or (ii) the shock system at midspan is forced into the uncovered cascade region.

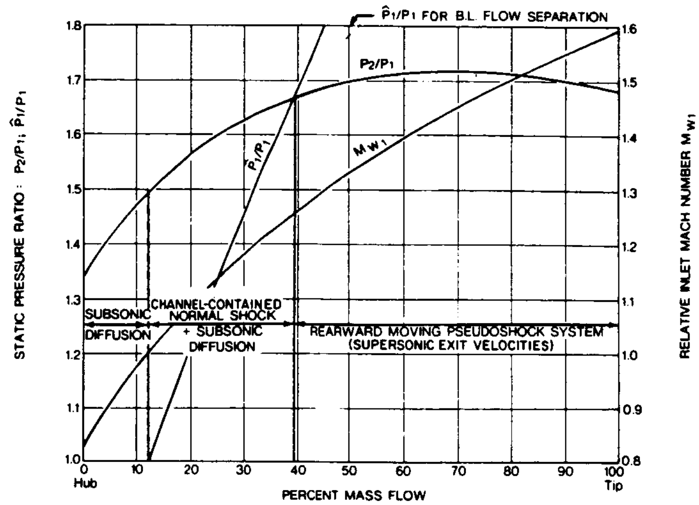

FIG. 15(a). ROTOR FLOW CONDITIONS: SPANWISE DISTRIBUTION OF STATIC PRESSURE RATIO AND INLET RELATIVE MACH NUMBER (Design Point).

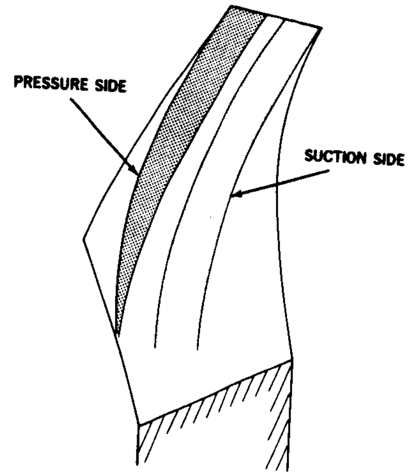

FIG. 15(b). ROTOR BLADE SHOCK/PSEUDOSHOCK INTERCEPTION AREA (Schematic).

5.2 Description of the Aero-Structural Design Interaction Problem

The problem of achieving acceptable stress levels is much more difficult for a rotor with swept leading edges than for a conventional design. The aerodynamic and structural requirements for the rotor blade are therefore closely coupled. Within the aerodynamic constraints, a number of design iterations were required to achieve acceptable stress levels and to optimize the design. The major aerodynamic constraints are that the rotor meet the design performance requirements and that the normal component of flow to the leading edge be maintained at a certain subsonic value. Because of the gradient of relative inflow Mach number, the angle of sweep must increase toward the tip to meet the condition of a subsonic normal component. In the present case, the maximum normal component Mach number was chosen to be 0.91 along these leading edges (actually lower near the hub). The value of 0.91 was chosen as a goal since it represented a normal Mach number sufficiently below sonic to avoid thickness-related shocks. Lower values can be chosen, but the severity of the blade leading edge excursions increase as the normal Mach number is lowered. For the fan design tip speed, the excursions of the swept leading edge are large and it was necessary to use a compound sweep configuration to minimize bending stresses. The major variables available to control blade stresses are the location of the sweep reversal point, the local section properties of chord length, maximum thickness, thickness distribution, and the stacking of the blade sections.

Because of the large leading edge excursions, the centers of gravity of the blade sections can no longer be stacked on a radial line. In addition to the centrifugal tensile stresses, large bending moments about both principal axes of inertia of the blade sections were found to occur (Fig. 16). Achievement of acceptable stress levels required the use of a carefully chosen sweep reversal point and the development of an effective nonradial stacking procedure.

Typically, the most critical problem was the bending moments about the minor axis of inertia, and a special stacking procedure was used to minimize these moments. A near-optimum procedure for nonradial stacking is as follows. The blade sections were stacked starting at the tip and moving inward. The addition of each incremental blade section was made so that the center of gravity of the entire portion of the blade above this section falls on the axis of minimum inertia of the new section. The center of gravity of the new upper portion was then reevaluated before the next incremental section was added in the same manner. This procedure nearly minimizes the critical bending stresses around the axis of minimum inertia. The result is not completely optimum because of the

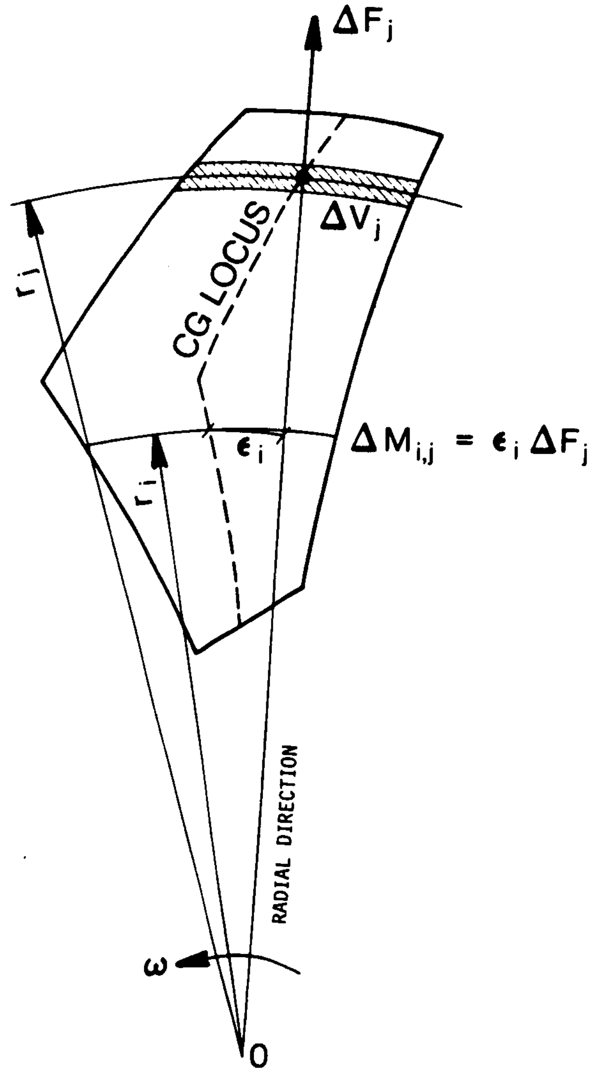

FIG. 16. BLADE CENTRIFUGAL FORCES AND MOMENTS.

complexity of the actual situation in which the stresses are determined by the complex interaction of many effects. Further improvements were made by iterative changes around the result of the above stacking procedure, particularly with the intention of relieving local stress concentrations. To the extent that high stresses arise due to bending around the axis of maximum inertia, these can be relieved largely by changing the location of the sweep reversal point and varying the local section chord and thickness.

5.3 Determination of the Subsonic Rotor Leading Edge Geometry

At each leading edge point, the relative Mach vector M_{W_1} defines a Mach cone. To a prescribed value of the subsonic velocity component $M_{W_{1L}}$ perpendicular to the leading edge, there corresponds a coaxial cone with smaller aperture. The subsonic leading edge elements must only satisfy the condition that they lie on such cones. Their direction otherwise is arbitrary.

Referring to Fig. 17, a particular sweep direction can be defined by specifying that each leading edge element be swept in the plane formed by the relative inlet velocity, W, and the radius (W-r) plane. This yields the shortest leading edge line from hub to tip, since it maximizes the radial projection of every leading edge segment.

Sweeping in the W-r plane however, does not result in a blade with minimum stresses. The resulting stacking of the CG's of the profiles in fact was shown to generate substantial bending moments around their axis of minimum inertia. The main parameter used to minimize bending stresses is the lateral sweep angle, ν, between the radial plane passing through the leading edge element dl and the W-r plane. The situation is illustrated in Fig. 17. The geometric analysis used for this design is described in Appendix B, and only some pertinent results are cited below. They are expressed by the two following equations for the cylindrical coordinates θ_L and z_L of the leading edge points in function of the relative flow angle β_1, the lateral sweep angle ν, the slope ε_{W_1} of the relative velocity and the projection μ'' of the Mach cone angle μ in the W-r plane (see Appendix B):

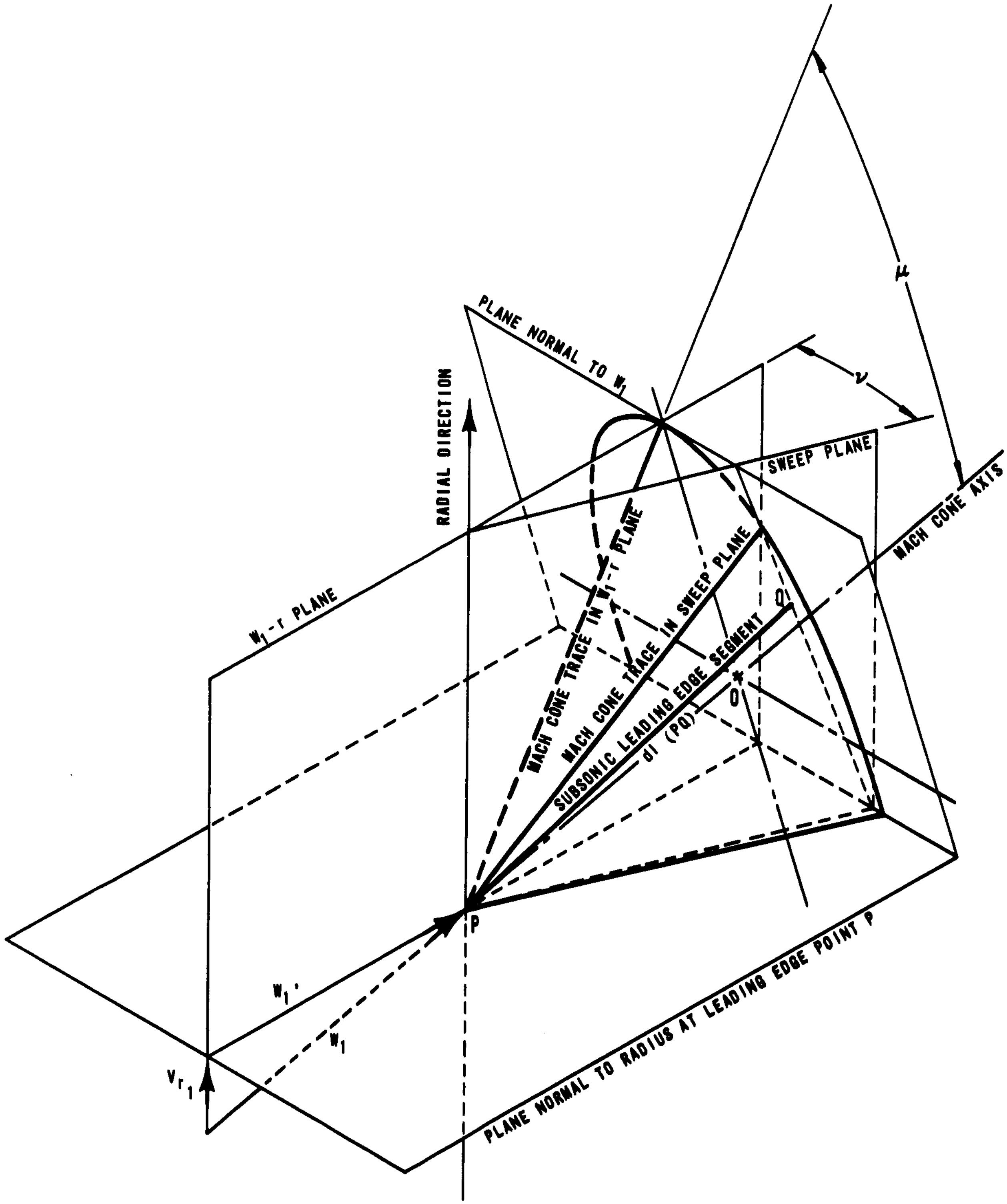

FIG. 17. SONIC SWEPT LEADING EDGE ELEMENT.

$$\theta_L(r) = \theta_{L_1} \pm \int_{r_{M_W}=1}^{r} \left[\frac{\cos(\beta_1 + \nu)}{\tan(\mu'' \pm \varepsilon_{W_1})} \cdot \frac{1}{\rho\cos\nu}\right] d\rho \qquad (1)$$

$$Z_L(r) = Z_{L_1} \pm \int_{r_{M_W}=1}^{r} \left[\frac{\sin(\beta_1 + \nu)}{\tan(\mu'' \pm \varepsilon_{W_1})\cos\nu}\right] d\rho \qquad (2)$$

$$\varepsilon_{W_1} = \sin^{-1}\left(\frac{V_{r_1}}{W_1}\right) \qquad (3)$$

The relation between μ" and μ is given by the formula

$$\tan\mu'' = \frac{\pm \sin\varepsilon_{W_1} \cos\varepsilon_{W_1} \tan^2\nu + \sqrt{\tan^2\mu(1+\sin^2\varepsilon_{W_1}\tan^2\nu) - \cos^2\varepsilon_{W_1}\tan^2\nu}}{1 + \sin^2\varepsilon_{W_1}\tan^2\nu} \qquad (4)$$

In the above relations the (+) sign applies for backward, the (-) sign for forward sweep.

The formulae define a sonic leading edge, i.e., leading edge points lying on the Mach cones of the adjacent points. A subsonic leading edge is simply obtained by using in the formulae μ values corresponding to relative Mach numbers increased by a factor $f = 1/M_{1_L}$, i.e. $M^1_{W_1} = M_{W_1}/M_{W_{1_L}}$ where

$M_{W_{1L}}$ is the subsonic Mach number of the relative velocity component perpendicular to the leading edge. This simple relationship is illustrated in Fig. 18.

The second design parameter used to minimize the bending stresses was the sweep reversal radius. By proper selection of the point of sweep reversal, the center of gravity of the blade can be located in such as way as to project radially on, or near, the axis of maximum inertia of the hub section. From a structural viewpoint, the compound sweep blade of Fig. 6 could be considered as a blade with hub and tip sections designed and stacked according to conventional practice and fitted with an additional front section to materialize the subsonic leading edge configuration. The above CG stacking condition then could be fulfilled by similarly fitting a rear section to restore the symmetry of the mass distribution with respect to the axis of maximum inertia of the profiles. This, however, would maximize the additional blade mass and the elongation of the profile chord lengths required by the compound sweep design, which is structurally and aerodynamically undesirable. Proper selection of the radius of sweep reversal thus is necessary to ensure minimum blade stress and aerodynamic performance penalties. Adjustments of the profile chord lengths can be used only to compensate for a slightly off-optimum location of the sweep reversal point. Accordingly, the optimum stacking should yield hub stresses exceeding those of a conventional blade only by the contribution due to the blade mass added to incorporate the subsonic leading edge configuration.

From the preliminary design iterations, the meridional projection of the subsonic leading edge line and its sweep reversal point were known with sufficient accuracy to define the radial distribution of the relative Mach numbers M_{W_1} (r) and the relative flow angles β_1 (r) and ε_{W_1} (r) at the leading edge for final design. Those data were interpolated on the streamlines between stations 9, 10, 11, 12 of the R-121 flow calculation. (For the axial station nomenclature, refer to Fig. 14 and Appendix A.) Table 3 presents the interpolated inlet Mach numbers M_{W_1}, together with the selected Mach factors f and the corresponding Mach numbers $M_{W_{1L}}$ of the relative velocity component perpendicular to the leading edge and M_{W_1}' of the relative velocities, introduced in Eqs. 1, 2 and 4.

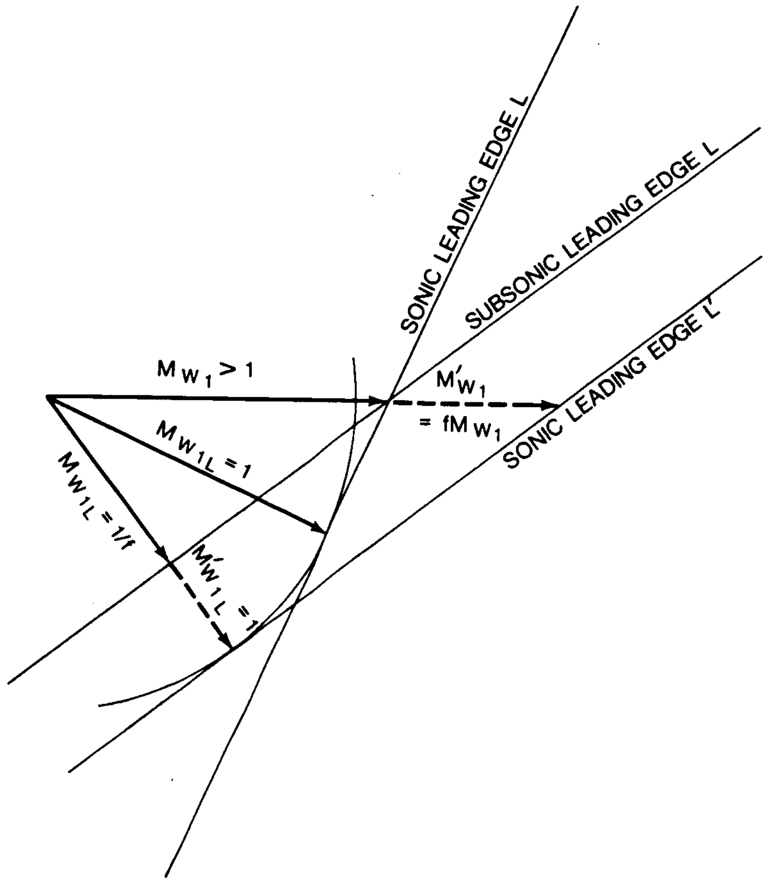

FIG. 18. SONIC AND SUBSONIC LEADING EDGES.

TABLE 3. Interpolated Aerodynamic Data for Final Subsonic Leading Edge Design

Leading Edge Radius (mm)	Relative Mach Nr. M_{w1}	Mach Factor f	$M'_{w1} = f\,M_{w1}$	M_{w1_L}
110	.829	1.206	1.000	.829
116	.859	1.170	1.005	.855
122	.888	1.140	1.012	.877
129	.924	1.118	1.033	.894
136	.959	1.107	1.062	.903
143	.994	1.102	1.095	.908
150	1.028	1.100	1.131	.909
160	1.078		1.186	
170	1.127		1.240	
180	1.185		1.304	
190	1.242		1.366	
200	1.302		1.432	
210	1.363		1.499	
220	1.422		1.564	
230	1.481		1.629	
240	1.539		1.693	
249	1.588	1.100	1.747	.909

It will be seen that forward sweep starts immediately at the hub by setting $M'_{W_1} = 1$, i.e., by requiring that $M_{W_1} \equiv M_{W_{1L}} = .829$ at the hub section. The selected values of $M_{W_{1L}}$ increase gradually to .91 at approximately 1/3 of the span in accordance with the decreasing thickness and camber of the profiles, and then remain constant up to the tip section.

The cylindrical coordinates in the lateral sweep angle ν of the subsonic leading edge line are listed in the outlined columns of Table 4, which reproduces the input/output data of the computerized calculation.

5.4 Rotor Blade Profile Definition and Stacking Procedure

The optimum profile stacking configuration can be described as follows: At every blade section along the span, the CG of the upper blade portion projects radially on or near the axis of minimum inertia of that section. This means that the radial projections of the individual CG's of the upper profiles must straddle the axis of minimum inertia of the lower section (subsequently referred to as i-straddling). This is achieved by iterative selection of the lateral sweep angle ν along the span. During that iteration, the radial location of the point of sweep reversal initially selected is kept unchanged. When adequate i-straddling is obtained for all blade sections, the CG straddling with respect to the axis of maximum inertia (I-straddling) of the hub section is checked and the radial location of the point of sweep reversal modified accordingly.

The first preliminary design investigations were carried out with double circular arc profiles. In the course of the profile stacking iterations, it appeared that using airfoil sections with CG's shifting progressively backward in the lower span portion with forward leading edge sweep, and forward in the upper portion with backward sweep, i.e., a blade configuration with minimum chordwise excursion of the profile CG's, could substantially contribute to minimize bending stresses.

A simple analytical blade thickness distribution was used to simplify the design iterations involving changes in section properties to help relieve stresses. The thickness distribution is written in the following parametric form

$$t(x) = kx^n (c-x) \qquad (5)$$

TABLE 4. CYLINDRICAL COORDINATES AND LATERAL SWEEP ANGLE OF THE SUBSONIC ROTOR LEADING EDGE LINE.

	SWEEP INDICATOR	RADIUS (METERS)	RELATIVE VELOCITY (M/SEC)	RADIAL VELOCITY (M/SEC)	RELATIVE MACH NO.	ANGLE BETA(1) (DEGR.)	ANGLE NU (DEGR.)	ANGLE EPSILON(W) (DEGR.)	ANGLE MU (DEGR.)	ANGLE MU(W-R) (DEGR.)	FUNCTION THETA(R)	FUNCTION Z(R)	THETA (RADIANS)	Z (METERS)
1.	-1	0.11000	274.00	69.00	1.0000	36.800	15.000	14.586	90.000	90.000	1.51448	0.21170	0.0	0.0
2.	-1	0.11600	284.00	64.00	1.0050	36.000	15.200	13.024	84.283	84.261	1.90150	0.27434	-0.01037	-0.00148
3.	-1	0.12200	294.00	59.50	1.0120	35.150	15.000	11.676	81.168	81.129	2.03814	0.29791	-0.02220	-0.00320
4.	-1	0.12900	305.50	53.50	1.0330	34.100	14.300	10.086	75.479	75.395	2.44191	0.35480	-0.03776	-0.00547
5.	-1	0.13600	317.50	48.00	1.0620	33.050	13.000	8.695	70.326	70.202	2.84295	0.40108	-0.05629	-0.00813
6.	-1	0.14300	327.00	42.00	1.0950	32.050	9.700	7.379	65.957	65.855	3.24653	0.41436	-0.07758	-0.01100
7.	-1	0.15000	340.00	36.50	1.1310	31.000	5.000	6.163	62.150	62.114	3.65857	0.39872	-0.10177	-0.01386
8.	-1	0.16000	356.00	29.50	1.1860	29.550	0.600	4.753	57.476	57.476	4.11398	0.38233	-0.14079	-0.01775
		S W E E P	R E V E R S A L				-2.000			53.740	4.40314	0.36670		
9.	1	0.17000	373.00	23.00	1.2400	28.100	9.000	3.535	53.751	53.596	3.06939	0.39463	-0.18346	-0.02150
10.	1	0.18000	391.50	18.50	1.3040	27.200	8.000	2.708	50.074	49.899	3.50400	0.44492	-0.15055	-0.01730
11.	1	0.19000	410.00	13.50	1.3660	26.500	7.000	1.887	47.060	46.885	3.87483	0.48729	-0.11363	-0.01263
12.	1	0.20000	429.50	7.50	1.4320	25.900	6.000	1.001	44.293	44.131	4.24864	0.52891	-0.07302	-0.00755
13.	1	0.21000	448.50	0.50	1.4990	25.350	5.000	0.064	41.845	41.708	4.61808	0.56784	-0.02868	-0.00206
14.	1	0.22000	467.50	-7.50	1.5640	24.650	4.200	-0.919	39.746	39.633	4.98041	0.60361	0.01932	0.00379
15.	1	0.23000	486.00	-16.50	1.6290	23.900	4.000	-1.946	37.870	37.752	5.33953	0.65024	0.07090	0.01005
16.	1	0.24000	505.50	-27.50	1.6930	23.100	4.000	-3.119	36.204	36.070	5.73638	0.70451	0.12626	0.01682
17.	1	0.24900	521.50	-37.00	1.7470	22.200	4.000	-4.069	34.918	34.770	6.08336	0.74535	0.17946	0.02335

where c is the chord length and n, a shape parameter. By adding a leading and trailing edge thickness,

$$t_{LE} \equiv t_{TE} = \tau \nu C$$

where τ is the LE and TE thickness factor and $\nu = t_{max}/C$ the relative blade thickness, a practical blade thickness distribution is obtained. The abcissa for maximum thickness is given by

$$x_{t_{max}} = \frac{nc}{n+1} \tag{6}$$

the factor k by

$$k = \frac{\nu\ (1-\tau)}{\left(\frac{nc}{n+1}\right)^n \left(\frac{1}{n+1}\right)}$$

The complete non-dimensionalized formula is

$$\frac{t}{c} = \tau\ \nu + \frac{\nu(1-\tau)}{\left(\frac{n}{n+1}\right)^n \left(\frac{1}{n+1}\right)} \left(\frac{x}{c}\right)^n \left(1 - \frac{x}{c}\right) \tag{7}$$

For n = 1, $(^x/_c)_{t_{max}} = .5$. Furthermore, the second derivative is constant, so that the resulting profile is essentially a double circular arc profile for small thickness.

For n > 1, $(x/c)_{t_{max}} > 1/2$ and the profile CG shifts toward the trailing edge. Since the first and second derivatives of the thickness distribution are continuous, the profile curvature is continuous.

Using profiles with circular mean camber lines and n varying from 1 to 1.8 from the hub to the point of sweep reversal, and back to 1 at the tip section, a favorable blade configuration was obtained. However, manufacturing difficulties and the extreme sensitivity to tolerance and foreign object damage of thin profiles with n > 1.5 lead to the selection of n=1, i.e., essentially double circular arc profiles for final rotor blade design.

The blade cascade geometry was defined by means of conventional procedures and criteria. Figure 19 shows representative streamline velocity triangles, together with the corresponding relative flow deceleration rates W_2/W_1 and static pressure ratios P_2/P_1, the selected cascade solidities $\sigma = c/s$ and the resulting D-factor values. The hub and tip cascade solidities are equivalent to those which would have been selected for a conventional design with identical rotor inlet and exit flow conditions. The 30% streamline velocity triangles are representative of the conditions at the sweep reversal section (r = 170mm).

The flow deviation angles δ at rotor exit were calculated with Carter's empirical formula (Ref. 13)

$$\delta = m\phi/\sqrt{\sigma} \qquad (8)$$

with $m = 0.23 + 0.05\,\beta_{2ax}$ (circular mean camber line). For small camber angles ϕ, Eq. (8) gives unacceptably low deviation angles, especially in transonic cascades with shock-boundary layer flow interaction. A minimum deviation angle of 2^{o} was arbitrarily assumed and the calculated δ- values were faired gradually to the minimum value toward the tip section. The actual profiles were defined on coaxial cylinders for the most part of the blade. Three profiles were defined on cones in the hub region to ensure a smooth evolution of the profile geometry toward the conical hub section. Fig. 20 shows the relative inlet and exit angles β_1, β_2 with the tangential direction and the deviation angles δ used to define the cascade geometry. All profiles were set at a nominal incidence $i = +2°$ with respect to the suction surface. The selected profile sections are indicated on Fig. 21. Table 5 lists the profile design data defining the cylindrical and conical sections unwrapped on planes tangent to the cylinders and cones. (While all angles are conserved in the development of cylindrical sections, the profile camber angle is reduced in the developed conical sections by the sector angle formed by the radii passing through the leading and trailing edge points.)

The coordinates of the center of gravity of a cylindrical section are determined by the following simple relations:

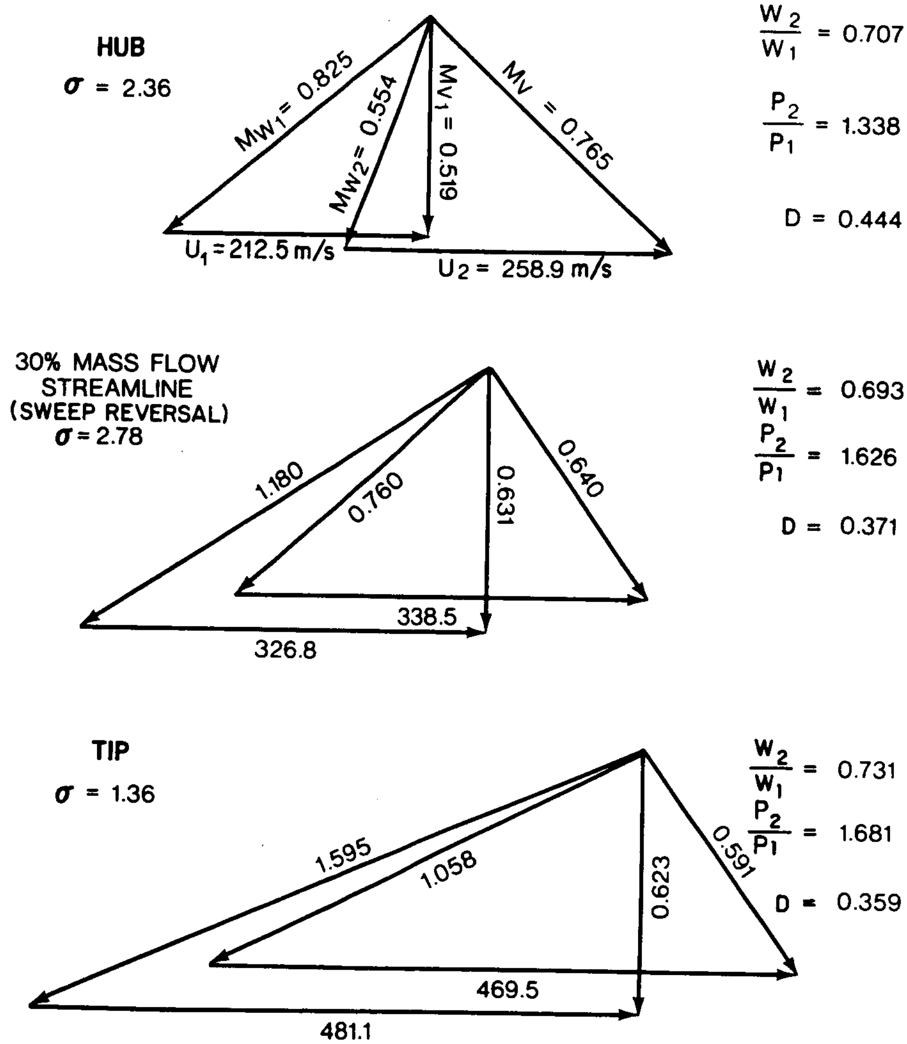

FIG. 19. ROTOR VELOCITY TRIANGLES (28 blades).

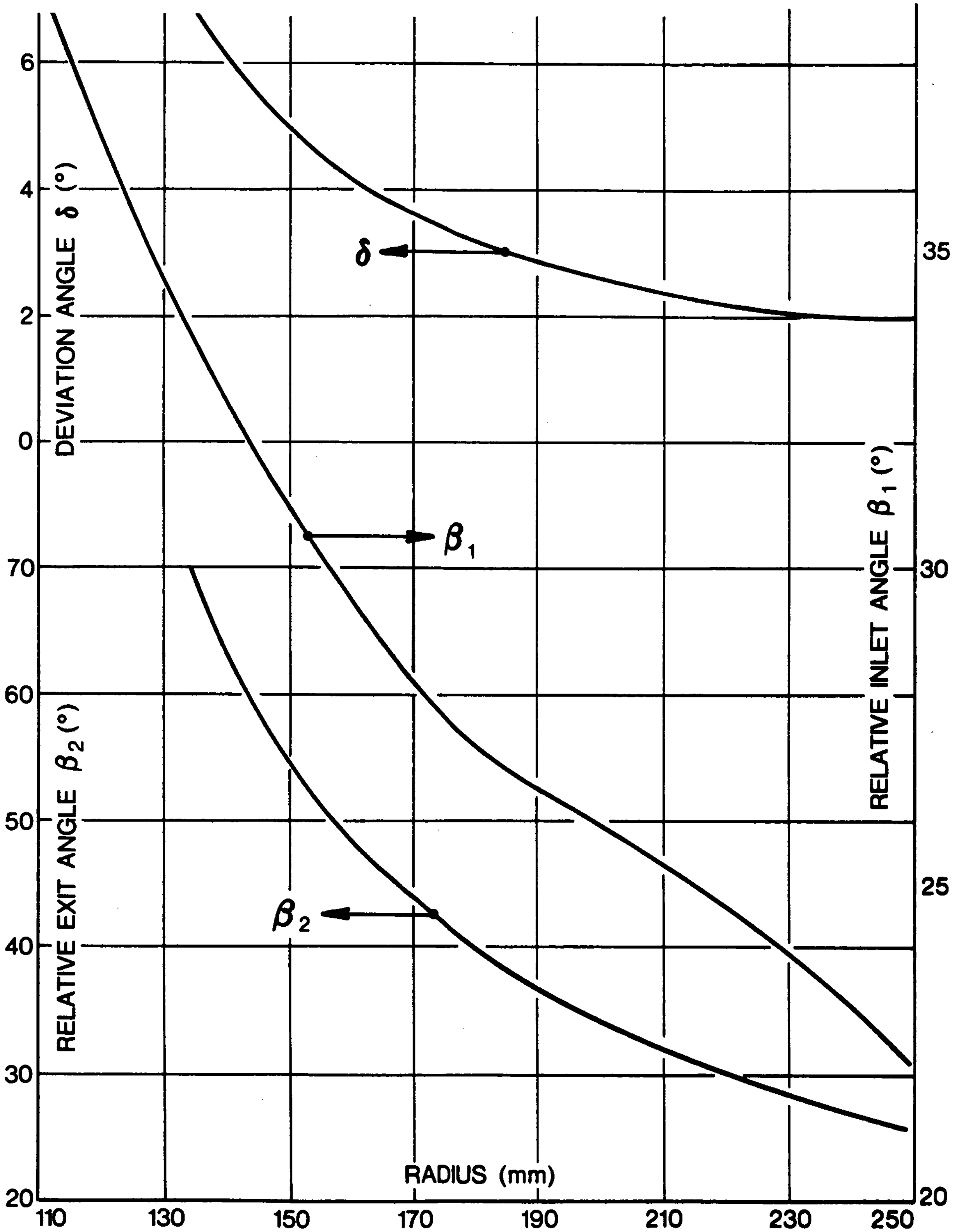

FIG. 20. RELATIVE ROTOR FLOW AND DEVIATION ANGLES.

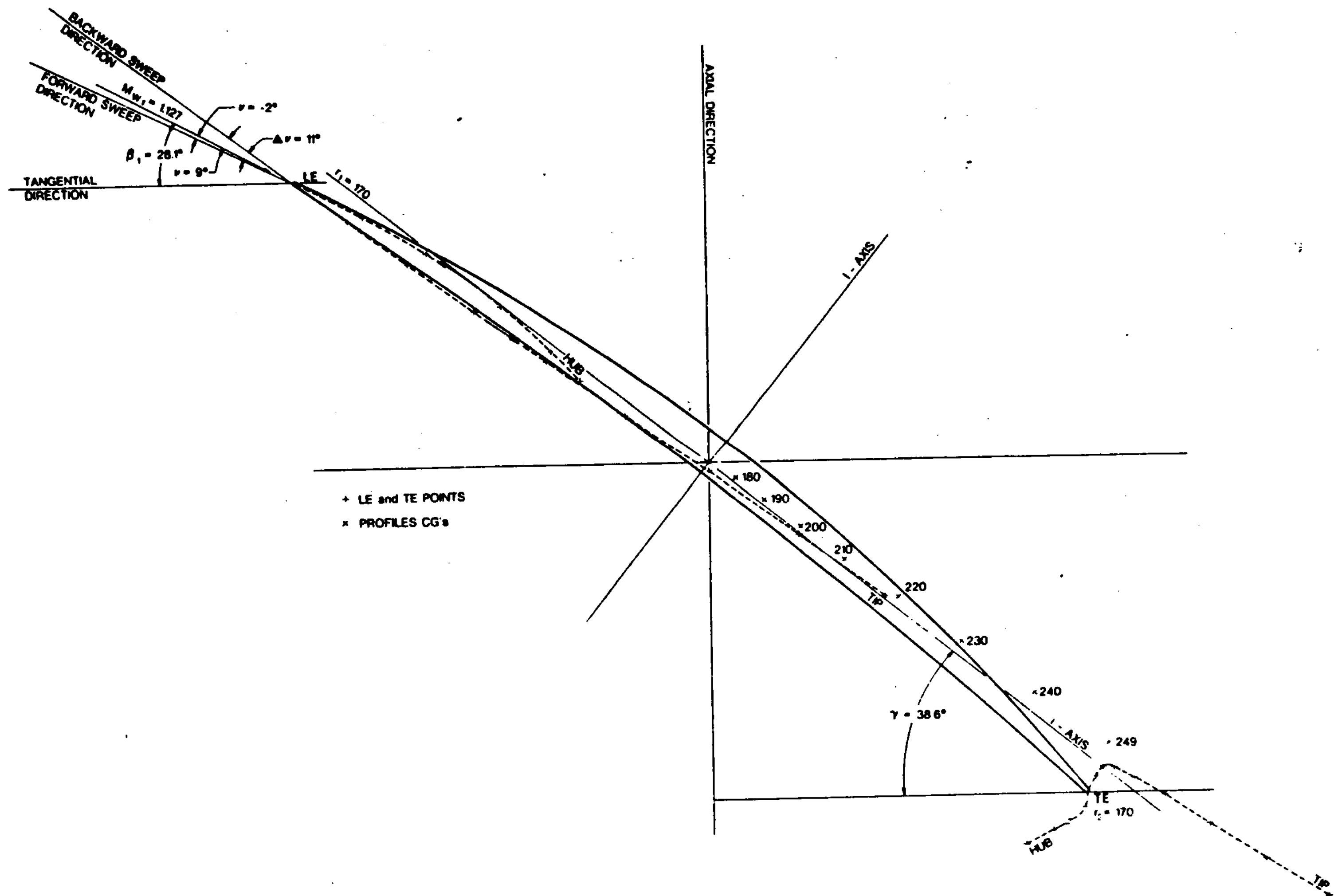

FIG 21. DEVELOPED CYLINDRICAL SWEEP REVERSAL SECTION WITH RADIAL PROJECTION OF PROFILE CG's AND LE AND TE LINES.

TABLE 5. Rotor Blade Profile Data
28 Blades (Developed Cylindrical and Conical Sections).

Section Radius (mm)	Mean Camber Angle Φ (°)	Setting Angle γ (°)	Chord Length c (mm)	Relative Thickness ϑ (%)
110/134	28.85	62.44*	64.55	10.77
122/140	24.70	56.45*	67.91	9.73
136/145	24.95	50.93*	74.73	8.03
150	26.10	46.05	85.20	6.18
160	20.90	41.95	95.20	4.95
170	17.00	38.60	105.90	4.00
180	13.70	36.05	102.30	│
190	10.90	33.95	97.70	│
200	8.70	32.25	92.90	│
210	6.90	30.75	88.20	│
220	5.60	29.40	83.80	│
230	4.70	28.25	80.20	│
240	3.90	27.05	77.20	│
249	3.30	25.85	75.00	4.00

*Angle between chord and tangent to the developed section circle at the trailing edge

$$\theta_{cg} = \theta_L + \frac{.5c \cos\gamma + d \sin\gamma}{r} \tag{9}$$

and

$$Z_{cg} = Z_L + .5\, c \sin\gamma - d \cos\gamma \tag{10}$$

where c is the chord length, and d is the distance of the CG to the profile chord in the developed section.

Figure 22 shows the situation for a developed conical section. From the aerodynamic design, the geometric characteristics of the profile, especially the inlet and exit angles β_{1_g} and β_{2_g} between the tangent to the mean camber line at LE and TE and the circumferential direction, are known. Also known are the inlet and exit radii r_1 and r_2 and the meridional projection c_m of the chord. Hence, from similar triangles in the meridional plane:

$$R_1 = \frac{c_m\, r_1}{r_2 - r_1} \qquad \text{Further,} \quad R_2 = R_1 + c_m$$

and with $m = R_1 \sin\psi$ and $\delta R = R_1 (1 - \cos\psi)$

$$c^2 = (c_m + \delta R)^2 + m^2 = c_m^2 + 2R_1R_2 (1 - \cos\psi) \tag{11}$$

In the developed section, the camber angle is

$$\Phi = \beta_{2_g} - \beta_{1_g} - \psi \tag{12}$$

and the setting angle is defined by

$$\sin\gamma = (c_m + \delta R)/c \tag{13}$$

Assuming a circular mean camber line in the developed section,

$$\beta_{2_g} = \gamma + \Phi/2 \tag{14}$$

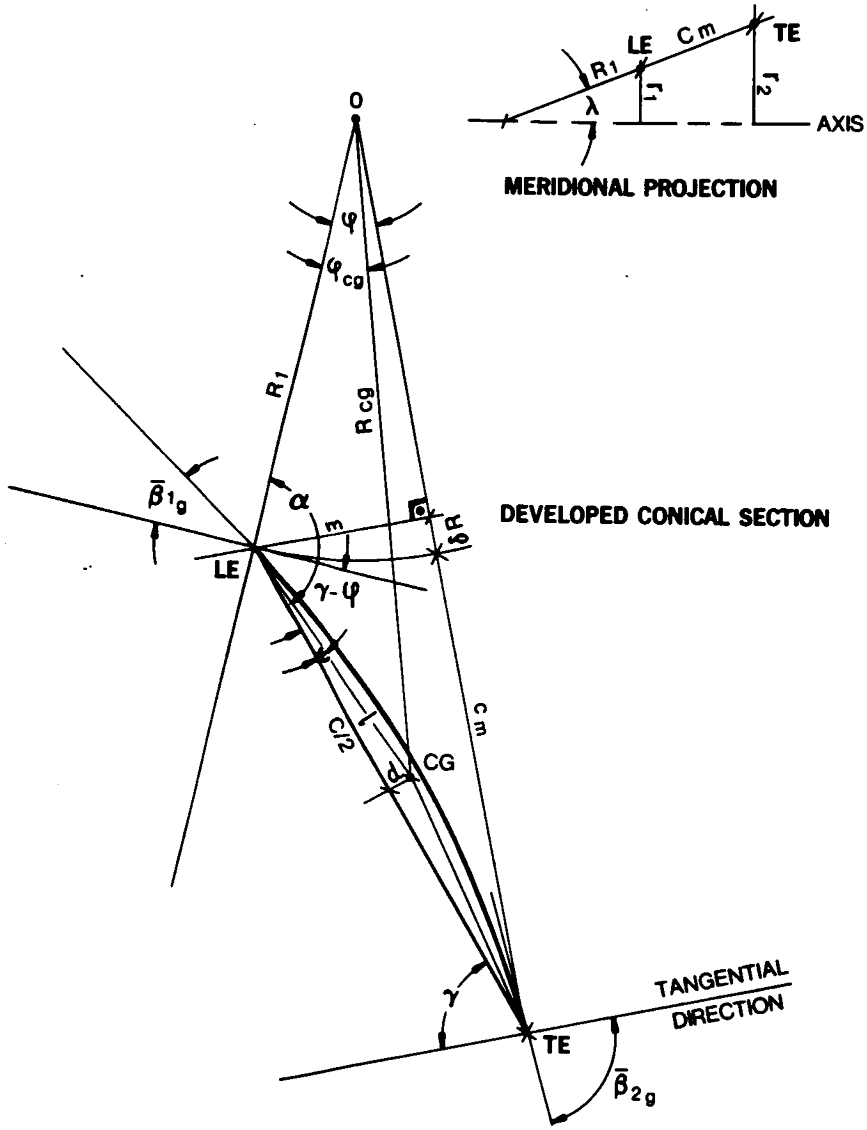

FIG. 22. DEFINITION OF CONICAL BLADE SECTIONS.

Equations (11)-(14) determine the four quantities c, ψ, Φ and γ. They must be solved by successive iterations. Assuming tentatively ψ, equation (11) gives c, equation (12) gives Φ, equation (13) gives γ, while ψ is iterated until equation (14) is satisfied.

After a profile is superimposed upon the circular mean camber line, CG distance d is known and the coordinates of the center of gravity are determined as follows:

$$\ell^2 = \frac{c^2}{4} + d^2 \text{ (symmetrical profile)}, \quad \varepsilon = \sin^{-1}\left({}^{d}/_{\ell}\right) \alpha = 90 + \gamma - \psi - \varepsilon$$

Hence, $R_{cg}^2 = R_2^2 + \ell^2 - 2 R_2 \ell \cos \alpha$ and from triangle O-LE-CG:

$$\sin \psi_{cg} = \ell \sin \alpha / R_{cg}$$

Finally, $r_{cg} = \frac{r_1}{R_1} R_{cg}$ and the cylindrical coordinates of the center of gravity are

$$\theta cg = \theta_L + \frac{R_{cg} \psi_{cg}}{r_{cg}} \tag{15}$$

$$Z_{cg} = Z_L + (R_{cg} - R_1) \cos \lambda \tag{16}$$

All CG stacking investigations, including preliminary bending stress evaluations, were carried out manually. However, as will be discussed later, verification of stress levels was carried out using computer programs at BBN and AVCO Lycoming. Figure 23 shows the final stacking of the profile CG's radially projected on the conical hub section, which was investigated by NASTRAN analysis. The corresponding distribution of the lateral sweep angle ν is shown on Table 4. The NASTRAN results indicated that the stress distribution at the hub section could be improved by a slight tangential shift of the first two conical sections in the rotation sense. $\Delta\theta_L$ - shifts of -.008 for the hub and -.004 for the next section were effected without readjusting the z - coordinates of the leading edge points. Those shifts are indicated on Fig. 23. Provision has been made in the i - straddling to generate a moment that continuously compensates the moment of the aerodynamic forces, (which are reflected in results hereafter).

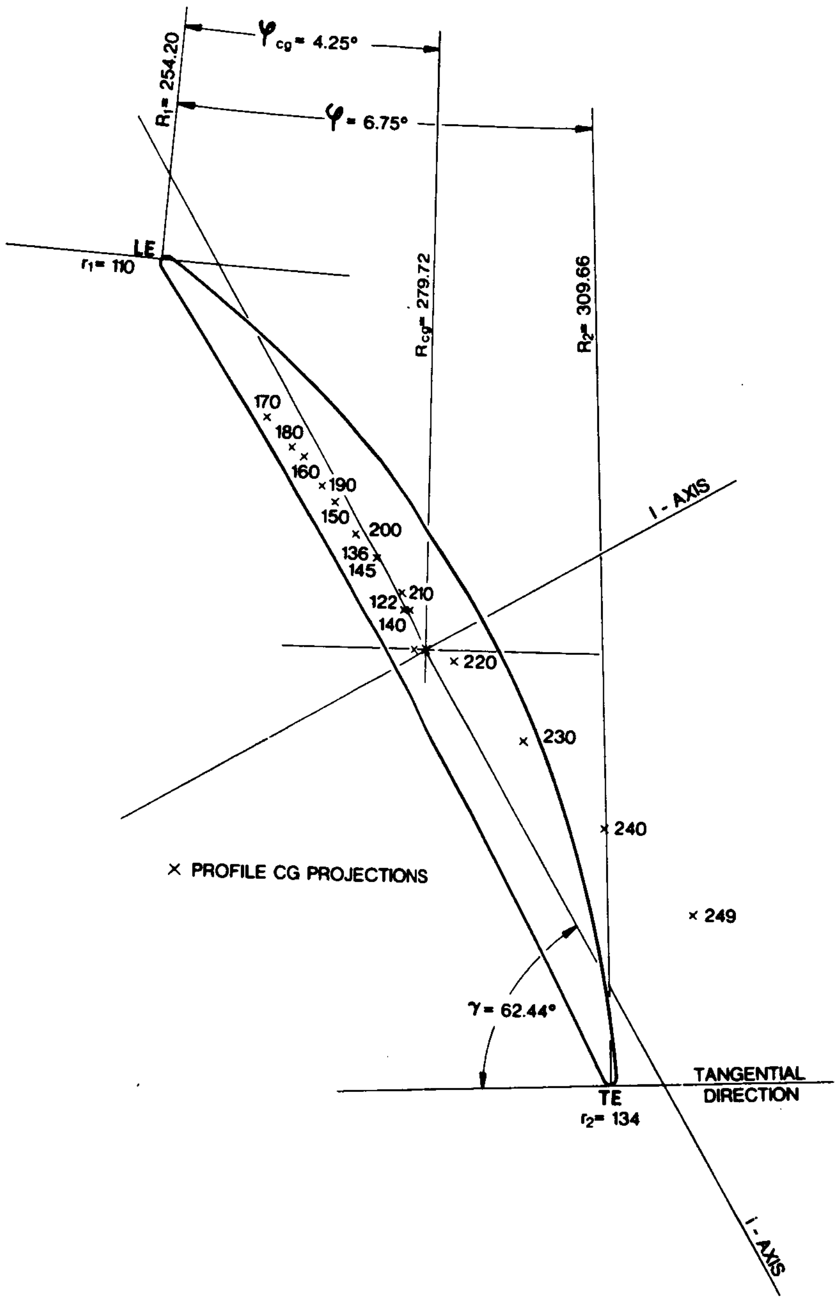

FIG. 23. CONICAL HUB SECTION DEVELOPED ONTO PLANE TANGENT TO CONE, WITH SUPERIMPOSED RADIAL PROJECTION OF PROFILE CG's.

The optimum radial distribution of the lateral sweep angle ν is different for forward and backward leading edge sweep directions. Consequently, a discontinuity of lateral sweep may occur at the sections above and below the point of sweep reversal. This, in turn, results in a high rate of curvature of the blade surface. Since the blade is defined by discrete sections, this appears only as a more or less pronounced concentration of the spanwise curvature of the blade surface in the sweep reversal region. Nevertheless, this local curvature increase generated prohibitive stresses near the trailing edge in several preliminarily generated configurations.

This problem was compounded by the additional bending moment around the I-axis of the section of sweep reversal, due to the rearward location of the CG of the upper blade portion with backward leading edge sweep. The difficulty increases since the sweep reversal was selected initially so as to minimize that moment and it was gradually moved inward from r_{sr} = 188 to 170 mm, still leaving the blade CG in a forward position with respect to the I-axis of the hub section. The stress concentration problem at the sweep reversal section was solved by means of an elaborate compromise of the profile stacking through that section, involving especially the selection of the critical lateral sweep angle discontinuity. For the final configuration, with r_{sr} = 170 mm, this was achieved at a late design state only, the last optimization step, which would have required the sweep reversal point to be set at 160 mm radius, or the profile chord lengths to be increased in the upper blade section. With the present stacking, the highest stress is 645 N/mm^2 (93.5 ksi), which is adequate for concept demonstration purposes. Figure 21 shows the developed sweep reversal section, together with the radial projections of the profile CG's of the upper blade portion and the leading and trailing edge lines. The upper profile CG's have been stacked to compensate for the aerodynamic moment and to minimize the additional TE tensile stress resulting from the rearward CG position of the upper blade portion.

Whereas the radial projection of the leading edge points indicates a smooth subsonic leading edge line, the trailing edge line does not appear to be as smooth as desirable. For manufacturing the blade was defined by flat sections generated from the blade configuration defined in the cylindrical coordinates used for the stacking investigations. Any minor irregularities of the trailing edge were smoothed out by a slight increasing of the chord lengths of a few local sections. All profile data are listed in Table 5.

5.5 A Review of the Rotor Blade Design Iterations for Stress Optimization

The main objective of the preliminary design effort (see Fig. 24) was to define a stacking configuration that maintains the subsonic leading edge concept, i.e., satisfies the acoustic rotor design requirements with as low a blade stress level as possible. A target design goal of 725 N/mm^2 (105 ksi) maximum steady state stress was sought for the design speed of 18,450 rpm. For the selected titanium blade, such a stress level is considered adequate for the demonstration purposes of this program.

As a first step in each iteration, both manual and computerized beam-type stress computations were carried out to develop a feel for the iterative stacking procedure and to ensure numerical agreement. The standard AVCO Lycoming blade stress computer program which was used treats the blade as a twisted, rotating cantilevered beam with variable section properties, and takes into account the shroud and aerodynamic forces and the centrifugal restoring moments. All trial blade stacking iterations were analyzed with this program.

Simultaneously, a quick, inexpensive and efficient finite element analysis was used at BBN to verify the results of blade iterations. The program, based on SAP, was operated in conjunction with a blade geometry generator which was based on the family of blade profile shapes, described previously by Eqs. 5-7, which reduce to a minimum the number of parameters required to specify a blade shape; namely, the leading and trailing edge coordinates, the section setting angle and camber, and the profile shape parameters. The program was therefore very well suited for iterative design studies. The purpose of the simultaneous effort was to provide further verification of the beam and manual analysis and to help identify stress concentration, which are neglected in the beam-type stress analysis program and in the manual calculations. These efforts were deemed necessary because the blade configuration differs radically from more conventional designs, and it was uncertain whether conventional design methods would be sufficiently accurate.

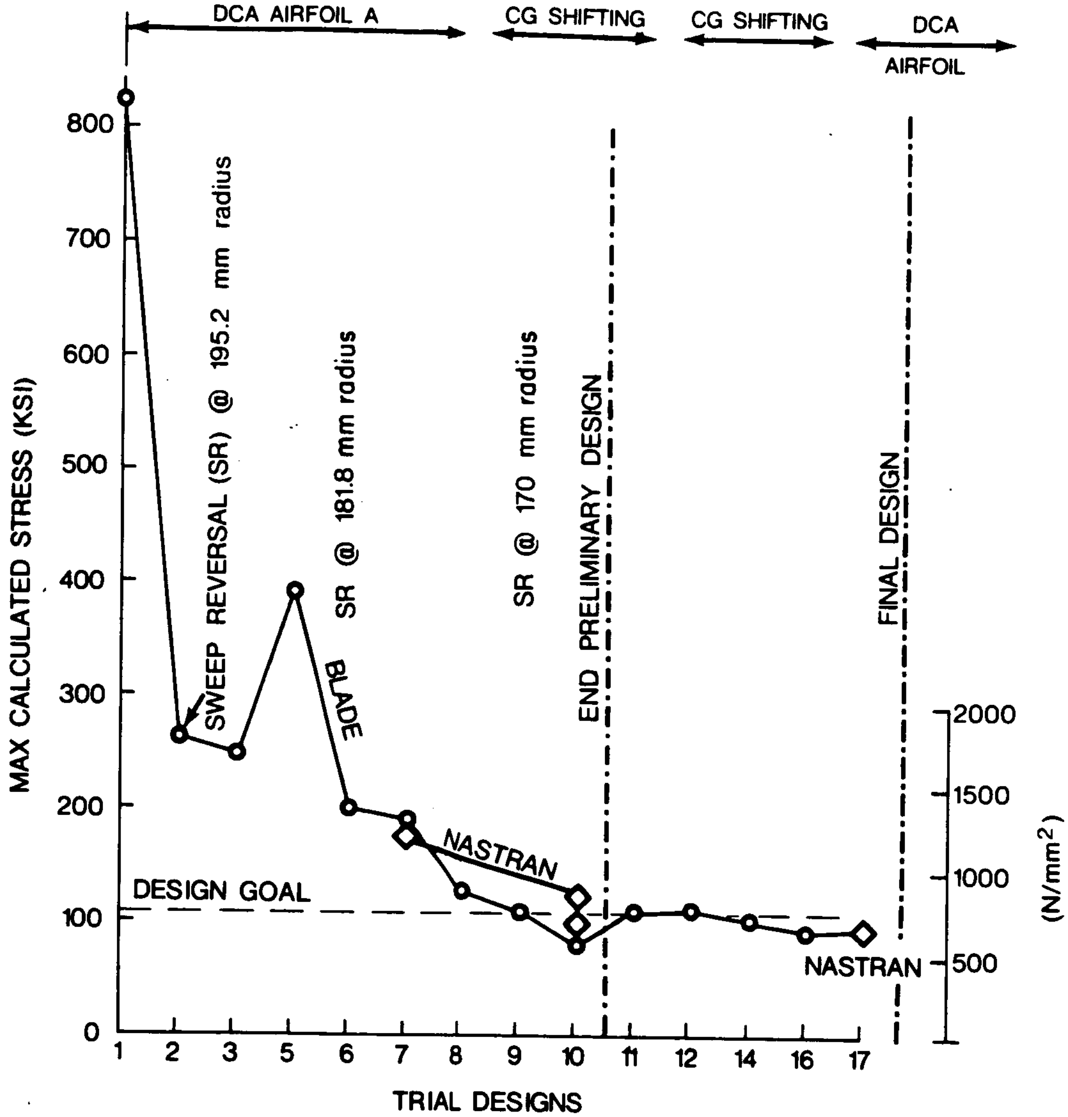

FIG. 24. OPTIMIZATION PROGRESS.

A NASTRAN stress analysis program was used by AVCO Lycoming on design iterations which were considered particularly important, and for the final stress computations verification.

The evolution of the maximum blade stress levels as the blade design evolved through the series of trial designs is shown in Fig. 24. The results of the first design substantiated the impractical stress level of a blade with simple forward leading edge sweep. The initial sweep reversal radius (SR) was selected at 195.2 mm. The stacking for trial design 2 was such that the center of gravity of each of the 13 cylindrical blade sections used to define the blade projected radially down onto the axis of minimum inertia (i-axis) of the airfoil section immediately below. For Iteration 3, all section CG's were projected onto the i-axis of the hub section. For Iteration 5, all section CG's above the sweep reversal section were projected onto the SR section i-axis, while the stacking of Iteration 3 was kept for the lower blade sections. As can be seen, the resulting misalignment of the upper blade portion with respect to the hub section produced higher hub stresses. However, this design also showed the lowest stress level for the upper blade portion.

For Iteration 6, the sweep reversal radius was lowered and the misalignment was corrected by introducing a discontinuity of the lateral sweep angle, (i.e., the angle between the sweep direction and the radial plane containing the relative inlet velocity), at the point of sweep reversal. By varying this parameter, a number of stacking combinations involving individual compromises within the upper and lower blade sections, were investigated. Iteration 7 shows the best result obtained with this stacking concept.

With the stress level still substantially beyond the preliminary design goal of 105 ksi, a detailed investigation of the stress pattern in design 7 was performed using the NASTRAN stress program. The excellent correlation which was obtained substantiated the beam-theory analysis method as a useful approach to analyze blade stacking changes.

Subsequent iterations were conducted with the optimum stacking concept described in Sec. 5.4. This stacking satisfies the condition that, at every section along the span, the CG of the entire blade portion above the section projects radially onto the i-axis of the section. As shown by Iteration 8, this reduced the maximum stress level very nearly to the preliminary design target value.

The new stacking concept confirmed the necessity of a lateral sweep angle discontinuity at the point of sweep reversal to achieve proper stacking of the profile CG's across that section. This discontinuity, however, resulted in a rapid change of the spanwise curvature of the blade surface in the trailing edge region, which in turn results in a local stress concentration that was not shown by the simplified analysis. Iterations 1-8 were conducted with double circular arc profiles (DCA). Iterations 9 and 10 used new profiles featuring rearward CG shifts from the hub to the section of sweep reversal, and forward CG shifts from that section to the tip (see previous section). In this way, the CG excursions from a radial line were minimized within the leading and trailing edge envelope and the stresses were reduced to the target level.

Figures 25 and 26 show the moments about the axes of minimum inertia and maximum stress distributions for Design 10 as calculated by the standard blade stress program. The influence of aerodynamic loads and centrifugal restoring moments are also shown. (Design 10 was chosen for further study since this is the design which first indicated stresses below the design goal.)

A detailed investigation of Design 10 was also performed with the NASTRAN program. The results showed local high stresses of 96 ksi at the trailing edge of the sweep reversal section and 110 ksi at the leading edge of the hub section. By slightly increasing the chord length of the sweep reversal section, and slight re-alignment of the conical hub, these stresses were brought down to 84 and 96 ksi, respectively. The NASTRAN finite element representation of this configuration, called Design 10A, is shown in Fig. 27. The stress distributions of the suction and pressure surfaces are shown in Fig. 28.

During the entire iteration process, it was apparent that the radial location of the point of sweep reversal would have to be moved substantially inward from its initially assumed location in order to avoid a large moment about the I-axis of the hub section. Moving the point of sweep reversal inboard, however, increases the bending moment about the I-axis of the sweep reversal section, thereby increasing the tensile stress at the trailing edge of that section. To minimize the local trailing edge stress concentration the radial location of the sweep reversal section was moved inboard cautiously. Even so, the blade CG remained ahead of the hub section I-axis, and resulted in an additional bending stress (on the order of 120 N/mm^2) at the hub section leading edge.

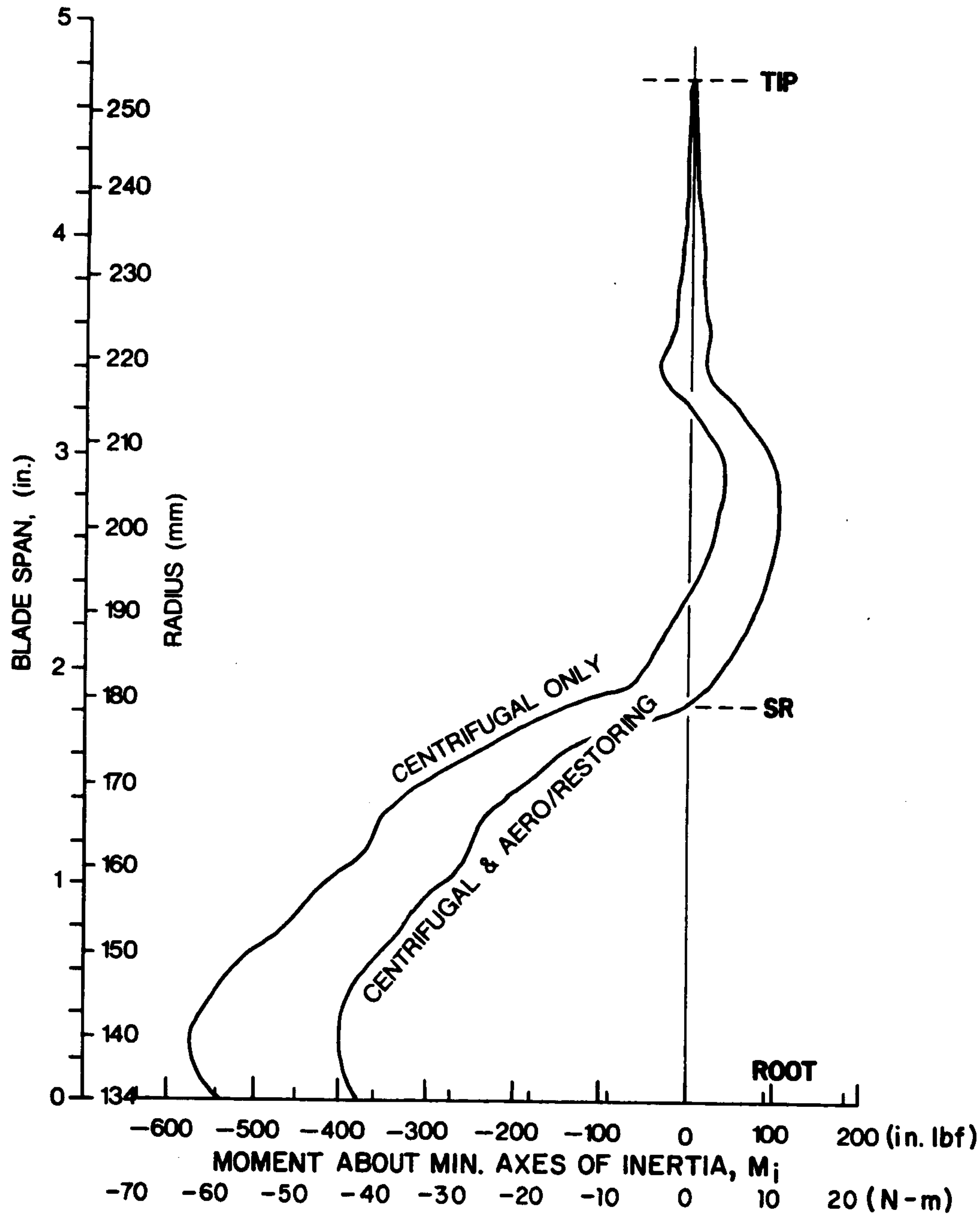

FIG. 25. SECTION MOMENT DISTRIBUTION [Preliminary Design 10].

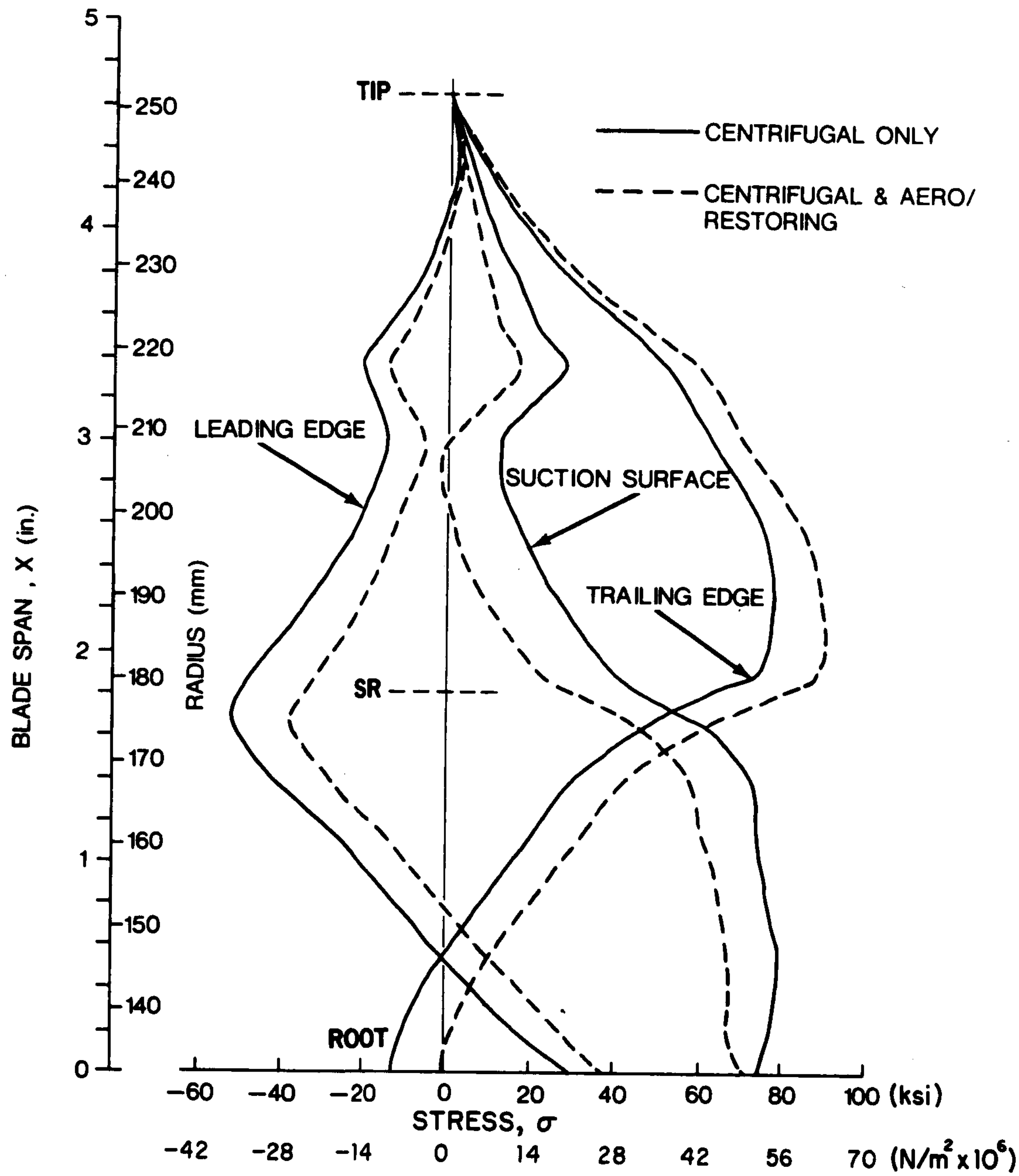

FIG. 26. MAX STRESS DISTRIBUTION [Preliminary Design 10].

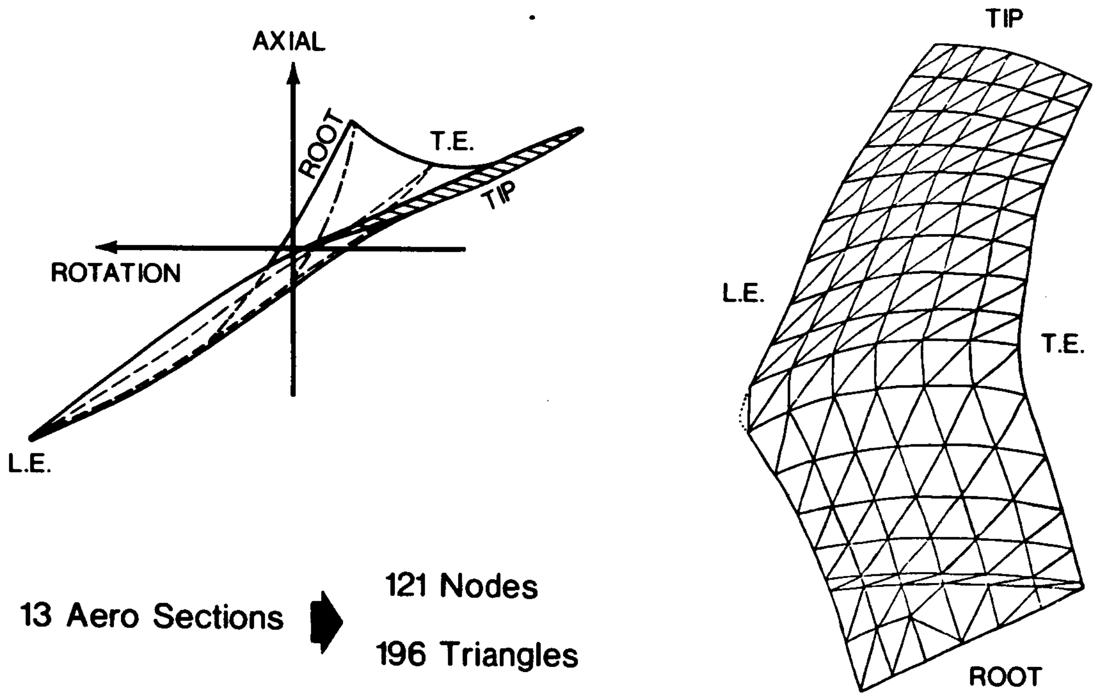

FIG. 27. NASTRAN ANALYSIS [Preliminary Design 10A].

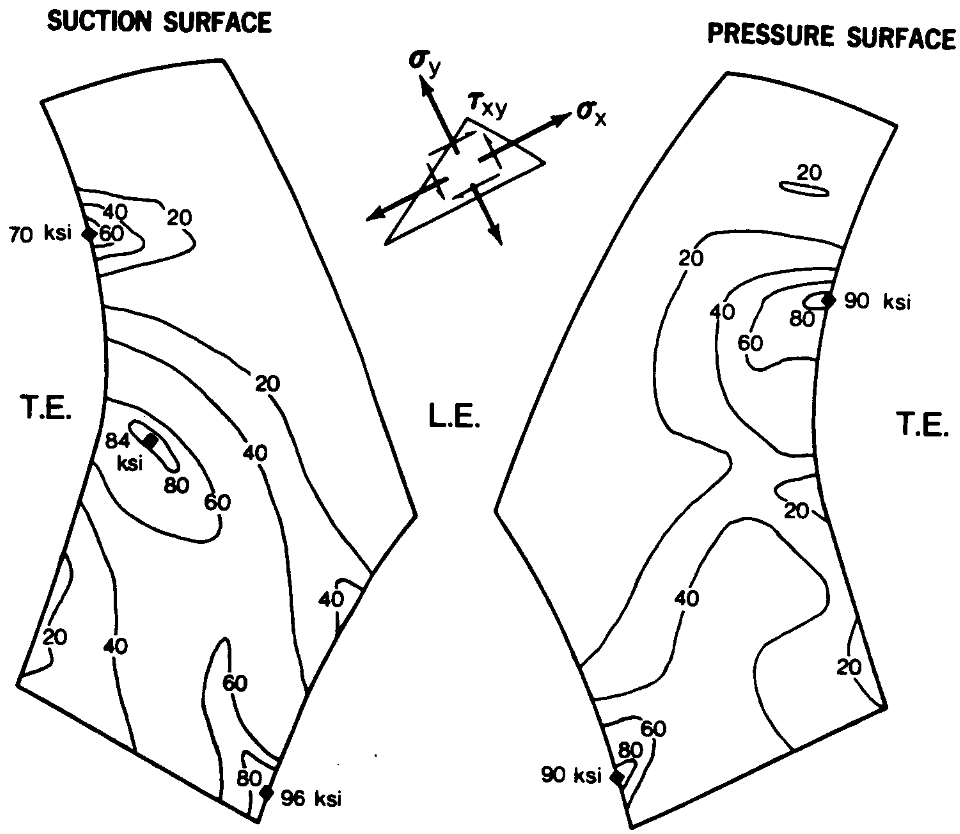

$\tau_{MAX} = \begin{cases} 96 \text{ ksi} & \text{Rotation Only} \\ 116 \text{ ksi} & \text{Rotation, Aero/Restoring} \end{cases}$

FIG. 28. EXAMPLE OF INTERIM RESULTS OF NASTRAN STRESS ANALYSIS MAX SHEAR CRITERION [Preliminary Design 10A].

Prior to the selection and analysis of the final blade design, several intermediate designs were investigated based on local shifts of the CG location within the indificual airfoil profiles. (Noted as Designs 11 through 16 in Fig. 24.) The polynomial blade sections had been evolving toward n=1 or a DCA profile. For manufacturing reasons, however, double circular arc profiles were specified for the final design. This raised the stresses to virtually the level of iteration 9, and additional stacking iterations were required to achieve the design objective. In particular, the relative blade thickness was increased from 10.00 to 10.77% at the hub section. This resulted in a 10% decrease in the stress level. Additional reductions were achieved through a judicious balancing of the profile stacking in the lower blade portion and lateral sweep angle discontinuity at the sweep reversal section.

A check was performed to see if the DCA profiles allowed adequate flow area margins. On an average basis, the rotor throat passage area has a large margin to sonic throat area because of the comparatively high mean relative inlet Mach number level $\overline{M}_{W_1} = 1.33$ and the positive inlet incidence of 2° selected for optimum blading efficiency. The throat hub region is most susceptible to local throat choking because of the transonic inlet flow conditions and the higher relative blade thickness. Because of unknown 3-dimensional flow effects, it is difficult to determine local blade stream tube areas and no definite section throat area margins thus were specified for the design. A check, however, was tentatively made for the rotor hub section. On the two-dimensional basis of the developed section of Fig. 23 the ratio of throat to inlet passage width is 1.045. At the throat location, however, the channel height has decreased from 139 to 136.3 mm. Assuming that all individual stream tube heights are reduced in the same proportion, the effective geometric throat/inlet area ratio thus is $A_{min}/A_{in} = 1.045 \times 136.3/139 = 1.027$. With a relative inlet Mach number of .825, the sonic area ratio A_{in}/A_S is 1.0285, thus $A_{min}/A_S = 1.027 \times 1.0285 = 1.055$, i.e., a 5.5% choke area margin.

In the hub region, the flow has the tendency to be deflected inwards because of the forward leading edge sweep. On the other hand, the increasing density toward the tip at rotor exit combines with the essentially constant axial velocity of free-vortex flow to shift the streamline pattern outwards at rotor exit. Those compensating effects cannot be quantified at the throat location and the comparatively large 5.5% margin thus was judged adequate to account for the possibility of unfavorable three-dimensional effects and for the suction side boundary layer growth upstream of the throat in the absence of a detached leading edge shock. In summary, in spite of the selection of DCA profiles, the individual rotor section throat margins are adequate.

5.6 Final Rotor Blade Stress Analysis

The stress analysis for the final design iteration was performed using NASTRAN. The loads considered in this run were based on the maximum operating speed of 18,450 rpm. In addition to the major contribution of the centrifugal load, aerodynamic gas pressure loads, the centrifugal load and the torsional restraints of the part span shroud were applied to the blade. The resulting von Mises effective stress patterns over the pressure and suction surfaces of the blade are shown in Figs. 29a and 29b. An independent verification of these results was performed using the SAP program at BBN.

The maximum stress level of 645 N/mm^2 (93.5 ksi) is at the root near the leading edge on the suction surface. The high stress region of 90 ksi, however, extends only over a small portion of the suction surface (Fig. 29b) and so should not pose a problem for the planned test program. The permissible number of start/maximum speed/stop cycles is approximately 500, considering a notch condition (SCF = 3.5) at the juncture of the blade airfoil and the base shroud.

The tendency of the blade to untwist at the shroud location is small since there is only 1/2 degree difference in untwist between the shrouded and unshrouded NASTRAN results. The most significant load on the shroud, therefore, is the bending load due to the centilevered mass. The maximum shroud stress of 78.7 ksi is at the blade-shroud juncture, and is conservative in that the large fairing radius at the juncture was not included in the calculation. Because of the constraining effect of the mid-span shroud, the untwist of the blade at the shroud location is negligibly small. The untwist of the tip section calculated from the NASTRAN results is .36°, thus increasing the tip incidence from 2 to 2.4° at the design speed, a value well within the blade incidence design tolerance. However, radial growth of the shroud has not been accounted for and, if such growth occurs, undesirable increased tip incidence angle could result, due to the consequences of shroud sections "unlocking".

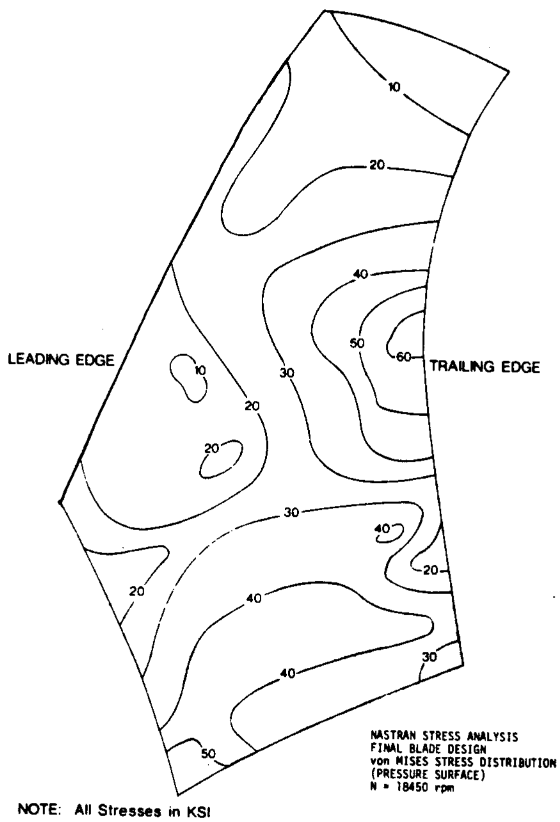

FIG. 29a.

Pressure surface

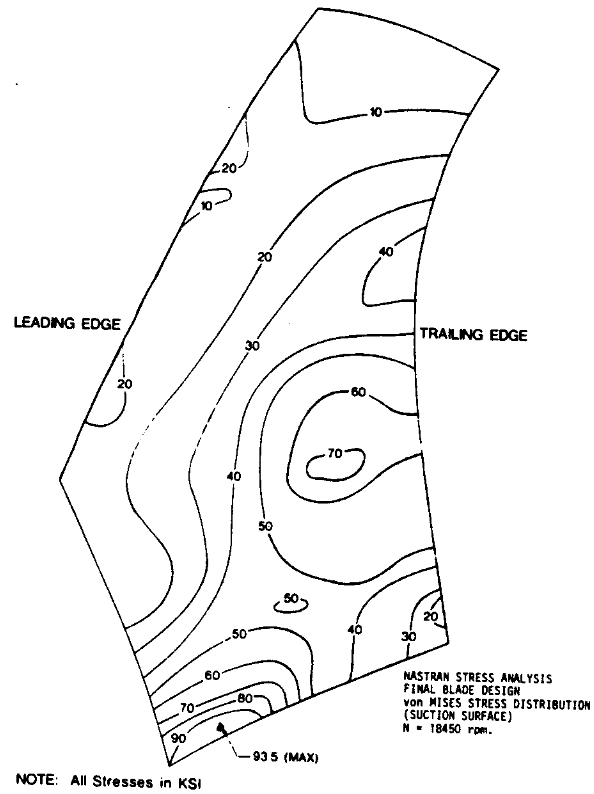

FIG. 29b.

Suction surface

FIG. 29 NASTRAN STRESS ANALYSIS: FINAL ROTOR BLADE DESIGN

The magnitude of the stresses in the fan blade airfoil are acceptable for an experimental program. The computed stresses in this design exceed AVCO Lycoming practice for titanium blades for longtime service operation, but fall within acceptable limits for the planned experimental program.

5.7 Rotor Blade Vibration and Flutter

The avoidance of large amplitudes of resonant vibration of the rotor blades over the full operating range is necessary to ensure the structural integrity of the fan. The design procedure included an assessment of the natural frequencies of the rotor blade so that the forced vibration response is minimized, and the self-excited response is eliminated. The design goal for the minimization of forced vibration is ensuring that the rotor blade cannot resonate with the first three rotational orders of excitation due to possible inlet distortions. Although higher excitation orders will exist in the intake, it is considered that these levels will be minimal in the clean inflow expected in the acoustic test facilities and, thus, they will not generate significant resonant stress levels in the blade. The avoidance of self-excited blade vibration flutter is mandatory, since the associated stress levels usually lead to blade failure in a very short time. The two flutter phenomena that were considered in the design are subsonic positive stalled flutter at part-speed operation and supersonic unstalled flutter at design speed. The criteria for avoidance of these flutter conditions are based on extensive experience by the engine manufacturers and are expressed in terms of a reduced velocity parameter: $u/b\omega$, where u = air velocity over the blade (m/sec), b = blade semichord (m), and ω = frequency of vibration in the flutter mode (rads/sec). The empirical design limit values for this parameter under positive stalled flow are 6.7 and 2.4 for the first bending and first torsion modes, respectively. The supersonic unstalled flutter design limit at first torsion frequency was:

$$\frac{u}{b\omega}\left(\frac{M^2-1}{M}\right) < 1.05 \text{ , where } M = \text{Mach number.}$$

The coefficients are calculated at 3/4 span. (Since supersonic unstalled flutter usually occurs in vibration modes which are predominantly torsional, only this mode is considered.)

A free-standing blade, assumed fixed at the base, was used in the calculation of the resonant frequencies. The natural frequencies for the unshrouded blade are shown in the excitation diagram of Fig. 30. This design is clearly unsatisfactory since the natural frequency of the first bending mode has a second order resonance in the operating speed range. The stall flutter coefficients are 3.44 and 1.53 for bending and torsion, respectively. These values are within the safe limits which were established as design criteria. The supersonic unstalled flutter parameter is 1.16 and exceeds the safe upper limit.

A partspan shroud is required to raise both the first bending and torsion natural frequencies and avoid forced and self-excited vibrations (flutter). As a physical model, the shroud was assumed to restrict the blade motion to a uniform translation at three representative points.

The design analysis was checked by mounting two spare blades in a fixture which clamped at the root and partspan shroud locations. An acoustically coupled exciter was used to vibrate the blade so that the frequencies and mode shapes could be obtained. The comparison between the measured and theoretical static frequencies shown in Fig. 31, is considered good, especially in view of the unusual blade shape. The "measured" frequency line in Fig. 31 is actually the theoretical centrifugal stiffening line originating at the measured static frequencies of the first three modes.

Figure 31 shows the excitation diagram and calculated and measured frequencies for the final airfoil with the partspan shroud located at 64% of the span (201 mm radius). The first bending natural frequency has been raised so that it clears the first three excitation orders in the operating speed range. The fourth excitation order of the first mode, (e.g., four equally spaced front struts) however should be avoided. Based on the measured frequencies, the stalled flutter coefficients are 1.5 and 1.0 for bending and torsion, respectively. The supersonic unstalled flutter coefficient is .75. These values meet the design criteria. The excitation diagram shows that the torsion and bending modes are not coincident in the operating speed range. This ensures that the modes are decoupled.

Strain gauges will be used during the test program to ensure that safe steady and vibrating stress levels are not exceeded. In order to locate the strain gauges appropriately, a vibratory stress survey was conducted using strain gauges during the static vibration tests: Fig. 32 shows the results of this test, normalized for each mode. The vibratory stress distributions, shown as

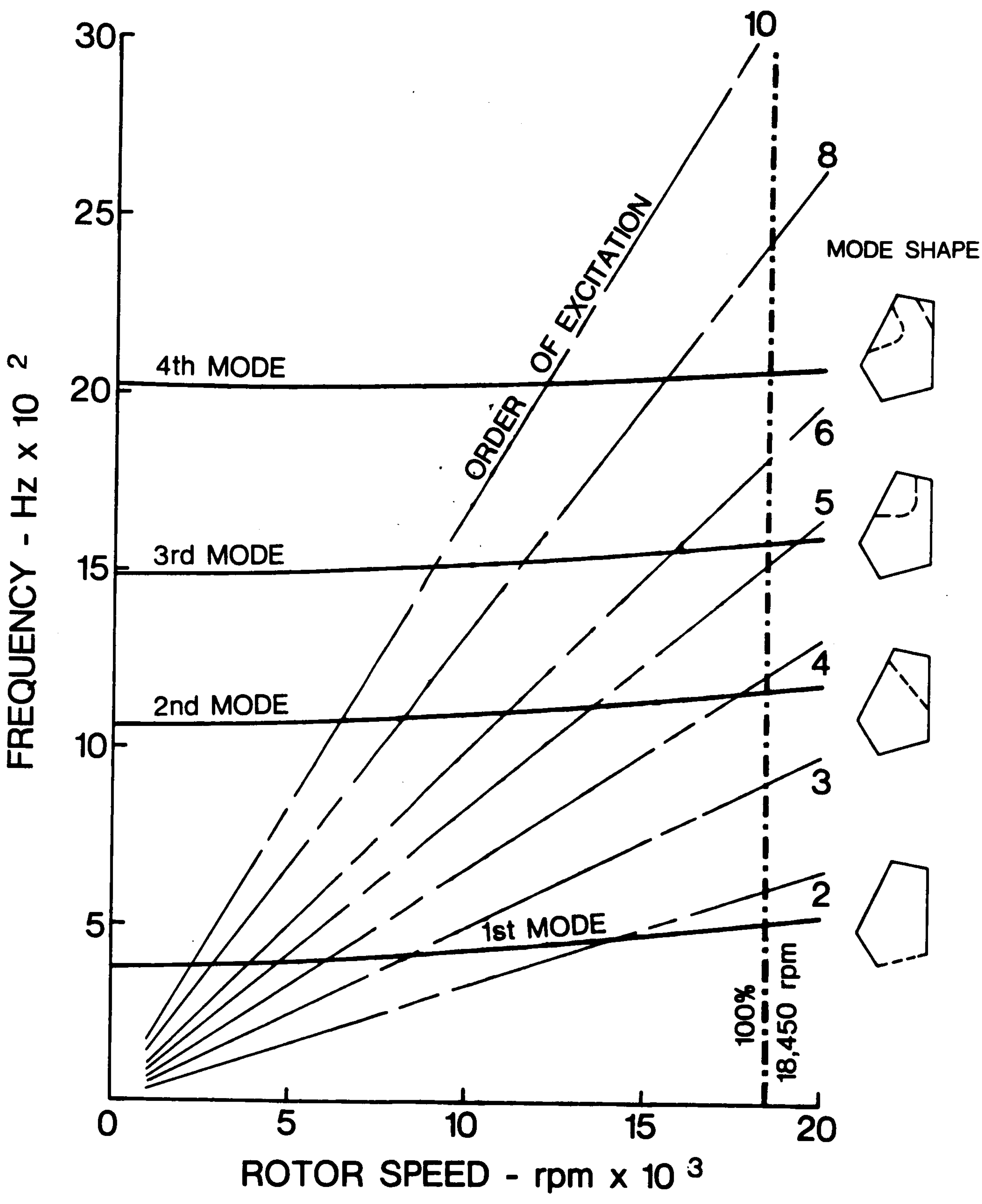

FIG. 30 RESONANCE DIAGRAM OF FINAL BLADE BEFORE SHROUD WAS ADDED.

PARTSPAN SHROUD LOCATED AT 64% SPAN (r = 201 mm)

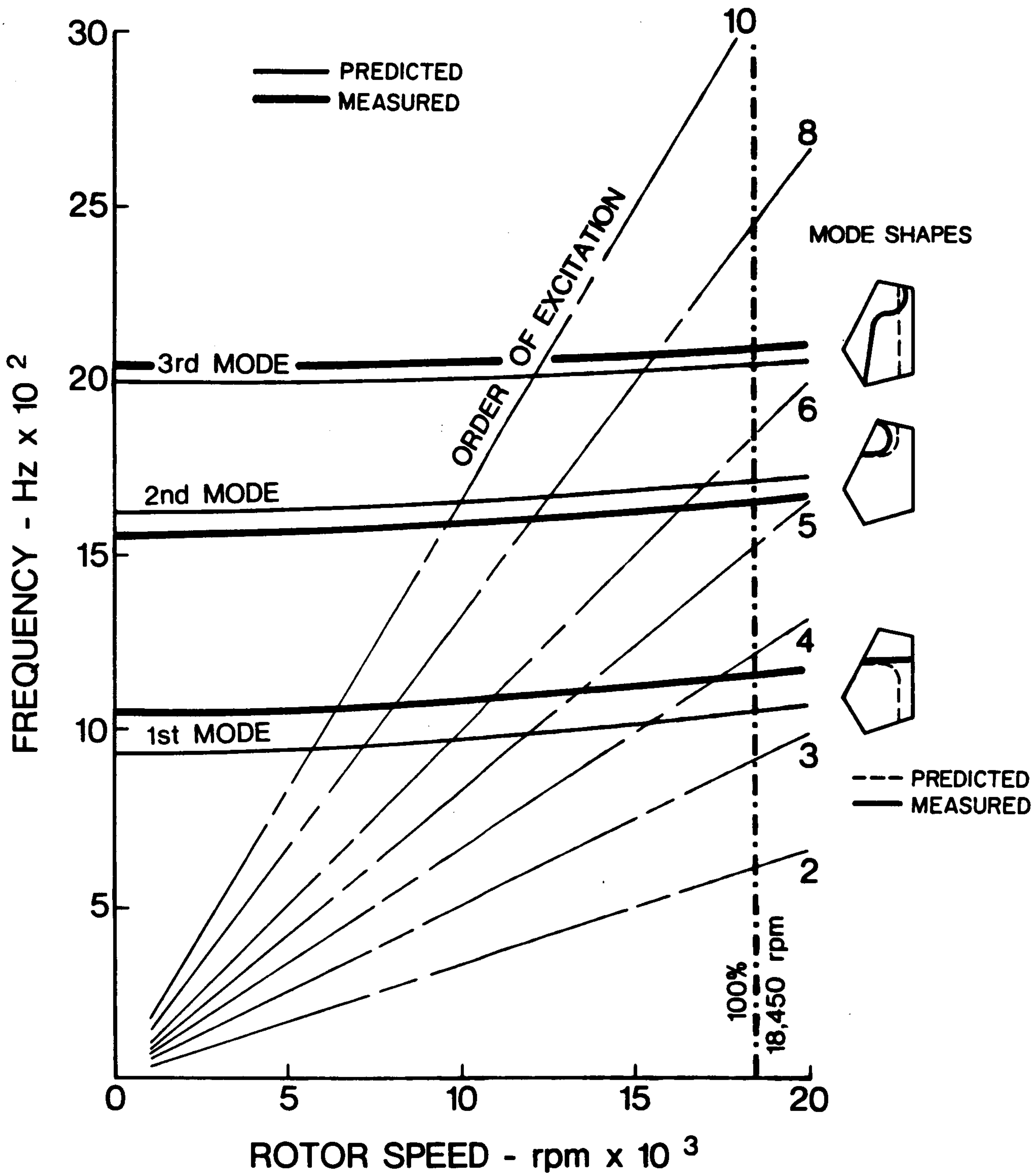

FIG. 31 RESONANCE DIAGRAM OF FINAL (SHROUDED) BLADE.

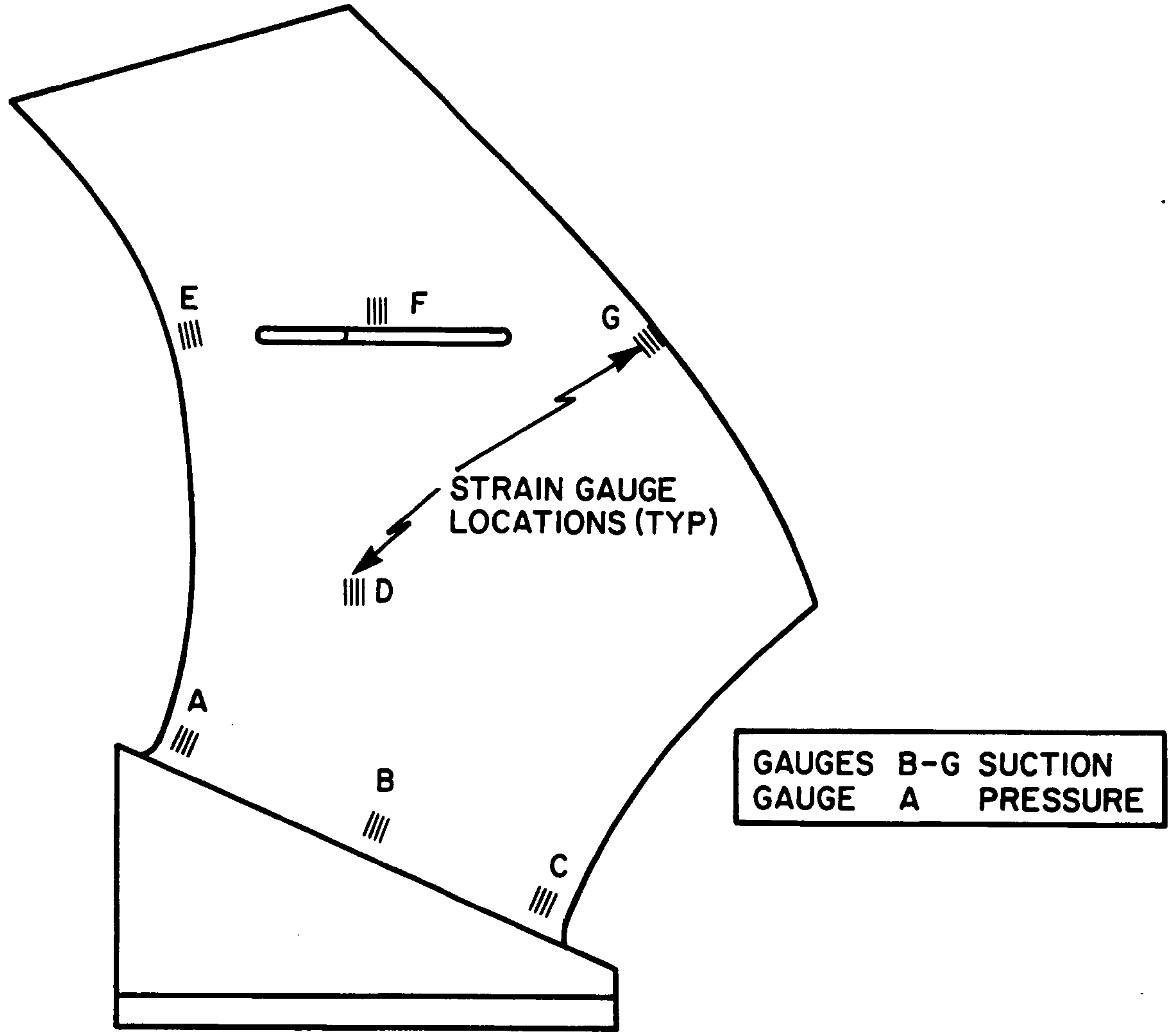

GAUGE	MODE 1 1074 Hz	MODE 2 1534 Hz	MODE 3 2109 Hz
A	0.06	0.45	0.70
B	0.06	0.38	0.22
C	0.03	1.00	0.65
D	0.02	0	0.37
E	0.33	0.65	0.30
F	1.00	0.55	1.00
G	0.13	0.18	0.43

NORMALIZED STRESS LEVELS

FIG. 32. MEASURED AND NORMALIZED STRESS DISTRIBUTIONS DURING STATIC VIBRATION TESTS ON BLADE S/N 17.

the combined steady and alternating stresses in the blade, are plotted for each mode in conjunction with calculated steady stresses at each gauge location used. Figure 33 shows the Goodman diagram for the blade material and the vibrating stresses measured in each mode proportioned for the most critical location. From this diagram it is seen that location 'F' is the most critical location in terms of combined stress in the first mode of vibration. Location 'C' is seen to be the most critical for the second and third modes of vibration. It is therefore recommended that strain gauges at positions 'C' and 'F' are used to monitor the steady and vibrating stresses during the rig running.

5.8 Attachment and Disk Analysis

The fan disk stresses were computed by a Lycoming finite element program which evaluates the loading variation throughout the disk accounting for the effects of rotation, temperature gradients and elastic-plastic conditions.

Low cycle fatigue (LCF) life was evaluated for the significant regions, i.e., the disk serrations, the bolt holes and the disk bore, utilizing statistical minimum fatigue property data for Timkin 17-22AS material. The stress/strain ranges utilized in the life evaluation are the stabilized values corresponding to start/stop excursions to 18,450 rpm design speed.

Stress concentration factors (SCF) were evaluated for those areas of the disk containing a high stress gradient, i.e., the serrations and bolt holes. This was accomplished by ratioing the peak stresses determined by finite element analyses with the nominal stresses in each of the two regions.

Nominal radial and tangential stress distributions for the fan disk are shown in Fig. 34, while the nominal stresses in the serration are shown in Fig. 35. The finite element models for the bolt holes and serrations are handled separately.

Stress distributions about the disk bolt-holes are given in Fig. 36 from which an SCF of 2.06 was calculated, so that the resulting LCF life is in excess of 100,000 "start/stop" cycles based on the material S-N data of Fig. 37. It has been concluded that the disk bore also has a calculated life of at least 100,000 cycles.

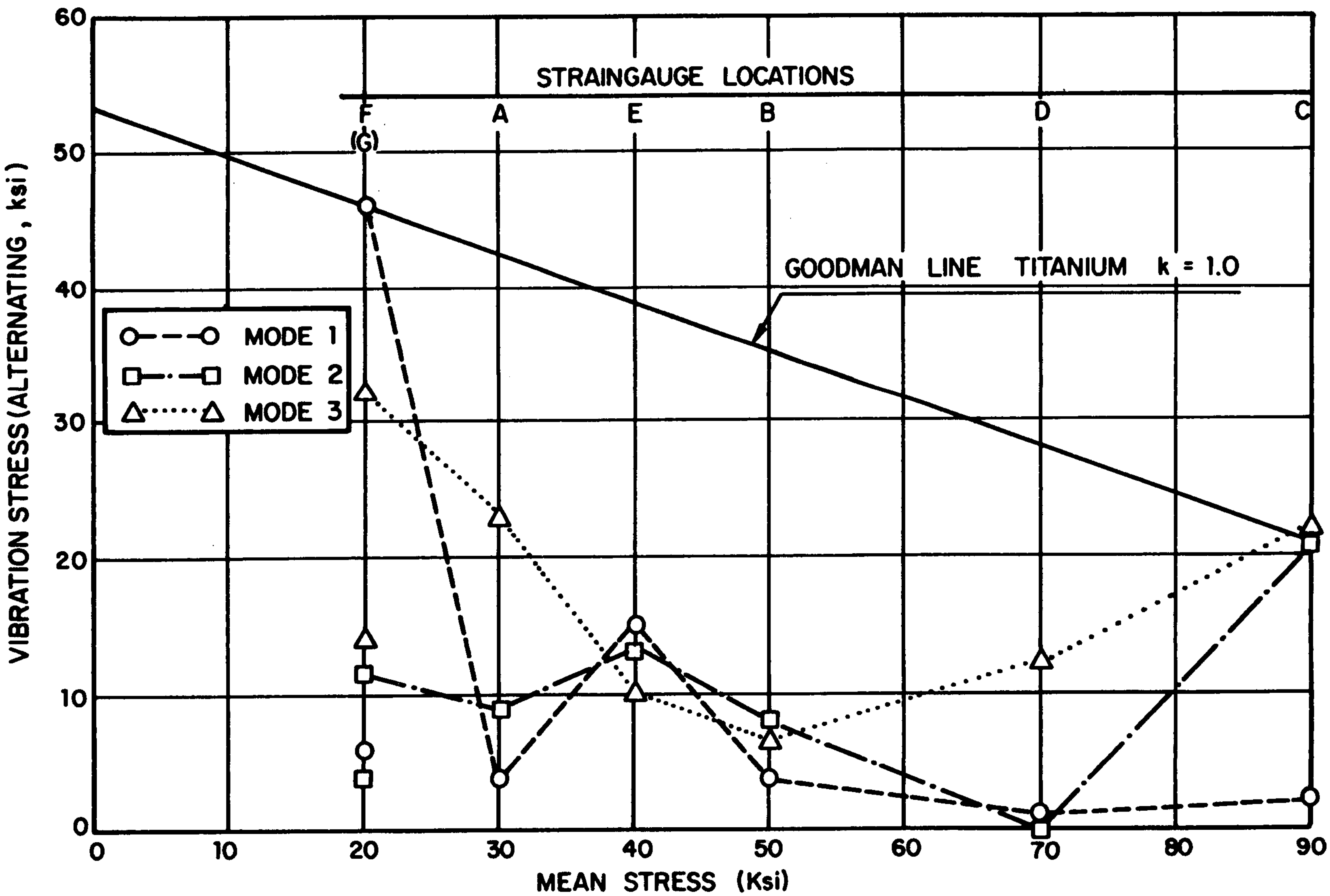

FIG. 33. DETERMINATION OF CRITICAL VIBRATORY STRESS LOCATIONS, (Shrouded Blade).

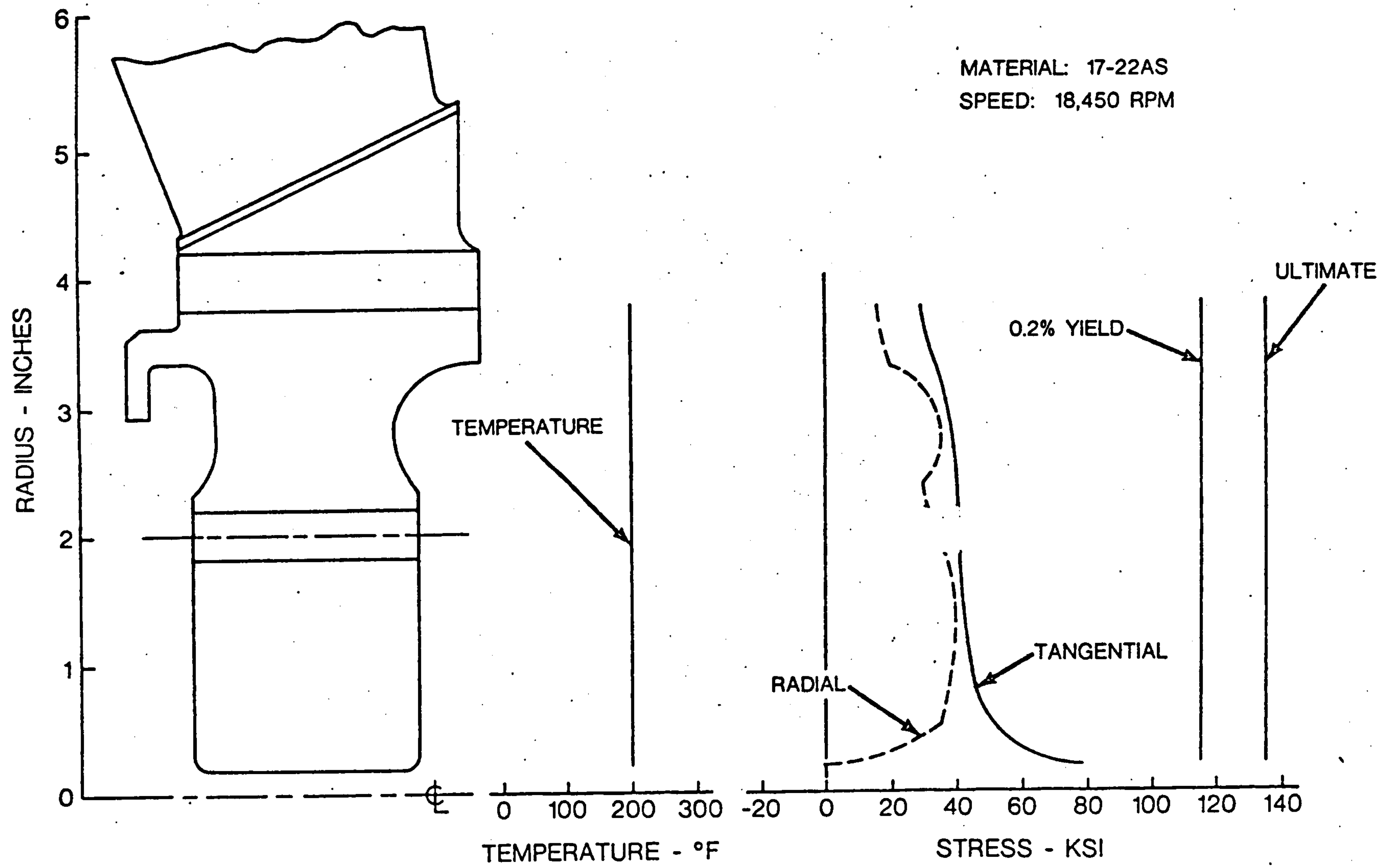

FIG. 34. DISK STRESSES.

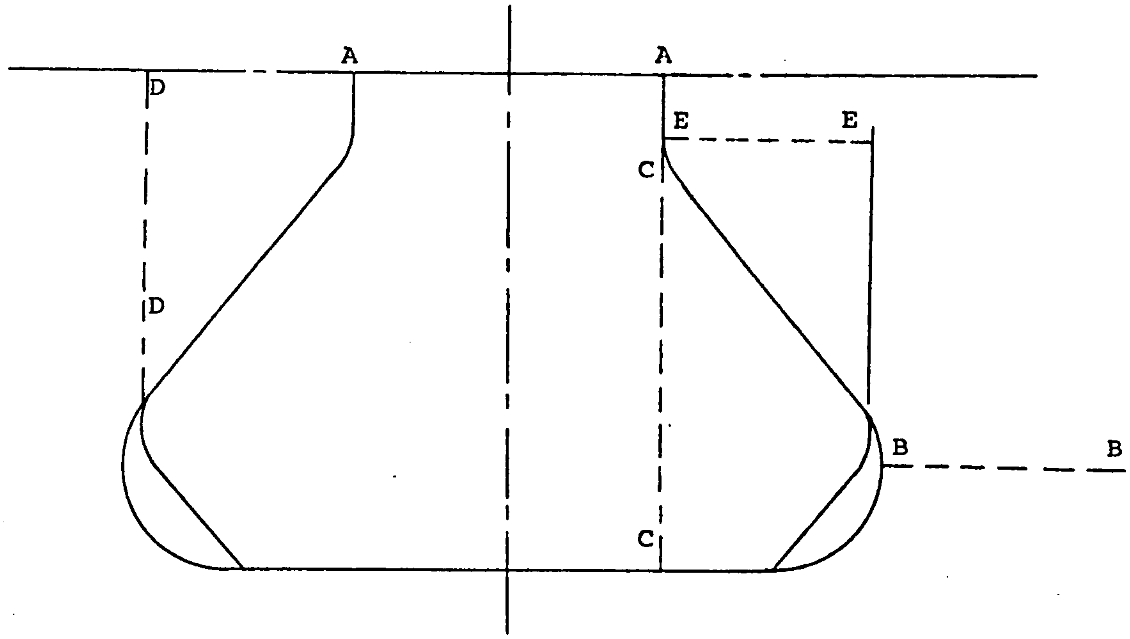

Part	Location	Type of Stress*	Stress Level (ksi)	Yield Strength Disk (ksi)	Yield Strength Blade (ksi)
Blade	A-A	Tensile	49.20	-	100,000
	C-C	Shear	21.00	-	50,000
Disk	B-B	Tensile	53.07	115,000	-
	D-D	Shear	17.36	57,500	-
	E-E	Bearing	61.03	-	-

*Includes C.F. and Bending Effect

Blade Material: Titanium 6AL-4V
Disk Material: 17-22AS

Temperature: 200°F
Speed: 18,450 rpm

FIG. 35. DISK/BLADE ATTACHMENT STRESSES.

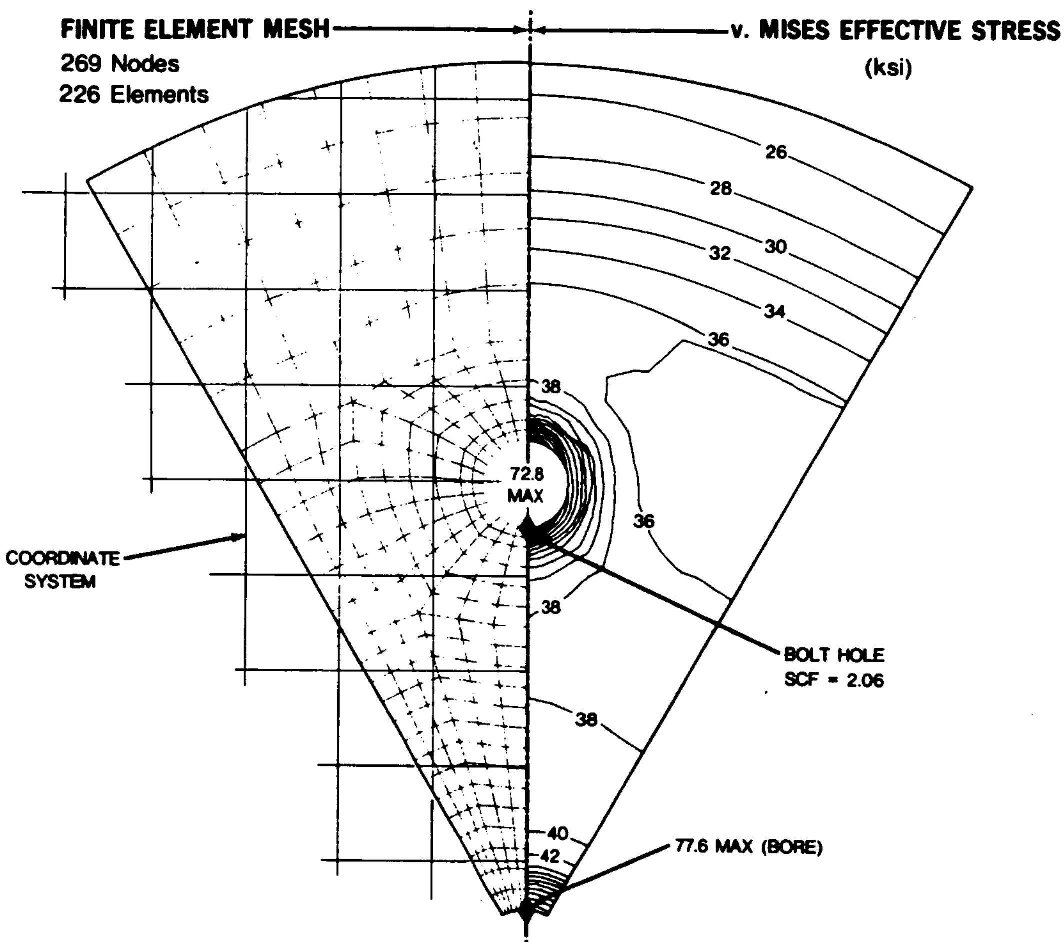

FIG. 36. DISK FINITE ELEMENT STRESS ANALYSIS.

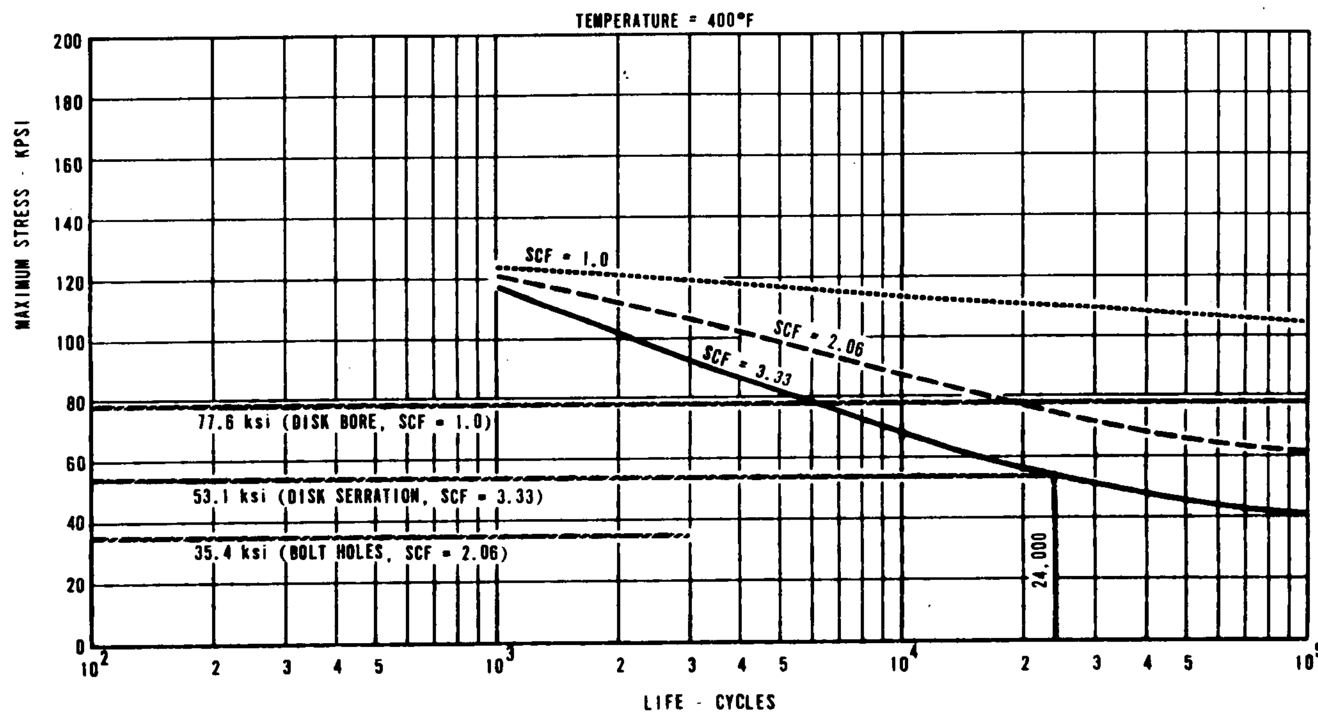

FIG. 37. MINIMUM DISK LOW CYCLE FATIGUE LIFE.

Blade root attachment stresses and corresponding material properties are also summarized in Fig. 35. The bending effects in both the root and tenon have been included. The axial width of the base-shrouded dovetail root was determined by a permissible bearing stress of 420 N/mm^2 (61.0 ksi). This is less than the compression yield limit, yet somewhat beyond the level at which fretting can occur under prolonged operation, but which should be satisfactory for a limited experimental program.

From a disk serration finite element analysis, the SCF was calculated to be 3.33 which is consistent with values measured from photo-elastic analyses of similar blade root configurations. The corresponding LCF life is 24,000 "start/stop" cycles based on the appropriate curve of Fig. 37. These fatigue lives are ample for the anticipated program of testing.

SECTION 6

DETAILED STATOR DESIGN

This section describes the detailed design of the fan stator which embodies the stator noise reduction concept described earlier. The stator uses vanes with varying sweepback angle to meet the criterion of a constant subsonic rotor wake trace speed along the stator vane span. The use of circumferential vane skew (lean) was avoided primarily to simplify the manufacturing problem. The stator vane number was chosen to cut off the radiation from residual sources due to end effects in the hub region of the vanes at blade passage frequency. The corresponding residual sources at the tip cannot be cut off because the spinning speed of wake disturbance pattern is supersonic at the tip.

To determine the proper vane sweep angle distribution, the rotor wakes were assumed to be convected with the mean flow. The spatial location of the wake centerline surfaces could then be computed from the mean flow properties by integration downstream from initial points on the rotor trailing edge. Since the rotor wake pattern spins fixed with respect to the rotor, it is possible to find leading edge lines whose shape is such that their point of intersection with the rotor wake centerlines travels at constant speed. Moving medium effects were taken into account in the actual calculation of a vane leading edge shape (see Appendix C for details). The trace speed was made constant and subsonic relative to the local flow velocity vector at all points on the vane span. The stator vane sweep distribution was designed to have an effective spanwise trace speed corresponding to a Mach number of 0.8 for the traveling load distribution.

The fundamental acoustical analysis which underlies the stator design concept is presented in Appendix C. In the remainder of this section, the methods for determination of the vane leading edge shape, and vane number are described, and the aerodynamic design considerations for the stator are reviewed.

6.1 Acoustic Aspects of Stator Design

The major noise producing mechanism of the stator is the interaction between the stator blades and the wakes shed by the rotor. This interaction causes fluctuating lift at the stator blades; the fluctuating lift in turn can be a potential source of noise. The fluctuating lift is restricted essentially near the stator blade leading edges (SBLE); this fact is made abundantly clear from the analytical work of Filotas (Ref. 10). It is also well known (e.g., Lighthill, Ref. 15) that any fluctuating lift, whether at the leading or trailing edge, whether acoustically compact or not, whether in a stationary or moving acoustic medium, acts as a dipole source of sound.

However, irrespective of the *nature* of the sources (i.e., whether monopole, dipole or quadrupole, etc.), there are certain aspects of acoustics of stationary and uniformly moving media which need to be considered before approaching the specific task of stator design and related acoustic problems. Discussion of these fundamental aspects is provided in Appendices C.1 and C.2, and their application to the stator design of this fan is described below.

6.1.1 Criteria for non-radiation

Acoustic wavelengths at rotor blade passage frequency are small compared to the stator blade span. In this case, the criterion for non-radiation due to unsteady forces is that the trace phase velocity of the force disturbance be subsonic relative to the local gas flow. Skewing, or sweeping of the stator blade, increasing the separation between rotor and stator, and shaping the rotor blade are techniques which can be used to reduce the phase trace speed.

Proper modification of leading edge profiles can reduce the phase trace speed along the leading edge and also the relative angle between that velocity and the local flow. Both effects are important as it is the trace velocity relative to the local gas-properties flow which must be kept subsonic.

Each individual wake shed by a rotor blade suffers a lag in the circumferential direction. The net effect of this lag on the nature of impingement of the wake on an unswept SBLE is that the wake hits the SBLE at the hub first and the impingement process propagates radially outwards towards the SBLE tip with a spanwise varying phase or trace velocity $c_o(r)$. Sweeping back the SBLE enhances this phase lag effect, in the sense that the spanwise trace velocity of wake impingement is reduced. A criterion along the lines of Eqs. (C.62) and (C.63) is used to guarantee that the wake trace Mach number m_o is less than m_u everywhere along the swept back SBLE. The nature of the wake phase lag and the calculation of the SBLE sweep angle is described more fully below. The successful analysis of a rotor wake tracing along the leading edge of a stator requires understanding of a set of transformations between stator-fixed coordinates and moving medium coordinates. The derivation of the trace velocity in stator-fixed coordinates, and subsequent Gallilean transformations to gas-fixed coordinates is given in Appendix E.

6.1.2 Estimate of rotor viscous wake

Estimates of the magnitude of the rotor viscous wake at the leading edge of the stator have been made. The method of estimation involved modeling the rotor blade wakes as the wakes behind isolated airfoils. The method is somewhat crude, as it ignores the interference between wakes and the axial pressure gradient. The variation of angle of attack at the stator which results from the estimated velocity fluctuations is as much as 10 degrees from the mean. Experience with axial flow turbomachinery wakes indicates that the estimated rotor wake amplitudes at the stator leading edge are likely to predict higher resultant angle of attack fluctuations than will exist in the actual rotor wake. This is due to the higher rate of decay of rotor blade viscous wakes in turbomachines when compared to isolated viscous wakes in free flow (see, for example, Lakshminarayana and Raj; Ref. 16).

6.1.3 Computation of rotor wake distortion

Contours of constant phase for rotor wakes at different axial locations were computed by use of a stepwise integration of the phase lag of the wake relative to a point in the rotor, as a function of radius. Cylindrical helical flow was assumed (radial flow velocity was assumed to be zero). Axial and tangential velocities used in this calculation were provided by AVCO's aerodynamic design program (Appendix A). Contours of constant phase calculated at several stations downstream of the rotor are shown in Fig. 38 (see Fig. 14 and Appendix A for Station Locations). Contours of constant phase versus axial location on cylindrical surfaces, shown in Fig. 39 and contours of constant phase in the axial/radial plane, shown in Fig. 40, were derived by cross-plotting from Fig. 38.

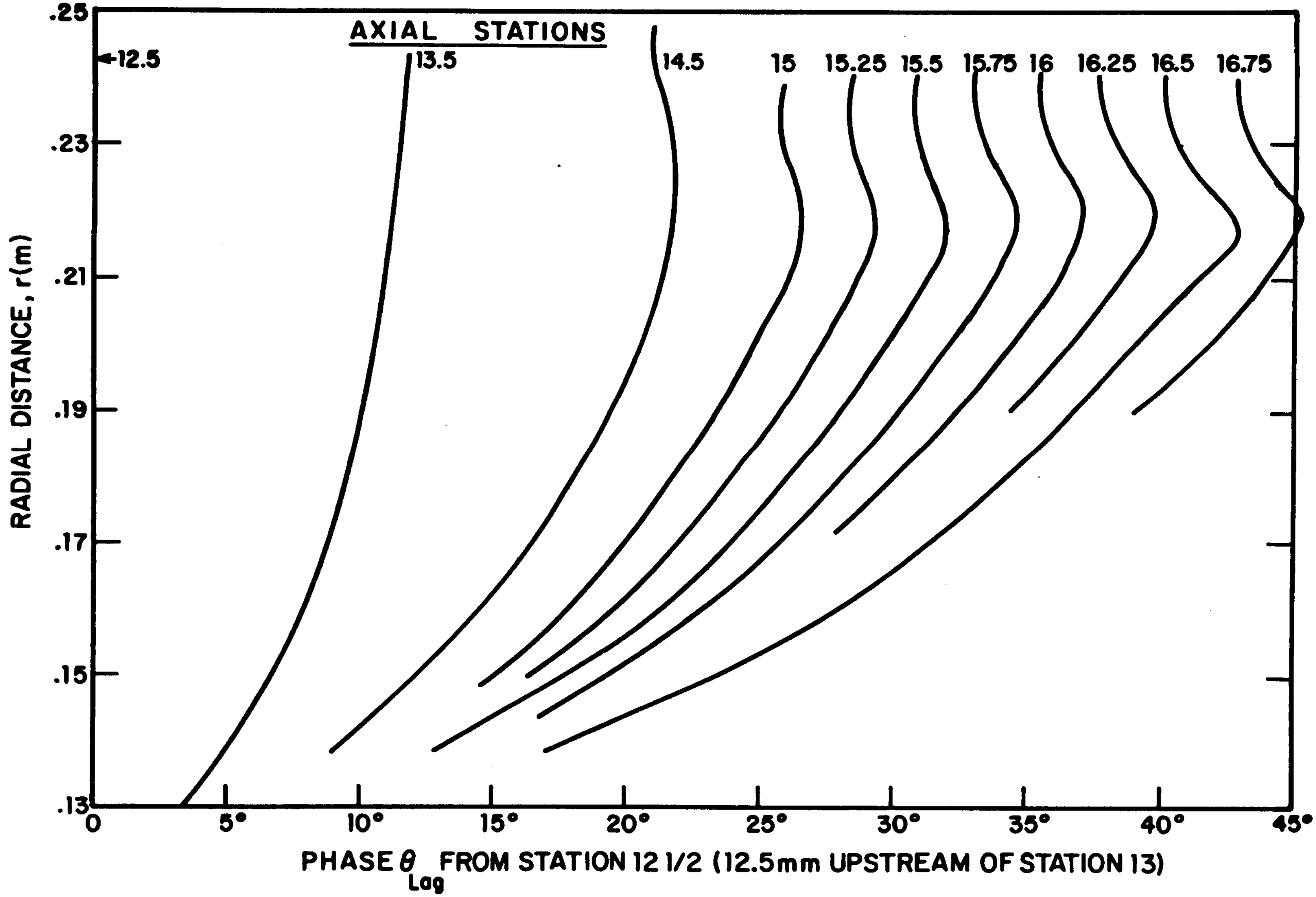

FIG. 38. PHASE vs RADIUS AT DIFFERENT AXIAL POSITIONS.

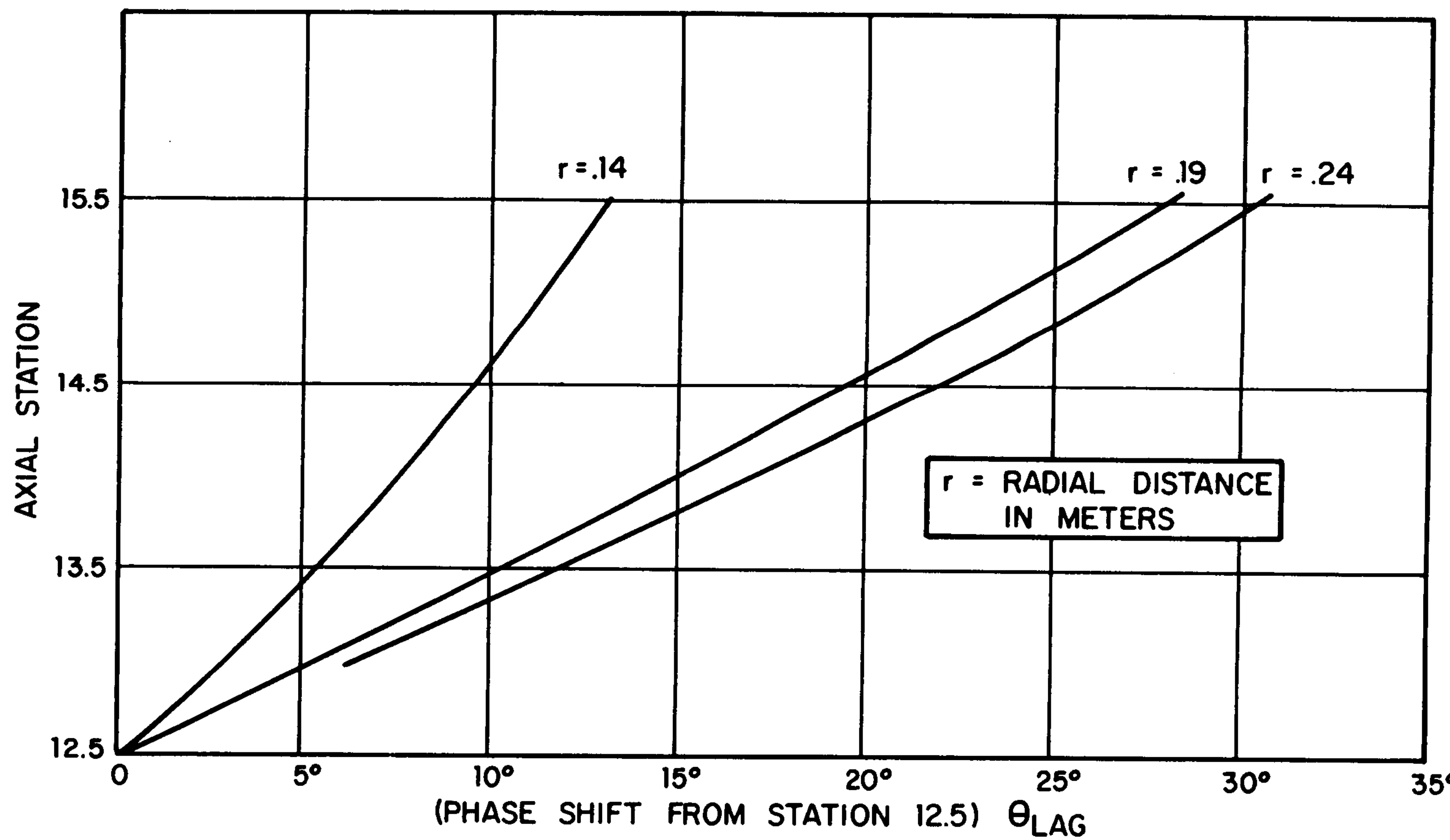

FIG. 39. PHASE vs AXIAL LOCATION ON CYLINDRICAL SURFACES.

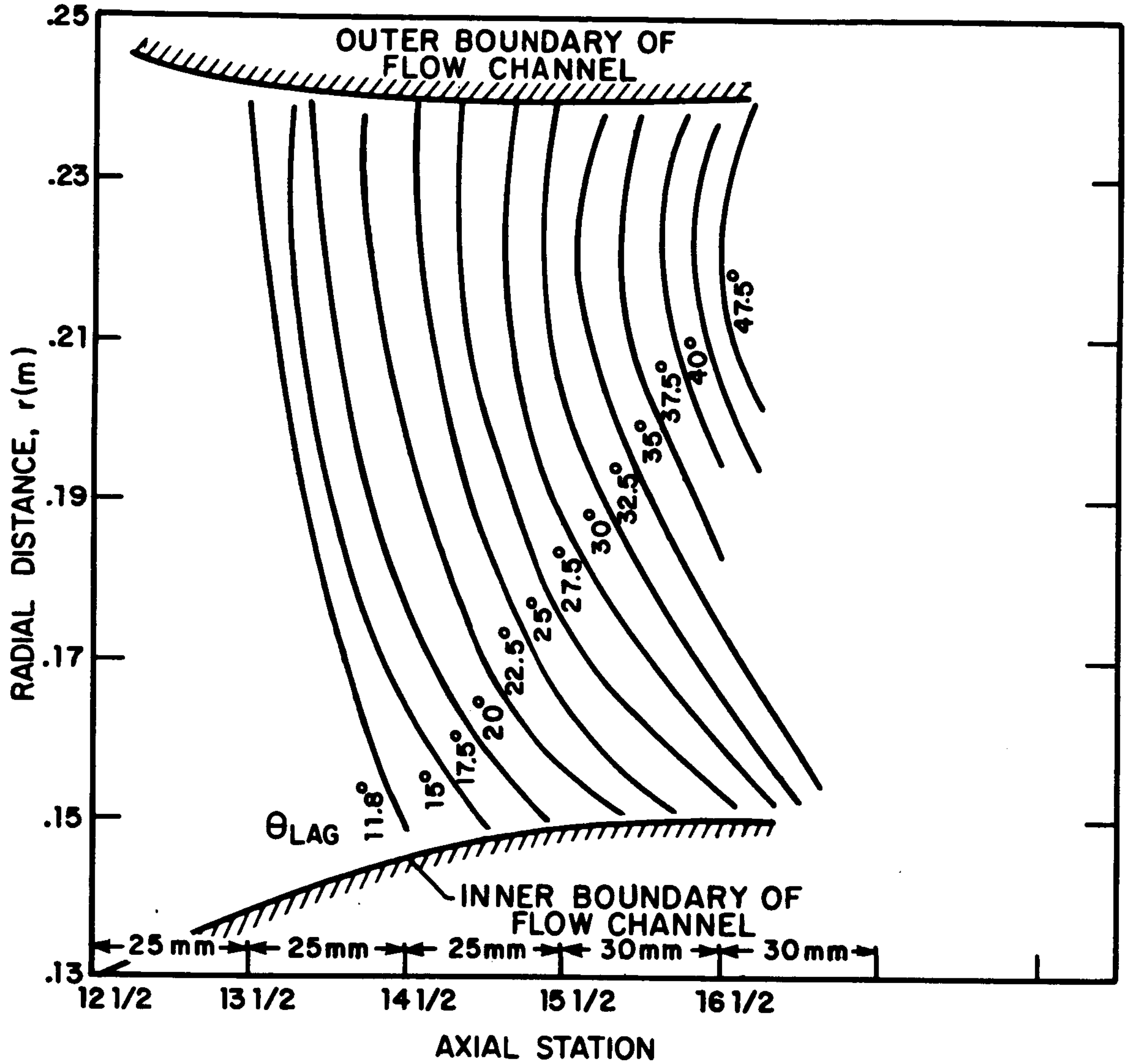

FIG 40. CONTOURS OF CONSTANT PHASE IN Y-Z PLANE.

Figure 41 illustrates, in stationary coordinates, the flow and blade motion geometry and the equations used in the calculation of the constant phase contours. The two terms $\Theta(\alpha)$ and $\Theta(\omega)$ in the calculations represent the angular translation of a fluid particle and the angular rotation of the rotor, respectively, in the time required for the fluid particle to flow from axial Station 1 to Station 2. The trace velocity, relative to local flow, for a number of constant-sweep-angle stators is shown in Fig. 42 The very high trace velocities near the tips result from reduced wake "windup" in that region, thus illustrating the limited effectiveness of constant angle swept stators.

6.1.4 Mach .78 leading edge stator

A blade leading edge sweep profile for trace speeds less than Mach 0.8 was developed for the final rotor and flow path design using an iterative method to achieve a nearly uniform trace velocity. The blade has a minimum sweep angle of 25 degrees at approximately 1/3 of the span from the root. Sweep at the root and tip are 30 and 40 degrees, respectively. Figure 43 shows the sweep profile as well as the trace and acoustic speeds as a function of radius.

The calculations assume a rotor blade reference axis at the axial location 12-1/2 mm. forward of the root at Station 13. It also assumes a stator leading edge which is radial, when projected in the r, θ plane, and has its root 12.5 mm. downstream of Station 15.

The inflow-induced radiation from an array of such variably-swept stator vanes is now restricted to the tip regions when discontinuities occur. The limitation of such radiation depends upon proper choice of the number of swept leading edge stators, which in turn depends upon the rotor blade number, rotation speed, and moving medium acoustical considerations. The computation of vane numbers is discussed below.

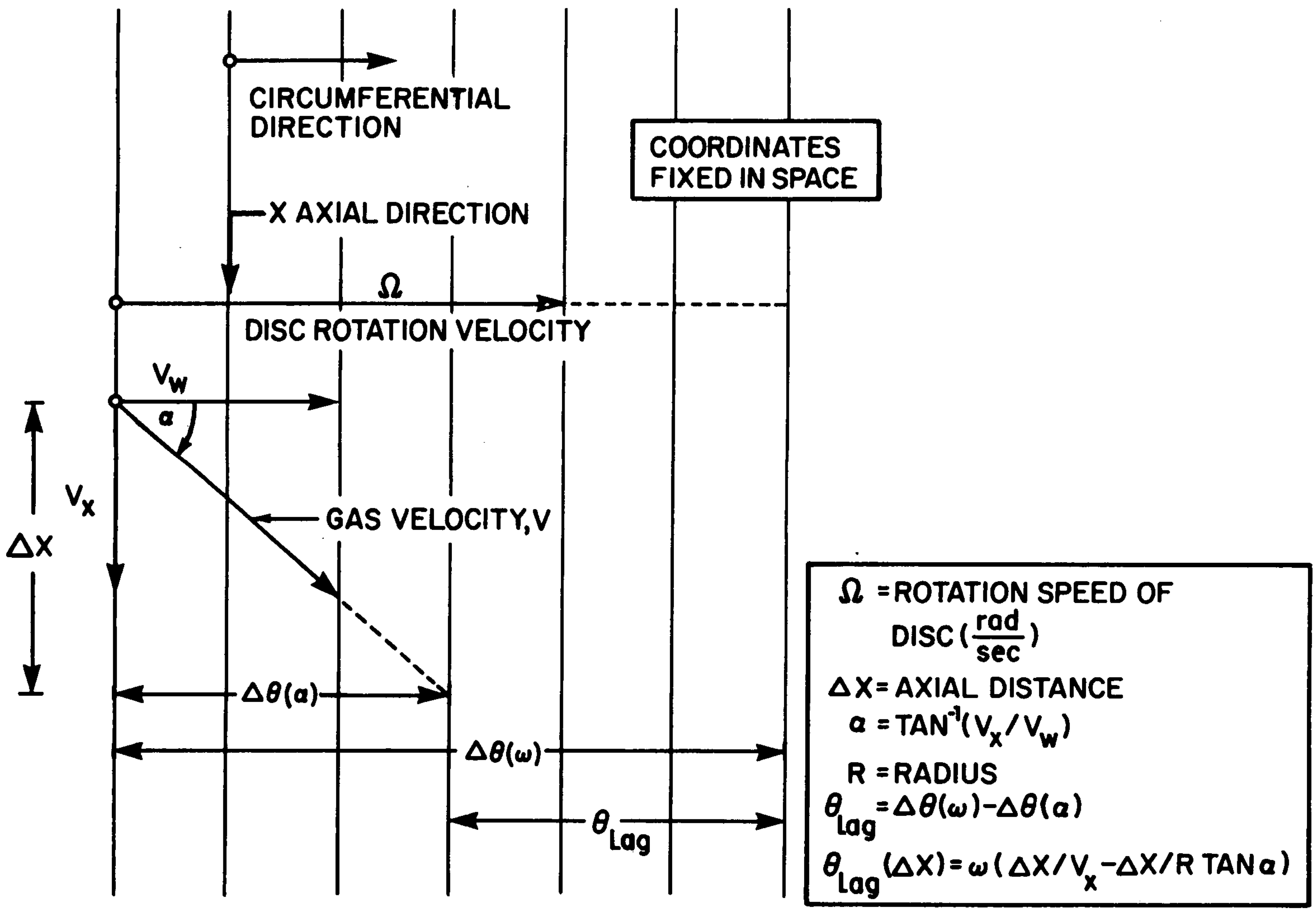

FIG. 41. PHASE LAG, θ_{lag}, RELATIVE TO POINT OF ORIGIN FIXED ON ROTATING ACTUATOR.

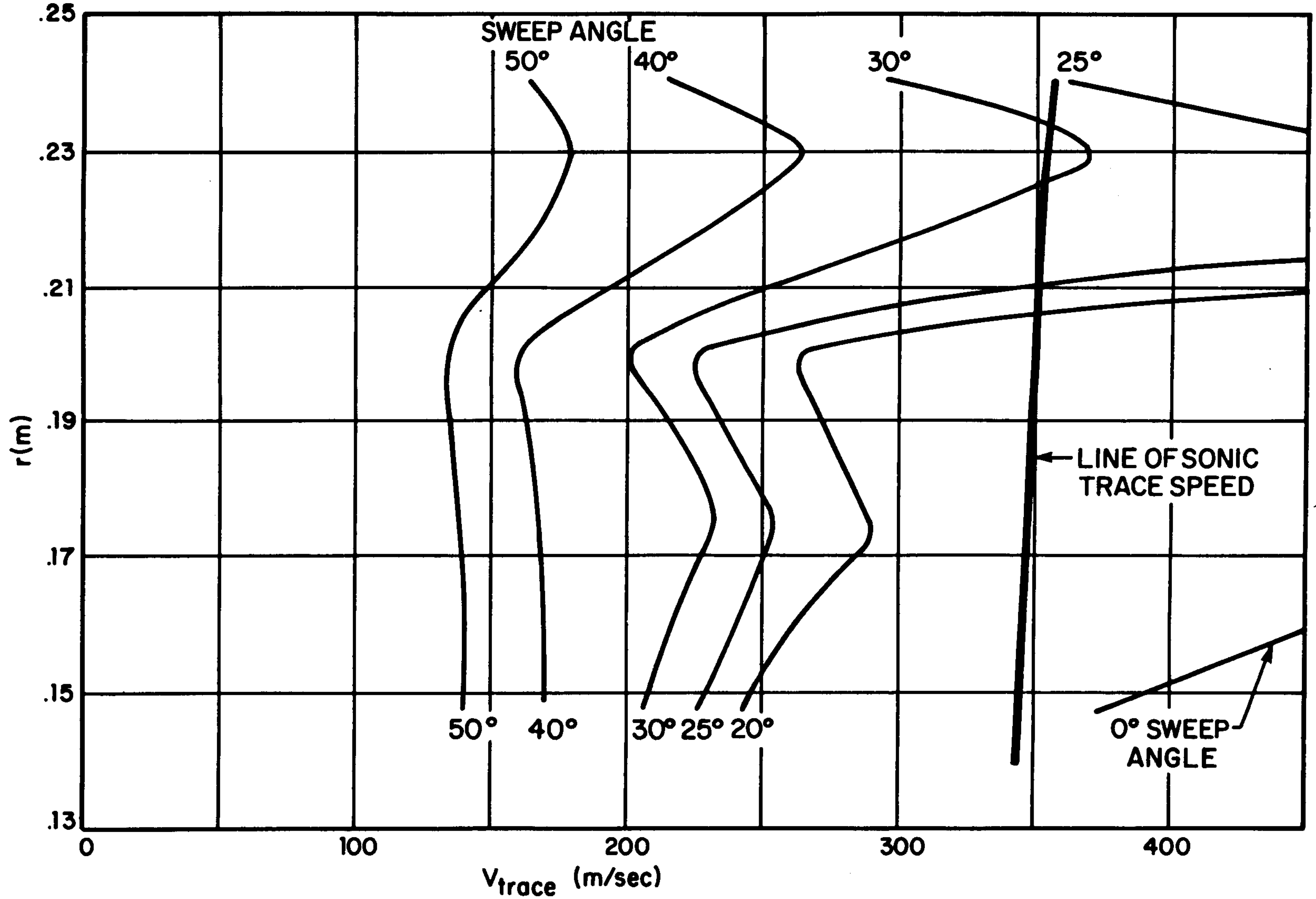

FIG. 42. TRACE VELOCITY FOR DIFFERENT SWEEP ANGLES.

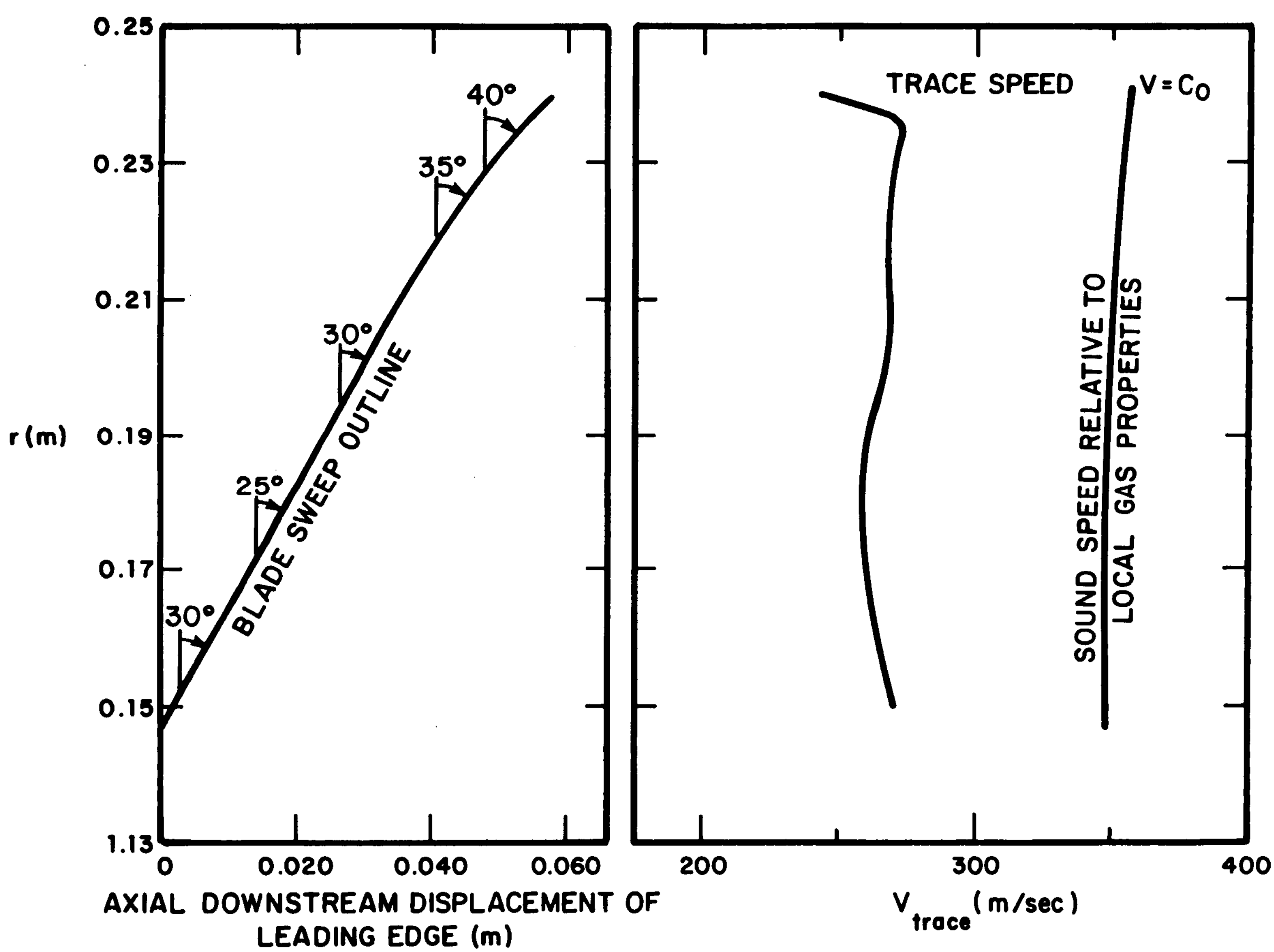

FIG. 43. MACH .78 LEADING EDGE PROFILE (FINAL VANE DESIGN).

6.2 Analysis For Determination Of Number Of Stator Blades

This section determines the appropriate minimum number V of stator blades so that the acoustic noise radiated from the stator at the **rotor** blade passage frequency f_r is minimized.

Since the swept back SBLE derived in the above section is of finite extent, the end effects at the SBLE hub and tip from the wake/SBLE interactions remain as potential sources of noise. The aim here is to seek a partial *circumferential* cancellation of these end sources. Thus, two discrete circumferential arrays exist, one at the SBLE hub and the other at the SBLE tips. Since the circumferential phase velocity c_o is higher at the tip than at the hub, one concentrates on the discrete circumferential array made up of uncancelled sources at the SBLE tips. Also, as discussed in Appendix C, the discussion of a discrete array must be limited to only one frequency ω_o. Choosing ω_o to correspond to the fundamental rotor harmonic, (i.e., to the rotor blade passage frequency f_r), one obtains

$$\omega_o = \Omega B \quad , \tag{17}$$

where Ω is the shaft rotation in radian/sec ($\Omega \simeq 1940$ rad/sec) and B is the number of rotor blades (B = 28). The blade passage frequency f_r is given by

$$f_r = \frac{\omega_o}{2\pi} \simeq 8600 \text{ Hz} \tag{18}$$

For the circumferential phase velocity c_o

$$c_o = \Omega r_t \quad , \tag{19}$$

where r_t is the radius at the stator tip ($r_t \simeq 0.24$m $\simeq 0.79$ ft). The corresponding Mach number m_o is therefore given by

$$m_o = \frac{c_o}{c} \approx 1.27 \qquad (20)$$

With reference to results of Appendix C.2, (Eq. C.60), m_1 is the Mach number of the gas flow parallel to the array, and m_r is the gas Mach number normal to the array. Since the array under consideration is oriented circumferentially, the gas Mach number m_c in the circumferential direction plays the role of m_1 and the gas Mach number m_a in the axial direction plays the role of m_r; the radial gas Mach number, normal to the duct walls, is to a good approximation zero. Thus, we have

$$m_1 \equiv m_c \simeq 0.353 \qquad (21)$$

$$m_r \equiv m_a \approx 0.582 \qquad (22)$$

Note that m_c is directed the same way as the shaft rotation Ω or the phase Mach number m_o. Hence, first one would like to find from Eqs. C.62 and C.63 whether $m_o < m_u$ - one of the two necessary conditions for no radiation to occur. Substituting the quoted values in Eq. C.62, one finds that

$$m_o < m_u, \quad \text{for } \frac{\pi}{2} < \alpha \lesssim \frac{\pi}{4} \quad , \qquad (23)$$

in other words, the condition for no radiation is satisfied for angles α that are sufficiently remote from the axial direction.

In order to satisfy the second condition for (partial) cancellation of radiation from the fundamental rotor harmonic, it is required that

$$\frac{2\pi}{d_t} > 2\,\frac{2\pi}{\lambda_r}\,\frac{(1-m_a^2\cos^2\alpha)^{1/2}}{(1-m_c^2-m_a^2\cos^2\alpha)}\quad , \tag{24}$$

where d_t is the circumferential spacing between two adjacent SBLE tips. The spacing, d_t, is related to the number of stator blades by the relation

$$d_t = \frac{2\pi r_t}{V} \tag{25}$$

The right hand side of Eq.(24) is the radiation span ($k_{a_{o+}} - k_{a_{o-}}$) obtained from Eq. C.60, where $2\pi/\lambda_r$ has been substituted for k_{a_o}, λ_r being the acoustic wavelength at frequency f_r. Taking sound speed c in the gas to be about 365 m/s (1200 ft/sec), the wavelength at blade passage frequency is

$$\lambda_r = \frac{c}{f_r} \approx 0.14 \text{ ft} \approx 0.043 \text{ m} \tag{26}$$

Thus, substituting Eq. 25 in Eq. 24 , the velocity is

$$V > \frac{4\pi r_t}{\lambda_r}\,\frac{(1-m_a^2\cos^2\alpha)^{1/2}}{(1-m_c^2-m_a^2\cos^2\alpha)} \tag{27}$$

Since the first necessary condition (Eq. 23) is satisfied only for a restricted range of angles α, it would not pay to find the maximum possible value of V for arbitrary α. Instead, Eq. 27 is evaluated for $\alpha = \pi/4$ (as α goes from $\pi/2$ to $\pi/4$ to 0, V evaluated from Eq. 27 increases), and the result is

$$V \geq 92 \tag{28}$$

One can now examine the application of traditional analyses (e.g., Tyler and Sofrin (Ref. 11)) of noise generated by rotor-stator interaction, the anlysis that is used primarily for low-speed compressors (i.e., analysis is based on stationary medium acoustics) that involve subsonic circumferential phase speeds (i.e., $\Omega r_t < c$) and are acoustically compact (i.e., $d_t < \lambda_r/2$).

An arbitrary component (say, the predominant component of wake velocity deficit pattern that generates fluctuating lift at SBLE) $a(x,r,\theta,t)$ of rotor-generated flow field near the stator may be decomposed into circumferential harmonics as follows

$$a(x,r,\theta,t) = \sum_{n=-\infty}^{+\infty} A_n(x,r)\, e^{i[nB(\theta-\Omega t)]} , \qquad (29)$$

where x and r are the axial and radial locations (and for our case of interest denote the locations of SBLE tips) and θ is the circumferential angle.

The noise sources (in particular, the fluctuating lift ℓ generated at SBLE tips) at the stator due to the *nth* rotor harmonic may then be viewed as composed of a sum of stator/rotor harmonics mn. A typical interaction harmonic $L_{mn}(s,r,\theta,t)$ may be written as

$$L_{mn}(x,r,\theta,t) = L_{mn}(x,r)\, e^{i(m\theta-nB\Omega t)} , \qquad (30)$$

where

$$m = nB + kV , \qquad (31)$$

and where k can assume arbitrary integral values (positive, negative or zero).

The circumferential phase velocity $c_o(r)_{mn}$ associated with Eqs. 30 and 31 can be written as

$$c_o(r)_{mn} = \frac{nB\Omega r}{nB+kV} , \qquad (32)$$

Similarly, from Eq. 19, the circumferential phase velocity for *all* the rotor harmonics n is Ωr and assumes the value Ωr_t at the SBLE tips. This same value is recovered for the interaction modes from Eq. 32, for the stator fundamental mode, i.e., for the case k = 0.

Figure 44 depicts the situation in terms of these rotor-stator interaction harmonics. The harmonics lie at the intersections of vertical lines passing through the nB axis for n = 0, ±1, ±2 ... and horizontal lines passing through the m axis for k = 0, ±1, ±2 ... The rotor fundamental tone occurring at the blade passage frequency f_r (see Eqs. 17 and 18) corresponds to vertical straight lines passing through n = ±1 (i.e., nB = ±28). Similarly, n*th* rotor harmonic corresponds to frequency nf_r. The fact that attention was turned to the *stator* fundamental harmonic at frequency f_r (see Eqs. 19 and 20) means that the k = 0 stator mode was examined at f_r. From Eq. 23, one finds that this stator fundamental harmonic barely escapes radiation. From Eq. 32, it can be seen that the same situation applies to stator fundamental harmonics (i.e., k = 0 modes) for *all* rotor harmonics (i.e., arbitrary n). Thus, the straight line in Fig. 44 passing through these k = 0 modes separates the radiating and non-radiating harmonics.

The criterion of Eq. (24) was applied to prevent the next candidate stator harmonics (k = ±1 modes for n = ±1) from radiating at the blade passage frequency f_r (*only*). The straight line joining these k = -1, +1 modes thus also separates the radiating and non-radiating harmonics. The flow-induced assymmetry in radiation span along wavenumber is reflected in Fig. 44 by assymmetry of radiating and non-radiating harmonics around m and nB axes. Incidentally, stator harmonics lying in the upper right and lower left quadrants of the m, nB plane possess circumferential velocities that are oriented in the same direction as shaft rotation Ω, and the harmonics lying in the upper left and lower right quadrants possess velocities that are oriented in the direction opposed to Ω.

Finally, note that the relatively high number V of stator blades indicated by Eq. 28 may cause design problems of aerodynamic nature. For example, relatively high solidity at the hub, particularly for the scale model fan, is unacceptable. Therefore, a compromise number of 59 was selected for V. Such a choice ensures circumferential cancellation at the SBLE hub, but not at the tip. In other words, with reference to Fig. 44, k = ±1 modes would radiate from the SBLE tips.

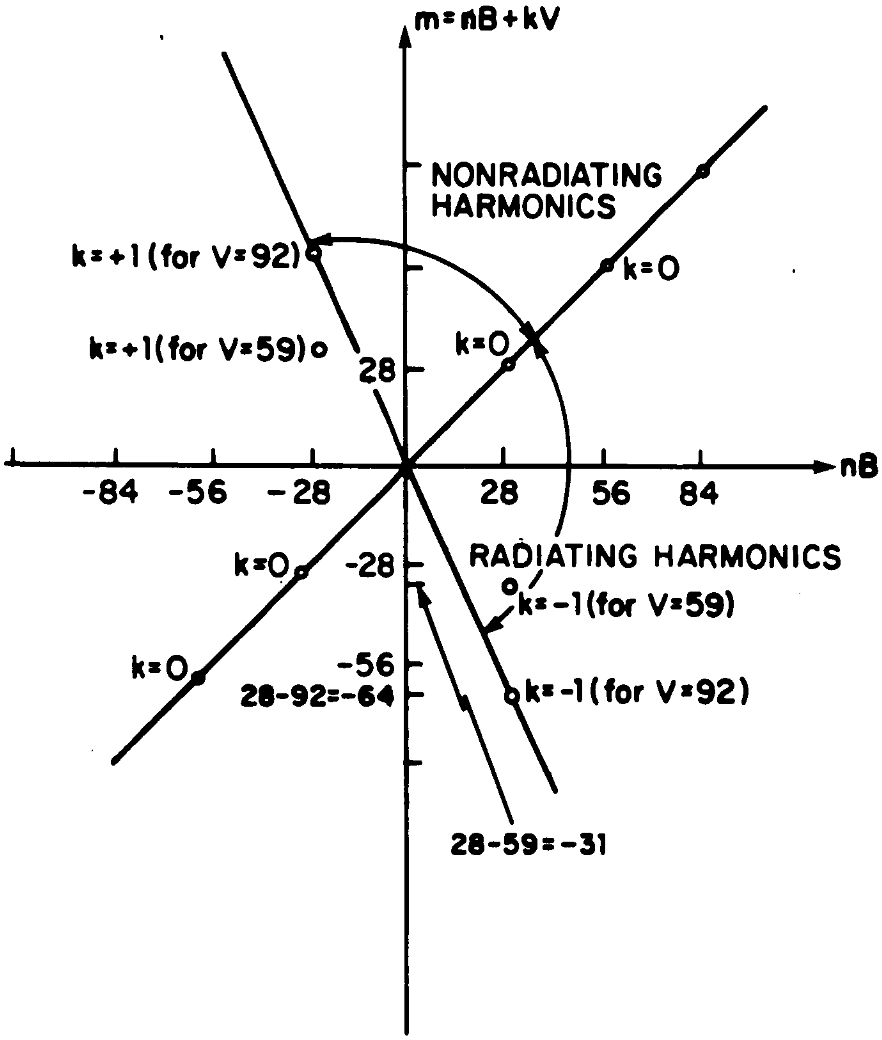

FIG. 44. SKETCH OF RADIATING AND NON-RADIATING ROTOR/STATOR INTERACTION OF HARMONICS (nB,m).

6.3 Stator Aerodynamic Design Considerations

The stator is characterized by a backward leading edge sweep varying from 25 to 40° in the meridional plane. The axial spacing between rotor trailing edge (TE) and stator leading edge (LE) varies approximately from two to three rotor hub chords along the span.

A minimum number of 59 blades was specified by acoustic considerations. This, in conjunction with a tentatively selected hub cascade solidity $\sigma_{hub} = 2$, resulted in a chord length of approximately 30mm.

The meridional contour of the stator was shown in Fig. 14. Radial station 17 crosses the leading edge, 19 the trailing edge, and 18 crosses both the leading and trailing edges. Radial equilibrium along those stations is markedly influenced by the varying degree of stator turning, resulting in peculiar tangential velocity distributions that have been input in R-121, together with the corresponding total pressure loss distributions. The flow conditions from rotor exit station 13 to stator inlet stations 16, 17, 18, and 19, have been calculated according to constant rotor exit momentum $V_u \cdot r$ specified along the streamlines.

The meridional flow pattern (Fig. 14) shows the radial streamline shifts induced by the swept back stator configuration, especially in the hub region, where $V_u \cdot r$ is large and has a strong effect on radial equilibrium. In the axisymmetric flow case, the streamlines approaching the leading edge are deflected inboard. Looking at the lower portion of station 17, the flow at the hub section has already undergone the major part of its turning, and $V_u \cdot r$ thus increases markedly from the hub to the 30% streamline on that station. This substantial departure from free-vortex flows generates an increase of the axial velocity component toward the hub and a corresponding increase of the mass flow density ρV_x, in turn resulting in inboard streamline shifts between leading edge and station 17. This characteristic pattern is found along the entire span, but disappears gradually toward the tip section because of the decreasing value of the V_u^2/r-term.

The meridional streamline curvature term V_m^2/R_c has a strong effect in this flow field region. The determination of R_c however is very approximative even with the spline-on spline procedure used in R-121, so that the interpolated values of the flow conditions at the stator leading edge cannot be expected to be smooth. Fig. 45 shows the radial distribution of the inlet angles α_3 determined by V_x-interpolation and constant $V_u \cdot r$ along the streamlines, and the smooth distribution assumed for blading design. The maximum smoothing error does not exceed 1-1.5°, which is well within the accuracy that can be expected from the axisymmetric analysis.

Figure 45 also shows the stator exit flow deviation angles δ calculated with Carter's formula [Equation (8), circular mean camber lines]. The blade sections are stacked with the leading edge in a meridional plane. All profiles were set at 0° nominal incidence. Table 6 lists the profile data defining plane sections perpendicular to the radius in the leading edge plane.

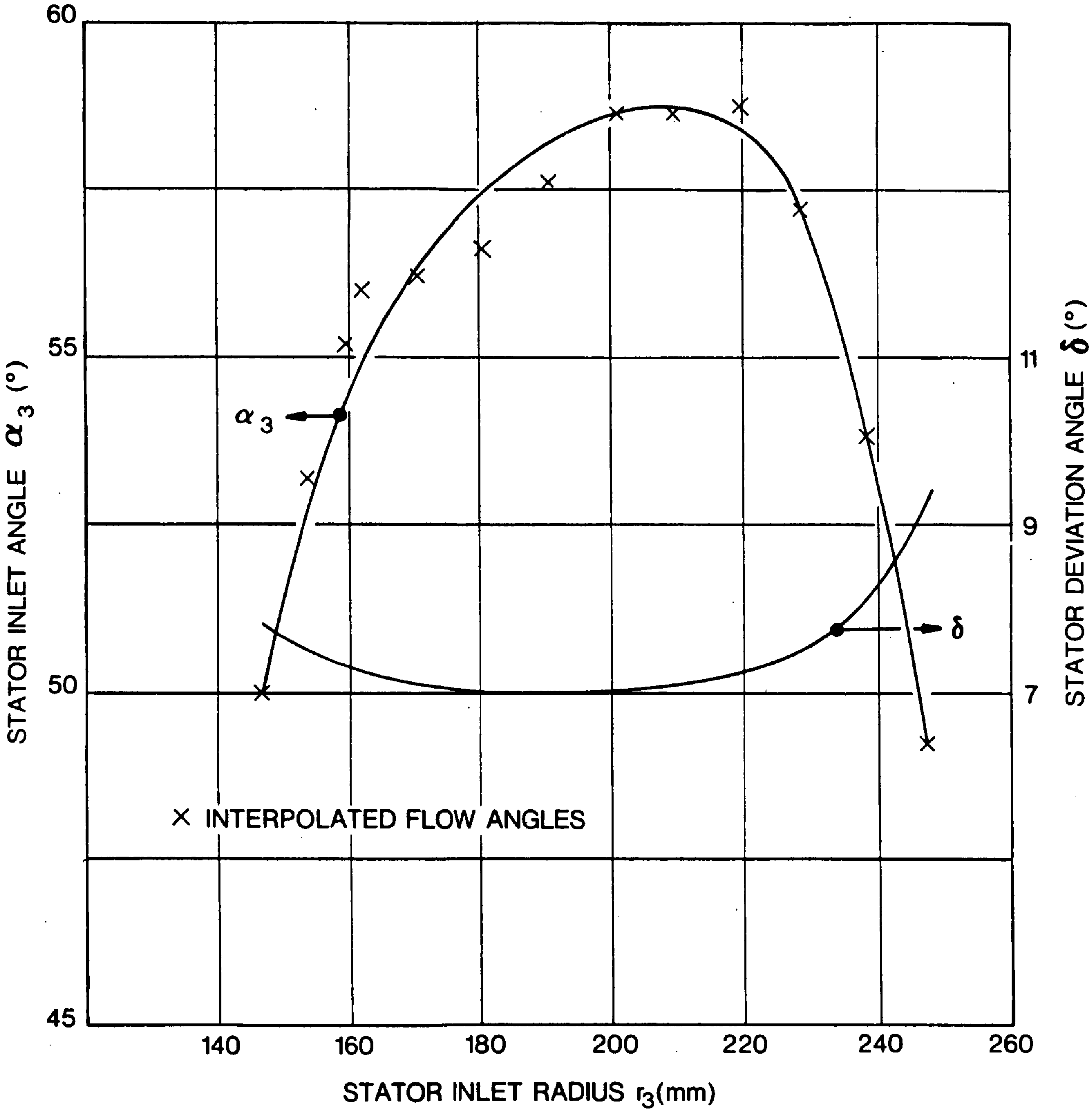

FIG. 45. STATOR INLET FLOW AND DEVIATION ANGLES.

TABLE 6. STATOR BLADE DATA

59 Blades (Plane Sections)

Section Radius (mm)	147	154	160	171	191	210	228	236	242	248
Mean Camber Angle Φ (°)	47.80	44.90	43.00	40.80	38.90	38.40	40.00	43.1	46.50	50.20
Setting Angle γ (°)	73.90	75.05	75.80	76.70	77.55	77.90	77.50	76.55	75.45	74.30
Chord Length c (mm)	31.3	31.3	31.5	31.85	33.05	34.80	36.90	37.9	38.75	39.60
Diffusion Factor D	.396									.288
Rel. Thickness ν (%)	6.0	-	-	-	-	-	-	-	-	6.0
Axial Coordinate of L.E. z_L (mm)*	0	4.1	7.8	14.0	25.1	35.0	47.4	53.7	58.7	64.0

*Leading Edge swept back in a meridional plane.

SECTION 7

COMMENTS ON RESIDUAL NOISE SOURCES AND NOISE LEVELS OF THE SWEPT ROTOR AND STATOR FAN STAGE

The object of the Low Source Noise Fan Program is to design fan components for minimal noise generation. This has been done by first using physical models for each of the component noise mechanisms, and calculating the appropriate parameters from the particular baseline fan design, then modifying the component geometry to minimize noise generation. All sources of noise cannot be eliminated, and indeed all sources have not been attacked in this study.

7.1 Residual Sources for a Fan outside the Laboratory Environment.

As has been previously discussed in detail, the compound sweep required on the rotor blades for structural reasons will lead to a conical shock at the sweep reversal point. However, in some future fan designs, the location of the sweep reversal point at a radius less than that at which the critical relative Mach number occurs will eliminate the source of noise. Rotor discrete frequency mechanisms which cannot be eliminated include the so-called Gutin noise sources associated with steady loads and thickness noise. However, the non-radial blading may cause these mechanisms to excite high order duct modes and thus reduce the radiation to the far field. Rotor broadband mechanisms are relatively poorly understood quantitatively (in the absence of inflow turbulence), and thus are difficult to attack at the source. Shock/turbulence interaction in the channel may cause some forward radiated noise, and quite likely causes aft-radiated broadband noise.

Stator noise mechanisms are much better understood and can be attacked with much more confidence than some rotor mechanisms. The uncancelled tip radiation (calculated in Appendix C) is the only discrete-frequency mechanism inherently associated with the subsonic trace speed swept stator concept, assuming that the rotor wake field can be accurately specified. Stator broadband mechanisms not attacked by the swept leading edge include vortex shedding and flow separation at the trailing edge.

Other broadband noise from an installed fan comes from the exhaust jet and duct boundary layer turbulence interaction with the lip of the fan duct.

7.2 Prediction of Noise Levels and Noise Reduction of the Swept Rotor and Stator Fan.

Despite intensive research efforts in the past twenty years which have led to a good understanding of noise mechanisms and scaling laws, the ability to predict fan noise for an arbitrary design on a component-by-component basis is quite limited. For conventional fans, useful semi-empirical correlations of data have been made using scaling laws which are based on assumed mechanisms. Thus, for conventional fans, one can predict within a few dB the expected sound power and directivity. However, the applicability of those correlations to a fan of unconventional component design is doubtful.

For the subject fan design, the prediction of residual noise from the rotor requires the knowledge of the strength of the conical shock upstream of the rotor, which is not presently known due to the cessation of activity on the 3-D compressible flow program. The stator discrete noise has been calculated directly for basic principles and is presented in Appendix C.

However, the main noise source of interest, rotor multiple pure tones cannot be reliably estimated without detailed information on shock structure and duct propagation characteristics. In the interest of providing an estimate of the benefits of eliminating MPT noise, a computer program published by Burdsall *et al.*, (Ref. 20) was exercised (see Appendix D for details). The results summarized below for a full scale (a 40,000 lb thrust) counterpart of the 20 inch fan built in this program, show that elimination of the shock-generated MPT's reduces the overall and perceived noise levels by 4-6 dB, and reduces the tonal content in the 1/3 octave band containing the blade passage frequency by about 10 dB.

TABLE 7. ORDER-OF-MAGNITUDE EMPIRICAL ESTIMATE OF NOISE LEVELS FROM FULL SCALE SINGLE STAGE FAN.

Spectrum Component	Overall PWL (dB re 10^{-12}w)	OASPL*(@150') dB(re $2x10^{-5}N/m^2$)	PNL*(@150')
M.P.T.(conventional blades)	152-154	104-106	117-119
B.P. Tone	143	95	108
Broadband Mechanisms	150	103	114
TOTAL			
with MPT's	153.5-155.2	105.3-107.2	118-120
without MPT's	150	103	114

*Valid in the forward-radiated direction at azimuths from 40-80° from fan axis (± 3 dB); to scale to greater distances, subtract 20 log r/150, where r is distance in feet.

SECTION 8

MECHANICAL DESIGN ASPECTS AND FACILITY INTEGRATION

The fan rig is built to conventional standards and is designed to interface with the NASA W-2 and W-8 test facilities. The W-2, acoustic facility is arranged for the measurement of forward and rearward radiated noise; thus, the rig casings have flanges at both ends which mate with the facility mounting flanges. The manner in which this is accomplished is shown schematically in Fig. 12. In the reverse flow mode, for backward radiated noise, an additional flow path adaptor supplied by NASA and not shown in Fig. 12 is fitted to the fan outlet flanges. In the W-8 facility the fan is mounted on its rear flange with the flow entering from the bellmouth. All detailed performance measurements of the fan will be made in the W-8 facility.

A flow path adaptor fits over the facility bearing housing to control the fan outlet flow and into this adaptor is fastened the inner shroud of the stator vane assembly. The outer shroud of the stator vane assembly is located in the fan casing and provision is made for axial adjustment of the stator by relocating the spacers at the inner and outer shrouds. The fan outer casing is split in the vertical plane for assembly purposes. The section of the outer casing in the area of the blade tips is relieved and an abradable shroud lining is installed to prevent blade tip damage in case of tip rubs. Figure 46 shows the engineering cross-section of the fan which details all the major components. Strain gauges will be applied to the rotor blades, the wires being led down the front and rear faces of the disc. In the W-2 facility the slipring is installed at the driven end of the rig shaft and, thus, the strain gauge wiring will pass down the length of the hollow shaft. When the fan is running in the W-8 aerodynamic facility, the strain gauge wiring will be led forward through the driveshaft adaptor which is fitted in place of the spinner support cone. A static fairing is installed over the slipring to provide a smooth flow profile into the fan, in place of the spinner.

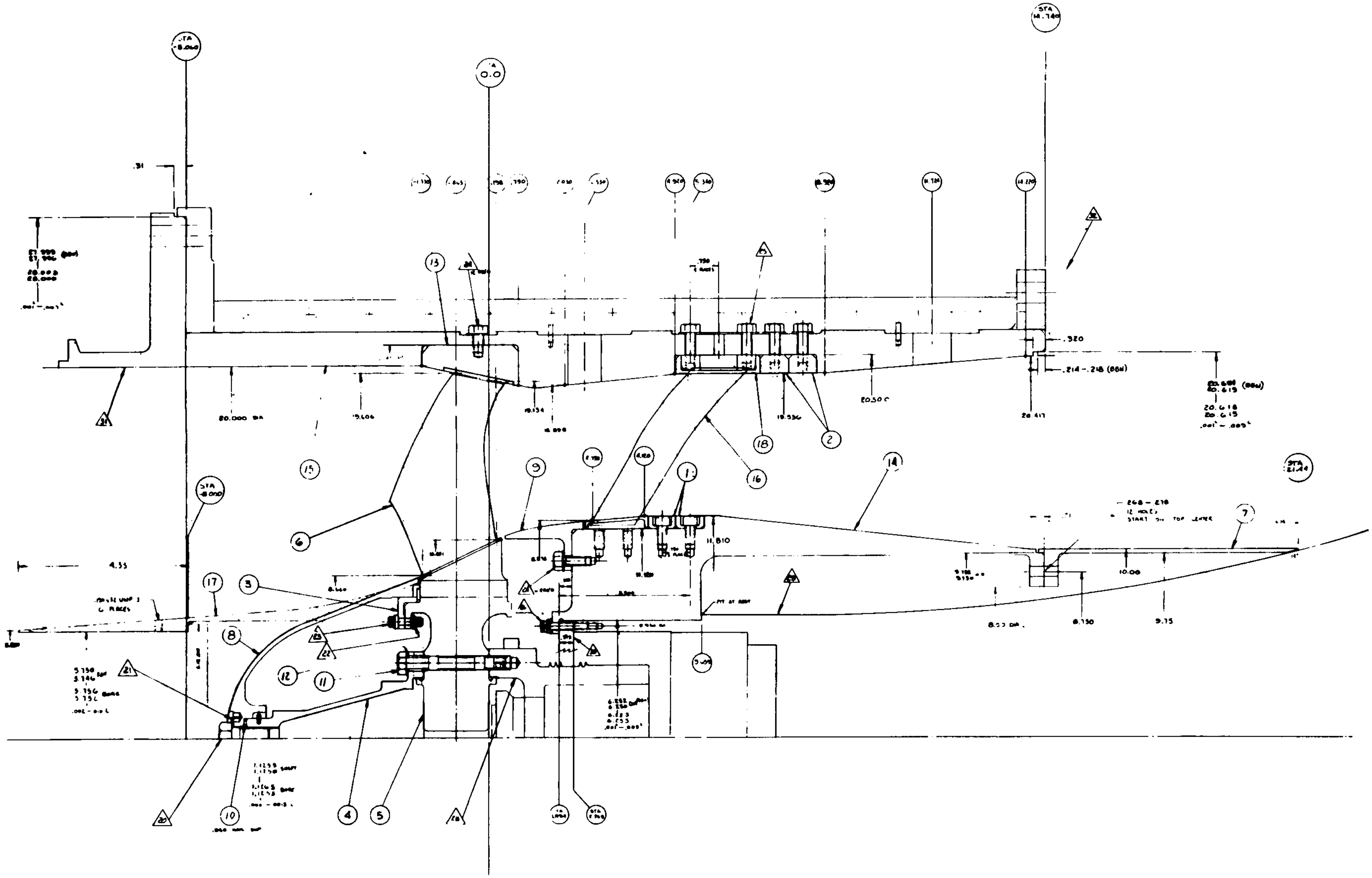

FIG. 46. DETAILED CROSS-SECTION OF FAN RIG.

SECTION 9

CONCLUDING REMARKS

A research program was undertaken to try to demonstrate that source noise reduction concepts which are based upon full and rigorous application of fundamental aeroacoustic principles can be implemented on turbofans in the currently-operating range of tip speeds and pressure ratios, utilizing the existing design and manufacturing capabilities of the aircraft engine industry, without serious compromise of the noise reduction concept.

The subsonic leading edge rotor blade concept has significant potential as a practical solution to rotor-generated noise due to its inherent lack of sensitivity to off-design-point operating conditions, and the large family of detailed edge and generating surface contours available for fans in various speed ranges. The aerodynamic behavior of subsonic leading edge rotors in supersonic absolute inflow velocities is largely unknown at this point in time. However, it is believed that the characterizations of such flow fields, to the extent necessary in developing actual engines using the subsonic leading edge rotor principle, would at this time require considerably less effort than has been expended historically in understanding aerodynamic behavior of conventional rotors.

The subsonic trace speed stator vane concept can be implemented through application of moving medium acoustic principles and a knowledge of the details of the rotor wake field, the lack of the latter being a current limitation. However, the subsonic trace speed concept can, in principle, be successfully implemented by use of conservative assumptions about the rotor wake field.

APPENDIX A

COMPUTER LISTING OF AERATHERMODYNAMIC PARAMETERS FOR FINAL ROTOR, STATOR & FLOW PATH DESIGN

APPENDIX A: DETAILED AEROTHERMODYNAMIC DATA

This appendix contains a computer listing of the aerothermodynamic data for the final design of the fan.

The first four pages, A-6 to A-9 are input data to AVCO Lycoming Program R121 at various axial stations. All units in the SI system and headings on the columns are self-explanatory. The three parameters in the left hand column are:

TOT PRESS = Total Pressure Ratio

TOT TEMP = Total Temperature Ratio

VU = Absolute Tangential Velocity Component of the Air (m/sec)

The remaining pages are detailed output at the various axial stations, the non-obvious terms of which are defined below.

Coded Term	*Meaning*	*Units*
A STATIC	ambient sound speed	m/sec
A TOTAL	sound speed based on total temperature	
ALPHA BAR	$\sin^{-1}$ (Vm/V)= angle of flow made by V in tangential direction measured on a cone	degrees
ALPHA	$\sin^{-1}$ (Vx/V) = angle made by projection of absolute velocity vector (on a cylinder)	degrees
BETA	angle that the relative velocity vector makes with a cylinder	degrees
V	absolute velocity	m/s
VM	meridional component of V	m/s
VR	radial component of V	m/s
S-VALUE	radial length measured along a station cut (origin at hub)	m
% SPAN	percent radial distance compared to full span measured from hub	---
VX	axial component of absolute velocity	m/s
VU	tangential component of absolute velocity	m/s
W	relative velocity	m/s
WU	tangential component of relative velocity	m/s
MV	Mach number of absolute velocity V	---
MVX	Mach number of VX	---
MVM	Mach number of VM	---

Coded Term	*Meaning*	*Units*
R-ADC	streamline radius of curvature in meridional plane	m
RHO	fluid density	Kg/m^3
ROTOR EFF	polytropic rotor efficiency	
S-VALUE	radial length measured along a station cut (origin at hub)	m
STAT PRESS	static pressure	bars
STAT TEMP	static temperature	° Kelvin
TO/TO (TO/TO)T	Similar definitions for the stagnation temperatures.	
TOT PRESS	total pressure ratio	--------
TOT TEMP	total temperature	° Kelvin
U	rotational speed	m/s
V	absolute velocity	m/s
VM	meridional component of V	m/s
VR	radial component of V	m/s
VU	tangential component of absolute velocity	m/s
VX	axial component of absolute velocity	m/s
W	relative velocity	m/s
WU	tangential component of relative velocity	m/s
X-VALUE	axial location of station re:origin (station 4)	m

Coded Term	*Meaning*	*Units*
% AREA	% of annulus area taken up by a stream tube from the preceding area to that where % AREA is indicated	%

FLOW CONDITIONS IN MULTI-STAGE AXIAL COMPRESSORS AND TURBINES

AVCO-LYCOMING PROGRAM R121   N. BERNSTEIN

AVCO-BBN FAN

NO. OF STATIONS=23   NO. OF STREAMLINES=15   GAS CONST R= 287.100   EXIT OF INLET GUIDE VANE = STATION 12

DISTANCES ARE IN METERS, VELOCITIES ARE M./SEC.

INPUT TO AXIAL STATION 1

HUB RADIUS	HUB STATION	TIP RADIUS	TIP STATION	MACH NUMBER	MASS FLOW RATE	RPM
0.0500	-0.2600	0.2540	-0.2600	0.4000	31.2000	18450.0

TOT PRESS	1.013	1.013	1.013	1.013	1.013	1.013	1.013	1.013	1.013	1.013	1.013	1.013	1.013	1.013	1.013
TOT TEMP	288.00	288.00	288.00	288.00	288.00	288.00	288.00	288.00	288.00	288.00	288.00	288.00	288.00	288.00	288.00
VU	0.0	0.0	0.0	0.0	0.0	0.0	0.0	0.0	0.0	0.0	0.0	0.0	0.0	0.0	0.0

INPUT TO AXIAL STATION 2

HUB RADIUS	HUB STATION	TIP RADIUS	TIP STATION	MACH NUMBER	MASS FLOW RATE	RPM
0.0500	-0.2300	0.2540	-0.2300	0.4000	31.2000	18450.0

TOT PRESS	1.013	1.013	1.013	1.013	1.013	1.013	1.013	1.013	1.013	1.013	1.013	1.013	1.013	1.013	1.013
TOT TEMP	288.00	288.00	288.00	288.00	288.00	288.00	288.00	288.00	288.00	288.00	288.00	288.00	288.00	288.00	288.00
VU	0.0	0.0	0.0	0.0	0.0	0.0	0.0	0.0	0.0	0.0	0.0	0.0	0.0	0.0	0.0

INPUT TO AXIAL STATION 3

HUB RADIUS	HUB STATION	TIP RADIUS	TIP STATION	MACH NUMBER	MASS FLOW RATE	RPM
0.0500	-0.2000	0.2540	-0.2000	0.4000	31.2000	18450.0

TOT PRESS	1.013	1.013	1.013	1.013	1.013	1.013	1.013	1.013	1.013	1.013	1.013	1.013	1.013	1.013	1.013
TOT TEMP	288.00	288.00	288.00	288.00	288.00	288.00	288.00	288.00	288.00	288.00	288.00	288.00	288.00	288.00	288.00
VU	0.0	0.0	0.0	0.0	0.0	0.0	0.0	0.0	0.0	0.0	0.0	0.0	0.0	0.0	0.0

INPUT TO AXIAL STATION 4

HUB RADIUS	HUB STATION	TIP RADIUS	TIP STATION	MACH NUMBER	MASS FLOW RATE	RPM
0.0502	-0.1700	0.2540	-0.1700	0.4000	31.2000	18450.0

TOT PRESS	1.013	1.013	1.013	1.013	1.013	1.013	1.013	1.013	1.013	1.013	1.013	1.013	1.013	1.013	1.013
TOT TEMP	288.00	288.00	288.00	288.00	288.00	288.00	288.00	288.00	288.00	288.00	288.00	288.00	288.00	288.00	288.00
VU	0.0	0.0	0.0	0.0	0.0	0.0	0.0	0.0	0.0	0.0	0.0	0.0	0.0	0.0	0.0

INPUT TO AXIAL STATION 5

HUB RADIUS	HUB STATION	TIP RADIUS	TIP STATION	MACH NUMBER	MASS FLOW RATE	RPM
0.0540	-0.1400	0.2540	-0.1400	0.4000	31.7000	18450.0

TOT PRESS	1.013	1.013	1.013	1.013	1.013	1.013	1.013	1.013	1.013	1.013	1.013	1.013	1.013	1.013	1.013
TOT TEMP	288.00	288.00	288.00	288.00	288.00	288.00	288.00	288.00	288.00	288.00	288.00	288.00	288.00	288.00	288.00

VU	0.0	0.0	0.0	0.0	0.0	0.0	0.0	0.0	0.0	0.0	0.0	0.0	0.0	0.0	0.0

INPUT TO AXIAL STATION 6

HUB RADIUS	HUB STATION	TIP RADIUS	TIP STATION	MACH NUMBER	MASS FLOW RATE	RPM
0.0610	-0.1100	0.2540	-0.1100	0.4000	31.2000	18450.0

TOT PRESS	1.013	1.013	1.013	1.013	1.013	1.013	1.013	1.013	1.013	1.013	1.013	1.013	1.013	1.013	1.013
TOT TEMP	288.00	288.00	288.00	288.00	288.00	288.00	288.00	288.00	288.00	288.00	288.00	288.00	288.00	288.00	288.00
VU	0.0	0.0	0.0	0.0	0.0	0.0	0.0	0.0	0.0	0.0	0.0	0.0	0.0	0.0	0.0

INPUT TO AXIAL STATION 7

HUB RADIUS	HUB STATION	TIP RADIUS	TIP STATION	MACH NUMBER	MASS FLOW RATE	RPM
0.0707	-0.0800	0.2540	-0.0800	0.4000	31.2000	18450.0

TOT PRESS	1.013	1.013	1.013	1.013	1.013	1.013	1.013	1.013	1.013	1.013	1.013	1.013	1.013	1.013	1.013
TOT TEMP	288.00	288.00	288.00	288.00	288.00	288.00	288.00	288.00	288.00	288.00	288.00	288.00	288.00	288.00	288.00
VU	0.0	0.0	0.0	0.0	0.0	0.0	0.0	0.0	0.0	0.0	0.0	0.0	0.0	0.0	0.0

INPUT TO AXIAL STATION 8

HUB RADIUS	HUB STATION	TIP RADIUS	TIP STATION	MACH NUMBER	MASS FLOW RATE	RPM
0.0780	-0.0600	0.2540	-0.0600	0.5000	31.2000	18450.0

TOT PRESS	1.013	1.013	1.013	1.013	1.013	1.013	1.013	1.013	1.013	1.013	1.013	1.013	1.013	1.013	1.013
TOT TEMP	288.00	288.00	288.00	288.00	288.00	288.00	288.00	288.00	288.00	288.00	288.00	288.00	288.00	288.00	288.00
VU	0.0	0.0	0.0	0.0	0.0	0.0	0.0	0.0	0.0	0.0	0.0	0.0	0.0	0.0	0.0

INPUT TO AXIAL STATION 9

HUB RADIUS	HUB STATION	TIP RADIUS	TIP STATION	MACH NUMBER	MASS FLOW RATE	RPM
0.0860	-0.0400	0.2540	-0.0400	0.5000	31.2000	18450.0

TOT PRESS	1.013	1.013	1.013	1.013	1.013	1.013	1.013	1.013	1.013	1.013	1.013	1.013	1.013	1.013	1.013
TOT TEMP	288.00	288.00	288.00	288.00	288.00	288.00	288.00	288.00	288.00	288.00	288.00	288.00	288.00	288.00	288.00
VU	0.0	0.0	0.0	0.0	0.0	0.0	0.0	0.0	0.0	0.0	0.0	0.0	0.0	0.0	0.0

INPUT TO AXIAL STATION 10

HUB RADIUS	HUB STATION	TIP RADIUS	TIP STATION	MACH NUMBER	MASS FLOW RATE	RPM
0.0940	-0.0200	0.2540	-0.0200	0.5000	31.2000	18450.0

TOT PRESS	1.013	1.013	1.013	1.013	1.013	1.013	1.013	1.013	1.013	1.013	1.013	1.013	1.013	1.013	1.013
TOT TEMP	288.00	288.00	288.00	288.00	288.00	288.00	288.00	288.00	288.00	288.00	288.00	288.00	288.00	288.00	288.00
VU	0.0	0.0	0.0	0.0	0.0	0.0	0.0	0.0	0.0	0.0	0.0	0.0	0.0	0.0	0.0

INPUT TO AXIAL STATION 11

HUB RADIUS	HUB STATION	TIP RADIUS	TIP STATION	MACH NUMBER	MASS FLOW RATE	RPM
0.1020	0.0	0.2540	0.0	0.5000	31.2000	18450.0

TOT PRESS	1.013	1.013	1.013	1.013	1.013	1.013	1.013	1.013	1.013	1.013	1.013	1.013	1.013	1.013	1.013
TOT TEMP	288.00	288.00	288.00	288.00	288.00	288.00	288.00	288.00	288.00	288.00	288.00	288.00	288.00	288.00	288.00
VU	0.0	0.0	0.0	0.0	0.0	0.0	0.0	0.0	0.0	0.0	0.0	0.0	0.0	0.0	0.0

INPUT TO AXIAL STATION 12

HUB RADIUS	HUB STATION	TIP RADIUS	TIP STATION	MACH NUMBER	MASS FLOW RATE	RPM
0.1100	0.0200	0.2490	0.0430	0.5000	31.7000	18450.0

TOT PRESS	1.013	1.013	1.013	1.013	1.013	1.013	1.013	1.013	1.013	1.013	1.013	1.013	1.013	1.013	1.013
TOT TEMP	288.00	288.00	288.00	288.00	288.00	288.00	288.00	288.00	288.00	288.00	288.00	288.00	288.00	288.00	288.00
VU	0.0	0.0	0.0	0.0	0.0	0.0	0.0	0.0	0.0	0.0	0.0	0.0	0.0	0.0	0.0

INPUT TO AXIAL STATION 13

HUB RADIUS	HUB STATION	TIP RADIUS	TIP STATION	MACH NUMBER	MASS FLOW RATE	RPM
0.1340	0.0700	0.2430	0.0715	0.8000	32.2000	18450.0

TOT PRESS	1.661	1.661	1.661	1.661	1.661	1.661	1.661	1.661	1.661	1.661	1.661	1.661	1.661	1.661	1.661
TOT TEMP	338.10	336.30	335.20	334.70	334.70	334.60	334.60	334.60	334.80	335.70	338.70	340.70	342.80	345.10	347.60

INPUT TO AXIAL STATION 14

HUB RADIUS	HUB STATION	TIP RADIUS	TIP STATION	MACH NUMBER	MASS FLOW RATE	RPM
0.1420	0.0950	0.2400	0.0900	0.8000	32.2000	18450.0

TOT PRESS	1.661	1.661	1.661	1.661	1.661	1.661	1.661	1.661	1.661	1.661	1.661	1.661	1.661	1.661	1.661
TOT TEMP	338.10	336.30	335.20	334.70	334.70	334.60	334.60	334.60	334.80	335.70	338.70	340.70	342.80	345.10	347.60
VU	0.0	0.0	0.0	0.0	0.0	0.0	0.0	0.0	0.0	0.0	0.0	0.0	0.0	0.0	0.0

INPUT TO AXIAL STATION 15

HUB RADIUS	HUB STATION	TIP RADIUS	TIP STATION	MACH NUMBER	MASS FLOW RATE	RPM
0.1450	0.1150	0.2395	0.1150	0.8000	32.2000	18450.0

TOT PRESS	1.661	1.661	1.661	1.661	1.661	1.661	1.661	1.661	1.661	1.661	1.661	1.661	1.661	1.661	1.661
TOT TEMP	338.10	336.30	335.20	334.70	334.70	334.60	334.60	334.60	334.80	335.70	338.70	340.70	342.80	345.10	347.60
VU	0.0	0.0	0.0	0.0	0.0	0.0	0.0	0.0	0.0	0.0	0.0	0.0	0.0	0.0	0.0

INPUT TO AXIAL STATION 16

HUB RADIUS	HUB STATION	TIP RADIUS	TIP STATION	MACH NUMBER	MASS FLOW RATE	RPM
0.1470	0.1350	0.2420	0.1350	0.5000	32.7000	18450.0

TOT PRESS	1.661	1.661	1.661	1.661	1.661	1.661	1.661	1.661	1.661	1.661	1.661	1.661	1.661	1.661	1.661
TOT TEMP	335.70	335.50	335.30	335.10	335.00	334.90	334.80	335.00	335.70	337.00	338.70	339.60	340.50	341.40	342.40
VU	0.0	0.0	0.0	0.0	0.0	0.0	0.0	0.0	0.0	0.0	0.0	0.0	0.0	0.0	0.0

INPUT TO AXIAL STATION 17

HUB RADIUS	HUB STATION	TIP RADIUS	TIP STATION	MACH NUMBER	MASS FLOW RATE	RPM
0.1490	0.1550	0.2440	0.1550	0.5000	32.7000	18450.0

TOT PRESS	1.634	1.638	1.645	1.649	1.654	1.661	1.661	1.661	1.661	1.661	1.661	1.661	1.661	1.661	1.661
TOT TEMP	335.70	335.50	335.30	335.10	335.00	334.90	334.80	335.00	335.70	337.00	338.70	339.60	340.50	341.40	342.40
VU	60.00	76.30	91.90	107.20	117.70	132.60	126.00	120.30	115.80	113.30	116.10	118.50	121.10	124.00	127.50

INPUT TO AXIAL STATION 18

HUB RADIUS	HUB STATION	TIP RADIUS	TIP STATION	MACH NUMBER	MASS FLOW RATE	RPM
0.1500	0.1750	0.2460	0.1750	0.5000	32.7000	18450.0

TOT PRESS	1.620	1.620	1.620	1.621	1.627	1.636	1.646	1.654	1.661	1.661	1.661	1.661	1.661	1.661	1.661
TOT TEMP	335.70	335.50	335.30	335.10	335.00	334.90	334.80	335.00	335.70	337.00	338.70	339.60	340.50	341.40	342.40
VU	0.0	0.0	0.0	8.00	23.60	54.90	79.50	99.60	114.80	112.50	115.20	117.50	120.20	123.00	126.10

INPUT TO AXIAL STATION 19

HUB RADIUS	HUB STATION	TIP RADIUS	TIP STATION	MACH NUMBER	MASS FLOW RATE	RPM
0.1500	0.1950	0.2480	0.1950	0.5000	32.7000	18450.0

TOT PRESS	1.620	1.620	1.620	1.620	1.620	1.620	1.620	1.627	1.635	1.643	1.652	1.656	1.658	1.661	1.661
TOT TEMP	335.70	335.50	335.30	335.10	335.00	334.90	334.80	335.00	335.70	337.00	338.70	339.60	340.50	341.40	342.40
VU	0.0	0.0	0.0	0.0	0.0	0.0	0.0	21.50	47.50	67.40	87.80	101.30	115.30	122.10	125.20

INPUT TO AXIAL STATION 20

HUB RADIUS	HUB STATION	TIP RADIUS	TIP STATION	MACH NUMBER	MASS FLOW RATE	RPM
0.1500	0.2150	0.2480	0.2150	0.5000	32.7000	18450.0

TOT PRESS	1.620	1.620	1.620	1.620	1.620	1.620	1.620	1.620	1.620	1.620	1.625	1.629	1.634	1.638	1.641
TOT TEMP	335.70	335.50	335.30	335.10	335.00	334.90	334.80	335.00	335.70	337.00	338.70	339.60	340.50	341.40	342.40
VU	0.0	0.0	0.0	0.0	0.0	0.0	0.0	0.0	0.0	0.0	15.00	27.30	39.80	53.00	62.60

INPUT TO AXIAL STATION 21

HUB RADIUS	HUB STATION	TIP RADIUS	TIP STATION	MACH NUMBER	MASS FLOW RATE	RPM
0.1500	0.2400	0.2480	0.2400	0.5000	32.7000	18450.0

TOT PRESS	1.620	1.620	1.620	1.620	1.620	1.620	1.620	1.620	1.620	1.620	1.620	1.620	1.620	1.620	1.620
TOT TEMP	335.70	335.50	335.30	335.10	335.00	334.90	334.80	335.00	335.70	337.00	338.70	339.60	340.50	341.40	342.40
VU	0.0	0.0	0.0	0.0	0.0	0.0	0.0	0.0	0.0	0.0	0.0	0.0	0.0	0.0	0.0

INPUT TO AXIAL STATION 22

HUB RADIUS	HUB STATION	TIP RADIUS	TIP STATION	MACH NUMBER	MASS FLOW RATE	RPM
0.1500	0.2600	0.2480	0.2600	0.5000	32.7000	18450.0

TOT PRESS	1.620	1.620	1.620	1.620	1.620	1.620	1.620	1.620	1.620	1.620	1.620	1.620	1.620	1.620	1.620
TOT TEMP	335.70	335.50	335.30	335.10	335.00	334.90	334.80	335.00	335.70	337.00	338.70	339.60	340.50	341.40	342.40
VU	0.0	0.0	0.0	0.0	0.0	0.0	0.0	0.0	0.0	0.0	0.0	0.0	0.0	0.0	0.0

INPUT TO AXIAL STATION 23

HUB RADIUS	HUB STATION	TIP RADIUS	TIP STATION	MACH NUMBER	MASS FLOW RATE	RPM
0.1500	0.2900	0.2480	0.2900	0.5000	32.7000	18450.0

TOT PRESS	1.620	1.620	1.620	1.620	1.620	1.620	1.620	1.620	1.620	1.620	1.620	1.620	1.620	1.620	1.620
TOT TEMP	335.70	335.50	335.30	335.10	335.00	334.90	334.80	335.00	335.70	337.00	338.70	339.60	340.50	341.40	342.40
VU	0.0	0.0	0.0	0.0	0.0	0.0	0.0	0.0	0.0	0.0	0.0	0.0	0.0	0.0	0.0

STREAMLINE DEFINITION	0.0	0.050	0.100	0.150	0.200	0.300	0.400	0.500	0.600	0.700	0.800	0.850	0.900	0.950	1.000

STATION NUMBER 1 DOWNSTREAM OF REMOTE

RADIUS	A STATIC	ALPHA BAR	ALPHA	A TOTAL	BETA	BETA BAR	V	VM	VR
0.05000	334.17236	89.99997	89.99997	340.23535	124.04436	124.04436	142.98244	142.98244	0.0
0.07483	334.17334	89.99997	89.99997	340.23535	135.32292	135.32161	142.97168	142.97168	1.3662596
0.09328	334.17456	89.99997	89.99997	340.23535	141.58029	141.57729	142.95544	142.95544	2.1015692
0.10863	334.17578	89.99997	89.99997	340.23535	145.74748	145.74355	142.94293	142.94293	2.4519930
0.12207	334.17651	89.99997	89.99997	340.23535	148.78746	148.78342	142.93391	142.93391	2.5577154
0.14527	334.17725	89.99997	89.99997	340.23535	153.01785	153.01431	142.92493	142.92493	2.5070333
0.16525	334.17725	89.99997	89.99997	340.23535	155.88664	155.88402	142.92305	142.92305	2.2364960
0.18305	334.17700	89.99997	89.99997	340.23535	157.99701	157.99532	142.92668	142.92668	1.8734684
0.19927	334.17676	89.99997	89.99997	340.23535	159.63429	159.63330	142.93030	142.93030	1.4788704
0.21427	334.17651	89.99997	89.99997	340.23535	160.95290	160.95241	142.93205	142.93205	1.0799446
0.22828	334.17627	89.99997	89.99997	340.23535	162.04410	162.04387	142.93567	142.93567	0.6991677
0.23498	334.17627	89.99997	89.99997	340.23535	162.52396	162.52385	142.93567	142.93567	0.5128775
0.24148	334.17603	89.99997	89.99997	340.23535	162.96704	162.96698	142.93744	142.93744	0.3348243
0.24782	334.17603	89.99997	89.99997	340.23535	163.37822	163.37922	142.93744	142.93744	0.1641465
0.25400	334.17603	89.99997	89.99997	340.23535	163.76099	163.76099	142.93744	142.93744	0.0

S-VALUE	% SPAN	VX	VU	W	WU	MV	MVX	MW	MVM
0.0	0.0	142.98244	0.0	172.55811	-96.60394	0.42787	0.42787	0.51637	0.4278703
0.02483	12.17362	142.96515	0.0	203.33710	-144.58589	0.42784	0.42782	0.60848	0.4278368
0.04328	21.21402	142.93909	0.0	230.03235	-180.21828	0.42779	0.42774	0.68836	0.4277867
0.05863	28.74194	142.92189	0.0	253.94121	-209.88914	0.42775	0.42768	0.75990	0.4277477
0.07207	35.33066	142.91103	0.0	275.78909	-235.85805	0.42772	0.42765	0.82528	0.4277198
0.09527	46.70258	142.90294	0.0	314.97363	-280.67944	0.42769	0.42763	0.94253	0.4276919
0.11525	56.49356	142.90555	0.0	349.80005	-319.26978	0.42769	0.42763	1.04675	0.4276863
0.13305	65.27221	142.91440	0.0	381.46118	-353.67310	0.42770	0.42766	1.14149	0.4276975
0.14927	73.17368	142.92264	0.0	410.68774	-385.01343	0.42771	0.42769	1.22895	0.4277086
0.16427	80.52478	142.92798	0.0	437.96729	-413.98755	0.42771	0.42770	1.31059	0.4277142
0.17828	87.39366	142.93396	0.0	463.64331	-441.06079	0.42773	0.42772	1.38742	0.4277253
0.18498	90.67471	142.93474	0.0	475.96240	-453.99292	0.42773	0.42772	1.42428	0.4277253
0.19148	93.86475	142.93704	0.0	487.97021	-466.56616	0.42773	0.42773	1.46022	0.4277310
0.19782	96.97093	142.93733	0.0	499.68921	-478.80908	0.42773	0.42773	1.49529	0.4277310
0.20400	100.00000	142.93744	0.0	511.14038	-490.74780	0.42773	0.42773	1.52955	0.4277310

X-VALUE	U	STAT PRESS	STAT TEMP	TOT PRESS	TOT TEMP	% AREA	EPS	RADC	RHO
-0.26000	96.60394	0.89364	277.82690	1.01350	288.00000	0.0	0.0	1000000.56250	1.1203518
-0.26000	144.58589	0.89366	277.82837	1.01350	288.00000	4.99896	0.54754	1000000.56250	1.1203671
-0.26000	180.21828	0.89368	277.83081	1.01350	288.00000	4.99932	0.84233	1000000.56250	1.1203909
-0.26000	209.88914	0.89370	277.83252	1.01350	288.00000	4.99980	0.98288	1000000.56250	1.1204090
-0.26000	235.85805	0.89372	277.83374	1.01350	288.00000	5.00023	1.02533	1000000.56250	1.1204214
-0.26000	280.67944	0.89373	277.83496	1.01350	288.00000	10.00085	1.00507	1000000.56250	1.1204348
-0.26000	319.26978	0.89373	277.83521	1.01350	288.00000	10.00097	0.89662	1000000.56250	1.1204367
-0.26000	353.67310	0.89372	277.83472	1.01350	288.00000	10.00064	0.75105	1000000.56250	1.1204319
-0.26000	385.01343	0.89372	277.83423	1.01350	288.00000	10.00022	0.59284	1000000.56250	1.1204271
-0.26000	413.98755	0.89372	277.83398	1.01350	288.00000	10.00003	0.43291	1000000.56250	1.1204243
-0.26000	441.06079	0.89371	277.83350	1.01350	288.00000	9.99950	0.28026	1000000.56250	1.1204195
-0.26000	453.99292	0.89371	277.83350	1.01350	288.00000	4.99995	0.20559	1000000.56250	1.1204195
-0.26000	466.56616	0.89371	277.83325	1.01350	288.00000	4.99973	0.13421	1000000.56250	1.1204166
-0.26000	478.80908	0.89371	277.83325	1.01350	288.00000	4.99959	0.06580	1000000.56250	1.1204166
-0.26000	490.74780	0.89371	277.83325	1.01350	288.00000	5.00001	0.0	1000000.56250	1.1204166

STATION NUMBER 2 DOWNSTREAM OF REMOTE

RADIUS	A STATIC	ALPHA BAR	ALPHA	A TOTAL	BETA	BETA BAR	V	VM	VP
0.05000	334.38550	89.99997	89.99997	340.23535	124.51761	124.51750	140.46753	140.46753	0.3881592
0.07512	334.40210	89.99997	89.99997	340.23535	135.97998	135.97763	140.26939	140.26939	1.8117838
0.09372	334.34750	89.99997	89.99997	340.23535	142.11404	142.10895	140.91397	140.91397	2.6890888
0.10915	334.29907	89.99997	89.99997	340.23535	146.14653	146.14052	141.49156	141.49156	3.0161028
0.12262	334.25952	89.99997	89.99997	340.23535	149.07373	149.06783	141.95976	141.95976	3.0737810
0.14580	334.20020	89.99997	89.99997	340.23535	153.14616	153.14134	142.65691	142.65691	2.9110422
0.16572	334.15991	89.99997	89.99997	340.23535	155.91740	155.91402	143.12785	143.12785	2.5415678
0.18345	334.13232	89.99997	89.99997	340.23535	157.96762	157.96548	143.44855	143.44855	2.1021681
0.19959	334.11328	89.99997	89.99997	340.23535	159.56703	159.56577	143.67026	143.67026	1.6461249
0.21450	334.10059	89.99997	89.99997	340.23535	160.86224	160.86159	143.81847	143.81847	1.1987543
0.22843	334.09277	89.99997	89.99997	340.23535	161.94060	161.94032	143.90942	143.90942	0.7740275
0.23508	334.09009	89.99997	89.99997	340.23535	162.41653	162.41637	143.93785	143.93785	0.5690317
0.24155	334.08862	89.99997	89.99997	340.23535	162.85727	162.85721	143.95757	143.95757	0.3716807
0.24786	334.08765	89.99997	89.99997	340.23535	163.26741	163.26741	143.96638	143.96638	0.1824148
0.25400	334.08740	89.99997	89.99997	340.23535	163.64995	163.64995	143.96999	143.96000	0.0000369

S-VALUE	% SPAN	VX	VU	W	WU	MV	MVX	MW	MVM
0.0	0.0	140.46698	0.0	170.49004	-96.60394	0.42008	0.42007	0.50983	0.4200766
0.02512	12.31602	140.25769	0.0	201.84416	-145.13982	0.41946	0.41943	0.60360	0.4194632
0.04372	21.43272	140.88831	0.0	229.44119	-181.07048	0.42146	0.42138	0.68623	0.4214591
0.05915	28.99681	141.45941	0.0	253.95222	-210.88356	0.42325	0.42315	0.75966	0.4232484
0.07262	35.59651	141.92648	0.0	276.17383	-236.89542	0.42470	0.42460	0.82623	0.4246992
0.09580	46.96286	142.62720	0.0	315.75879	-281.69629	0.42686	0.42677	0.94482	0.4268606
0.11572	56.72551	143.10529	0.0	350.71191	-320.17700	0.42832	0.42825	1.04953	0.4283214
0.13345	65.41643	143.43314	0.0	382.36133	-354.43311	0.42932	0.42927	1.14434	0.4293166
0.14959	73.32693	143.66083	0.0	411.50781	-385.61328	0.43000	0.42998	1.23164	0.4300046
0.16450	80.63669	143.81348	0.0	438.67090	-414.42529	0.43046	0.43045	1.31299	0.4304646
0.17843	87.46606	143.90733	0.0	464.21387	-441.34424	0.43075	0.43074	1.38048	0.4307469
0.18508	90.72784	143.93672	0.0	476.46240	-454.20093	0.43084	0.43083	1.42615	0.4308354
0.19155	93.89940	143.95709	0.0	488.39990	-466.70190	0.43090	0.43089	1.46189	0.4308963
0.19786	96.98793	143.96626	0.0	500.04834	-478.87573	0.43092	0.43092	1.49676	0.4309240
0.20400	100.00000	143.96999	0.0	511.42993	-490.74780	0.43094	0.43094	1.53083	0.4309351

X-VALUE	U	STAT PRESS	STAT TEMP	TOT PRESS	TOT TEMP	% AREA	EPS	RADC	RHO
-0.23000	96.60394	0.89764	278.18164	1.01350	288.00000	0.0	0.15833	-2.72655	1.1239309
-0.23000	145.13982	0.89795	278.20923	1.01350	288.00000	5.06920	0.74008	4.21312	1.1242113
-0.23000	181.07048	0.89693	278.11914	1.01350	288.00000	5.06360	1.09245	3.56926	1.1232996
-0.23000	210.88356	0.89602	278.03784	1.01350	288.00000	5.04795	1.22144	3.78605	1.1224804
-0.23000	236.89542	0.89527	277.97192	1.01350	288.00000	5.03163	1.24069	4.23600	1.1218147
-0.23000	281.69629	0.89416	277.87305	1.01350	288.00000	10.03608	1.16925	5.41892	1.1208191
-0.23000	320.17700	0.89341	277.80615	1.01350	288.00000	10.00429	1.01747	7.08657	1.1201429
-0.23000	354.43311	0.89289	277.76050	1.01350	288.00000	9.98225	0.83967	9.35258	1.1196823
-0.23000	385.61328	0.89254	277.72876	1.01350	288.00000	9.96714	0.65649	12.74821	1.1193628
-0.23000	414.42529	0.89230	277.70752	1.01350	288.00000	9.95679	0.47758	18.34706	1.1191502
-0.23000	441.34424	0.89215	277.69458	1.01350	288.00000	9.95044	0.30817	30.09950	1.1190186
-0.23000	454.20093	0.89210	277.69043	1.01350	288.00000	4.97331	0.22651	41.56696	1.1189775
-0.23000	466.70190	0.89207	277.68774	1.01350	288.00000	4.97266	0.14793	65.94783	1.1189489
-0.23000	478.87573	0.89206	277.68628	1.01350	288.00000	4.97225	0.07260	143.17305	1.1189365
-0.23000	490.74780	0.89205	277.68579	1.01350	288.00000	4.97228	0.00001	-4515.19922	1.1189308

GAMMA	ETAP	DP/(PT-P)	DP/(PTR-P)	P0/P0	(P0/P0)T	T0/T0	(T0/T0)T
1.40002	0.0	0.03336	0.02244	1.00000	1.00000	1.00000	1.00000
1.40002	0.0	0.03584	0.01692	1.00000	1.00000	1.00000	1.00000
1.40002	0.0	0.02713	0.00976	1.00000	1.00000	1.00000	1.00000
1.40002	0.0	0.01932	0.00556	1.00000	1.00000	1.00000	1.00000
1.40002	0.0	0.01299	0.00309	1.00000	1.00000	1.00000	1.00000
1.40002	0.0	0.00358	0.00062	1.00000	1.00000	1.00000	1.00000
1.40002	0.0	-0.00274	-0.00037	1.00000	1.00000	1.00000	1.00000
1.40002	0.0	-0.00658	-0.00075	1.00000	1.00000	1.00000	1.00000
1.40002	0.0	-0.00991	-0.00087	1.00000	1.00000	1.00000	1.00000
1.40002	0.0	-0.01188	-0.00088	1.00000	1.00000	1.00000	1.00000
1.40002	0.0	-0.01305	-0.00082	1.00000	1.00000	1.00000	1.00000
1.40002	0.0	-0.01343	-0.00079	1.00000	1.00000	1.00000	1.00000
1.40002	0.0	-0.01367	-0.00074	1.00000	1.00000	1.00000	1.00000
1.40002	0.0	-0.01380	-0.00070	1.00000	1.00000	1.00000	1.00000
1.40002	0.0	-0.01384	-0.00065	1.00000	1.00000	1.00000	1.00000

STATION NUMBER 3 DOWNSTREAM OF REMOTE

RADIUS	A STATIC	ALPHA BAR	ALPHA	A TOTAL	BETA	BETA BAR	V	VM	VR
0.05000	334.85551	89.99997	89.99997	340.23535	125.73836	125.73705	134.25523	134.25523	-1.2074396
0.07573	334.73022	89.99997	89.99997	340.23535	137.03702	137.02516	136.30038	136.30038	3.9253893
0.09451	334.54077	89.99997	89.99997	340.23535	142.81116	142.79575	138.60764	138.60764	4.6306391
0.10998	334.41650	89.99997	89.99997	340.23535	146.61655	146.60147	140.09854	140.09854	4.7423630
0.12344	334.32642	89.99997	89.99997	340.23535	149.38835	149.37512	141.16943	141.16943	4.5804310
0.14654	334.19849	89.99997	89.99997	340.23535	153.26402	153.25456	142.67670	142.67670	4.0854712
0.16535	334.11719	89.99997	89.99997	340.23535	155.92703	155.92085	143.62378	143.62378	3.4520950
0.18396	334.06348	89.99997	89.99997	340.23535	157.91385	157.91008	144.24768	144.24768	2.7907017
0.19998	334.02734	89.99997	89.99997	340.23535	159.47523	159.47316	144.66667	144.66667	2.1628656
0.21479	334.00342	89.99997	89.99997	340.23535	160.74800	160.74701	144.94102	144.94102	1.5583096
0.22861	333.98828	89.99997	89.99997	340.23535	161.81313	161.81274	145.11414	145.11414	0.9960791
0.23522	333.98364	89.99997	89.99997	340.23535	162.28511	162.28490	145.16891	145.16891	0.7299188
0.24164	333.98022	89.99997	89.99997	340.23535	162.72296	162.72290	145.20956	145.20956	0.4746554
0.24790	333.97803	89.99997	89.99997	340.23535	163.13135	163.13135	145.23242	145.23242	0.2311084
0.25400	333.97754	89.99997	89.99997	340.23535	163.51357	163.51357	145.23953	145.23953	-0.0001302

S-VALUE	% SPAN	VX	VU	W	WU	MV	MVX	MW	MVM
0.0	0.0	134.24896	0.0	165.39886	-96.60394	0.40089	0.40087	0.49388	0.4008869
0.02573	12.61054	136.24384	0.0	199.94959	-146.29303	0.40719	0.40703	0.59734	0.4071947
0.04451	21.81805	138.53026	0.0	229.23320	-182.58092	0.41432	0.41409	0.68522	0.4143221
0.05999	29.40440	140.01825	0.0	254.51216	-212.48257	0.41893	0.41869	0.76106	0.4189343
0.07344	35.99756	141.09511	0.0	277.12085	-238.46851	0.42225	0.42203	0.82880	0.4222503
0.09654	47.32591	142.61819	0.0	317.04004	-283.12158	0.42692	0.42675	0.94866	0.4269220
0.11635	57.03412	143.58220	0.0	352.02075	-321.38892	0.42986	0.42974	1.05358	0.4298605
0.13396	65.66745	144.22050	0.0	383.57544	-355.41919	0.43180	0.43172	1.14821	0.4317972
0.14998	73.52129	144.65050	0.0	412.57178	-386.37695	0.43310	0.43305	1.23514	0.4330983
0.16479	80.77722	144.93265	0.0	439.56152	-414.97778	0.43395	0.43393	1.31604	0.4339507
0.17861	87.55623	145.11072	0.0	464.92554	-441.69873	0.43449	0.43448	1.39204	0.4344887
0.18522	90.79408	145.16707	0.0	477.08398	-454.46143	0.43466	0.43465	1.42846	0.4346587
0.19164	93.94261	145.20879	0.0	488.93262	-466.97183	0.43478	0.43478	1.46396	0.4347849
0.19790	97.00999	145.23224	0.0	500.49365	-479.95874	0.43486	0.43486	1.49858	0.4348562
0.20400	100.00000	145.23953	0.0	511.78882	-490.74780	0.43488	0.43488	1.53240	0.4348781

X-VALUE	U	STAT PRESS	STAT TEMP	TOT PRESS	TOT TEMP	% AREA	EPS	RADC	RHO
-0.20000	96.60394	0.90727	279.03076	1.01350	288.00000	0.0	-0.55371	1.99738	1.1325283
-0.20000	146.29303	0.90414	278.75537	1.01350	288.00000	5.21535	1.65032	1.02570	1.1297369
-0.20000	182.58092	0.90056	278.43994	1.01350	288.00000	5.15604	1.01451	1.33324	1.1265421
-0.20000	212.48257	0.89822	278.23315	1.01350	288.00000	5.10317	1.93984	1.62096	1.1244516
-0.20000	238.46851	0.89653	278.08325	1.01350	288.00000	5.06242	1.85936	1.95734	1.1229382
-0.20000	283.12158	0.89413	277.87036	1.01350	288.00000	10.06063	1.64096	2.69400	1.1207905
-0.20000	321.38892	0.89261	277.73535	1.01350	288.00000	9.99224	1.37729	3.64576	1.1194305
-0.20000	355.41919	0.89160	277.64600	1.01350	288.00000	9.94852	1.11212	4.94030	1.1185303
-0.20000	386.37695	0.89093	277.58569	1.01350	288.00000	9.91923	0.85664	6.82044	1.1179237
-0.20000	414.97778	0.89048	277.54614	1.01350	288.00000	9.89979	0.61602	9.84743	1.1175251
-0.20000	441.69873	0.89020	277.52124	1.01350	288.00000	9.88755	0.39329	15.53547	1.1172733
-0.20000	454.46143	0.89011	277.51343	1.01350	288.00000	4.94022	0.28809	20.93886	1.1171942
-0.20000	466.97183	0.89005	277.50757	1.01350	288.00000	4.93887	0.18729	31.27348	1.1171350
-0.20000	478.95874	0.89001	277.50415	1.01350	288.00000	4.93807	0.09117	61.15161	1.1171017
-0.20000	490.74780	0.89000	277.50317	1.01350	288.00000	4.93779	-0.00005	1257.41553	1.1170912

GAMMA	ETAP	DP/(PT-P)	DP/(PTP-P)	PO/PO	(PO/PO)T	TO/TO	(TO/TO)T
1.40002	0.0	0.08310	0.05526	1.00000	1.00000	1.00000	1.00000
1.40002	0.0	0.05353	0.02468	1.00000	1.00000	1.00000	1.00000
1.40002	0.0	0.03111	0.01092	1.00000	1.00000	1.00000	1.00000
1.40002	0.0	0.01875	0.00528	1.00000	1.00000	1.00000	1.00000
1.40002	0.0	0.01062	0.00248	1.00000	1.00000	1.00000	1.00000
1.40002	0.0	-0.00026	-0.00005	1.00000	1.00000	1.00000	1.00000
1.40002	0.0	-0.00663	-0.00088	1.00000	1.00000	1.00000	1.00000
1.40002	0.0	-0.01067	-0.00115	1.00000	1.00000	1.00000	1.00000
1.40002	0.0	-0.01329	-0.00118	1.00000	1.00000	1.00000	1.00000
1.40002	0.0	-0.01496	-0.00112	1.00000	1.00000	1.00000	1.00000
1.40002	0.0	-0.01604	-0.00102	1.00000	1.00000	1.00000	1.00000
1.40002	0.0	-0.01639	-0.00097	1.00000	1.00000	1.00000	1.00000
1.40002	0.0	-0.01667	-0.00092	1.00000	1.00000	1.00000	1.00000
1.40002	0.0	-0.01685	-0.00086	1.00000	1.00000	1.00000	1.00000
1.40002	0.0	-0.01690	-0.00081	1.00000	1.00000	1.00000	1.00000

STATION NUMBER 4 DOWNSTREAM OF REMOTE

RADIUS	A STATIC	ALPHA BAR	ALPHA	A TOTAL	BETA	BETA BAR	V	VM	VR
0.05020	336.35059	89.99997	89.99997	340.23535	130.27835	130.23404	114.63429	114.63429	6.4143686
0.07712	334.99341	89.99997	89.99997	340.23535	138.30585	138.23579	133.02946	133.02946	9.3231382
0.09590	334.68506	89.99997	89.99997	340.23535	143.60007	143.54477	136.85490	136.85490	8.6900969
0.11131	334.49365	89.99997	89.99997	340.23535	147.13084	147.08730	139.17584	139.17584	8.0252380
0.12466	334.35815	89.99997	89.99997	340.23535	149.72281	149.68900	140.79149	140.79149	7.3285437
0.14759	334.16333	89.99997	89.99997	340.23535	153.37177	153.35095	143.08653	143.08653	6.0899181
0.16721	334.04102	89.99997	89.99997	340.23535	155.91179	155.89932	144.50702	144.50702	4.9418087
0.18465	333.95923	89.99997	89.99997	340.23535	157.82533	157.81812	145.44930	145.44930	3.9046679
0.20051	333.90381	89.99997	89.99997	340.23535	159.34222	159.33835	146.08347	146.08347	2.9679165
0.21516	333.86694	89.99997	89.99997	340.23535	160.58777	160.58588	146.50516	146.50516	2.1200199
0.22885	333.84424	89.99997	89.99997	340.23535	161.63838	161.63762	146.76338	146.76338	1.3524141
0.23539	333.83716	89.99997	89.99997	340.23535	162.10628	162.10590	146.84354	146.84354	0.9928796
0.24176	333.83252	89.99997	89.99997	340.23535	162.54221	162.54204	146.89577	146.89577	0.6489538
0.24795	333.83008	89.99997	89.99997	340.23535	162.94983	162.94983	146.92363	146.92363	0.3193411
0.25400	333.82959	89.99997	89.99997	340.23535	163.33237	163.33237	146.92885	146.92885	0.0004891

S-VALUE	% SPAN	VX	VU	W	WU	MV	MVX	MW	MVM
0.0	0.0	114.45468	0.0	150.16042	-96.99036	0.34082	0.34028	0.44644	0.3408179
0.02692	13.20845	132.70236	0.0	199.72398	-148.97260	0.39711	0.39613	0.59620	0.3971106
0.04570	22.42175	136.57972	0.0	230.32018	-185.25151	0.40891	0.40808	0.68817	0.4089065
0.06111	29.98386	138.94426	0.0	256.13916	-215.02878	0.41608	0.41539	0.76575	0.4160792
0.07446	36.53671	140.60063	0.0	278.96436	-240.82965	0.42108	0.42051	0.83433	0.4210798
0.09739	47.78571	142.95688	0.0	319.01636	-285.12769	0.42819	0.42781	0.95467	0.4281934
0.11701	57.41283	144.42249	0.0	353.88794	-323.03931	0.43260	0.43235	1.05941	0.4326026
0.13445	65.96944	145.39687	0.0	385.24731	-356.73535	0.43553	0.43537	1.15357	0.4355301
0.15031	73.75185	146.05331	0.0	414.01196	-387.38281	0.43750	0.43741	1.23991	0.4375016
0.16496	80.94185	146.48982	0.0	440.75806	-415.69702	0.43881	0.43877	1.32016	0.4388130
0.17865	87.66083	146.75714	0.0	465.87769	-442.15674	0.43962	0.43960	1.39549	0.4396163
0.18519	90.87053	146.84018	0.0	477.91504	-454.79639	0.43987	0.43986	1.43158	0.4398657
0.19156	93.99226	146.89433	0.0	489.64404	-467.08984	0.44003	0.44002	1.46673	0.4400283
0.19775	97.03323	146.92328	0.0	501.08862	-479.06494	0.44011	0.44011	1.50103	0.4401150
0.20380	100.00000	146.92895	0.0	512.27075	-490.74780	0.44013	0.44013	1.53453	0.4401312

X-VALUE	U	STAT PRESS	STAT TEMP	TOT PRESS	TOT TEMP	% AREA	EPS	RADC	RHO
-0.17000	96.99036	0.93522	281.46094	1.01350	288.00000	0.0	3.20766	0.27141	1.1573458
-0.17000	148.97260	0.90912	279.19385	1.01350	288.00000	5.52822	4.01877	0.63303	1.1341839
-0.17000	185.25151	0.90328	278.68018	1.01350	288.00000	5.24009	3.64065	0.86113	1.1289730
-0.17000	215.02878	0.89967	278.36133	1.01350	288.00000	5.15085	3.30566	1.08932	1.1257477
-0.17000	240.82965	0.89713	278.13623	1.01350	288.00000	5.08310	2.98374	1.31514	1.1234732
-0.17000	285.12769	0.89347	277.81201	1.01350	288.00000	10.06749	2.43931	1.83077	1.1202030
-0.17000	323.03931	0.89119	277.60889	1.01350	288.00000	9.96241	1.95977	2.46445	1.1181545
-0.17000	356.73535	0.88966	277.47290	1.01350	288.00000	9.89700	1.53832	3.30556	1.1167860
-0.17000	387.38281	0.88863	277.38086	1.01350	288.00000	9.85343	1.16413	4.52531	1.1158609
-0.17000	415.65702	0.88794	277.31934	1.01350	288.00000	9.82457	0.82913	6.54271	1.1152439
-0.17000	442.15674	0.88752	277.28174	1.01350	288.00000	9.80707	0.52709	10.75996	1.1148643
-0.17000	454.79639	0.88739	277.27002	1.01350	288.00000	4.89840	0.38741	15.21457	1.1147470
-0.17000	467.08984	0.88730	277.26245	1.01350	288.00000	4.89656	0.25312	24.67680	1.1146698
-0.17000	479.06494	0.88726	277.25830	1.01350	288.00000	4.89546	0.12414	56.91873	1.1146288
-0.17000	490.74780	0.88725	277.25757	1.01350	288.00000	4.89523	0.00019	-377.01587	1.1146221

GAMMA	ETAP	DP/(PT-P)	DP/(PTR-P)	PO/PO	(PO/PO)T	TO/TO	(TO/TO)T
1.40002	0.0	0.26315	0.16985	1.00000	1.00000	1.00000	1.00000
1.40002	0.0	0.04560	0.02021	1.00000	1.00000	1.00000	1.00000
1.40002	0.0	0.02410	0.00819	1.00000	1.00000	1.00000	1.00000
1.40002	0.0	0.01258	0.00345	1.00000	1.00000	1.00000	1.00000
1.40002	0.0	0.00512	0.00117	1.00000	1.00000	1.00000	1.00000
1.40002	0.0	-0.00550	-0.00094	1.00000	1.00000	1.00000	1.00000
1.40002	0.0	-0.01178	-0.00157	1.00000	1.00000	1.00000	1.00000
1.40002	0.0	-0.01596	-0.00172	1.00000	1.00000	1.00000	1.00000
1.40002	0.0	-0.01877	-0.00168	1.00000	1.00000	1.00000	1.00000
1.40002	0.0	-0.02069	-0.00156	1.00000	1.00000	1.00000	1.00000
1.40002	0.0	-0.02179	-0.00141	1.00000	1.00000	1.00000	1.00000
1.40002	0.0	-0.02211	-0.00133	1.00000	1.00000	1.00000	1.00000
1.40002	0.0	-0.02227	-0.00124	1.00000	1.00000	1.00000	1.00000
1.40002	0.0	-0.02232	-0.00116	1.00000	1.00000	1.00000	1.00000
1.40002	0.0	-0.02230	-0.00109	1.00000	1.00000	1.00000	1.00000

STATION NUMBER 5 DOWNSTREAM OF REMOTE

RADIUS	A STATIC	ALPHA BAR	ALPHA	A TOTAL	BETA	BETA BAR	V	VM	VP
0.05400	336.31006	89.99997	89.99997	340.23535	132.63942	132.15840	115.23050	115.23050	20.9831696
0.08006	334.90552	89.99997	89.99997	340.23535	139.27437	139.06346	134.13176	134.13176	16.3023682
0.09842	334.49609	89.99997	89.99997	340.23535	143.94479	143.80153	139.14619	139.14619	14.2224617
0.11353	334.24023	89.99997	89.99997	340.23535	147.14690	147.04417	142.18593	142.18593	12.5808897
0.12663	334.05737	89.99997	89.99997	340.23535	149.53735	149.46158	144.31880	144.31880	11.2101583
0.14015	333.79199	89.99997	89.99997	340.23535	152.05851	152.01524	147.35640	147.35640	8.9931059
0.16844	333.62851	89.99997	89.99997	340.23535	155.39569	155.37073	149.19269	149.19269	7.1574068
0.18561	333.52197	89.99997	89.99997	340.23535	157.26215	157.24805	150.38264	150.38264	5.5856047
0.20123	333.45093	89.99997	89.99997	340.23535	158.75975	158.75227	151.16821	151.16821	4.2074280
0.21567	333.40454	89.99997	89.99997	340.23535	160.00127	159.99771	151.67928	151.67928	2.9811096
0.22918	333.37524	89.99997	89.99997	340.23535	161.05470	161.05333	152.00102	152.00102	1.8789492
0.23563	333.36572	89.99997	89.99997	340.23535	161.52554	161.52483	152.10643	152.10643	1.3687286
0.24191	333.35889	89.99997	89.99997	340.23535	161.96524	161.96492	152.17003	152.17003	0.8851172
0.24803	333.35449	89.99997	89.99997	340.23535	162.37686	162.37680	152.22841	152.22841	0.4292357
0.25400	333.35254	89.99997	89.99997	340.23535	162.76410	162.76410	152.24841	152.24841	-0.0018906

S-VALUE	% SPAN	VX	VU	W	WU	MV	MVX	MW	MVM
0.0	0.0	113.30389	0.0	155.44545	-104.33228	0.34263	0.33690	0.46221	0.3426317
0.02606	13.02875	133.13737	0.0	204.71173	-154.64658	0.40051	0.39754	0.61125	0.4005963
0.04442	22.21132	138.41743	0.0	235.60785	-190.12996	0.41590	0.41381	0.70437	0.4159875
0.05953	29.76439	141.62825	0.0	261.37500	-219.31737	0.42540	0.42373	0.78200	0.4254004
0.07263	36.31535	143.88275	0.0	284.02734	-244.62950	0.43202	0.43071	0.85024	0.4320180
0.09515	47.57622	147.08171	0.0	323.64111	-288.14868	0.44146	0.44064	0.96959	0.4414617
0.11444	57.22182	149.02090	0.0	357.99487	-325.42578	0.44718	0.44667	1.07303	0.4471815
0.13161	65.80258	150.27887	0.0	388.84473	-358.58789	0.45089	0.45059	1.16587	0.4508927
0.14723	73.61345	151.10965	0.0	417.12988	-388.77441	0.45334	0.45317	1.25095	0.4533447
0.16167	80.83517	151.64598	0.0	443.43189	-416.68384	0.45494	0.45485	1.33001	0.4549406
0.17518	87.58836	151.98941	0.0	468.14600	-442.78247	0.45595	0.45591	1.40426	0.4559457
0.18163	90.81572	152.10027	0.0	479.99292	-455.25488	0.45627	0.45626	1.43984	0.4562749
0.18791	93.95547	152.17735	0.0	491.53931	-467.38867	0.45650	0.45650	1.47450	0.4565048
0.19403	97.01474	152.22780	0.0	502.80938	-479.21143	0.45666	0.45665	1.50833	0.4566562
0.20000	100.00000	152.24841	0.0	513.82178	-490.74780	0.45672	0.45672	1.54138	0.4567189

X-VALUE	U	STAT PRESS	STAT TEMP	TOT PRESS	TOT TEMP	% AREA	EPS	RADC	RHO
-0.14000	104.33228	0.93443	281.39258	1.01350	288.00000	0.0	10.40195	0.25519	1.1566448
-0.14000	154.64658	0.90745	279.04736	1.01350	288.00000	5.67079	6.08099	0.50501	1.1326962
-0.14000	190.12996	0.89972	278.36548	1.01350	288.00000	5.32113	5.86659	0.67333	1.1257987
-0.14000	219.31737	0.89491	277.93994	1.01350	288.00000	5.19768	5.07628	0.84893	1.1214914
-0.14000	244.62950	0.89140	277.63574	1.01350	288.00000	5.10804	4.45502	1.03034	1.1184273
-0.14000	288.14868	0.88655	277.19482	1.01350	288.00000	10.08299	3.40891	1.46321	1.1139927
-0.14000	325.42578	0.88352	276.92407	1.01350	288.00000	9.94611	2.74978	2.01421	1.1112710
-0.14000	358.58789	0.88154	276.74658	1.01350	288.00000	9.86368	2.12860	2.77115	1.1094933
-0.14000	388.77441	0.88022	276.62866	1.01350	288.00000	9.81004	1.59491	3.88089	1.1083126
-0.14000	416.68384	0.87937	276.55176	1.01350	288.00000	9.77507	1.12617	5.63848	1.1075411
-0.14000	442.78247	0.87883	276.50317	1.01350	288.00000	9.75368	0.70828	8.90169	1.1070547
-0.14000	455.25488	0.87865	276.48706	1.01350	288.00000	4.87046	0.51558	11.57684	1.1068954
-0.14000	467.38867	0.87852	276.47607	1.01350	288.00000	4.86809	0.33325	16.48030	1.1067839
-0.14000	479.21143	0.87844	276.46875	1.01350	288.00000	4.86643	0.16118	28.12714	1.1067104
-0.14000	490.74780	0.87841	276.46558	1.01350	288.00000	4.86570	-0.00071	115.44453	1.1066709

GAMMA	ETAP	DP/(PT-P)	DP/(PTR-P)	PO/PC	(PO/PO)T	TO/TO	(TO/TO)T
1.40002	0.0	-0.01013	-0.00578	1.00000	1.00000	1.00000	1.00000
1.40002	0.0	-0.01599	-0.00676	1.00000	1.00000	1.00000	1.00000
1.40002	0.0	-0.03234	-0.01059	1.00000	1.00000	1.00000	1.00000
1.40002	0.0	-0.04180	-0.01115	1.00000	1.00000	1.00000	1.00000
1.40002	0.0	-0.04844	-0.01087	1.00000	1.00000	1.00000	1.00000
1.40002	0.0	-0.05771	-0.00973	1.00000	1.00000	1.00000	1.00000
1.40002	0.0	-0.06271	-0.00834	1.00000	1.00000	1.00000	1.00000
1.40002	0.0	-0.06559	-0.00711	1.00000	1.00000	1.00000	1.00000
1.40002	0.0	-0.06731	-0.00608	1.00000	1.00000	1.00000	1.00000
1.40002	0.0	-0.06828	-0.00522	1.00000	1.00000	1.00000	1.00000
1.40002	0.0	-0.06899	-0.00453	1.00000	1.00000	1.00000	1.00000
1.40002	0.0	-0.06929	-0.00423	1.00000	1.00000	1.00000	1.00000
1.40002	0.0	-0.06954	-0.00396	1.00000	1.00000	1.00000	1.00000
1.40002	0.0	-0.06981	-0.00371	1.00000	1.00000	1.00000	1.00000
1.40002	0.0	-0.07000	-0.00348	1.00000	1.00000	1.00000	1.00000

STATION NUMBER 6 DOWNSTREAM OF REMOTE

RADIUS	A STATIC	ALPHA BAR	ALPHA	A TOTAL	BETA	BETA BAR	V	VM	VP
0.06100	335.63354	89.99997	89.99997	340.23535	134.48979	133.38412	124.69940	124.69940	34.0003510
0.08462	335.03760	89.99997	89.99997	340.23535	141.47260	140.97743	132.47052	132.47052	24.7060547
0.10217	334.59912	89.99997	89.99997	340.23535	145.36488	145.05702	137.90211	137.90211	20.7650299
0.11672	334.32324	89.99997	89.99997	340.23535	148.15138	147.94281	141.20772	141.20772	17.9065247
0.12940	334.12305	89.99997	89.99997	340.23535	150.28011	150.13229	143.55585	143.55585	15.6571655
0.15130	333.83081	89.99997	89.99997	340.23535	153.39259	153.31348	146.91670	146.91670	12.1743479
0.17011	333.64868	89.99997	89.99997	340.23535	155.65945	155.61578	148.97009	148.97009	9.4775257
0.18689	333.52783	89.99997	89.99997	340.23535	157.42072	157.39694	150.31824	150.31824	7.2714520
0.20218	333.44604	89.99997	89.99997	340.23535	158.84920	158.83685	151.22211	151.22211	5.4129696
0.21634	333.39185	89.99997	89.99997	340.23535	160.04405	160.03825	151.81670	151.81670	3.8145885
0.22960	333.35913	89.99997	89.99997	340.23535	161.06737	161.06519	152.17830	152.17830	2.4167013
0.23594	333.34937	89.99997	89.99997	340.23535	161.52838	161.52724	152.28349	152.28349	1.7758026
0.24211	333.34351	89.99997	89.99997	340.23535	161.96077	161.96027	152.34691	152.34691	1.1654692
0.24813	333.34131	89.99997	89.99997	340.23535	162.36774	162.36763	152.37199	152.37199	0.5799960
0.25430	333.34229	89.99997	89.99997	340.23535	162.75203	162.75203	152.36200	152.36200	0.0070609

S-VALUE	% SPAN	VX	VU	W	WU	MV	MVX	MW	MVM
0.0	0.0	119.97464	0.0	171.58138	-117.85683	0.37153	0.35746	0.51122	0.3715343
0.02362	12.23686	130.14626	0.0	210.39543	-163.45581	0.39539	0.38845	0.62798	0.3953900
0.04117	21.33118	136.32977	0.0	240.76743	-197.36252	0.41214	0.40744	0.71957	0.4121413
0.05572	28.87123	140.06775	0.0	266.04565	-225.47882	0.42237	0.41896	0.79577	0.4223688
0.06840	35.44170	142.69945	0.0	288.26538	-249.97734	0.42965	0.42709	0.86275	0.4296496
0.09030	46.78534	146.41141	0.0	327.12915	-292.28247	0.44009	0.43858	0.97992	0.4400933
0.10911	56.53502	148.66830	0.0	360.83057	-328.64380	0.44649	0.44558	1.08147	0.4464878
0.12589	65.22737	150.14226	0.0	391.10303	-361.06226	0.45069	0.45016	1.17262	0.4506917
0.14118	73.15240	151.12520	0.0	418.86914	-390.61914	0.45351	0.45322	1.25618	0.4535130
0.15534	80.48900	151.76877	0.0	444.69940	-417.98145	0.45537	0.45523	1.33386	0.4553701
0.16860	87.35725	152.15910	0.0	468.97363	-443.59692	0.45650	0.45644	1.40681	0.4564995
0.17494	90.64209	152.27313	0.0	480.61157	-455.84790	0.45683	0.45680	1.44176	0.4568285
0.18111	93.83946	152.34245	0.0	491.95581	-467.77246	0.45703	0.45701	1.47582	0.4570267
0.18713	96.95660	152.37198	0.0	503.03003	-479.39771	0.45711	0.45710	1.50905	0.4571050
0.19300	100.00000	152.36200	0.0	513.85547	-490.74780	0.45707	0.45707	1.54152	0.4570737

X-VALUE	U	STAT PRESS	STAT TEMP	TOT PRESS	TOT TEMP	% AREA	EPS	RADC	RHO
-0.11000	117.85683	0.92136	290.26221	1.01350	288.00000	0.0	15.82253	0.43054	1.1450634
-0.11000	163.45581	0.90996	279.26758	1.01350	288.00000	5.65681	10.74874	0.46694	1.1349335
-0.11000	197.36252	0.90166	278.53687	1.01350	288.00000	5.39269	8.66043	0.62258	1.1275244
-0.11000	225.47882	0.89647	278.07788	1.01350	288.00000	5.23952	7.28529	0.77819	1.1228838
-0.11000	249.97734	0.89272	277.74512	1.01350	288.00000	5.13393	6.26152	0.94437	1.1195278
-0.11000	292.28247	0.88727	277.25928	1.01350	288.00000	10.10839	4.75331	1.33233	1.1146393
-0.11000	328.64380	0.88388	276.95703	1.01350	288.00000	9.94803	3.64764	1.81611	1.1116037
-0.11000	361.06226	0.88164	276.75635	1.01350	288.00000	9.85136	2.77269	2.45782	1.1095905
-0.11000	390.61914	0.88012	276.62061	1.01350	288.00000	9.78864	2.05133	3.37651	1.1082315
-0.11000	417.98145	0.87914	276.53101	1.01350	288.00000	9.74784	1.43978	4.91844	1.1073332
-0.11000	443.59692	0.87853	276.47632	1.01350	288.00000	9.72333	0.90994	8.39036	1.1067858
-0.11000	455.84790	0.87835	276.46021	1.01350	288.00000	4.85466	0.66815	12.70243	1.1066265
-0.11000	467.77246	0.87824	276.45068	1.01350	288.00000	4.85239	0.43832	25.00371	1.1065302
-0.11000	479.39771	0.87820	276.44678	1.01350	288.00000	4.85122	0.21776	277.56763	1.1064920
-0.11000	490.74780	0.87822	276.44849	1.01350	288.00000	4.85118	0.00266	-36.10771	1.1065073

GAMMA	ETAP	DP/(PT-P)	DP/(PTP-P)	P0/P0	(P0/P0)T	T0/T0	(T0/T0)T
1.40002	0.0	-0.16534	-0.08872	1.00000	1.00000	1.00000	1.00000
1.40002	0.0	0.02367	0.00964	1.00000	1.00000	1.00000	1.00000
1.40002	0.0	0.01706	0.00550	1.00000	1.00000	1.00000	1.00000
1.40002	0.0	0.01312	0.00349	1.00000	1.00000	1.00000	1.00000
1.40002	0.0	0.01007	0.00228	1.00000	1.00000	1.00000	1.00000
1.40002	0.0	0.00568	0.00098	1.00000	1.00000	1.00000	1.00000
1.40002	0.0	0.00284	0.00039	1.00000	1.00000	1.00000	1.00000
1.40002	0.0	0.00081	0.00009	1.00000	1.00000	1.00000	1.00000
1.40002	0.0	-0.00067	-0.00006	1.00000	1.00000	1.00000	1.00000
1.40002	0.0	-0.00172	-0.00014	1.00000	1.00000	1.00000	1.00000
1.40002	0.0	-0.00222	-0.00015	1.00000	1.00000	1.00000	1.00000
1.40002	0.0	-0.00221	-0.00014	1.00000	1.00000	1.00000	1.00000
1.40002	0.0	-0.00209	-0.00013	1.00000	1.00000	1.00000	1.00000
1.40002	0.0	-0.00179	-0.00010	1.00000	1.00000	1.00000	1.00000
1.40002	0.0	-0.00142	-0.00008	1.00000	1.00000	1.00000	1.00000

STATION NUMBER 7 DOWNSTREAM OF SHOCK

RADIUS	A STATIC	ALPHA BAR	ALPHA	A TOTAL	BETA	BETA BAR	V	VM	VP
0.07070	335.03711	89.99997	89.99997	340.23535	137.53284	135.87709	132.47841	132.47841	43.8096619
0.09140	334.58862	89.99997	89.99997	340.23535	142.83290	141.98268	138.02740	138.02740	33.6834106
0.10754	334.21054	89.99997	89.99997	340.23535	146.06674	145.54672	142.53075	142.53075	27.8922882
0.12113	333.93970	89.99997	89.99997	340.23535	148.45753	148.10968	145.67274	145.67274	23.8422394
0.13322	333.73535	89.99997	89.99997	340.23535	150.34097	150.09705	147.99673	147.99673	20.6958771
0.15415	333.43457	89.99997	89.99997	340.23535	153.18758	153.05930	151.34656	151.34656	15.8985357
0.17229	333.24805	89.99997	89.99997	340.23535	155.32657	155.25674	153.38936	153.38936	12.2691612
0.18852	333.13013	89.99997	89.99997	340.23535	157.02921	156.99155	154.66483	154.66483	9.3464365
0.20338	333.05688	89.99997	89.99997	340.23535	158.43507	158.41568	155.45129	155.45129	6.0097004
0.21718	333.01294	89.99997	89.99997	340.23535	159.62424	159.61528	155.92160	155.92160	4.8208046
0.23013	332.98657	89.99997	89.99997	340.23535	160.64619	160.64291	156.20059	156.20059	2.9910393
0.23633	332.97729	89.99997	89.99997	340.23535	161.10486	161.10316	156.29945	156.29945	2.1565123
0.24236	332.96973	89.99997	89.99997	340.23535	161.53325	161.53259	156.38213	156.38213	1.3730574
0.24825	332.96265	89.99997	89.99997	340.23535	161.93378	161.93365	156.45821	156.45821	0.6420782
0.25400	332.95532	89.99997	89.99997	340.23535	162.30882	162.30892	156.53415	156.53415	-0.0261401

S-VALUE	% SPAN	VX	VU	W	WU	MV	MVX	MW	MVM
0.0	0.0	125.02495	0.0	190.28802	-136.59798	0.39541	0.37317	0.56796	0.3954141
0.02070	11.29087	133.85427	0.0	224.10713	-176.55721	0.41253	0.40006	0.66980	0.4125286
0.03684	20.05973	139.77493	0.0	251.93977	-207.74658	0.42647	0.41822	0.75383	0.4264694
0.05049	27.54742	143.70837	0.0	275.74146	-234.12131	0.43622	0.43034	0.82572	0.4362247
0.06252	34.10541	146.54253	0.0	296.86499	-257.34399	0.44346	0.43910	0.88952	0.4434553
0.08345	45.52654	150.50919	0.0	334.04932	-297.79736	0.45390	0.45139	1.00184	0.4539018
0.10158	55.41707	152.85789	0.0	366.47583	-332.83081	0.46029	0.45881	1.09971	0.4602858
0.11782	64.27817	154.38216	0.0	395.69727	-364.21851	0.46428	0.46343	1.18782	0.4642775
0.13268	72.38658	155.29765	0.0	422.57178	-392.93994	0.46674	0.46628	1.26977	0.4667410
0.14648	79.91417	155.84706	0.0	447.63672	-419.60352	0.46821	0.46799	1.34420	0.4682148
0.15943	86.97639	156.17195	0.0	471.25806	-444.61865	0.46909	0.46900	1.41525	0.4690897
0.16562	90.35805	156.28458	0.0	482.60718	-456.59644	0.46940	0.46936	1.44937	0.4693997
0.17166	93.65149	156.37610	0.0	493.68457	-468.26196	0.46966	0.46964	1.48267	0.4696587
0.17755	96.86349	156.45688	0.0	504.51196	-479.63867	0.46990	0.46989	1.51522	0.4698972
0.18330	100.00000	156.53415	0.0	515.10815	-490.74780	0.47014	0.47014	1.54708	0.4701356

X-VALUE	U	STAT PRESS	STAT TEMP	TOT PRESS	TOT TEMP	% AREA	EPS	RADC	RHO
-0.08000	136.59798	0.90995	279.26660	1.01350	288.00000	0.0	19.31084	0.60553	1.1349230
-0.08000	176.55721	0.90146	278.51978	1.01350	288.00000	5.63661	14.12477	0.58771	1.1273499
-0.08000	207.74658	0.89436	277.89111	1.01350	288.00000	5.39707	11.28522	0.69530	1.1209993
-0.08000	234.12131	0.88930	277.44043	1.01350	288.00000	5.24658	9.41908	0.83277	1.1164608
-0.08000	257.34399	0.88549	277.10083	1.01350	288.00000	5.13832	8.03860	0.98988	1.1130476
-0.08000	297.79736	0.87992	276.60181	1.01350	288.00000	10.10791	6.02989	1.39652	1.1080437
-0.08000	332.83081	0.87648	276.29199	1.01350	288.00000	9.94322	4.58782	1.99092	1.1049442
-0.08000	364.21851	0.87431	276.09668	1.01350	288.00000	9.84631	3.46451	2.93745	1.1029902
-0.08000	392.93994	0.87297	275.97534	1.01350	288.00000	9.78669	2.54760	4.55957	1.1017790
-0.08000	419.60352	0.87216	275.90234	1.01350	288.00000	9.75010	1.77176	7.36434	1.1010523
-0.08000	444.61865	0.87168	275.85913	1.01350	288.00000	9.72900	1.09721	11.31530	1.1006193
-0.08000	456.59644	0.87151	275.84375	1.01350	288.00000	4.85799	0.79055	12.72209	1.1004658
-0.08000	468.26196	0.87137	275.83081	1.01350	288.00000	4.85536	0.50307	13.20389	1.1003380
-0.08000	479.63867	0.87124	275.81885	1.01350	288.00000	4.85324	0.23513	12.64084	1.1002197
-0.08000	490.74780	0.87111	275.80713	1.01350	288.00000	4.85146	-0.00957	11.53938	1.1001015

GAMMA	ETAP	DP/(PT-P)	DP/(PTP-P)	PO/PO	(PO/PO)T	TO/TO	(TO/TO)T
1.40002	0.0	-0.12375	-0.06340	1.00000	1.00000	1.00000	1.00000
1.40002	0.0	-0.08211	-0.03070	1.00000	1.00000	1.00000	1.00000
1.40002	0.0	-0.06524	-0.01965	1.00000	1.00000	1.00000	1.00000
1.40002	0.0	-0.06128	-0.01544	1.00000	1.00000	1.00000	1.00000
1.40002	0.0	-0.05983	-0.01294	1.00000	1.00000	1.00000	1.00000
1.40002	0.0	-0.05816	-0.00974	1.00000	1.00000	1.00000	1.00000
1.40002	0.0	-0.05713	-0.00771	1.00000	1.00000	1.00000	1.00000
1.40002	0.0	-0.05561	-0.00620	1.00000	1.00000	1.00000	1.00000
1.40002	0.0	-0.05373	-0.00505	1.00000	1.00000	1.00000	1.00000
1.40002	0.0	-0.05191	-0.00417	1.00000	1.00000	1.00000	1.00000
1.40002	0.0	-0.05072	-0.00352	1.00000	1.00000	1.00000	1.00000
1.40002	0.0	-0.05060	-0.00328	1.00000	1.00000	1.00000	1.00000
1.40002	0.0	-0.05081	-0.00307	1.00000	1.00000	1.00000	1.00000
1.40002	0.0	-0.05146	-0.00292	1.00000	1.00000	1.00000	1.00000
1.40002	0.0	-0.05255	-0.00279	1.00000	1.00000	1.00000	1.00000

STATION NUMBER 8 DOWNSTREAM OF REMOTE

RADIUS	A STATIC	ALPHA BAR	ALPHA	A TOTAL	BETA	BETA BAR	V	VM	VR
0.07900	334.51025	89.99997	89.99997	340.23535	139.28667	137.31848	138.97368	138.97368	49.9544525
0.09672	334.13428	89.99997	89.99997	340.23535	143.56335	142.48828	143.42525	143.42525	30.3134155
0.11179	333.81226	89.99997	89.99997	340.23535	146.40668	145.73305	147.12537	147.12537	32.7358093
0.12473	333.56421	89.99997	89.99997	340.23535	148.56413	148.11094	149.91234	149.91234	27.9642944
0.13622	333.36841	89.99997	89.99997	340.23535	150.29425	149.97635	152.07629	152.07629	24.2216187
0.15540	333.07617	89.99997	89.99997	340.23535	152.97021	152.80515	155.24237	155.24237	18.4350128
0.17298	332.89233	89.99997	89.99997	340.23535	155.02211	154.93425	157.20354	157.20354	14.0323687
0.18580	332.77930	89.99997	89.99997	340.23535	156.68350	156.63763	158.39351	158.39351	10.5048742
0.20432	332.71289	89.99997	89.99997	340.23535	158.07231	158.04953	159.09013	159.09013	7.6220007
0.21783	332.67554	89.99997	89.99997	340.23535	159.25601	159.24573	159.48146	159.48146	5.2459688
0.23053	332.65625	89.99997	89.99997	340.23535	160.27998	160.27617	159.68053	159.68053	3.2669477
0.23661	332.65234	89.99997	89.99997	340.23535	160.74313	160.74110	159.72327	159.72327	2.3984127
0.24255	332.65210	89.99997	89.99997	340.23535	161.17928	161.17841	159.72644	159.72644	1.5883360
0.24834	332.65649	89.99997	89.99997	340.23535	161.59286	161.59259	159.67899	159.67899	0.8234487
0.25400	332.66797	89.99997	89.99997	340.23535	161.98869	161.98868	159.56055	159.56055	0.0845216

S-VALUE	% SPAN	VX	VU	W	WU	MV	MVX	MW	MVM
0.0	0.0	129.68512	0.0	204.99951	-150.70209	0.41545	0.38769	0.61283	0.4154541
0.01372	10.63398	137.93207	0.0	235.53900	-186.83635	0.42924	0.41280	0.70492	0.4292443
0.03379	19.19685	143.43723	0.0	261.30103	-215.94522	0.44074	0.42969	0.78278	0.4407429
0.04673	26.54990	147.28104	0.0	283.77588	-240.94608	0.44043	0.44154	0.85074	0.4494257
0.05822	33.08148	150.13498	0.0	303.93555	-263.15332	0.45618	0.45036	0.91171	0.4561809
0.07840	44.54413	154.14391	0.0	339.68555	-302.13599	0.46609	0.46279	1.01984	0.4660867
0.09598	54.53537	156.57600	0.0	371.06274	-336.11694	0.47224	0.47025	1.11466	0.4722253
0.11180	63.52336	158.04477	0.0	399.43433	-366.68701	0.47597	0.47492	1.20030	0.4759716
0.12632	71.77255	158.90744	0.0	425.59668	-394.74414	0.47816	0.47761	1.27917	0.4781604
0.13983	79.44824	159.39516	0.0	450.05469	-420.85034	0.47939	0.47913	1.35283	0.4793904
0.15253	86.66243	159.64711	0.0	473.14624	-445.38696	0.48002	0.47992	1.42233	0.4800166
0.15861	90.12106	159.70526	0.0	484.24927	-457.14966	0.48015	0.48010	1.45572	0.4801507
0.16455	93.49217	159.71854	0.0	495.08838	-468.61499	0.48016	0.48014	1.48831	0.4801606
0.17034	96.78290	159.67685	0.0	505.67944	-479.80664	0.48001	0.48001	1.52012	0.4800116
0.17600	100.00000	159.56052	0.0	516.03589	-490.74780	0.47964	0.47964	1.55120	0.4796390

X-VALUE	U	STAT PRESS	STAT TEMP	TOT PRESS	TOT TEMP	% AREA	EPS	RADC	RHO
-0.06000	150.70209	0.89999	278.38940	1.01350	288.00000	0.0	21.06659	0.88705	1.1260309
-0.06000	186.83635	0.89293	277.76367	1.01350	288.00000	5.59616	15.90862	0.80290	1.1197157
-0.06000	215.94522	0.88692	277.22876	1.01350	288.00000	5.37765	12.85608	0.85909	1.1143322
-0.06000	240.94608	0.88232	276.81689	1.01350	288.00000	5.23825	10.75080	0.97269	1.1101980
-0.06000	263.15332	0.87870	276.49170	1.01350	288.00000	5.13382	9.16469	1.11969	1.1069403
-0.06000	302.13599	0.87332	276.00757	1.01350	288.00000	10.10305	6.91996	1.54575	1.1021013
-0.06000	336.11694	0.86995	275.70264	1.01350	288.00000	9.94248	5.12118	2.26708	1.0990601
-0.06000	366.68701	0.86789	275.51563	1.01350	288.00000	9.84846	3.80773	3.55299	1.0971985
-0.06000	394.74414	0.86668	275.40576	1.01350	288.00000	9.79269	2.74609	5.96741	1.0961037
-0.06000	420.85034	0.86600	275.34375	1.01350	288.00000	9.75988	1.88502	10.60195	1.0954866
-0.06000	445.38696	0.86565	275.31201	1.01350	288.00000	9.74253	1.17231	24.74722	1.0951719
-0.06000	457.14966	0.86557	275.30518	1.01350	288.00000	4.86644	0.86039	93.23456	1.0951042
-0.06000	468.61499	0.86557	275.30469	1.01350	288.00000	4.86537	0.56976	-34.26683	1.0950994
-0.06000	479.80664	0.86565	275.31226	1.01350	288.00000	4.86555	0.29547	-11.37441	1.0951748
-0.06000	490.74780	0.86586	275.33105	1.01350	288.00000	4.86753	0.03035	-5.55191	1.0953617

GAMMA	ETAP	DP/(PT-P)	DP/(PTR-P)	PO/PO	(PO/PO)T	TO/TO	(TO/TO)T
1.40002	0.0	-0.09625	-0.04478	1.00000	1.00000	1.00000	1.00000
1.40002	0.0	-0.07617	-0.02698	1.00000	1.00000	1.00000	1.00000
1.40002	0.0	-0.06242	-0.01817	1.00000	1.00000	1.00000	1.00000
1.40002	0.0	-0.05616	-0.01390	1.00000	1.00000	1.00000	1.00000
1.40002	0.0	-0.05308	-0.01141	1.00000	1.00000	1.00000	1.00000
1.40002	0.0	-0.04941	-0.00836	1.00000	1.00000	1.00000	1.00000
1.40002	0.0	-0.04764	-0.00657	1.00000	1.00000	1.00000	1.00000
1.40002	0.0	-0.04613	-0.00530	1.00000	1.00000	1.00000	1.00000
1.40002	0.0	-0.04475	-0.00435	1.00000	1.00000	1.00000	1.00000
1.40002	0.0	-0.04362	-0.00364	1.00000	1.00000	1.00000	1.00000
1.40002	0.0	-0.04255	-0.00307	1.00000	1.00000	1.00000	1.00000
1.40002	0.0	-0.04182	-0.00282	1.00000	1.00000	1.00000	1.00000
1.40002	0.0	-0.04083	-0.00258	1.00000	1.00000	1.00000	1.00000
1.40002	0.0	-0.03928	-0.00233	1.00000	1.00000	1.00000	1.00000
1.40002	0.0	-0.03687	-0.00206	1.00000	1.00000	1.00000	1.00000

STATION NUMBER 9 DOWNSTREAM OF REMOTE

RADIUS	A STATIC	ALPHA BAR	ALPHA	A TOTAL	BETA	BETA BAR	V	VM	VR
0.08600	333.79736	89.99997	89.99997	340.23535	140.57603	138.44377	147.29565	147.29565	55.1027679
0.10272	333.52148	89.99997	89.99997	340.23535	144.07872	142.84366	150.38770	150.38770	44.1514740
0.11662	333.25488	89.99997	89.99997	340.23535	146.56349	145.76408	153.31310	153.31310	37.0983276
0.12876	333.03320	89.99997	89.99997	340.23535	148.50229	147.95380	155.70538	155.70538	31.8606720
0.13965	332.84692	89.99997	89.99997	340.23535	150.08218	149.69353	157.68207	157.68207	27.6626282
0.15892	332.56567	89.99997	89.99997	340.23535	152.58504	152.38287	160.62175	160.62175	20.9904785
0.17586	332.39355	89.99997	89.99997	340.23535	154.55809	154.45247	162.39343	162.39343	15.7819462
0.19117	332.30615	89.99997	89.99997	340.23535	156.20280	156.14941	163.28696	163.28696	11.5792379
0.20529	332.27905	89.99997	89.99997	340.23535	157.61496	157.58972	163.56198	163.56198	8.1780500
0.21849	332.28931	89.99997	89.99997	340.23535	158.84308	158.83237	163.45753	163.45753	5.4433870
0.23093	332.31323	89.99997	89.99997	340.23535	159.91066	159.90701	163.21463	163.21463	3.2325373
0.23691	332.32300	89.99997	89.99997	340.23535	160.38785	160.38611	163.11456	163.11456	2.2774868
0.24274	332.32593	89.99997	89.99997	340.23535	160.82663	160.82597	163.08371	163.08371	1.3891811
0.24844	332.31860	89.99997	89.99997	340.23535	161.22638	161.22627	163.15921	163.15921	0.5379806
0.25400	332.29590	89.99997	89.99997	340.23535	161.58516	161.58510	163.39151	163.39151	-0.3189327

S-VALUE	% SPAN	VX	VU	W	WU	MV	MVX	MW	MVM
0.0	0.0	136.60048	0.0	222.04671	-166.15875	0.44127	0.40923	0.66521	0.4412726
0.01572	9.95312	143.76057	0.0	248.98972	-198.44249	0.45091	0.43104	0.74655	0.4509085
0.03062	18.22713	148.75691	0.0	272.50732	-225.28951	0.46005	0.44638	0.81771	0.4600475
0.04276	25.45128	152.41093	0.0	293.44995	-248.73430	0.46754	0.45764	0.88114	0.4675371
0.05365	31.93336	155.23663	0.0	312.47412	-269.77100	0.47374	0.46639	0.93879	0.4737375
0.07292	43.40736	159.24429	0.0	346.49536	-307.01758	0.48298	0.47884	1.04189	0.4829775
0.08986	53.48643	161.62474	0.0	376.55640	-339.73975	0.48856	0.48625	1.13286	0.4885577
0.10517	62.60310	162.87587	0.0	403.82373	-369.33862	0.49138	0.49014	1.21522	0.4913750
0.11929	71.00874	163.35741	0.0	429.03052	-396.62915	0.49224	0.49163	1.29117	0.4922428
0.13249	78.86238	163.36687	0.0	452.66919	-422.12695	0.49191	0.49164	1.36227	0.4919133
0.14493	86.26567	163.18262	0.0	475.09033	-446.17480	0.49115	0.49105	1.42965	0.4911469
0.15091	89.82838	163.09866	0.0	485.92285	-457.72778	0.49093	0.49078	1.46220	0.4908314
0.15674	93.29974	163.07779	0.0	496.54248	-468.99707	0.49073	0.49072	1.49414	0.4907342
0.16244	96.68503	163.15833	0.0	506.97168	-479.99951	0.49097	0.49097	1.52556	0.4909722
0.16800	100.00000	163.39120	0.0	517.23315	-490.74780	0.49170	0.49170	1.55654	0.4917048

X-VALUE	U	STAT PRESS	STAT TEMP	TOT PRESS	TOT TEMP	% AREA	EPS	RADC	RHO
-0.04000	166.15875	0.89665	277.20386	1.01350	288.00000	0.0	21.96848	2.82458	1.1140823
-0.04000	198.44249	0.88153	276.74595	1.01350	288.00000	5.52461	17.07266	1.33144	1.1094856
-0.04000	225.28951	0.87661	276.30371	1.01350	288.00000	5.33778	14.00329	1.17731	1.1050606
-0.04000	248.73430	0.87253	275.93579	1.01350	288.00000	5.21371	11.80735	1.20472	1.1013861
-0.04000	269.77100	0.86912	275.62769	1.01350	288.00000	5.11714	10.10386	1.32190	1.0983133
-0.04000	307.01758	0.86400	275.16211	1.01350	288.00000	10.07594	7.50905	1.84659	1.0936804
-0.04000	339.73975	0.86087	274.87720	1.01350	288.00000	9.92438	5.57700	3.19720	1.0908537
-0.04000	369.33862	0.85929	274.73242	1.01350	288.00000	9.84146	4.06645	9.41457	1.0894175
-0.04000	396.62915	0.85880	274.68774	1.01350	288.00000	9.80167	2.86597	-17.52237	1.0889740
-0.04000	422.12695	0.85898	274.70459	1.01350	288.00000	9.78893	1.90839	-6.42792	1.0891428
-0.04000	446.17480	0.85941	274.74414	1.01350	288.00000	9.79119	1.13484	-6.60065	1.0895338
-0.04000	457.72778	0.85959	274.76050	1.01350	288.00000	4.89685	0.80002	-10.33841	1.0896050
-0.04000	468.99707	0.85965	274.76538	1.01350	288.00000	4.89723	0.48806	585.16309	1.0897446
-0.04000	479.99951	0.85951	274.75317	1.01350	288.00000	4.89631	0.18892	6.59732	1.0896235
-0.04000	490.74780	0.85910	274.71533	1.01350	288.00000	4.89266	-0.11184	2.73173	1.0892487

GAMMA	ETAP	DP/(PT-P)	DP/(PTR-P)	PO/PO	(PO/PO)T	TO/TO	(TO/TO)T
1.40002	0.0	-0.11753	-0.05138	1.00000	1.00000	1.00000	1.00000
1.40002	0.0	-0.09455	-0.03247	1.00000	1.00000	1.00000	1.00000
1.40002	0.0	-0.08149	-0.02332	1.00000	1.00000	1.00000	1.00000
1.40002	0.0	-0.07462	-0.01834	1.00000	1.00000	1.00000	1.00000
1.40002	0.0	-0.07102	-0.01528	1.00000	1.00000	1.00000	1.00000
1.40002	0.0	-0.06654	-0.01139	1.00000	1.00000	1.00000	1.00000
1.40002	0.0	-0.06326	-0.00889	1.00000	1.00000	1.00000	1.00000
1.40002	0.0	-0.05910	-0.00695	1.00000	1.00000	1.00000	1.00000
1.40002	0.0	-0.05369	-0.00537	1.00000	1.00000	1.00000	1.00000
1.40002	0.0	-0.04754	-0.00409	1.00000	1.00000	1.00000	1.00000
1.40002	0.0	-0.04215	-0.00315	1.00000	1.00000	1.00000	1.00000
1.40002	0.0	-0.04043	-0.00283	1.00000	1.00000	1.00000	1.00000
1.40002	0.0	-0.04002	-0.00262	1.00000	1.00000	1.00000	1.00000
1.40002	0.0	-0.04151	-0.00255	1.00000	1.00000	1.00000	1.00000
1.40002	0.0	-0.04577	-0.00264	1.00000	1.00000	1.00000	1.00000

STATION NUMBER 10 DOWNSTREAM OF REMOTE

RADIUS	A STATIC	ALPHA BAR	ALPHA	A TOTAL	BETA	BETA BAR	V	VM	VR
0.09400	332.96069	89.99997	89.99997	340.23535	141.35446	139.25219	156.47755	156.47755	58.2834167
0.10894	332.83228	89.99997	89.99997	340.23535	144.46144	143.13026	157.83749	157.83749	48.1080627
0.12173	332.61279	89.99997	89.99997	340.23535	146.65601	145.74753	160.13309	160.13309	41.2342834
0.13308	332.39282	89.99997	89.99997	340.23535	148.35989	147.71819	162.40120	162.40120	35.8218689
0.14334	332.19580	89.99997	89.99997	340.23535	149.76199	149.30157	164.40349	164.40349	31.2392273
0.16166	331.89917	89.99997	89.99997	340.23535	152.04825	151.81122	167.37210	167.37210	23.5096283
0.17787	331.73438	89.99997	89.99997	340.23535	153.92841	153.81093	168.99915	168.99915	17.1662140
0.19261	331.68018	89.99997	89.99997	340.23535	155.55983	155.50645	169.53094	169.53094	11.9074116
0.20628	331.70858	89.99997	89.99997	340.23535	157.01062	156.98959	169.24834	169.24834	7.6425743
0.21911	331.79257	89.99997	89.99997	340.23535	158.31114	158.30453	168.42232	168.42232	4.3621664
0.23127	331.90405	89.99997	89.99997	340.23535	159.47212	159.47058	167.32591	167.32591	2.1281090
0.23714	331.96118	89.99997	89.99997	340.23535	160.00116	160.00044	166.75713	166.75713	1.4326353
0.24288	332.01465	89.99997	89.99997	340.23535	160.49495	160.49461	166.22366	166.22366	1.0307426
0.24850	332.06006	89.99997	89.99997	340.23535	160.95196	160.95154	165.77133	165.77133	0.9426079
0.25400	332.09253	89.99997	89.99997	340.23535	161.36987	161.36943	165.44620	165.44620	1.2039051

S-VALUE	% SPAN	VX	VU	W	WU	MV	MVX	MW	MVM
0.0	0.0	145.21900	0.0	239.72772	-191.61542	0.46996	0.43614	0.71999	0.4699580
0.01494	9.33487	150.32727	0.0	263.06348	-210.45125	0.47423	0.45166	0.79038	0.4742253
0.02773	17.33305	154.72312	0.0	284.50879	-235.16512	0.48144	0.46520	0.85538	0.4814399
0.03908	24.42215	158.40131	0.0	304.07446	-257.07422	0.48858	0.47655	0.91480	0.4885821
0.04934	30.83847	161.40823	0.0	322.03223	-276.90479	0.49490	0.48588	0.96940	0.4948993
0.06766	42.28584	165.71275	0.0	354.31836	-312.29492	0.50429	0.49929	1.06755	0.5042859
0.08387	52.41611	168.12505	0.0	382.92773	-343.61743	0.50944	0.50681	1.15432	0.5094411
0.09861	61.63150	169.11226	0.0	408.91162	-372.11304	0.51113	0.50987	1.23285	0.5111277
0.11228	70.17252	169.07570	0.0	432.97314	-398.52344	0.51023	0.50971	1.30528	0.5102314
0.12511	78.19325	168.26581	0.0	455.59839	-423.32471	0.50761	0.50744	1.37314	0.5076126
0.13727	85.79677	167.31238	0.0	477.13672	-446.83496	0.50414	0.50410	1.43757	0.5041394
0.14314	89.46390	166.75096	0.0	487.57642	-458.17334	0.50234	0.50232	1.46877	0.5023392
0.14888	93.05038	166.22046	0.0	497.83228	-469.26196	0.50065	0.50064	1.49943	0.5006515
0.15450	96.56117	165.76865	0.0	507.92871	-480.11621	0.49922	0.49921	1.52963	0.4992209
0.16000	100.00000	165.44182	0.0	517.88599	-490.74780	0.49819	0.49818	1.55946	0.4981930

X-VALUE	U	STAT PRESS	STAT TEMP	TOT PRESS	TOT TEMP	% AREA	EPS	RADC	RHO
-0.02000	181.61542	0.87121	275.81592	1.01350	288.00000	0.0	21.86812	-1.68012	1.1001902
-0.02000	210.45125	0.86886	275.60327	1.01350	288.00000	5.44362	17.74582	2.83861	1.0980701
-0.02000	235.16512	0.86485	275.23999	1.01350	288.00000	5.30154	14.92179	1.45452	1.0944557
-0.02000	257.07422	0.86086	274.87598	1.01350	288.00000	5.19068	12.74289	1.32053	1.0908413
-0.02000	276.90479	0.85729	274.55029	1.01350	288.00000	5.09650	10.95370	1.44446	1.0876131
-0.02000	312.29492	0.85195	274.06030	1.01350	288.00000	10.03286	8.07466	2.25268	1.0827665
-0.02000	343.61743	0.84999	273.78784	1.01350	288.00000	9.88350	5.82002	6.45792	1.0800791
-0.02000	372.11304	0.84802	273.69949	1.01350	288.00000	9.81060	4.02763	-8.41318	1.0791960
-0.02000	398.52344	0.84854	273.74609	1.01350	288.00000	9.78003	2.58813	-2.83817	1.0796652
-0.02000	423.32471	0.85004	273.88477	1.01350	288.00000	9.80432	1.48414	-1.91911	1.0810337
-0.02000	446.83496	0.85203	274.06787	1.01350	288.00000	9.84046	0.72873	-1.67914	1.0828428
-0.02000	458.17334	0.85306	274.16260	1.01350	288.00000	4.93611	0.49224	-1.70197	1.0837765
-0.02000	469.26196	0.85403	274.25098	1.01350	288.00000	4.94711	0.35529	-1.85486	1.0846500
-0.02000	480.11621	0.85484	274.32568	1.01350	288.00000	4.95726	0.32580	-2.27796	1.0853891
-0.02000	490.74780	0.85543	274.37915	1.01350	288.00000	4.96536	0.41693	-3.67505	1.0859194

GAMMA	ETAP	DP/(PT-P)	DP/(PTR-P)	PO/PO	(PO/PO)T	TO/TO	(TO/TO)T
1.40002	0.0	-0.12171	-0.05039	1.00000	1.00000	1.00000	1.00000
1.40002	0.0	-0.09603	-0.03212	1.00000	1.00000	1.00000	1.00000
1.40002	0.0	-0.08587	-0.02431	1.00000	1.00000	1.00000	1.00000
1.40002	0.0	-0.08281	-0.02035	1.00000	1.00000	1.00000	1.00000
1.40002	0.0	-0.08194	-0.01779	1.00000	1.00000	1.00000	1.00000
1.40002	0.0	-0.08058	-0.01410	1.00000	1.00000	1.00000	1.00000
1.40002	0.0	-0.07784	-0.01127	1.00000	1.00000	1.00000	1.00000
1.40002	0.0	-0.07306	-0.00890	1.00000	1.00000	1.00000	1.00000
1.40002	0.0	-0.06632	-0.00688	1.00000	1.00000	1.00000	1.00000
1.40002	0.0	-0.05785	-0.00516	1.00000	1.00000	1.00000	1.00000
1.40002	0.0	-0.04790	-0.00370	1.00000	1.00000	1.00000	1.00000
1.40002	0.0	-0.04242	-0.00307	1.00000	1.00000	1.00000	1.00000
1.40002	0.0	-0.03653	-0.00248	1.00000	1.00000	1.00000	1.00000
1.40002	0.0	-0.03034	-0.00193	1.00000	1.00000	1.00000	1.00000
1.40002	0.0	-0.02380	-0.00143	1.00000	1.00000	1.00000	1.00000

STATION NUMBER 11 DOWNSTREAM OF REMOTE

RADIUS	A STATIC	ALPHA BAR	ALPHA	A TOTAL	BETA	BETA BAR	V	VM	VR
0.10200	332.40161	89.99997	89.99997	340.23535	142.51183	140.52463	162.31140	162.31140	59.1394653
0.11551	332.12558	89.99997	89.99997	340.23535	144.92371	143.50395	165.10808	165.10808	52.0063477
0.12728	331.78882	89.99997	89.99997	340.23535	146.61185	145.58415	168.46385	168.46385	46.0022888
0.13781	331.48047	89.99997	89.99997	340.23535	147.96024	147.21400	171.47137	171.47137	40.5556488
0.14739	331.22388	89.99997	89.99997	340.23535	149.11739	148.57944	173.93394	173.93394	35.4465179
0.16459	330.86597	89.99997	89.99997	340.23535	151.12502	150.85428	177.30563	177.30563	26.3209076
0.17992	330.70093	89.99997	89.99997	340.23535	152.80813	152.77373	178.83090	178.83090	18.4306057
0.19396	330.69995	89.99997	89.99997	340.23535	154.53362	154.48592	178.84811	178.84811	11.6985540
0.20706	330.84253	89.99997	89.99997	340.23535	156.08260	156.07013	177.52402	177.52402	6.0695763
0.21946	331.11206	89.99997	89.99997	340.23535	157.57414	157.57327	174.99455	174.99455	1.5863800
0.23124	331.49097	89.99997	89.99997	340.23535	159.02324	159.02231	171.37135	171.37135	-1.6968784
0.23712	331.70508	89.99997	89.99997	340.23535	159.72260	159.71991	169.28664	169.28664	-2.8768129
0.24282	331.93848	89.99997	89.99997	340.23535	160.41200	160.40747	166.98243	166.98243	-3.7327261
0.24844	332.18872	89.99997	89.99997	340.23535	161.09135	161.08551	164.47681	164.47681	-4.2460070
0.25400	332.45435	89.99997	89.99997	340.23535	161.76202	161.75575	161.76967	161.76967	-4.3940334

S-VALUE	% SPAN	VX	VU	W	WU	MV	MVX	MW	MVM
0.0	0.0	151.15393	0.0	255.30843	-197.07208	0.48830	0.45473	0.76807	0.4882991
0.01351	8.89078	156.70358	0.0	277.60107	-223.16306	0.49712	0.47182	0.83583	0.4971249
0.02528	16.63318	162.06128	0.0	298.06322	-245.88948	0.50774	0.48845	0.89835	0.5077442
0.03581	23.55606	166.60634	0.0	316.65845	-266.21460	0.51729	0.50261	0.95529	0.5172895
0.04539	29.85864	170.28377	0.0	333.64404	-284.71973	0.52512	0.51410	1.00731	0.5251250
0.06259	41.17615	175.34108	0.0	364.05322	-317.95850	0.53588	0.52905	1.10030	0.5358835
0.07792	51.26483	177.89673	0.0	390.90259	-347.59326	0.54079	0.53791	1.18204	0.5407904
0.09196	60.50121	178.46510	0.0	415.21851	-374.72632	0.54082	0.53966	1.25557	0.5408168
0.10506	69.11945	177.42023	0.0	437.66357	-400.04346	0.53658	0.53627	1.32298	0.5365816
0.11746	77.27716	174.98737	0.0	458.69995	-424.00781	0.52851	0.52848	1.38533	0.5285055
0.12934	85.09012	171.36295	0.0	478.68506	-446.95776	0.51697	0.51695	1.44404	0.5169714
0.13512	88.89423	169.26219	0.0	488.40796	-458.13135	0.51035	0.51028	1.47242	0.5103528
0.14082	92.64180	166.94170	0.0	497.96997	-469.13818	0.50306	0.50293	1.50019	0.5030553
0.14644	96.34100	164.42198	0.0	507.40015	-480.00244	0.49513	0.49497	1.52744	0.4951306
0.15200	100.00000	161.70988	0.0	516.72314	-490.74780	0.48659	0.48641	1.55427	0.4865921

X-VALUE	U	STAT PRESS	STAT TEMP	TOT PRESS	TOT TEMP	% AREA	EPS	RADC	RHO
0.0	197.07208	0.86102	274.89038	1.01350	288.00000	0.0	21.36807	1.76261	1.0909853
0.00000	223.16306	0.85603	274.43481	1.01350	288.00000	5.43222	18.35082	0.95161	1.0864697
0.00000	245.88948	0.84997	273.97793	1.01350	288.00000	5.28042	15.84699	0.93916	1.0809660
0.00000	266.21460	0.84445	273.36914	1.01350	288.00000	5.15498	13.68098	1.08098	1.0759525
0.00000	284.71973	0.83989	272.94580	1.01350	288.00000	5.04897	11.75886	1.37286	1.0717936
0.00000	317.95850	0.83356	272.35645	1.01350	288.00000	9.91786	8.53708	2.87515	1.0660172
0.00000	347.59326	0.83065	272.08472	1.01350	288.00000	9.76307	5.91811	-22.89766	1.0633593
0.00000	374.72632	0.83063	272.08325	1.01350	288.00000	9.70051	3.75043	-2.19191	1.0633450
0.00000	400.04346	0.83314	272.31787	1.01350	288.00000	9.70806	1.95033	-1.10497	1.0656404
0.00000	424.00781	0.83791	272.76172	1.01350	288.00000	9.77375	0.51941	-0.71656	1.0699863
0.00000	446.95776	0.84464	273.38623	1.01350	288.00000	9.89345	-0.56734	-0.52018	1.0761213
0.00000	458.13135	0.84847	273.73950	1.01350	288.00000	5.00579	-0.97372	-0.45526	1.0796013
0.00000	469.13818	0.85265	274.12500	1.01350	288.00000	5.05221	-1.28089	-0.40386	1.0834055
0.00000	480.00244	0.85716	274.53833	1.01350	288.00000	5.10465	-1.47027	-0.36197	1.0874949
0.0	490.74780	0.86198	274.97778	1.01350	288.00000	5.16393	-1.55647	-0.32687	1.0918522

GAMMA	ETAP	DP/(PT-P)	DP/(PTR-P)	P0/P0	(P0/P0)T	T0/T0	(T0/T0)T
1.40002	0.0	-0.07160	-0.02836	1.00000	1.00000	1.00000	1.00000
1.40002	0.0	-0.08965	-0.02894	1.00000	1.00000	1.00000	1.00000
1.40002	0.0	-0.10016	-0.02809	1.00000	1.00000	1.00000	1.00000
1.40002	0.0	-0.10747	-0.02651	1.00000	1.00000	1.00000	1.00000
1.40002	0.0	-0.11144	-0.02455	1.00000	1.00000	1.00000	1.00000
1.40002	0.0	-0.11385	-0.02053	1.00000	1.00000	1.00000	1.00000
1.40002	0.0	-0.11150	-0.01680	1.00000	1.00000	1.00000	1.00000
1.40002	0.0	-0.10507	-0.01338	1.00000	1.00000	1.00000	1.00000
1.40002	0.0	-0.09330	-0.01013	1.00000	1.00000	1.00000	1.00000
1.40002	0.0	-0.07425	-0.00692	1.00000	1.00000	1.00000	1.00000
1.40002	0.0	-0.04580	-0.00368	1.00000	1.00000	1.00000	1.00000
1.40002	0.0	-0.02865	-0.00215	1.00000	1.00000	1.00000	1.00000
1.40002	0.0	-0.00861	-0.00060	1.00000	1.00000	1.00000	1.00000
1.40002	0.0	0.01464	0.00096	1.00000	1.00000	1.00000	1.00000
1.40002	0.0	0.04143	0.00255	1.00000	1.00000	1.00000	1.00000

STATION NUMBER 12 DOWNSTREAM OF IGV

RADIUS	A STATIC	ALPHA BAR	ALPHA	A TOTAL	BETA	BETA BAR	V	VM	VR
0.11000	331.41162	89.99997	89.99997	340.23535	143.39019	140.99460	172.13541	172.13541	68.5568390
0.12216	330.50610	89.99997	89.99997	340.23535	144.59225	142.79619	180.63029	180.63029	63.3883667
0.13441	329.68409	89.99997	89.99997	340.23535	145.41249	144.09555	187.99208	187.99208	57.3126068
0.14433	328.96777	89.99997	89.99997	340.23535	146.09729	145.14795	194.16370	194.16370	50.8704529
0.15326	328.36816	89.99997	89.99997	340.23535	146.74255	146.07036	199.17371	199.17371	44.3743591
0.16916	327.46509	89.99997	89.99997	340.23535	148.02559	147.71391	206.47411	206.47411	31.8993530
0.18318	326.88559	89.99997	89.99997	340.23535	149.30710	149.10301	211.01193	211.01193	20.0416565
0.19590	326.54761	89.99997	89.99997	340.23535	150.57855	150.55823	213.61481	213.61481	8.6932230
0.20766	326.40576	89.99997	89.99997	340.23535	151.84837	151.84694	214.69646	214.69646	-2.3592434
0.21870	326.45166	89.99997	89.99997	340.23535	153.14523	153.10152	214.34767	214.34767	-13.1755447
0.22918	326.69458	89.99997	89.99997	340.23535	154.49930	154.36440	212.48944	212.48944	-23.2961121
0.23426	326.88501	89.99997	89.99997	340.23535	155.19588	155.00352	211.01854	211.01854	-27.8572540
0.23925	327.12329	89.99997	89.99997	340.23535	155.90697	155.65294	209.16583	209.16583	-32.0104370
0.24415	327.40723	89.99997	89.99997	340.23535	156.63124	156.31433	206.93222	206.93222	-35.7062683
0.24900	327.73608	89.99997	89.99997	340.23535	157.36694	156.98954	204.31203	204.31203	-38.8580475

S-VALUE	% SPAN	VX	VU	W	WU	MV	MVX	MW	MVM
0.0	0.0	157.80412	0.0	273.49414	-212.52963	0.51940	0.47643	0.82524	0.5194006
0.01234	9.46920	165.14259	0.0	298.73438	-237.93889	0.54653	0.51177	0.90387	0.5465263
0.02474	17.56111	179.04269	0.0	320.56738	-259.65845	0.57022	0.54307	0.97235	0.5702188
0.03480	24.69577	187.39176	0.0	339.76831	-278.82422	0.59022	0.56960	1.03293	0.5902210
0.04385	31.12399	194.16766	0.0	356.83081	-296.07104	0.60656	0.59131	1.08668	0.6065561
0.05996	42.55951	203.09506	0.0	386.54932	-326.78564	0.63052	0.62295	1.18043	0.6305225
0.07417	52.64499	210.05801	0.0	412.01392	-353.87793	0.64552	0.64260	1.26042	0.6455215
0.08706	61.79555	213.43785	0.0	434.59398	-378.45996	0.65416	0.65362	1.33084	0.6541613
0.09899	70.25894	214.68350	0.0	455.03101	-401.19653	0.65776	0.65772	1.39406	0.6577594
0.11018	78.20030	213.94235	0.0	473.78979	-422.53052	0.65660	0.65536	1.45133	0.6565984
0.12080	85.74338	211.20954	0.0	491.13989	-442.79419	0.65042	0.64650	1.50336	0.6504223
0.12595	89.39539	209.17169	0.0	499.37891	-452.60400	0.64554	0.63989	1.52769	0.6455436
0.13100	92.98256	206.70189	0.0	507.36133	-462.23950	0.63941	0.63188	1.55098	0.6394098
0.13598	96.51424	203.82837	0.0	515.11743	-471.72559	0.63203	0.62255	1.57332	0.6320331
0.14089	100.00000	200.59279	0.0	522.67456	-481.08765	0.62340	0.61203	1.59480	0.6234041

X-VALUE	U	STAT PRESS	STAT TEMP	TOT PRESS	TOT TEMP	% AREA	EPS	RADC	RHO
0.02000	212.52963	0.84323	273.25562	1.01350	288.00000	0.0	23.47025	0.45049	1.0748358
0.02218	237.93889	0.82723	271.76440	1.01350	288.00000	6.15003	20.54413	0.57449	1.0602331
0.02404	259.65845	0.81294	270.41406	1.01350	288.00000	5.80571	17.75017	0.79272	1.0471125
0.02568	278.82422	0.80065	269.24048	1.01350	288.00000	5.54276	15.18864	1.17799	1.0357885
0.02716	296.07104	0.79049	268.25977	1.01350	288.00000	5.32539	12.97210	1.88693	1.0263834
0.02979	326.78564	0.77540	266.78613	1.01350	288.00000	10.27030	8.88755	4032.98438	1.0123472
0.03211	353.87793	0.76585	265.84351	1.01350	288.00000	9.89923	5.45010	-2.42858	1.0034285
0.03421	378.45996	0.76032	265.29346	1.01350	288.00000	9.66218	2.33234	-1.37136	0.9982473
0.03616	401.19653	0.75801	265.06299	1.01350	288.00000	9.51378	-0.62962	-0.99678	0.9960803
0.03799	422.53052	0.75876	265.13745	1.01350	288.00000	9.43137	-3.52409	-0.77799	0.9967800
0.03972	442.79419	0.76272	265.52223	1.01350	288.00000	9.41060	-6.29424	-0.62254	1.0004930
0.04056	452.60400	0.76584	265.84204	1.01350	288.00000	4.71449	-7.58595	-0.55796	1.0034151
0.04139	462.23950	0.76975	266.22949	1.01350	288.00000	4.73132	-8.80306	-0.49702	1.0070744
0.04220	471.72559	0.77444	266.69189	1.01350	288.00000	4.75548	-9.93615	-0.43941	1.0114536
0.04300	481.08765	0.77991	267.22827	1.01350	288.00000	4.78835	-10.96286	-0.38553	1.0165443

GAMMA	STAGE EFF	DP/(PT-P)	DP/(PTR-P)	PO/PO	(PO/PO)T	TO/TO	(TO/TO)T	P/P	V/V
1.40002	0.0	-0.11667	-0.04327	1.00000	1.00000	1.00000	1.00000	0.97934	1.0605249
1.40002	0.0	-0.19290	-0.05796	1.00000	1.00000	1.00000	1.00000	0.96636	1.0940123
1.40002	0.0	-0.22645	-0.06330	1.00000	1.00000	1.00000	1.00000	0.95643	1.1159191
1.40002	0.0	-0.25910	-0.06499	1.00000	1.00000	1.00000	1.00000	0.94813	1.1323385
1.40002	0.0	-0.28450	-0.06468	1.00000	1.00000	1.00000	1.00000	0.94119	1.1451111
1.40002	0.0	-0.32320	-0.06142	1.00000	1.00000	1.00000	1.00000	0.93023	1.1645088
1.40002	0.0	-0.35436	-0.05698	1.00000	1.00000	1.00000	1.00000	0.92199	1.1798925
1.40002	0.0	-0.39449	-0.05259	1.00000	1.00000	1.00000	1.00000	0.91535	1.1943922
1.40002	0.0	-0.41658	-0.04852	1.00000	1.00000	1.00000	1.00000	0.90982	1.2093935
1.40002	0.0	-0.45074	-0.04461	1.00000	1.00000	1.00000	1.00000	0.90554	1.2248812
1.40002	0.0	-0.48513	-0.04062	1.00000	1.00000	1.00000	1.00000	0.90301	1.2399349
1.40002	0.0	-0.50067	-0.03853	1.00000	1.00000	1.00000	1.00000	0.90262	1.2465162
1.40002	0.0	-0.51541	-0.03639	1.00000	1.00000	1.00000	1.00000	0.90277	1.2526140
1.40002	0.0	-0.52912	-0.03422	1.00000	1.00000	1.00000	1.00000	0.90349	1.2581234
1.40002	0.0	-0.54163	-0.03202	1.00000	1.00000	1.00000	1.00000	0.90479	1.2629805

STATION NUMBER 13 DOWNSTREAM OF ROTOR 1

RADIUS	A STATIC	ALPHA BAR	ALPHA	A TOTAL	BETA	BETA BAR	V	VM	VR
0.13400	348.77612	43.12003	40.86371	368.57300	110.89253	109.42480	266.64063	182.25668	60.7645721
0.14219	349.44604	46.14806	44.59865	367.59424	119.31000	118.00581	255.23265	184.05661	58.9398193
0.14960	350.06641	48.21997	47.14270	366.99463	125.17992	124.16835	246.50407	183.81763	49.5625763
0.15648	350.74512	49.56891	48.82025	366.72192	129.61102	128.86948	239.54132	182.33572	41.3636322
0.16299	351.50488	50.38475	49.96642	366.72192	133.13802	132.61275	232.80998	180.18343	34.2372437
0.17518	352.52417	52.14665	51.92133	366.66724	138.53311	138.30241	225.64600	178.16656	22.5075494
0.18643	353.24219	53.73389	53.65866	366.66724	142.45117	142.37500	219.95326	177.34358	13.1361732
0.19623	353.71729	55.25044	55.24005	366.66724	145.40166	145.39127	216.09741	177.55678	4.9390055
0.20581	354.12378	56.54526	56.54326	366.77637	147.68004	147.67709	213.68059	178.28044	-2.6982260
0.21618	354.77319	57.28389	57.24086	367.26733	149.48167	149.44037	212.50826	178.79558	-10.2532425
0.22523	356.45069	56.55426	56.42052	368.89893	150.96526	150.84181	212.61511	177.40785	-17.8199310
0.22969	357.53052	55.88629	55.69398	369.98267	151.65187	151.46965	212.97356	176.32648	-21.6482086
0.23413	358.66431	55.16359	54.87364	371.11694	152.34238	152.08780	213.21638	175.08723	-25.5624390
0.23856	359.91431	54.30629	53.90569	372.35522	153.05753	152.71532	213.58876	173.46568	-29.5475922
0.24300	361.29159	53.29829	52.75896	373.69678	153.82426	153.37724	213.68500	171.32367	-33.5828705

S-VALUE	% SPAN	VX	VU	W	WU	MV	MVX	MW	MVM
0.0	0.0	169.37576	104.62721	153.25705	-64.27122	0.76450	0.48276	0.55410	0.5225607
0.00819	7.51450	174.36436	176.82440	208.46819	-97.98840	0.73039	0.49897	0.59657	0.5267096
0.01560	14.30784	177.00981	164.24171	222.16536	-124.77391	0.70416	0.50565	0.63464	0.5250936
0.02248	20.62418	177.58200	155.35034	234.19081	-146.96606	0.68295	0.50630	0.66770	0.5198525
0.02930	26.60083	176.90076	149.14134	244.93214	-165.76100	0.66542	0.50327	0.69653	0.5126057
0.04119	37.78314	176.72768	138.46587	267.83984	-199.98701	0.64009	0.50132	0.75078	0.5054024
0.05244	48.10295	176.85640	130.11031	290.49341	-230.07768	0.62267	0.50067	0.82236	0.5020453
0.06294	57.73392	177.48907	123.17340	312.61719	-257.29956	0.61092	0.50178	0.88381	0.5019737
0.07281	66.79404	178.26003	117.79422	333.42740	-281.76245	0.60341	0.50338	0.94156	0.5034410
0.08219	75.39279	178.50134	114.85602	351.65894	-302.81372	0.59990	0.50314	0.99122	0.5030715
0.09124	83.69670	176.51060	117.18210	364.12085	-317.97876	0.59648	0.49519	1.02152	0.4977065
0.09570	87.79231	174.99251	119.44336	369.17456	-324.34375	0.59569	0.48945	1.03257	0.4931788
0.10014	91.86609	173.21115	121.85378	374.02417	-330.51279	0.59475	0.48293	1.04282	0.4881646
0.10457	95.92943	170.93062	124.61870	378.40601	-336.30469	0.59344	0.47402	1.05138	0.4819638
0.10901	100.00000	167.99997	127.70857	382.32129	-341.78638	0.59145	0.46500	1.05821	0.4741972

X-VALUE	U	STAT PRESS	STAT TEMP	TOT PRESS	TOT TEMP	% AREA	EPS	RADC	RHO
0.07000	258.89844	1.12838	302.75488	1.66130	338.09985	0.0	22.50610	-0.19664	1.2981730
0.07011	274.71289	1.16518	303.91309	1.66130	336.29980	5.50513	18.67662	-0.21634	1.3354034
0.07021	289.01563	1.19333	304.98950	1.66130	335.19995	5.25783	15.64220	-0.24725	1.3628368
0.07031	302.31641	1.21596	306.17163	1.66130	334.69995	5.12807	13.11104	-0.29192	1.3833170
0.07040	314.90234	1.23454	307.40951	1.66130	334.69995	5.06469	10.95356	-0.35336	1.3983822
0.07057	338.45288	1.26115	309.29540	1.66130	334.59985	10.03083	7.28667	-0.59630	1.4202833
0.07072	360.18759	1.27926	310.54639	1.66130	334.59985	9.89868	4.24790	-1.48981	1.4348230
0.07087	380.47314	1.29136	311.38232	1.66130	334.59985	9.79348	1.59400	7.45100	1.4445095
0.07100	399.55688	1.29908	312.09888	1.66130	334.79980	9.70263	-0.96719	1.18691	1.4499053
0.07113	417.66992	1.30358	313.24805	1.66130	335.69995	9.64757	-3.28750	0.64968	1.4494963
0.07126	435.16089	1.30616	316.22705	1.66130	338.69995	9.72257	-5.76486	0.46127	1.4396768
0.07132	443.78711	1.30699	318.15259	1.66130	340.69995	4.94213	-7.05220	0.41709	1.4308662
0.07138	452.36670	1.30703	320.18091	1.66130	342.79980	5.01203	-8.39510	0.39236	1.4228344
0.07144	460.92359	1.30926	322.42456	1.66130	345.09985	5.00477	-9.80741	0.38574	1.4143782
0.07150	469.49512	1.31130	324.90576	1.66130	347.59985	5.19055	-11.30432	0.40334	1.4057579

GAMMA	ROTOR EFF	DP/(PT-P)	DP/(PTR-P)	PO/PO	(PO/PO)T	TO/TO	(TO/TO)T	P/P	W/W
1.39949	0.87961	1.67471	0.60035	1.63917	1.63917	1.17396	1.17396	1.33817	0.7066222
1.39952	0.90994	1.91434	0.58513	1.63917	1.63917	1.16771	1.16771	1.40853	0.6978379
1.39953	0.92961	1.89665	0.56166	1.63917	1.63917	1.16389	1.16389	1.46793	0.6930379
1.39954	0.93885	1.95122	0.53622	1.63917	1.63917	1.16215	1.16215	1.51871	0.6892661
1.39954	0.93885	1.99117	0.51068	1.63917	1.63917	1.16215	1.16215	1.56173	0.6861295
1.39954	0.94073	2.04013	0.45937	1.63917	1.63917	1.16180	1.16180	1.62645	0.6928905
1.39954	0.94073	2.07314	0.41225	1.63917	1.63917	1.16180	1.16180	1.67037	0.7050573
1.39954	0.94073	2.09751	0.36962	1.63917	1.63917	1.16180	1.16180	1.69844	0.7193481
1.39954	0.93699	2.11778	0.33119	1.63917	1.63917	1.16250	1.16250	1.71379	0.7327577
1.39952	0.92055	2.13874	0.29646	1.63917	1.63917	1.16562	1.16562	1.71805	0.7422256
1.39948	0.86998	2.16699	0.26505	1.63917	1.63917	1.17604	1.17604	1.71250	0.7413791
1.39945	0.83945	2.18500	0.25048	1.63917	1.63917	1.18299	1.18299	1.70659	0.7392674
1.39942	0.80980	2.20792	0.23674	1.63917	1.63917	1.19028	1.19028	1.69915	0.7371948
1.39939	0.77981	2.23721	0.22384	1.63917	1.63917	1.19826	1.19826	1.69059	0.7346014
1.39935	0.74984	2.27485	0.21181	1.63917	1.63917	1.20694	1.20694	1.68135	0.7314710

STATION NUMBER 14 DUMMY

RADIUS	A STATIC	ALPHA BAR	ALPHA	A TOTAL	BETA	BETA BAR	V	VM	VR
0.14200	346.96729	48.62823	47.98125	368.49194	113.98497	113.50478	277.88013	208.53191	43.9699554
0.14866	347.68652	50.63708	50.17250	367.52100	120.20946	119.79980	266.67212	206.17610	37.1590881
0.15493	348.31909	52.12085	51.77863	366.92651	124.95053	124.62018	258.28149	203.86362	31.7877808
0.16091	348.97510	53.13885	52.88315	366.65601	128.68156	128.42230	251.82848	201.48590	27.3307800
0.16658	349.69653	53.76962	53.57822	366.65601	131.71085	131.51172	246.76163	199.04961	23.4697723
0.17764	350.68726	55.18826	55.08504	366.60181	136.56836	136.45849	239.19356	196.38573	17.1818237
0.18792	351.39185	56.51488	56.46567	366.60181	140.22852	140.17596	233.95322	195.12386	11.9091663
0.19762	351.82959	57.84673	57.83000	366.60181	143.01360	142.99579	230.63263	195.26001	7.0245953
0.20681	352.13135	59.07162	59.06993	366.70996	145.09708	145.09528	229.18530	196.59766	2.2847052
0.21552	352.57593	59.89583	59.89381	367.15702	146.59103	146.58890	229.67984	198.69958	-2.5245199
0.22391	353.91235	59.52280	59.50372	368.81494	147.54945	147.52972	232.30709	200.28712	-7.8069115
0.22801	354.74658	59.14397	59.10730	369.88965	147.87013	147.83260	234.60291	201.39706	-10.8523121
0.23206	355.58374	58.77623	58.71295	371.01416	148.13040	148.06641	237.16920	202.81523	-14.2954178
0.23605	356.47632	58.36391	58.26144	372.24194	148.33443	148.23192	240.11357	204.43198	-18.2507935
0.24000	357.42236	57.91545	57.75536	373.57178	148.49223	148.33377	243.43442	206.25363	-22.8960266

S-VALUE	% SPAN	VX	VU	W	WU	MV	MVX	MW	MVM
0.0	0.0	203.84357	183.66225	227.39993	-90.69273	0.80088	0.58750	0.65539	0.6010131
0.00666	6.79097	202.79987	169.13136	237.59363	-119.07689	0.76699	0.58328	0.68336	0.5929942
0.01295	13.19221	201.37009	158.58417	247.72702	-140.74200	0.74151	0.57812	0.71121	0.5852783
0.01854	19.29951	199.62364	151.06625	257.17700	-159.82339	0.72162	0.57203	0.73695	0.5773647
0.02471	25.17931	197.66112	145.84428	265.81738	-176.17671	0.70565	0.56524	0.76014	0.5692067
0.03568	36.36400	195.62266	136.55112	285.07959	-206.64737	0.68207	0.55786	0.81292	0.5600024
0.04598	46.85965	194.76009	129.07669	304.67554	-233.99533	0.66579	0.55425	0.86705	0.5552885
0.05570	56.75992	195.13361	122.73930	324.42017	-259.07935	0.65552	0.55463	0.92209	0.5549846
0.06489	66.12886	196.58438	117.79332	343.57397	-281.76660	0.65085	0.55827	0.97570	0.5583077
0.07363	75.03111	198.68355	115.20116	360.85059	-301.21704	0.65143	0.56352	1.02347	0.5635654
0.08202	83.58615	200.13492	117.87059	373.07007	-314.74829	0.65665	0.56549	1.05413	0.5659229
0.08613	87.76961	201.10446	120.32352	378.28516	-320.21704	0.66133	0.56690	1.06635	0.5677209
0.09018	91.89656	202.31079	122.94394	383.44019	-325.41113	0.66699	0.56805	1.07834	0.5703726
0.09417	95.97102	203.61566	125.94481	388.29785	-330.12549	0.67359	0.57119	1.08927	0.5734798
0.09812	100.00000	204.97885	129.30490	392.88647	-334.39380	0.68108	0.57749	1.09922	0.5770585

X-VALUE	U	STAT PRESS	STAT TEMP	TOT PRESS	TOT TEMP	% AREA	EPS	RADC	RHO
0.09500	274.35498	1.08919	299.75464	1.66130	338.09985	0.0	12.17245	-0.14126	1.2656202
0.09466	287.20825	1.12583	300.97998	1.66130	336.29980	5.16710	10.38315	-0.19668	1.3028736
0.09434	299.32617	1.15333	302.06470	1.66130	335.19995	5.08720	8.97055	-0.26820	1.3299084
0.09403	310.88965	1.17473	303.19849	1.66130	334.69995	5.04093	7.79599	-0.36096	1.3495178
0.09374	322.02100	1.19187	304.45337	1.66130	334.69995	5.04196	6.77146	-0.48125	1.3635578
0.09318	343.19849	1.21701	306.17969	1.66130	334.59985	10.08122	5.01924	-0.88038	1.3844728
0.09266	363.07202	1.23426	307.41138	1.66130	334.59985	10.04392	3.49916	-2.72555	1.3984718
0.09216	381.81885	1.24508	308.17773	1.66130	334.59985	9.99221	2.06169	1.86558	1.4072247
0.09169	399.56006	1.24999	308.70874	1.66130	334.79980	9.91908	0.66586	0.63472	1.4103451
0.09125	416.41821	1.24930	309.49805	1.66130	335.69995	9.84228	-0.72797	0.36776	1.4060707
0.09082	432.61890	1.24394	311.88135	1.66130	338.69995	9.84153	-2.23288	0.25350	1.3892374
0.09051	440.54077	1.23904	313.37476	1.66130	340.69995	4.94928	-3.08889	0.21707	1.3771696
0.09040	448.35522	1.23309	314.87866	1.66130	342.79980	4.97041	-4.04184	0.18836	1.3640099
0.09020	456.07031	1.22614	316.48657	1.66130	345.09985	4.99293	-5.12194	0.16497	1.3494339
0.09000	463.69873	1.21820	318.19604	1.66130	347.59985	5.02093	-6.37349	0.14500	1.3334970

GAMMA	ETAP	DP/(PT-P)	DP/(PTR-P)	PO/PO	(PO/PO)T	TO/TO	(TO/TO)T
1.39887	0.0	-0.07355	-0.14990	1.00000	1.63917	1.00000	1.17396
1.39896	0.0	-0.07932	-0.12422	1.00000	1.63917	1.00000	1.16771
1.39901	0.0	-0.08548	-0.10769	1.00000	1.63917	1.00000	1.16389
1.39904	0.0	-0.09258	-0.09739	1.00000	1.63917	1.00000	1.16215
1.39904	0.0	-0.09998	-0.09035	1.00000	1.63917	1.00000	1.16215
1.39904	0.0	-0.11031	-0.07519	1.00000	1.63917	1.00000	1.16180
1.39904	0.0	-0.11778	-0.06297	1.00000	1.63917	1.00000	1.16180
1.39904	0.0	-0.12510	-0.05417	1.00000	1.63917	1.00000	1.16180
1.39903	0.0	-0.13551	-0.04907	1.00000	1.63917	1.00000	1.16250
1.39899	0.0	-0.15149	-0.04761	1.00000	1.63917	1.00000	1.16562
1.39884	0.0	-0.17519	-0.05064	1.00000	1.63917	1.00000	1.17604
1.39875	0.0	-0.19174	-0.05380	1.00000	1.63917	1.00000	1.18299
1.39865	0.0	-0.21178	-0.05777	1.00000	1.63917	1.00000	1.19028
1.39853	0.0	-0.23612	-0.06280	1.00000	1.63917	1.00000	1.19826
1.39841	0.0	-0.26598	-0.06910	1.00000	1.63917	1.00000	1.20694

STATION NUMBER 15   DUMMY

RADIUS	A STATIC	ALPHA BAR	ALPHA	A TOTAL	BETA	BETA BAR	V	VM	VP
0.14500	346.97485	49.65587	49.49113	368.49194	115.47198	115.34265	277.83228	211.75552	22.7875061
0.15139	347.23047	51.98189	51.82019	367.52100	120.90739	120.76085	269.63279	212.42192	22.8361664
0.15742	347.63525	53.57610	53.42903	366.92651	125.13889	124.99425	262.85840	211.50810	21.8566589
0.16217	348.19067	54.60666	54.47888	366.65601	128.54774	128.41602	257.21143	209.67764	20.3237610
0.16972	348.87476	55.21181	55.10414	366.65601	131.36697	131.25311	252.52441	207.39000	18.5299835
0.17528	349.81322	56.56184	56.49173	366.60181	135.93184	135.85573	245.52390	204.88510	14.9229097
0.18321	350.41821	57.88824	57.84311	366.60181	139.33729	139.28770	241.16014	204.26584	12.0637131
0.19857	350.73950	59.23593	59.20208	366.60181	141.91497	141.87859	238.80850	205.20370	10.4744825
0.20743	350.96558	60.42973	60.40132	366.70996	143.88158	143.85005	237.97772	206.98152	9.9405613
0.21584	351.40381	61.16489	61.13570	367.19702	145.35439	145.32204	238.51300	208.94019	10.2551680
0.22294	352.78735	60.69972	60.66452	368.81494	146.33144	146.29340	240.82147	210.01251	11.2557688
0.22791	353.66455	60.25854	60.21762	369.88965	146.67841	146.63480	242.65814	210.69356	12.1177025
0.23182	354.53955	59.83026	59.78098	371.01416	146.95648	146.90462	244.88501	211.71306	13.3047142
0.23568	355.45435	59.37247	59.31067	372.24194	147.15439	147.09018	247.60109	213.06017	14.9198990
0.23950	356.39575	58.90300	58.82213	373.57178	147.26869	147.18553	250.97682	214.82449	17.1291504

S-VALUE	% SPAN	VX	VU	W	WU	MV	MVX	MW	MVM
0.0	0.0	210.52585	175.86220	234.30389	-100.28917	0.80073	0.60675	0.67528	0.6102906
0.00639	6.76541	211.19086	166.07019	247.20056	-126.43201	0.77653	0.60822	0.71192	0.6117606
0.01242	13.14020	210.37578	156.07335	258.19555	-148.06801	0.75613	0.60516	0.74269	0.6084196
0.01817	19.22820	208.69034	148.97328	267.60986	-166.28404	0.73871	0.59936	0.76857	0.6021920
0.02372	25.09689	206.56053	144.07628	275.85645	-181.89613	0.72383	0.59208	0.79070	0.5944540
0.03428	36.27092	204.34093	135.29256	294.17749	-211.09831	0.70187	0.58414	0.84096	0.5856985
0.04421	46.78516	203.90929	128.19394	313.16577	-237.37808	0.68821	0.58190	0.89369	0.5829201
0.05357	56.68950	204.93620	122.15134	332.40527	-261.50488	0.68087	0.58430	0.94773	0.5850601
0.06243	66.05827	206.74268	117.43953	350.87549	-283.32373	0.67807	0.58907	0.99974	0.5897487
0.07084	74.96609	208.68835	115.03239	367.22998	-301.99659	0.67874	0.59387	1.04504	0.5945871
0.07894	83.53630	209.71066	117.85468	378.44189	-314.82227	0.68262	0.59444	1.07272	0.5952949
0.08291	87.73128	210.34480	120.37939	383.09790	-319.95654	0.68613	0.59476	1.08322	0.5957440
0.08682	91.87206	211.29450	123.07011	387.72876	-324.82495	0.69071	0.59597	1.09361	0.5971493
0.09068	95.96062	212.53712	126.14145	392.14624	-329.21752	0.69659	0.59793	1.10322	0.5994023
0.09450	100.00000	214.14050	129.57477	396.41357	-333.15796	0.70393	0.60085	1.11228	0.6027695

X-VALUE	U	STAT PRESS	STAT TEMP	TOT PRESS	TOT TEMP	% AREA	EPS	RADC	RHO
0.11500	280.15137	1.08936	299.76782	1.66130	338.09985	0.0	6.17770	-0.41859	1.2657595
0.11500	292.50220	1.11552	300.19116	1.66130	336.29980	5.21514	6.17144	-0.41108	1.2943316
0.11500	304.14136	1.13755	300.87988	1.66130	335.19995	5.11991	5.93138	-0.41618	1.3168736
0.11500	315.25732	1.15635	301.82716	1.66130	334.69995	5.07605	5.56234	-0.44599	1.3343859
0.11500	325.97241	1.17237	303.02393	1.66130	334.69995	5.06565	5.12613	-0.51638	1.3475733
0.11500	346.39087	1.19590	304.65552	1.66130	334.59985	10.12147	4.17687	-1.03587	1.3672667
0.11500	365.57202	1.21048	305.71045	1.66130	334.59985	10.06799	3.38580	11.94099	1.3791618
0.11500	383.65625	1.21829	306.27124	1.66130	334.59985	9.98892	2.92590	1.18144	1.3855095
0.11500	400.76343	1.22127	306.66846	1.66130	334.79980	9.80257	2.75276	0.71123	1.3871021
0.11500	417.02905	1.22056	307.44409	1.66130	335.69995	9.80598	2.81321	0.50273	1.3827982
0.11500	432.67700	1.21647	309.90186	1.66130	338.69995	9.80245	3.07228	0.35471	1.3672342
0.11500	440.33594	1.21277	311.46606	1.66130	340.69995	4.92974	3.29710	0.29780	1.3562307
0.11500	447.89526	1.20791	313.03223	1.66130	342.79980	4.95092	3.60302	0.24854	1.3440361
0.11500	455.35913	1.20168	314.67432	1.66130	345.39985	4.97115	4.01552	0.20731	1.3301287
0.11500	462.73291	1.19385	316.37085	1.66130	347.59985	4.99204	4.57237	0.17378	1.3143797

GAMMA	ETAP	DP/(PT-P)	DP/(PTP-P)	PO/PO	(PO/PO)T	TO/TO	(TO/TO)T
1.39887	0.0	0.00030	0.00046	1.00000	1.63917	1.00000	1.17396
1.39896	0.0	-0.01926	-0.02499	1.00000	1.63917	1.00000	1.16771
1.39901	0.0	-0.03107	-0.03414	1.00000	1.63917	1.00000	1.16389
1.39904	0.0	-0.03779	-0.03604	1.00000	1.63917	1.00000	1.16215
1.39904	0.0	-0.04154	-0.03511	1.00000	1.63917	1.00000	1.16215
1.39904	0.0	-0.04751	-0.03190	1.00000	1.63917	1.00000	1.16180
1.39904	0.0	-0.05568	-0.03047	1.00000	1.63917	1.00000	1.16180
1.39904	0.0	-0.06438	-0.02939	1.00000	1.63917	1.00000	1.16180
1.39903	0.0	-0.06984	-0.02736	1.00000	1.63917	1.00000	1.16250
1.39899	0.0	-0.07000	-0.02441	1.00000	1.63917	1.00000	1.16562
1.39884	0.0	-0.06582	-0.02170	1.00000	1.63917	1.00000	1.17604
1.39875	0.0	-0.06221	-0.02023	1.00000	1.63917	1.00000	1.18299
1.39865	0.0	-0.05881	-0.01895	1.00000	1.63917	1.00000	1.19028
1.39853	0.0	-0.05622	-0.01804	1.00000	1.63917	1.00000	1.19826
1.39841	0.0	-0.05496	-0.01766	1.00000	1.63917	1.00000	1.20694

STATION NUMBER 16   DUMMY

RADIUS	A STATIC	ALPHA BAR	ALPHA	A TOTAL	BETA	BETA BAR	V	VM	VR
0.14700	345.73022	50.16205	50.01509	367.18921	116.74282	116.62404	276.94336	212.65370	21.6552887
0.15320	346.31274	53.00620	52.92970	367.08643	121.33545	121.26480	272.55884	217.69302	16.1997528
0.15920	346.91089	54.83967	54.79639	366.98096	125.01518	124.97299	267.98608	219.08780	12.2560816
0.16482	347.48706	55.95918	55.92230	366.87378	128.09193	128.06380	263.46460	218.31709	9.8141575
0.17023	348.07300	56.56913	56.54729	366.81934	130.73472	130.71227	259.17261	216.29039	8.6024122
0.18058	349.13403	57.72231	57.69859	366.76514	135.28494	135.25965	251.52251	212.65488	9.1045437
0.19038	349.97046	58.69722	58.66267	366.71069	138.96783	138.92926	245.21828	209.52290	10.9158897
0.19972	350.76001	59.64574	59.60382	366.81958	141.93906	141.89235	240.33252	207.38715	11.9945135
0.20864	351.62085	60.47557	60.42673	367.19971	144.30396	144.24997	236.92017	206.15517	12.9807758
0.21723	352.64111	60.96959	60.90829	367.90308	146.18231	146.11636	234.79446	205.09514	14.4522057
0.22557	353.79614	59.89714	59.81163	368.81494	147.75403	147.66512	233.28372	201.82007	16.7037811
0.22969	354.40234	59.09699	58.98212	369.29517	148.51425	148.40829	232.49927	199.47237	18.1287689
0.23380	355.03296	58.19056	58.06009	369.77490	149.30098	149.17268	231.51610	196.74477	19.8110657
0.23789	355.70532	57.11870	56.95299	370.25293	150.14449	149.98750	230.18922	193.31230	21.6911621
0.24200	356.48755	55.84697	55.63589	370.78345	151.07181	150.87930	228.42012	189.02711	23.6937256

S-VALUE	% SPAN	VX	VU	W	WU	MV	MVY	MW	MVM
0.0	0.0	211.54820	177.41502	237.97650	-106.60036	0.80194	0.61189	0.68894	0.6150856
0.00630	6.62947	217.09942	164.09647	254.67780	-132.17615	0.78703	0.62686	0.73540	0.6286024
0.01220	12.83896	218.74472	154.32791	267.36365	-152.25314	0.77249	0.63055	0.77071	0.6315391
0.01782	18.75600	218.09639	147.48291	277.28979	-170.95996	0.75830	0.62764	0.79799	0.6282740
0.02323	24.45778	216.11926	142.78972	285.34546	-186.11969	0.74459	0.62090	0.81979	0.6213937
0.03358	35.34981	212.45988	134.31959	302.10545	-214.59376	0.72042	0.60853	0.86530	0.6090924
0.04338	45.66379	209.23836	127.40549	318.91323	-240.42850	0.70068	0.59787	0.91126	0.5986874
0.05272	55.48952	207.03999	121.45078	334.04517	-264.41821	0.68518	0.59026	0.95805	0.5912508
0.06164	64.88809	205.74608	116.75278	352.85449	-286.26768	0.67379	0.58514	1.00351	0.5862996
0.07023	73.92152	204.58531	114.29973	367.87842	-305.40210	0.66592	0.58015	1.04321	0.5815973
0.07857	82.70404	201.12762	117.00410	377.32788	-318.81812	0.65937	0.56848	1.06651	0.5704417
0.08269	87.04364	198.64685	119.44322	380.77271	-324.34351	0.65603	0.56051	1.07441	0.5628415
0.08680	91.36322	195.74480	122.02951	383.92798	-329.68506	0.65210	0.55134	1.08139	0.5541591
0.09089	95.67558	192.09148	124.96976	386.47952	-334.65820	0.64713	0.54003	1.08651	0.5434619
0.09500	100.00000	187.53629	128.23613	388.42480	-339.32666	0.64075	0.52607	1.08959	0.5302488

X-VALUE	U	STAT PRESS	STAT TEMP	TOT PRESS	TOT TEMP	% AREA	EPS	RADC	RHO
0.13500	284.01538	1.08900	297.60889	1.66130	335.69995	0.0	5.84477	3.59698	1.2745304
0.13500	296.18262	1.10415	298.60229	1.66130	335.50000	5.11778	4.26765	-1.14621	1.2870543
0.13500	307.58105	1.11987	299.62792	1.66130	335.29980	4.99826	3.20688	-0.69369	1.3018217
0.13500	318.44287	1.13531	300.62036	1.66130	335.09985	4.92856	2.57652	-0.59568	1.3154202
0.13500	328.90942	1.15000	301.63452	1.66130	335.00000	4.91105	2.27049	-0.56934	1.3279581
0.13500	348.90234	1.17603	303.47485	1.66130	334.89990	9.82290	2.45379	-0.62190	1.3497734
0.13500	367.83398	1.19717	304.93042	1.66130	334.79980	9.83575	2.98639	-0.78725	1.3674879
0.13500	385.86914	1.21371	306.30908	1.66130	335.00000	9.85340	3.31563	-1.12025	1.3801374
0.13500	403.12061	1.22589	307.81909	1.66130	335.69995	9.86630	3.61008	-3.17589	1.3870468
0.13500	419.70190	1.23425	309.61987	1.66130	337.00000	9.88969	4.04075	6.17544	1.3884869
0.13500	435.82227	1.24107	311.67651	1.66130	338.69995	9.99705	4.74756	3.20696	1.3869486
0.13500	443.78687	1.24451	312.76123	1.66130	339.59985	5.07877	5.21445	4.12194	1.3860731
0.13500	451.71460	1.24876	313.89136	1.66130	340.50000	5.14671	5.77916	-219.08662	1.3856878
0.13500	459.62817	1.25298	315.09888	1.66130	341.39990	5.22909	6.44261	-2.22973	1.3861504
0.13500	467.56299	1.26067	316.50562	1.66130	342.39990	5.32483	7.20072	-0.92980	1.3873568

GAMMA	ETAP	DP/(PT-P)	DP/(PTR-P)	PO/PO	(PO/PO)T	TO/TO	(TO/TO)T
1.39893	0.0	-0.00062	-0.00091	1.00000	1.63917	0.99290	1.16562
1.39898	0.0	-0.02083	-0.02537	1.00000	1.63917	0.99762	1.16493
1.39901	0.0	-0.03376	-0.03517	1.00000	1.63917	1.00030	1.16424
1.39903	0.0	-0.04165	-0.03806	1.00000	1.63917	1.00119	1.16354
1.39903	0.0	-0.04574	-0.03740	1.00000	1.63917	1.00090	1.16319
1.39903	0.0	-0.04271	-0.02824	1.00000	1.63917	1.00090	1.16285
1.39904	0.0	-0.02953	-0.01619	1.00000	1.63917	1.00060	1.16250
1.39903	0.0	-0.01033	-0.00480	1.00000	1.63917	1.00119	1.16319
1.39901	0.0	0.01031	0.00416	1.00000	1.63917	1.00269	1.16562
1.39896	0.0	0.03107	0.01127	1.00000	1.63917	1.00387	1.17014
1.39884	0.0	0.05532	0.01901	1.00000	1.63917	1.00000	1.17604
1.39877	0.0	0.07099	0.02407	1.00000	1.63917	0.99677	1.17917
1.39870	0.0	0.09010	0.03027	1.00000	1.63917	0.99329	1.18229
1.39862	0.0	0.11379	0.03809	1.00000	1.63917	0.98928	1.18542
1.39854	0.0	0.14295	0.04797	1.00000	1.63917	0.98504	1.18889

STATION NUMBER 17 DOWNSTREAM OF STATOR 1

RADIUS	A STATIC	ALPHA RAD	ALPHA	A TOTAL	BETA	BETA RAD	V	VM	VP
0.14900	351.04883	75.58359	75.54189	367.18921	134.39975	134.30298	241.07835	233.49255	10.1584930
0.15452	351.12207	71.44212	71.40759	367.08543	134.41766	134.36046	239.73096	227.27419	14.3522396
0.15955	350.94043	67.51062	67.48325	366.58096	134.40652	134.36795	240.25426	221.98311	11.5093842
0.16531	350.77417	63.54648	63.52391	366.87378	134.59406	134.56575	240.64445	215.44818	9.5705709
0.17063	350.61182	60.82048	60.80266	366.81934	135.18226	135.16238	241.41249	210.77641	8.0479964
0.18110	350.60303	56.62856	56.61903	366.76514	137.19865	137.18718	241.06277	201.31694	5.6936255
0.19116	350.95609	57.09749	57.09061	366.71069	140.36475	140.35617	237.75562	201.62276	4.9879389
0.20065	351.60718	59.06927	59.05856	366.81958	143.10994	143.09830	234.04636	200.76257	5.8391762
0.20972	352.48022	59.83202	59.80786	367.15971	145.48274	145.45679	230.43095	199.22046	8.7633572
0.21846	353.64746	60.07008	60.02380	367.90308	147.53824	147.48984	227.08151	196.79716	12.0101366
0.22701	355.01099	58.75591	58.68579	368.81494	149.38469	149.31546	223.83553	191.37172	14.1899433
0.23125	355.71802	57.76994	57.68733	369.29517	150.28786	150.20901	222.10336	187.95648	14.9957809
0.23550	356.41479	56.70590	56.61266	369.77490	151.17633	151.09048	220.60851	184.39876	15.4986382
0.23974	357.08813	55.54645	55.44476	370.25293	152.04082	151.95049	219.18289	180.73500	15.7304211
0.24400	357.78491	54.20724	54.09840	370.79345	152.98312	152.79001	218.00285	176.83041	15.7874308

S-VALUE	% SPAN	VX	VU	W	WU	MV	MVX	MW	MVM
0.0	0.0	232.70523	60.00000	326.26343	-227.87964	0.68674	0.66289	0.92940	0.6651284
0.00552	5.81440	226.82057	76.29999	317.88599	-222.25641	0.68278	0.64599	0.90534	0.6472797
0.01095	11.52403	221.68454	91.89999	310.52490	-217.12982	0.68460	0.63169	0.88484	0.6325378
0.01631	17.17203	215.23550	107.20000	302.40549	-212.20699	0.68694	0.61360	0.86211	0.6142076
0.02163	22.76584	210.62271	117.70000	298.93115	-211.97456	0.68855	0.60073	0.85260	0.6011674
0.03210	33.79868	201.23640	132.59999	296.22632	-217.30528	0.68757	0.57397	0.84491	0.5742019
0.04216	44.37773	201.56105	126.00000	316.01660	-243.34082	0.67737	0.57425	0.90034	0.5744302
0.05165	54.36502	200.67764	120.29999	334.35669	-267.37402	0.66565	0.57074	0.95094	0.5709854
0.06072	63.91275	199.02762	115.79999	351.34204	-289.40015	0.65374	0.56465	0.99677	0.5651961
0.06946	73.11339	196.43034	113.29999	366.16895	-308.78906	0.64211	0.55544	1.03541	0.5564783
0.07801	82.11188	190.84491	116.09999	375.01001	-322.50488	0.63050	0.53757	1.05633	0.5390586
0.08225	86.58326	187.35732	118.50000	378.30615	-328.31079	0.62463	0.52670	1.06350	0.5283861
0.08650	91.05020	183.74628	121.09999	381.44019	-333.90698	0.61897	0.51554	1.07021	0.5173712
0.09074	95.51858	180.04915	124.00000	384.35132	-339.20630	0.61381	0.50421	1.07635	0.5061355
0.09500	100.00000	176.12425	127.50000	386.72314	-343.92725	0.60931	0.49226	1.08088	0.4942366

X-VALUE	U	STAT PRESS	STAT TEMP	TOT PRESS	TOT TEMP	% AREA	EPS	RADC	RHO
0.15500	287.87964	1.19186	306.83594	1.63360	335.69995	0.0	4.70652	-0.39128	1.3529663
0.15500	298.55640	1.19899	306.95313	1.63770	335.50000	4.49061	3.62061	-1.37416	1.3605366
0.15500	309.03882	1.20219	306.62866	1.64470	335.29980	4.56874	2.07201	2.18976	1.3656158
0.15500	319.40698	1.20374	306.33472	1.64890	335.09985	4.67450	2.54601	0.91342	1.3686976
0.15500	329.67456	1.20510	306.05078	1.65440	335.00000	4.78165	2.18821	0.77097	1.3715000
0.15500	349.90527	1.21117	306.03418	1.66130	334.89990	9.86521	1.62065	1.39640	1.3784819
0.15500	369.34082	1.22200	306.72070	1.66130	334.79980	10.03018	1.41758	-6.58583	1.3976982
0.15500	387.67407	1.23441	307.79028	1.66130	335.00000	9.95694	1.66668	-1.75364	1.3969240
0.15500	405.20020	1.24696	309.32544	1.66130	335.69995	9.96957	2.52115	-1.32710	1.4041204
0.15500	422.08911	1.25916	311.38916	1.66130	337.00000	10.02412	3.40882	-1.17968	1.4084606
0.15500	438.60498	1.27128	313.82104	1.66130	338.69995	10.19975	4.25230	-1.01003	1.4110003
0.15500	446.81079	1.27739	315.08765	1.66130	339.59985	5.21399	4.57611	-1.00390	1.4120741
0.15500	455.00708	1.28326	316.33936	1.66130	340.50000	5.30510	4.82137	-1.19507	1.4129543
0.15500	463.20620	1.28859	317.55396	1.66130	341.39990	5.40394	4.99310	-2.00883	1.4134016
0.15500	471.42725	1.29322	318.81348	1.66130	342.39990	5.51567	5.12219	-19.41037	1.4129809

GAMMA	STAGE EFF	DP/(PT-P)	DP/(QTR-P)	PO/PO	(PO/PO)T	TO/TO	(TO/TO)T	P/P	V/V
1.39893	0.88923	0.17973	0.25378	0.98333	1.61184	1.00000	1.16562	1.09445	0.8704969
1.39898	0.89730	0.17023	0.19872	0.98570	1.61589	1.00000	1.16493	1.08590	0.8795897
1.39901	0.90893	0.15205	0.15286	0.99001	1.62279	1.00000	1.16424	1.07351	0.8965176
1.39903	0.91732	0.13010	0.11570	0.99254	1.62694	1.00000	1.16354	1.06027	0.9133844
1.39903	0.92542	0.10776	0.08640	0.99585	1.63236	1.00000	1.16319	1.04791	0.9314737
1.39903	0.93513	0.07241	0.04748	1.00000	1.63917	1.00000	1.16285	1.02988	0.9584143
1.39904	0.93699	0.05349	0.02914	1.00000	1.63917	1.00000	1.16250	1.02074	0.9695672
1.39903	0.93328	0.04626	0.02124	1.00000	1.63917	1.00000	1.16319	1.01706	0.9739439
1.39901	0.92055	0.04859	0.01918	1.00000	1.63917	1.00000	1.16562	1.01726	0.9726101
1.39896	0.89789	0.05833	0.02035	1.00000	1.63917	1.00000	1.17014	1.02018	0.9671502
1.39884	0.86998	0.07189	0.02322	1.00000	1.63917	1.00000	1.17604	1.02434	0.9594991
1.39877	0.85595	0.07866	0.02466	1.00000	1.63917	1.00000	1.17917	1.02634	0.9556733
1.39870	0.84240	0.08264	0.02545	1.00000	1.63917	1.00000	1.18229	1.02763	0.9528862
1.39862	0.82931	0.08459	0.02512	1.00000	1.63917	1.00000	1.18542	1.02760	0.9521857
1.39854	0.81527	0.08126	0.02333	1.00000	1.63917	1.00000	1.18889	1.02582	0.9543042

STATION NUMBER 18 DOWNSTREAM OF STATOR 2

RADIUS	A STATIC	ALPHA BAR	ALPHA	A TOTAL	BETA	BETA BAR	V	VM	VP
0.15000	354.84204	89.99997	89.99997	367.18921	143.89447	143.89000	211.41179	211.41179	3.8374949
0.15573	355.06689	89.99997	89.99997	367.08643	145.28609	145.26767	208.59053	208.59053	7.7204123
0.16129	355.19189	89.99997	89.99997	366.98096	146.49246	146.45940	206.57738	206.57738	10.3362160
0.16669	355.19312	87.77005	87.76633	366.87378	146.85233	146.80850	205.60533	205.44965	11.8676310
0.17193	355.04712	83.43370	83.42151	366.81934	146.44881	146.39935	206.38023	205.02644	12.5374336
0.18200	354.67896	74.77477	74.75067	366.76514	145.83867	145.79453	209.05261	201.71510	11.6054792
0.19173	354.18359	68.05736	68.03123	366.71069	145.88692	145.85190	212.75040	197.33850	10.1170998
0.20120	353.89014	62.55692	62.52862	366.81958	146.47491	146.44318	216.11292	191.79436	9.4025707
0.21056	354.04346	58.23790	58.20807	367.19971	147.61568	147.58545	218.08817	185.42766	8.9439602
0.21966	354.90283	58.77913	58.74612	367.90308	149.27786	149.24519	217.03992	185.60732	9.4527912
0.22848	356.07251	57.63718	57.59482	368.91494	150.91383	150.87405	215.21529	181.78719	10.3865166
0.23285	356.71582	56.70050	56.64778	369.29517	151.76122	151.71335	214.01962	178.88026	11.3140602
0.23722	357.38208	55.57361	55.49811	369.77490	152.65231	152.58620	212.61295	175.37453	13.1622543
0.24160	358.06616	54.34749	54.22989	370.25293	153.58990	153.49095	211.02563	171.47250	15.9235163
0.24600	358.81445	52.96010	52.77824	370.78345	154.57433	154.42751	209.33040	167.00822	19.1277924

S-VALUE	% SPAN	VX	VU	W	WU	MV	MVX	MW	MVM
0.0	0.0	211.37695	0.0	359.72803	-289.91177	0.59579	0.59569	1.01095	0.5957912
0.00573	5.96611	208.44760	0.0	366.11353	-300.88062	0.58747	0.58707	1.03111	0.5874682
0.01129	11.75788	206.31862	0.0	373.87695	-311.62451	0.58159	0.58087	1.05260	0.5815937
0.01669	17.38425	205.10660	8.00000	375.29224	-314.06177	0.57896	0.57745	1.05659	0.5784167
0.02193	22.83992	204.64275	23.59999	370.48462	-308.58252	0.58128	0.57628	1.04348	0.5774626
0.03200	33.33667	201.38097	54.90000	358.82031	-296.75415	0.58941	0.56778	1.01168	0.5687259
0.04173	43.46487	197.07899	79.50000	351.55298	-290.94165	0.60068	0.55643	0.99257	0.5571644
0.05120	53.33360	191.56374	99.59999	346.97363	-289.14648	0.61068	0.54131	0.98046	0.5419601
0.06056	63.08051	185.21184	114.79999	345.92090	-292.02369	0.61509	0.52313	0.97706	0.5237426
0.06966	72.56689	185.36644	112.50000	362.96460	-311.91870	0.61155	0.52230	1.02271	0.5229806
0.07848	81.75446	181.49022	115.20000	373.49608	-326.25952	0.60441	0.50970	1.04899	0.5105342
0.08285	86.30682	178.52209	117.50000	377.47754	-332.40210	0.59997	0.50046	1.05820	0.5014643
0.08722	90.85325	174.87990	120.20000	380.90674	-338.13281	0.59492	0.48934	1.06582	0.4907200
0.09160	95.41162	170.73155	123.00000	384.17554	-343.78491	0.58935	0.47682	1.07292	0.4788849
0.09600	100.00000	165.99982	126.09999	387.11279	-349.19116	0.59342	0.46263	1.07897	0.4656953

X-VALUE	U	STAT PRESS	STAT TEMP	TOT PRESS	TOT TEMP	% AREA	EPS	RADC	RHO
0.17500	289.91177	1.27432	313.50269	1.61980	335.69995	0.0	1.04008	-0.38282	1.4158039
0.17500	300.88062	1.28254	313.88940	1.61980	335.50000	4.60608	2.12113	-0.54768	1.4231834
0.17500	311.62451	1.28831	314.10303	1.61980	335.29980	4.63656	2.86802	-0.78658	1.4286194
0.17500	322.06177	1.29211	314.10156	1.62120	335.09985	4.65988	3.31149	-1.27843	1.4328403
0.17500	332.18262	1.29411	313.84302	1.62670	335.00000	4.66510	3.50584	-4.22895	1.4362383
0.17500	351.65430	1.29373	313.19116	1.63640	334.89990	9.38158	3.29828	1.05371	1.4388046
0.17500	370.44165	1.29005	312.31641	1.64610	334.79980	9.55859	2.93871	0.56975	1.4387312
0.17500	388.74658	1.28636	311.80005	1.65440	335.00000	9.79213	2.81001	0.53904	1.4369860
0.17500	406.82373	1.28626	312.07520	1.66130	335.69995	10.13476	2.76469	0.89292	1.4356127
0.17500	424.41870	1.29085	313.60400	1.66130	337.00000	10.30618	2.91929	3.35277	1.4337063
0.17500	441.45972	1.29819	315.70044	1.66130	338.69995	10.39744	3.27541	-5.03172	1.4322824
0.17500	449.90210	1.30274	316.95791	1.66130	339.59985	5.30350	3.62634	-2.48320	1.4320526
0.17500	458.33301	1.30790	319.05908	1.66130	340.50000	5.39699	4.30423	-2.01744	1.4322977
0.17500	466.78491	1.31357	319.29590	1.66130	341.39990	5.51152	5.32836	-2.15137	1.4320319
0.17500	475.29126	1.31957	320.65088	1.66130	342.39990	5.64967	6.57308	-2.93135	1.4334011

GAMMA	STAGE EFF	DP/(PT-P)	DP/(PTP-P)	PO/PO	(PO/PO)T	TO/TO	(TO/TO)T	P/P	V/V
1.39892	0.0	0.19666	0.09271	0.99155	1.59822	1.00000	1.16562	1.06918	0.8769422
1.39898	0.0	0.19044	0.09945	0.98907	1.59822	1.00000	1.16493	1.06968	0.8700699
1.39901	0.0	0.19462	0.10798	0.98486	1.59822	1.00000	1.16424	1.07164	0.8598281
1.39903	0.0	0.19852	0.11768	0.98320	1.59961	1.00000	1.16354	1.07341	0.8543946
1.39903	0.0	0.19812	0.12154	0.98326	1.60503	1.00000	1.16319	1.07396	0.8548863
1.39903	0.0	0.18342	0.11458	0.98501	1.61460	1.00000	1.16285	1.06817	0.8672123
1.39904	0.0	0.15491	0.08054	0.99085	1.62417	1.00000	1.16250	1.05569	0.8948280
1.39903	0.0	0.12168	0.05335	0.99585	1.63236	1.00000	1.16319	1.04208	0.9233808
1.39901	0.0	0.09485	0.03560	1.00000	1.63917	1.00000	1.16562	1.03152	0.9464360
1.39896	0.0	0.07880	0.02586	1.00000	1.63917	1.00000	1.17014	1.02516	0.9557797
1.39884	0.0	0.06828	0.02068	1.00000	1.63917	1.00000	1.17604	1.02116	0.9614885
1.39877	0.0	0.06604	0.01907	1.00000	1.63917	1.00000	1.17917	1.01985	0.9632134
1.39870	0.0	0.06517	0.01816	1.00000	1.63917	1.00000	1.18229	1.01920	0.9637567
1.39862	0.0	0.06700	0.01806	1.00000	1.63917	1.00000	1.18542	1.01938	0.9627833
1.39854	0.0	0.07157	0.01879	1.00000	1.63917	1.00000	1.18889	1.02037	0.9602603

STATION NUMBER 19 DOWNSTREAM OF STATOR 3

RADIUS	A STATIC	ALPHA BAR	ALPHA	A TOTAL	BETA	BETA BAR	V	VM	VR
0.15000	356.45313	89.99997	89.99997	367.19921	145.74590	145.74562	197.35828	197.35828	-0.9665785
0.15587	356.39917	89.99997	89.99997	367.08643	146.84358	146.84326	196.87273	196.87273	1.0392685
0.16173	356.40430	89.99997	89.99997	366.98096	147.92680	147.92412	195.83182	195.83182	2.8031292
0.16731	356.43677	89.99997	89.99997	366.87378	148.96964	148.96291	194.51869	194.51869	4.4826288
0.17273	356.53125	89.99997	89.99997	366.81934	149.95541	149.94241	193.13246	193.13246	6.2425556
0.18317	356.74683	89.99997	89.99997	366.76514	151.72537	151.69385	190.60461	190.60461	9.7769928
0.19313	356.89541	89.99997	89.99997	366.71069	153.23184	153.18239	188.63597	188.63597	12.3427410
0.20263	356.91895	83.49572	83.46893	366.81958	153.09026	153.02994	189.51053	188.28699	13.5808525
0.21176	357.08740	75.64619	75.61247	367.19971	152.88754	152.83066	191.60361	185.62245	12.9710839
0.22067	357.53467	69.69011	69.64857	367.90308	153.15173	153.10037	194.18201	182.10957	12.1307592
0.22946	358.23096	63.45070	63.40277	368.81494	153.74760	153.70096	196.43512	175.72115	11.3482323
0.23389	358.65015	59.07948	59.03085	369.29517	154.29182	154.24872	197.14012	169.12285	10.4810190
0.23846	359.19458	54.11331	54.06682	369.77490	155.27144	155.23418	196.69601	159.35884	9.3081579
0.24317	359.84717	51.29864	51.24742	370.25293	156.37263	156.34164	195.23595	152.34392	8.2637949
0.24800	360.76416	49.24694	49.21199	370.78345	157.70834	157.68359	191.78897	145.28581	7.2030640

S-VALUE	% SPAN	VX	VU	W	WU	MV	MVX	MW	MVM
0.0	0.0	197.35591	0.0	350.62964	-289.81177	0.55367	0.55367	0.98366	0.5536724
0.00587	6.09172	196.86998	0.0	359.95874	-301.34937	0.55239	0.55239	1.00999	0.5523939
0.01173	11.96654	195.81175	0.0	368.76953	-312.47534	0.54947	0.54941	1.03469	0.5494654
0.01731	17.66103	194.46703	0.0	377.27197	-323.25952	0.54573	0.54559	1.05945	0.5457312
0.02273	23.19556	193.03154	0.0	385.59399	-333.74048	0.54170	0.54142	1.08151	0.5416985
0.03317	33.84218	190.35368	0.0	401.56460	-353.90039	0.53429	0.53358	1.12675	0.5342854
0.04313	44.00890	188.23174	0.0	418.12109	-373.15112	0.52854	0.52741	1.17154	0.5285410
0.05263	53.70523	187.79657	21.50000	415.16333	-370.01172	0.53096	0.52616	1.16319	0.5275342
0.06176	63.02431	185.16864	47.50000	406.51221	-361.65796	0.53657	0.51855	1.13841	0.5199236
0.07067	72.11116	181.70509	67.39999	402.51563	-358.96362	0.54311	0.50822	1.12581	0.5093480
0.07946	81.08026	175.35432	87.79999	396.59888	-355.54590	0.54835	0.48950	1.10710	0.4905247
0.08389	85.60327	168.79776	101.29999	389.26660	-350.60815	0.54967	0.47065	1.08537	0.4715538
0.08846	90.26210	159.08676	115.29999	380.41309	-345.42578	0.54760	0.44290	1.05907	0.4436560
0.09317	95.07573	152.11961	122.09999	379.64307	-347.73584	0.54255	0.42273	1.05501	0.4233572
0.09800	100.00000	145.10713	125.20000	382.61230	-353.95532	0.53162	0.40222	1.06056	0.4027169

X-VALUE	U	STAT PRESS	STAT TEMP	TOT PRESS	TOT TEMP	% AREA	EPS	RADC	RHO
0.19500	289.81177	1.31545	316.35571	1.61980	335.69995	0.0	-0.28061	-28.10246	1.4483232
0.19500	301.34937	1.31667	316.24902	1.61980	335.50000	4.69313	0.30246	-1.54166	1.4501524
0.19500	312.47534	1.31947	316.25098	1.61980	335.29980	4.68948	0.82016	-0.99382	1.4532280
0.19500	323.25952	1.32303	316.20493	1.61980	335.09985	4.70776	1.32049	-0.84670	1.4569054
0.19500	333.74048	1.32687	316.47192	1.61980	335.00000	4.72954	1.85227	-0.80693	1.4603586
0.19500	353.90039	1.33389	316.85352	1.61980	334.89990	9.52034	2.94026	-0.94389	1.4663134
0.19500	373.15112	1.33929	317.12427	1.61980	334.79980	9.61226	3.75163	-1.30899	1.4709969
0.19500	391.51172	1.34271	317.16040	1.62670	335.00000	9.64176	4.13625	-2.52781	1.4745884
0.19500	409.15796	1.34423	317.46460	1.63500	335.69995	9.70294	4.00731	6.35978	1.4748363
0.19500	426.36377	1.34485	318.27246	1.64340	337.00000	9.87299	3.81944	2.02254	1.4717751
0.19500	443.34595	1.34449	319.53931	1.65160	338.69995	10.14391	3.70279	2.83333	1.4677296
0.19500	451.90820	1.34853	320.30371	1.65580	339.59985	5.26569	3.55306	-16.14482	1.4665556
0.19500	460.72583	1.35287	321.29321	1.65950	340.50000	5.52912	3.34856	-0.97334	1.4666319
0.19500	469.83594	1.36010	322.47998	1.66130	341.39990	5.82510	3.10950	-0.39031	1.4690485
0.19500	479.15552	1.37072	324.14478	1.66130	342.39990	6.07705	2.84181	-0.22353	1.4729137

GAMMA	STAGE EFF	DP/(PT-P)	DP/(PTR-P)	PO/PO	(PO/PO)T	TO/TO	(TO/TO)T	P/P	V/V
1.39893	0.0	0.11906	0.03521	1.00000	1.59822	1.00000	1.16562	1.03228	0.9335254
1.39898	0.0	0.10120	0.02763	1.00000	1.59822	1.00000	1.16403	1.02661	0.9438239
1.39901	0.0	0.09328	0.02384	1.00000	1.59822	1.00000	1.16424	1.02418	0.9479828
1.39903	0.0	0.09395	0.02337	0.99914	1.59822	1.00000	1.16354	1.02393	0.9460780
1.39903	0.0	0.09849	0.02551	0.99576	1.59822	1.00000	1.16319	1.02531	0.9358089
1.39902	0.0	0.11718	0.03380	0.98986	1.59822	1.00000	1.16285	1.03104	0.9117543
1.39904	0.0	0.13829	0.04357	0.98402	1.59822	1.00000	1.16250	1.03817	0.8866539
1.39903	0.0	0.15311	0.05154	0.98326	1.60503	1.00000	1.16319	1.04381	0.8769010
1.39901	0.0	0.15455	0.05347	0.98417	1.61322	1.00000	1.16562	1.04506	0.8785603
1.39896	0.0	0.14577	0.04434	0.98922	1.62151	1.00000	1.17014	1.04183	0.8946834
1.39884	0.0	0.13303	0.03702	0.99416	1.62960	1.00000	1.17604	1.03721	0.9127377
1.39877	0.0	0.12800	0.03428	0.99669	1.63375	1.00000	1.17917	1.03523	0.9211310
1.39870	0.0	0.12725	0.03286	0.99831	1.63641	1.00000	1.18229	1.03438	0.9251266
1.39862	0.0	0.13383	0.03329	1.00000	1.63917	1.00000	1.18542	1.03543	0.9251764
1.39854	0.0	0.14968	0.03592	1.00000	1.63917	1.00000	1.18889	1.03876	0.9161624

STATION NUMBER 20 DOWNSTREAM OF STATOR 4

RADIUS	A STATIC	ALPHA BAR	ALPHA	A TOTAL	BETA	BETA BAR	V	VM	VR
0.15000	357.52734	89.99997	89.99997	367.18921	147.11745	147.11740	187.36256	187.36256	0.2695813
0.15617	357.40088	89.99997	89.99997	367.08643	148.13799	148.13695	187.54880	187.54880	1.6701412
0.16211	357.28149	89.99997	89.99997	366.98096	149.07646	149.07339	187.64789	187.64789	2.9161844
0.16783	357.17456	89.99997	89.99997	366.87378	149.95259	149.94717	187.61234	187.61234	3.9193983
0.17336	357.14038	89.99997	89.99997	366.81934	150.78073	150.77319	187.40672	187.40672	4.6496964
0.18396	357.21924	89.99997	89.99997	366.76514	152.37178	152.36145	186.11627	186.11627	5.5156155
0.19404	357.40723	89.99997	89.99997	366.71069	153.90163	153.88922	183.75307	183.75307	6.0790310
0.20372	357.80908	89.99997	89.99997	366.81958	155.33406	155.31696	180.90147	180.90147	7.1678419
0.21307	358.47046	89.99997	89.99997	367.19971	156.62065	156.59557	178.19008	178.19008	8.7239094
0.22215	359.42358	89.99997	89.99997	367.90308	157.75441	157.72353	175.83438	175.83438	9.7396412
0.23096	360.38721	85.09819	85.09097	368.81494	157.95242	157.92291	175.54716	174.90514	9.5120106
0.23526	360.84058	81.07417	81.06378	369.29517	157.88493	157.86122	175.95352	173.82275	8.4445906
0.23952	361.28076	76.96732	76.95961	369.77490	157.88931	157.87714	176.49203	171.94592	6.0134153
0.24375	361.71924	72.57933	72.57785	370.25293	157.99646	157.99472	177.02972	168.90981	2.2256823
0.24800	362.25513	69.30307	69.30112	370.78345	159.31082	158.30875	177.12463	165.69362	-2.4083309

S-VALUE	% SPAN	VX	VU	W	WU	MV	MVX	MW	MVM
0.0	0.0	187.36237	0.0	345.10205	-289.81177	0.52405	0.52405	0.96525	0.5240510
0.00617	6.30088	187.54135	0.0	355.28003	-301.74390	0.52476	0.52474	0.99407	0.5247575
0.01211	12.35428	187.62521	0.0	365.11694	-313.20703	0.52521	0.52515	1.02193	0.5252102
0.01783	18.19261	187.57138	0.0	374.62646	-324.26318	0.52527	0.52515	1.04886	0.5252679
0.02336	23.83966	187.34903	0.0	383.81982	-334.95728	0.52474	0.52458	1.07470	0.5247424
0.03396	34.64812	186.03453	0.0	401.20581	-355.42505	0.52101	0.52079	1.12314	0.5210141
0.04404	44.93684	183.65248	0.0	417.51831	-374.90845	0.51413	0.51385	1.16819	0.5141280
0.05372	54.81644	180.75940	0.0	433.19556	-393.61548	0.50558	0.50518	1.21069	0.5055810
0.06307	64.36055	177.97639	0.0	448.59473	-411.68628	0.49708	0.49649	1.25141	0.4970944
0.07215	73.62743	175.56442	0.0	463.84985	-429.23071	0.48921	0.48846	1.29054	0.4892121
0.08096	82.60875	174.64629	15.00000	465.35425	-431.23413	0.48711	0.48461	1.29126	0.4853256
0.08526	86.99852	173.61751	27.29999	461.25073	-427.24463	0.48762	0.48115	1.27927	0.4817162
0.08952	91.34204	171.84073	39.79999	456.58154	-422.96729	0.48852	0.47564	1.26379	0.4759343
0.09375	95.66819	168.89514	53.00000	450.79712	-417.95630	0.48941	0.46692	1.24626	0.4669638
0.09800	100.00000	165.67612	62.59999	448.29980	-416.55542	0.48995	0.45735	1.23752	0.4573948

X-VALUE	U	STAT PRESS	STAT TEMP	TOT PRESS	TOT TEMP	% AREA	EPS	RADC	RHO
0.21500	289.81177	1.34351	318.26563	1.61980	335.69995	0.0	0.08244	4.03920	1.4703398
0.21500	301.74390	1.34284	318.02930	1.61980	335.50000	4.84717	0.51023	4.90601	1.4707003
0.21500	313.20703	1.34241	317.80981	1.61980	335.29980	4.84093	0.80045	8.28051	1.4712467
0.21500	324.26318	1.34236	317.61597	1.61980	335.09985	4.83989	1.19705	-37.92952	1.4720840
0.21500	334.95728	1.34285	317.55420	1.61980	335.00000	4.84103	1.42170	-3.87691	1.4729071
0.21500	355.42505	1.34632	317.69336	1.61980	334.80000	9.70365	1.69823	-1.11580	1.4760733
0.21500	374.90845	1.35271	318.02759	1.61980	334.79980	9.77153	1.80584	-0.69820	1.4815187
0.21500	393.61548	1.36058	318.74438	1.61980	335.00000	9.87359	2.27082	-0.59226	1.4867802
0.21500	411.68628	1.36932	319.92847	1.61980	335.69995	9.99477	2.80623	-0.61022	1.4897108
0.21500	429.23071	1.37543	321.64429	1.61980	337.00000	10.13369	3.17530	-0.62402	1.4894676
0.21500	446.23413	1.38202	323.39746	1.62530	338.69995	10.22498	3.11750	-0.61633	1.4884825
0.21500	454.54468	1.38505	324.22827	1.62940	339.59985	5.14215	2.78462	-0.64604	1.4879255
0.21500	462.76733	1.38782	325.03638	1.63360	340.50000	5.18140	2.00420	-0.71100	1.4871950
0.21500	470.95630	1.39050	325.84399	1.63770	341.39990	5.25300	0.75499	-0.80774	1.4863768
0.21500	479.15552	1.39340	326.82959	1.64060	342.39990	5.35222	-0.83281	-0.92024	1.4849796

GAMMA	STAGE EFF	DP/(PT-P)	DP/(PTR-P)	PO/PO	(PO/PO)T	TO/TO	(TO/TO)T	P/P	V/V
1.39893	0.0	0.09220	0.02490	1.00000	1.59822	1.00000	1.16562	1.02133	0.9493524
1.39898	0.0	0.08634	0.02174	1.00000	1.59822	1.00000	1.16493	1.01988	0.9526398
1.39901	0.0	0.07640	0.01790	1.00000	1.59822	1.00000	1.16424	1.01739	0.9582094
1.39903	0.0	0.06512	0.01420	1.00000	1.59822	1.00000	1.16354	1.01461	0.9644951
1.39903	0.0	0.05454	0.01109	1.00000	1.59822	1.00000	1.16319	1.01204	0.9703533
1.39903	0.0	0.04350	0.00773	1.00000	1.59822	1.00000	1.16285	1.00932	0.9764521
1.39904	0.0	0.04785	0.00750	1.00000	1.59822	1.00000	1.16250	1.01002	0.9741147
1.39903	0.0	0.06290	0.01015	0.99576	1.59822	1.00000	1.16319	1.01330	0.9545721
1.39901	0.0	0.08287	0.01446	0.99070	1.59822	1.00000	1.16562	1.01792	0.9299933
1.39896	0.0	0.10245	0.01889	0.98554	1.59822	1.00000	1.17014	1.02274	0.9055132
1.39884	0.0	0.11644	0.02288	0.98408	1.60365	1.00000	1.17604	1.02638	0.8936648
1.39877	0.0	0.11356	0.02464	0.98406	1.60770	1.00000	1.17917	1.02700	0.8925302
1.39870	0.0	0.11435	0.02509	0.98499	1.61184	1.00000	1.18229	1.02583	0.8972832
1.39862	0.0	0.10093	0.02192	0.98579	1.61589	1.00000	1.18542	1.02235	0.9067476
1.39854	0.0	0.07804	0.01601	0.98754	1.61875	1.00000	1.18889	1.01654	0.9235392

STATION NUMBER 21 DOWNSTREAM OF STATOR 5

RADIUS	A STATIC	ALPHA BAR	ALPHA	A TOTAL	BETA	BETA BAR	V	VM	VR
0.15000	357.88794	89.99997	89.99997	367.18921	147.60567	147.60567	183.87982	183.87982	-0.0647919
0.15626	357.80615	89.99997	89.99997	367.08642	148.69101	148.69096	183.63338	183.63338	0.4271557
0.16229	357.73438	89.99997	89.99997	366.98096	149.69435	149.69402	183.27248	183.27248	0.9159402
0.16810	357.66943	89.99997	89.99997	366.87378	150.62576	150.62505	182.82623	182.82623	1.4021158
0.17373	357.66040	89.99997	89.99997	366.81924	151.48653	151.48521	182.36720	182.36720	1.8947868
0.18450	357.69189	89.99997	89.99997	366.76514	153.01857	153.01578	181.50826	181.50826	2.8065958
0.19470	357.71289	89.99997	89.99997	366.71069	154.34084	154.33685	180.74690	180.74690	3.4068441
0.20442	357.89453	89.99997	89.99997	366.81958	155.49706	155.49312	180.05258	180.05258	3.4361267
0.21373	358.36328	89.99997	89.99997	367.19971	156.53699	156.53426	179.26534	179.26534	2.8837843
0.22271	359.17310	89.99997	89.99997	367.90308	157.48453	157.48332	178.38026	178.38026	1.9510231
0.23139	360.19287	89.99997	89.99997	368.81494	158.34196	158.34163	177.53531	177.53531	1.0704622
0.23564	360.72192	89.99997	89.99997	369.29517	158.73659	158.73642	177.17015	177.17015	0.7765324
0.23982	361.23657	89.99997	89.99997	369.77490	159.09929	159.09914	176.94559	176.94559	0.6857677
0.24394	361.72241	89.99997	89.99997	370.25293	159.41721	159.41704	176.99593	176.99593	0.6971716
0.24800	362.22070	89.99997	89.99997	370.78345	159.67577	159.67566	177.47614	177.47614	0.6323630

S-VALUE	% SPAN	VX	VU	W	WU	MV	MVX	MW	MVM
0.0	0.0	183.87981	0.0	343.22388	-289.81177	0.51379	0.51379	0.95903	0.5137916
0.00626	6.39199	183.63287	0.0	353.37622	-301.91650	0.51322	0.51322	0.98762	0.5132203
0.01229	12.53978	183.27019	0.0	363.19092	-313.55859	0.51231	0.51231	1.01525	0.5123144
0.01810	18.47427	182.82085	0.0	372.71729	-324.79663	0.51116	0.51114	1.04207	0.5111598
0.02373	24.21767	182.35736	0.0	382.01294	-335.67261	0.50989	0.50986	1.06809	0.5098892
0.03450	35.20268	181.48656	0.0	400.02295	-356.47339	0.50744	0.50738	1.11834	0.5074430
0.04470	45.61179	180.71478	0.0	417.35303	-376.18359	0.50529	0.50520	1.16673	0.5052848
0.05442	55.53004	180.01979	0.0	434.06836	-394.96387	0.50309	0.50300	1.21284	0.5030884
0.06373	65.03346	179.24214	0.0	450.18921	-412.95801	0.50023	0.50017	1.25674	0.5002335
0.07271	74.18996	178.36960	0.0	465.80371	-430.29468	0.49664	0.49661	1.29688	0.4966415
0.08139	83.05183	177.53299	0.0	481.03247	-447.07202	0.49299	0.49288	1.33549	0.4928895
0.08564	87.38400	177.16844	0.0	488.53149	-455.27344	0.49115	0.49115	1.35432	0.4911544
0.08982	91.65285	176.94426	0.0	495.99097	-463.35449	0.48983	0.48983	1.37304	0.4898329
0.09394	95.85881	176.99455	0.0	503.45459	-471.31641	0.48931	0.48931	1.39183	0.4893142
0.09800	100.00000	177.47501	0.0	510.96753	-479.15552	0.48997	0.48996	1.41065	0.4899668

X-VALUE	U	STAT PRESS	STAT TEMP	TOT PRESS	TOT TEMP	% AREA	EPS	RADC	RHO
0.24000	289.81177	1.35304	318.90771	1.61980	335.69995	0.0	-0.02019	-10.36648	1.4777880
0.24000	301.91650	1.35356	318.75122	1.61980	335.50000	4.91969	0.13328	-4.62942	1.4790812
0.24000	313.55859	1.35439	318.61597	1.61980	335.29999	4.92059	0.28635	-3.11482	1.4806175
0.24000	324.79663	1.35545	318.49658	1.61980	335.09985	4.92643	0.43041	-2.52531	1.4823351
0.24000	335.67261	1.35662	318.47998	1.61980	335.00000	4.93294	0.59531	-2.32864	1.4836903
0.24000	356.47339	1.35887	318.53491	1.61980	334.89990	9.88740	0.88598	-2.47211	1.4858904
0.24000	376.18359	1.36085	318.57178	1.61980	334.79980	9.91735	1.08002	-2.67810	1.4878807
0.24000	394.96387	1.36285	318.89648	1.61980	335.00000	9.94616	1.09350	-2.14583	1.4885597
0.24000	412.95801	1.36546	319.73755	1.61980	335.69995	9.98461	0.92174	-1.45036	1.4874930
0.24000	430.29468	1.36873	321.19629	1.61980	337.00000	10.04082	0.62668	-1.17021	1.4842749
0.24000	447.07202	1.37214	323.04883	1.61980	338.69995	10.11092	0.34547	-1.16488	1.4794388
0.24000	455.27344	1.37372	324.01514	1.61980	339.59985	5.08351	0.25113	-1.29184	1.4767208
0.24000	463.35449	1.37492	324.95679	1.61980	340.50000	5.09962	0.22206	-1.95147	1.4737272
0.24000	471.31641	1.37529	325.84985	1.61980	341.39990	5.11227	0.22568	-28.14140	1.4701986
0.24000	479.15552	1.37482	326.76782	1.61980	342.39990	5.11865	0.20415	1.58335	1.4654570

GAMMA	STAGE EFF	DP/(PT-P)	DP/(PTP-P)	PO/PO	(PO/PO)T	TO/TO	(TO/TO)T	P/P	V/V
1.39893	0.0	0.03449	0.00867	1.00000	1.59822	1.00000	1.16562	1.00709	0.9814117
1.39898	0.0	0.03870	0.00908	1.00000	1.59822	1.00000	1.16493	1.00798	0.9791232
1.39901	0.0	0.04318	0.00947	1.00000	1.59822	1.00000	1.16424	1.00892	0.9766828
1.39903	0.0	0.04720	0.00971	1.00000	1.59822	1.00000	1.16354	1.00976	0.9744894
1.39902	0.0	0.04973	0.00960	1.00000	1.59822	1.00000	1.16319	1.01026	0.9731091
1.39902	0.0	0.04597	0.00778	1.00000	1.59822	1.00000	1.16285	1.00932	0.9752412
1.39904	0.0	0.03045	0.00453	1.00000	1.59822	1.00000	1.16250	1.00601	0.9836401
1.39903	0.0	0.00879	0.00115	1.00000	1.59822	1.00000	1.16319	1.00167	0.9953074
1.39901	0.0	-0.01138	-0.00131	1.00000	1.59822	1.00000	1.16562	0.99791	1.0060339
1.39896	0.0	-0.02744	-0.00281	1.00000	1.59822	1.00000	1.17014	0.99513	1.0144787
1.39884	0.0	-0.04060	-0.00411	0.99662	1.59822	1.00000	1.17604	0.99285	1.0113249
1.39877	0.0	-0.04639	-0.00485	0.99411	1.59822	1.00000	1.17917	0.99182	1.0069141
1.39870	0.0	-0.05250	-0.00568	0.99155	1.59822	1.00000	1.18229	0.99070	1.0025692
1.39862	0.0	-0.06113	-0.00689	0.98907	1.59822	1.00000	1.18542	0.98913	0.9998090
1.39854	0.0	-0.07516	-0.00862	0.98732	1.59822	1.00000	1.18889	0.98667	1.0019836

STATION NUMBER 22 DUMMY

RADIUS	A STATIC	ALPHA BAR	ALPHA	A TOTAL	BETA	BETA BAR	V	VM	VR
0.15000	358.19116	89.99997	89.99997	367.19702	148.01904	148.01904	180.96040	180.96040	0.0212545
0.15633	358.08022	89.99997	89.99997	367.08887	149.07350	149.07339	180.95815	180.95815	0.4982136
0.16241	357.97070	89.99997	89.99997	366.98071	150.03105	150.03072	180.94122	180.94122	0.8832701
0.16827	357.86450	89.99997	89.99997	366.87231	150.90869	150.90820	180.89214	180.89214	1.1569118
0.17393	357.81714	89.99997	89.99997	366.81836	151.71799	151.71733	180.81126	180.81126	1.3302326
0.18474	357.80127	89.99997	89.99997	366.76416	153.18571	153.18495	180.41592	180.41592	1.4764080
0.19496	357.81470	89.99997	89.99997	366.70996	154.40417	154.40335	179.72661	179.72661	1.5327530
0.20471	357.99219	89.99997	89.99997	366.81836	155.64294	155.64191	179.06514	179.06514	1.6853523
0.21402	358.40918	89.99997	89.99997	367.19702	156.62070	156.61951	178.78384	178.78384	1.8083036
0.22299	359.10254	89.99997	89.99997	367.89917	157.43306	157.43185	179.05779	179.05779	1.9769096
0.23161	359.97144	89.99997	89.99997	368.81404	158.11417	158.11330	179.77165	179.77165	1.6799831
0.23581	360.42529	89.99997	89.99997	369.29883	158.42053	158.42000	180.20313	180.20313	1.3359737
0.23994	360.88403	89.99997	89.99997	369.78223	158.71751	158.71735	180.58023	180.58023	0.8471673
0.24400	361.35547	89.99997	89.99997	370.26489	159.01488	159.01488	180.82262	180.82262	0.2867502
0.24800	361.85624	89.99997	89.99997	370.80029	159.31523	159.31523	180.91196	180.91196	-0.2148188

S-VALUE	% SPAN	VX	VU	W	WU	MV	MVX	MW	MVM
0.0	0.0	180.96040	0.0	341.66870	-289.81177	0.50521	0.50521	0.95387	0.5052062
0.00633	6.45834	180.95746	0.0	352.10034	-302.04102	0.50536	0.50535	0.98330	0.5053563
0.01241	12.66209	180.93997	0.0	362.21924	-313.78833	0.50546	0.50546	1.01197	0.5054637
0.01827	18.64024	180.88843	0.0	372.04517	-325.10864	0.50548	0.50547	1.03063	0.5054766
0.02393	24.41679	180.80637	0.0	381.60205	-336.04688	0.50532	0.50530	1.06647	0.5053174
0.03474	35.44542	180.40988	0.0	399.93652	-356.93042	0.50423	0.50422	1.11776	0.5042350
0.04496	45.88213	179.72006	0.0	417.37158	-376.69263	0.50229	0.50227	1.16645	0.5022806
0.05471	55.82346	179.05721	0.0	434.16260	-395.51587	0.50019	0.50017	1.21277	0.5001928
0.06403	65.33873	178.77377	0.0	450.52417	-413.53174	0.49883	0.49880	1.25701	0.4988260
0.07299	74.47752	179.04688	0.0	466.56152	-430.93398	0.49863	0.49860	1.29924	0.4986258
0.08161	83.27815	179.76379	0.0	482.25562	-447.49609	0.49941	0.49938	1.33970	0.4994053
0.08581	87.56178	180.19817	0.0	489.94922	-455.60645	0.49997	0.49996	1.35936	0.4999735
0.08994	91.77290	180.57825	0.0	497.50854	-463.57910	0.50038	0.50038	1.37858	0.5003830
0.09400	95.91682	180.82239	0.0	504.91406	-471.42480	0.50040	0.50040	1.39778	0.5004000
0.09800	100.00000	180.91193	0.0	512.17090	-479.15552	0.49990	0.49990	1.41524	0.4999000

K-VALUE	U	STAT PRESS	STAT TEMP	TOT PRESS	TOT TEMP	% AREA	EPS	RADC	RHO
0.26000	289.81177	1.36093	319.43506	1.61980	335.69995	0.0	0.00673	20.95042	1.4839468
0.26000	302.04102	1.36079	319.23511	1.61980	335.50000	4.97090	0.15775	21.18242	1.4847240
0.26000	313.78833	1.36069	319.03760	1.61980	335.29980	4.96827	0.27069	33.81331	1.4855337
0.26000	325.10864	1.36067	318.84619	1.61980	335.09985	4.96693	0.36644	-73.01695	1.4864130
0.26000	336.04688	1.36082	318.76074	1.61980	335.00000	4.96660	0.42153	-11.48854	1.4869680
0.26000	356.93042	1.36181	318.73145	1.61980	334.99990	9.93865	0.46888	-3.58062	1.4881868
0.26000	376.69263	1.36358	318.75464	1.61980	334.79980	9.95685	0.48864	-2.35529	1.4900188
0.26000	395.51587	1.36550	319.07300	1.61980	335.00000	9.98308	0.53927	-2.53662	1.4906197
0.26000	413.53174	1.36674	319.82397	1.61980	335.69995	10.01109	0.60840	-5.46046	1.4884706
0.26000	430.83398	1.36693	321.07690	1.61980	337.00000	10.03476	0.63259	12.20694	1.4828787
0.26000	447.49609	1.36624	322.65210	1.61980	338.69995	10.05218	0.53544	4.11967	1.4748869
0.26000	455.60645	1.36573	323.47607	1.61980	339.59985	5.03082	0.42478	4.23980	1.4705811
0.26000	463.57910	1.36536	324.31006	1.61980	340.50000	5.03376	0.26880	9.36830	1.4664068
0.26000	471.42480	1.36535	325.16772	1.61980	341.39990	5.03867	0.00986	-8.23304	1.4625202
0.26000	479.15552	1.36582	326.15308	1.61980	342.39990	5.04751	-0.06803	-2.63507	1.4586049

GAMMA	ETAP	DP/(PT-P)	DP/(PTR-P)	PO/PO	(PO/PO)T	TO/TO	(TO/TO)T
1.39899	0.0	0.02956	0.00724	1.00000	1.59822	1.00000	1.16562
1.39900	0.0	0.02714	0.00617	1.00000	1.59822	1.00000	1.16493
1.39901	0.0	0.02372	0.00502	1.00000	1.59822	1.00000	1.16424
1.39902	0.0	0.01975	0.00389	1.00000	1.59822	1.00000	1.16354
1.39902	0.0	0.01594	0.00294	1.00000	1.59822	1.00000	1.16319
1.39903	0.0	0.01126	0.00183	1.00000	1.59822	1.00000	1.16285
1.39903	0.0	0.01057	0.00152	1.00000	1.59822	1.00000	1.16250
1.39902	0.0	0.01028	0.00132	1.00000	1.59822	1.00000	1.16319
1.39899	0.0	0.00505	0.00058	1.00000	1.59822	1.00000	1.16562
1.39893	0.0	-0.00715	-0.00075	1.00000	1.59822	1.00000	1.17014
1.39884	0.0	-0.02383	-0.00226	1.00000	1.59822	1.00000	1.17604
1.39880	0.0	-0.03245	-0.00293	1.00000	1.59822	1.00000	1.17917
1.39876	0.0	-0.03901	-0.00337	1.00000	1.59822	1.00000	1.18229
1.39871	0.0	-0.04108	-0.00340	1.00000	1.59822	1.00000	1.18542
1.39867	0.0	-0.03675	-0.00294	1.00000	1.59822	1.00000	1.18889

STATION NUMBER 23   DUMMY

RADIUS	A STATIC	ALPHA BAR	ALPHA	A TOTAL	BETA	BETA BAR	V	VM	VR
0.15000	358.31177	89.99997	89.99997	367.19702	148.19023	148.19023	179.75906	179.75906	0.0
0.15626	358.20630	89.99997	89.99997	367.09887	149.25345	149.25345	179.70229	179.70229	0.1638797
0.16246	358.10083	89.99997	89.99997	366.98071	150.21666	150.21661	179.64723	179.64723	0.3244463
0.16835	357.99512	89.99997	89.99997	366.87231	151.09491	151.09486	179.59204	179.59204	0.4734954
0.17403	357.94238	89.99997	89.99997	366.81836	151.89650	151.89635	179.56453	179.56453	0.6082769
0.18487	357.88565	89.99997	89.99997	366.76416	153.31483	153.31462	179.53531	179.53531	0.8132778
0.19511	357.83651	89.99997	89.99997	366.70996	154.53777	154.53749	179.50606	179.50606	0.8830458
0.20484	357.94263	89.99997	89.99997	366.81836	155.59660	155.59639	179.56122	179.56122	0.8030497
0.21414	358.31201	89.99997	89.99997	367.19702	156.51628	156.51617	179.75577	179.75577	0.6153533
0.22305	358.99707	89.99997	89.99997	367.89917	157.31825	157.31821	180.11363	180.11363	0.3936383
0.23165	359.89063	89.99997	89.99997	368.81494	158.02696	158.02690	180.58224	180.58224	0.2070187
0.23583	360.36279	89.99997	89.99997	369.29883	158.35393	158.35388	180.82910	180.82910	0.1404766
0.23995	360.83447	89.99997	89.99997	369.78223	158.66544	158.66544	181.07555	181.07555	0.0917400
0.24401	361.30542	89.99997	89.99997	370.26489	158.96263	158.96263	181.32184	181.32184	0.0497150
0.24800	361.82788	89.99997	89.99997	370.80029	159.24377	159.24377	181.59491	181.59491	0.0

S-VALUE	% SPAN	VX	VU	W	WU	MV	MVX	MW	MVM
0.0	0.0	179.75906	0.0	341.03394	-289.81177	0.50168	0.50168	0.95178	0.5016834
0.00636	6.48668	179.70221	0.0	351.50195	-302.09399	0.50167	0.50167	0.98128	0.5016726
0.01246	12.71817	179.64694	0.0	361.66553	-313.89307	0.50167	0.50167	1.00995	0.5016666
0.01825	18.72217	179.59142	0.0	371.54834	-325.26147	0.50166	0.50166	1.03786	0.5016606
0.02402	24.52214	179.56349	0.0	381.18628	-336.24341	0.50166	0.50165	1.06494	0.5016576
0.03487	35.58640	179.53346	0.0	399.77466	-357.19312	0.50165	0.50164	1.11703	0.5016499
0.04511	46.03534	179.50388	0.0	417.53394	-376.97778	0.50164	0.50164	1.16683	0.5016420
0.05484	55.96286	179.55942	0.0	434.60352	-395.77515	0.50165	0.50164	1.21417	0.5016480
0.06414	65.44553	179.75471	0.0	451.09253	-413.72998	0.50167	0.50167	1.25894	0.5016738
0.07305	74.54576	180.11319	0.0	467.08447	-430.96069	0.50171	0.50171	1.30108	0.5017133
0.08165	83.31396	180.58212	0.0	482.62012	-447.56250	0.50177	0.50177	1.34102	0.5017698
0.08583	87.58604	180.82904	0.0	490.22168	-455.65137	0.50180	0.50180	1.36036	0.5017973
0.08995	91.78867	181.07552	0.0	497.71606	-463.60864	0.50182	0.50182	1.37935	0.5018244
0.09401	95.92534	181.32184	0.0	505.10767	-471.44067	0.50185	0.50185	1.39801	0.5018519
0.09800	100.00000	181.59491	0.0	512.41260	-479.15552	0.50188	0.50189	1.41618	0.5018820

X-VALUE	U	STAT PRESS	STAT TEMP	TOT PRESS	TOT TEMP	% AREA	EPS	RADC	RHO
0.29000	289.81177	1.36414	319.65015	1.61980	335.69995	0.0	0.0	1000000.56250	1.4864540
0.29000	302.09399	1.36415	319.46021	1.61980	335.50000	4.99308	0.05225	1000000.56250	1.4873476
0.29000	313.89307	1.36415	319.26953	1.61980	335.29980	4.99177	0.10348	1000000.56250	1.4882402
0.29000	325.26147	1.36416	319.07910	1.61980	335.09985	4.99044	0.15106	1000000.56250	1.4891338
0.29000	336.24341	1.36416	318.98389	1.61980	335.00000	4.98942	0.19409	1000000.56250	1.4895792
0.29000	357.19312	1.36417	318.88892	1.61980	334.89990	9.97747	0.25955	1000000.56250	1.4900293
0.29000	376.97778	1.36417	318.79395	1.61980	334.79980	9.97609	0.28186	1000000.56250	1.4904804
0.29000	395.77515	1.36417	318.98462	1.61980	335.00000	9.97636	0.25624	1000000.56250	1.4895859
0.29000	413.72998	1.36415	319.65088	1.61980	335.69995	9.98254	0.19614	1000000.56250	1.4864607
0.29000	430.96069	1.36412	320.89867	1.61980	337.00000	9.99634	0.12522	1000000.56250	1.4806986
0.29000	447.56250	1.36409	322.50708	1.61980	338.69995	10.01741	0.06568	1000000.56250	1.4732256
0.29000	455.65137	1.36407	323.36401	1.61980	339.59985	5.01788	0.04451	1000000.56250	1.4693022
0.29000	463.60864	1.36405	324.22095	1.61980	340.50000	5.02399	0.02903	1000000.56250	1.4653988
0.29000	471.44067	1.36403	325.07788	1.61980	341.39990	5.03012	0.01571	1000000.56250	1.4615173
0.29000	479.15552	1.36401	326.03003	1.61980	342.39990	5.03707	0.0	1000000.56250	1.4572268

GAMMA	ETAP	DP/(PT-P)	DP/(PTR-P)	PO/PO	(PO/PO)T	TO/TO	(TO/TO)T
1.39899	0.0	0.01243	0.00298	1.00000	1.59822	1.00000	1.16562
1.39900	0.0	0.01299	0.00289	1.00000	1.59822	1.00000	1.16493
1.39901	0.0	0.01339	0.00277	1.00000	1.59822	1.00000	1.16424
1.39902	0.0	0.01346	0.00261	1.00000	1.59822	1.00000	1.16354
1.39902	0.0	0.01291	0.00234	1.00000	1.59822	1.00000	1.16319
1.39903	0.0	0.00915	0.00147	1.00000	1.59822	1.00000	1.16285
1.39903	0.0	0.00230	0.00033	1.00000	1.59822	1.00000	1.16250
1.39902	0.0	-0.00522	-0.00066	1.00000	1.59822	1.00000	1.16319
1.39899	0.0	-0.01024	-0.00118	1.00000	1.59822	1.00000	1.16562
1.39893	0.0	-0.01111	-0.00116	1.00000	1.59822	1.00000	1.17014
1.39884	0.0	-0.00849	-0.00082	1.00000	1.59822	1.00000	1.17604
1.39880	0.0	-0.00654	-0.00061	1.00000	1.59822	1.00000	1.17917
1.39876	0.0	-0.00516	-0.00046	1.00000	1.59822	1.00000	1.18229
1.39871	0.0	-0.00519	-0.00045	1.00000	1.59822	1.00000	1.18542
1.39867	0.0	-0.00710	-0.00059	1.00000	1.59822	1.00000	1.18889

APPENDIX B

GEOMETRIC CONSIDERATIONS FOR SUBSONIC LEADING EDGES ON TRANSONIC ROTOR BLADES

APPENDIX B: GEOMETRIC CONSIDERATIONS FOR SUBSONIC LEADING EDGES ON TRANSONIC ROTOR BLADES

We first note that a simple leading edge configuration is obtained by sweeping each leading edge element dl in the plane formed by the local relative velocity W_1 and the radius (W_1-r plane). This plane intersects the Mach cone along two generatrices that form the Mach cone angle μ with W. Any other plane through the apex cuts the cone along generatrices forming a smaller angle μ'' with W in the W-r projection. Since the radial projection of dl is essentially proportional to $\sin \mu''$, it follows that the simple case defined above yields the shortest possible swept blade length for a given annulus height and a given relative velocity distribution W(r). For structural reasons, however, the leading edge must be swept aside from the W_1-r plane.

The general situation is shown in Fig. B.1 (Refer also to Fig. 17).

1a shows the projection on a plane perpendicular to the radius passing through leading edge point P. The velocity triangle is projected in that plane for visualization convenience.

1b shows the projection on the W-r plane, with the Mach lines forming the Mach angle μ with W. In general, W forms an angle ε_{W_1} with plane 1a.

1c shows the projection on a plane perpendicular to W, intersecting the Mach cone along circle c.

1d shows the projection on a meridional plane.

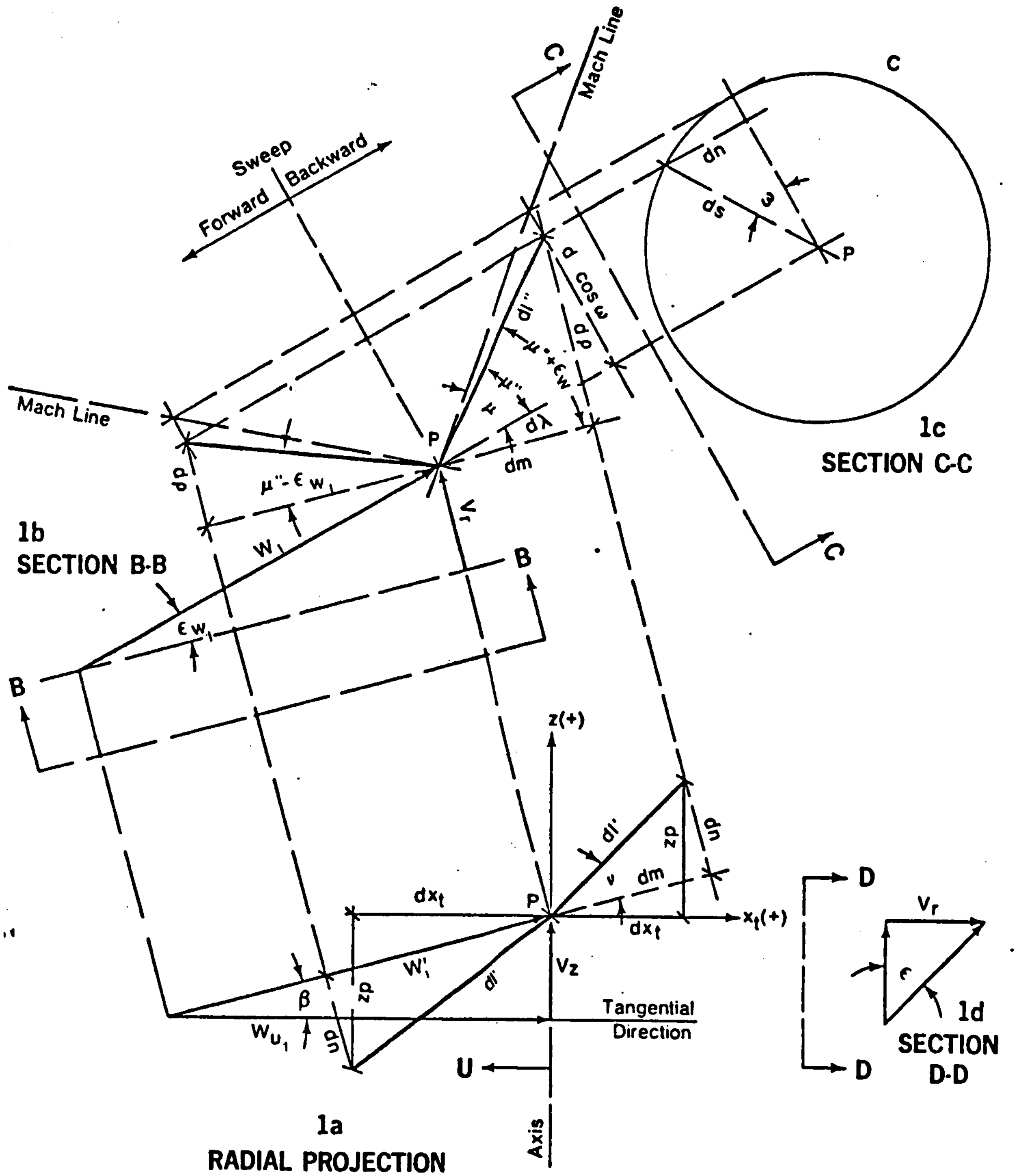

FIG B-1 SONIC SWEPT LEADING EDGE ELEMENT

On 1a, the leading edge element dl has the projection dl' and the radial planes passing through dl and W form the angle ν, which is a design parameter to be selected so as to minimize the blade bending stresses. The resulting lateral sweep component dn appears also on projection 1c and causes the Mach angle μ between dl and W to project into the W-r plane 1b with a smaller aperture μ''.

From 1a

$$dx_t = \pm dl' \cos(\beta + \nu)$$

$$dz = \pm dl' \sin(\beta + \nu)$$

In the above and the following relations, the top signs denote backwards, the bottom signs forward sweep.

Since

$$dl' = \frac{dm}{\cos\nu} = \frac{d\rho}{\tan(\mu'' \pm \varepsilon_{W_1}) \cdot \cos\nu}$$

$$\begin{bmatrix} \dfrac{dx_t}{dz} \end{bmatrix} = \frac{\begin{bmatrix} \cos \\ \sin \end{bmatrix} (\beta + \nu)}{\tan(\mu'' \pm \varepsilon_{W_1})} \quad \frac{1}{\cos\nu} \quad d\rho \tag{B.1}$$

From 1b and 1c

$$\tan\mu'' = \frac{ds \cos\omega}{d\lambda} = \tan\mu \cdot \cos\omega \tag{B.2}$$

and since

$$\sin \omega = \frac{dn}{ds} = \frac{dn}{dm} \frac{dm}{dl''} \frac{dl''}{ds} \frac{\cos \omega}{\cos \omega} =$$

$$= \tan \nu \cdot \cos (\mu'' \pm \varepsilon_{w_1}) \frac{\cos \omega}{\sin \mu''}$$

Therefore,

$$\cos\omega = \frac{1}{\sqrt{1 + \frac{\tan^2 \nu}{\sin^2 \mu''} \cos^2 (\mu'' \pm \varepsilon_w)}} \qquad (B.3)$$

which is introduced in Eqn. B.2, yielding

$$\tan^2 \mu'' = \frac{\tan^2 \mu}{1 + \frac{\tan^2 \nu}{\sin^2 \mu''} \cos^2 (\mu'' \pm \varepsilon_w)} \qquad (B.4)$$

Developing $\cos (\mu'' \pm \varepsilon_w)$, Eqn. B4 is reduced to a quadratic equation for $\tan \mu''$. The solution is

$$\tan \mu'' = \frac{\pm \sin \varepsilon_w \cos \varepsilon_w \tan^2 \nu + \sqrt{\tan^2 \mu \, (1 + \sin^2 \varepsilon_w \tan^2 \nu) - \cos^2 \varepsilon_w \tan^2 \nu}}{1 + \sin^2 \varepsilon_w \tan^2 \nu} \qquad (B.5)$$

(Only the (+) sign is valid in front of the radical, since tan μ'' must tend toward tan μ when ν tends toward 0).

We define the blade profiles and their stacking in cylindrical coordinates. The angular abcissa of leading edge point P(r) then is

$$\theta_L(r) = \theta_{L_1} + \int_{r_{M=1}}^{r} \frac{dx_t}{\rho} = \theta_{L_1} \pm \int_{r_{M=1}}^{r} \frac{\cos(\beta + \nu)}{\tan(\mu'' \pm \varepsilon_{W_1})} \frac{1}{\cos \nu} \frac{d\rho}{\rho} \quad (B.6)$$

$$Z_L(r) = Z'_{L_1} \pm \int_{r_{M=1}}^{r} \frac{\sin(\beta + \nu)}{\tan(\mu'' \pm \varepsilon_{W_1}) \cos \nu} d\rho \quad (B.7)$$

where $$\varepsilon_{W_1} = \text{arc} \sin \frac{V_r}{W_1} \quad (B.8)$$

Eqs. (B.6) and (B.7), together with (B.5) and (B.6), determine the cylindrical coordinates of the profile leading edges, for a blade with sonic leading edge.

With the section profile data, the stacking of the centers of gravity is determined, and the blade bending stresses can be calculated. However, it is advisable to iterate the leading edge coordinates until a favorable alignment of the CG's is achieved, prior to the calculation of stresses.

By optimum selection of the lateral sweep and of the radial location of the point of sweep reversal, it is expected that the additional stresses affecting the subsonic leading edge blade will be reduced to:

(a) Additional centrifugal stresses from the added blade mass necessary to materialize the subsonic leading edge configuration.

(b) Bending stresses from moments without substantial component in the direction of the axes of minimum inertia.

APPENDIX C

FUNDAMENTAL ACOUSTICAL ASPECTS OF STATOR DESIGN

APPENDIX C

FUNDAMENTAL ACOUSTICAL ASPECTS OF STATOR DESIGN

C.1 Continuous and Discrete Line Sources in a Stationary Acoustic Medium

Continuous Line Source

Consider a line monopole source of the type

$$q(x,t) = Q_o \, e^{i(k_o x - \omega_o t)} \quad , \tag{C.1}$$

where Q_o is the source strength per unit length. The line source of Eq. C.1 represents one wave traveling along the x-axis (see Fig. C.1) with a velocity c_o given by

$$c_o = \omega_o / k_o \tag{C.2}$$

One is interested (only) in the *far field* pressure $p(x,y,z,t)$ radiated by the line source. Define

$$r = (y^2+z^2)^{\frac{1}{2}} \tag{C.3}$$

Consider the case (referred to as Case No. 1) where the source velocity c_o is supersonic, i.e.,

$$|c_o| > c \quad , \tag{C.4}$$

or equivalently,

$$|k_o| < k_{a_o} = |\omega_o|/c \quad . \tag{C.5}$$

Here c is the sound speed for the medium and k_{a_o} is the acoustic wavenumber at frequency ω_o. For this case, the far field pressure $p(x,r,t)$ is non-zero; in other words the line source can radiate acoustic power. More specifically,

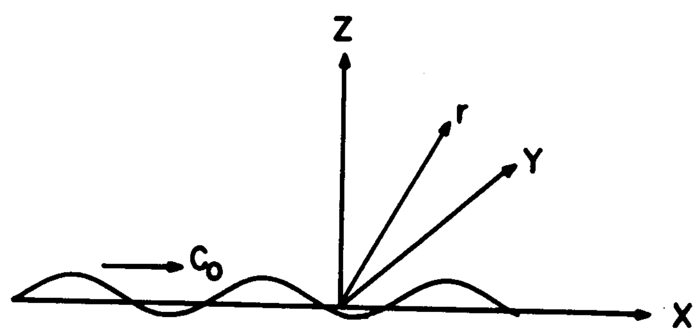

FIG. C.1. SKETCH OF A LINE MONOPOLE SOURCE.

$$p(x,r,t) = \text{constant} \times \frac{1}{(k_r r)^{1/2}} \, e^{i(k_o x + k_r r - \omega_o t)} \quad , \qquad (C.6)$$

where the radial wavenumber k_r is given by

$$k_r = (k_{a_o}^2 - k_o{}^2)^{1/2} \qquad (C.7)$$

Since $k_o{}^2 < k_{a_o}^2$ (see Eq. C.5), k_r is real and the sound is propagated radially outwards from the x-axis.

Now consider the alternate case (Case No. 2) where the source velocity c_o is subsonic, i.e.,

$$|c_o| < c \quad , \qquad (C.8)$$

or equivalently,

$$|k_o| > k_{a_o} . \qquad (C.9)$$

For this case, the far field pressure $p(x,r,t)$ is zero; in other words the line source cannot deliver any acoustic power. More specifically,

$$p(x,r,t,) = 0 \qquad (C.10)$$

This happens because the radial wavenumber k_r is imaginary,

$$k_r = +i \; (k_o^2 - k_{a_o}^2)^{1/2} \quad , \qquad (C.11)$$

and the *near field* pressure decays exponentially in the radial direction.

Let us reconsider the above results in terms of the spatial Fourier transform $\tilde{q}(k_1,t)$ of Eq. (C.1). First, define the general Fourier transforms.

$$\tilde{q}(k_1,t) = \frac{1}{2\pi} \int q(x,t)\, e^{-ik_1x}\, dx \tag{C.12}$$

$$q(x,t) = \int \tilde{q}(k_1,t)\, e^{ik_1x}\, dk_1 \tag{C.13}$$

Unless stated otherwise, the limits of integration are always to be taken from $-\infty$ to $+\infty$. For later use, the temporal Fourier transforms shall also be needed, defined as follows.

$$\tilde{q}(k_1,\omega) = \frac{1}{2\pi} \int \tilde{q}(k_1,t)\, e^{i\omega t}\, dt \tag{C.14}$$

$$= \frac{1}{(2\pi)^2} \int\int q(x,t)\, e^{-i(k_1x-\omega t)}\, dxdt \tag{C.15}$$

$$q(x,t) = \int\int \tilde{q}(k_1,\omega)\, e^{i(k_1x-\omega t)}\, dk_1 d\omega \tag{C.16}$$

$$= \int \tilde{q}(x,\omega)\, e^{i\omega t}\, d\omega \tag{C.17}$$

Substituting $q(x,t)$ of Eq. (C.1) into Eq. (C.12),

$$\tilde{q}(k_1,t) = Q_o e^{-i\omega_o t}\, \delta(k_1-k_o), \tag{C.18}$$

where δ is the Dirac delta function. Figure C.2 illustrates $\tilde{q}(k_1,t)$ for Case No. 1 (radiation) and for Case No. 2 (no radiation). The "radiation span" along the wavenumber k_1 is centered around the wavenumber $k_1 = 0$ and ranges from $-k_{a_o}$ to $+k_{a_o}$. This radiation span is shown in Fig. C.2 as a shaded strip.

Let us reformulate the condition of no radiation in terms of velocities and Mach numbers. The two extremes $-k_{a_o}$ and $+k_{a_o}$ of the radiation span correspond respectively to the lowest and the highest velocities that the source wave can have

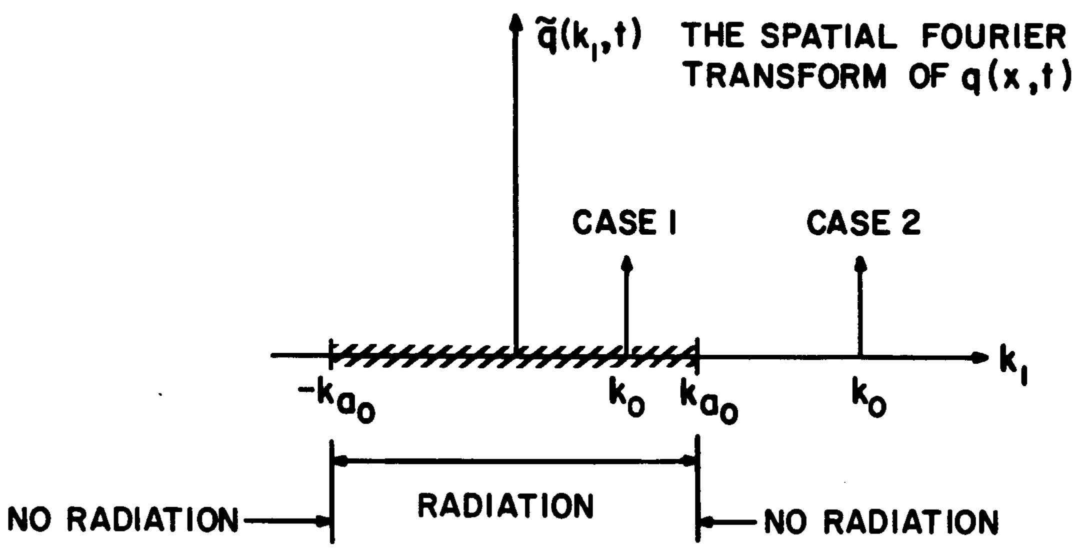

FIG. C.2. CASES OF RADIATION (No. 1) AND NO RADIATION (No. 2) ILLUSTRATED IN TERMS OF THE WAVENUMBER k_1.

for no radiation to occur (Case 2). These extreme velocities and Mach numbers are,

$$c_\ell = \frac{\omega_o}{-k_{a_o}} = -c$$

$$m_\ell = \frac{c_\ell}{c} = -1 \qquad (C.19)$$

$$c_u = \frac{\omega_o}{+k_{a_o}} = +c$$

$$m_u = \frac{c_u}{c} = +1 \qquad (C.20)$$

The source wave Mach number m_o is defined as:

$$m_o = \frac{c_o}{c} \qquad (C.21)$$

Thus, the condition of no radiation (Case 2) becomes

$$m_\ell < m_o < m_u \qquad (C.22)$$

Next, consider a spatially frozen but otherwise arbitrary pattern $q(x,t)$ traveling, as before, with fixed velocity c_o in the x-direction. Thus,

$$q(x,t) = Q(x-c_o t) \quad . \qquad (C.23)$$

In contrast to Eq. (C.1), for which there was one wavenumber k_o, one frequency ω_o, and one velocity c_o, for Eq. (C.23) there is a range of wavenumbers k_1, a corresponding range of frequencies ω, and one velocity c_o. Using Eq. (C.15), the Fourier transform of $q(x,t)$ of Eq. (C.23) is

$$\tilde{q}(k_1,\omega) = \frac{1}{(2\pi)^2} \int\int Q(x-c_o t)\, e^{-i(k_1 x-\omega t)}\, dxdt \qquad (C.24)$$

$$= \frac{1}{2\pi} \int \tilde{Q}(k)\, e^{-ik_1 c_o t+i\omega t}\, dt \qquad (C.25)$$

$$= \tilde{Q}(k)\ \delta(\omega-k_1 c_o)\ , \qquad (C.26)$$

where

$$\tilde{Q}(k) = \frac{1}{2\pi} \int Q(x)\, e^{-ik_1 x}\, dx \qquad (C.27)$$

Figure C.3 shows the straight lines along which $\tilde{q}(k_1,\omega)$ of Eq. (C.26) is non-zero. Analogous to Fig. C.2, straight lines corresponding to Case 1 (radiation) and Case 2 (no radiation) are illustrated. Notice that as frequency ω increases, the radiation span $2k_a$ over wavenumber k_1 also increases linearly. But, as long as the source velocity magnitude $|c_o|$ is subsonic, there is no radiation to the far field. Incidentially, the upper right and the lower left quadrants of ω-k_1 plane correspond to positive phase velocities, (i.e., velocities along increasing x), whereas the upper left and the lower right quadrants of ω-k_1 plane correspond to negative phase velocities.

This completes the discussion of a continuous frozen pattern of line sources in a stationary acoustic medium. Consideration of the fact that the acoustic medium is moving uniformly, will simply alter the radiation span along k_1, as will be discussed in Sec. C.2. However, a frozen convecting pattern along x_1, will or will not radiate, by exactly analogous rules as developed here, i.e., in terms of the convection or phase velocity c_o of the pattern.

Finally, note that for a continuous convecting line source of *finite* length, even if the convection velocity c_o is subsonic, there will be inevitable radiation from the two ends of the line source. For low enough frequencies, the two ends may be less than half an acoustic wavelength apart, in which case there may

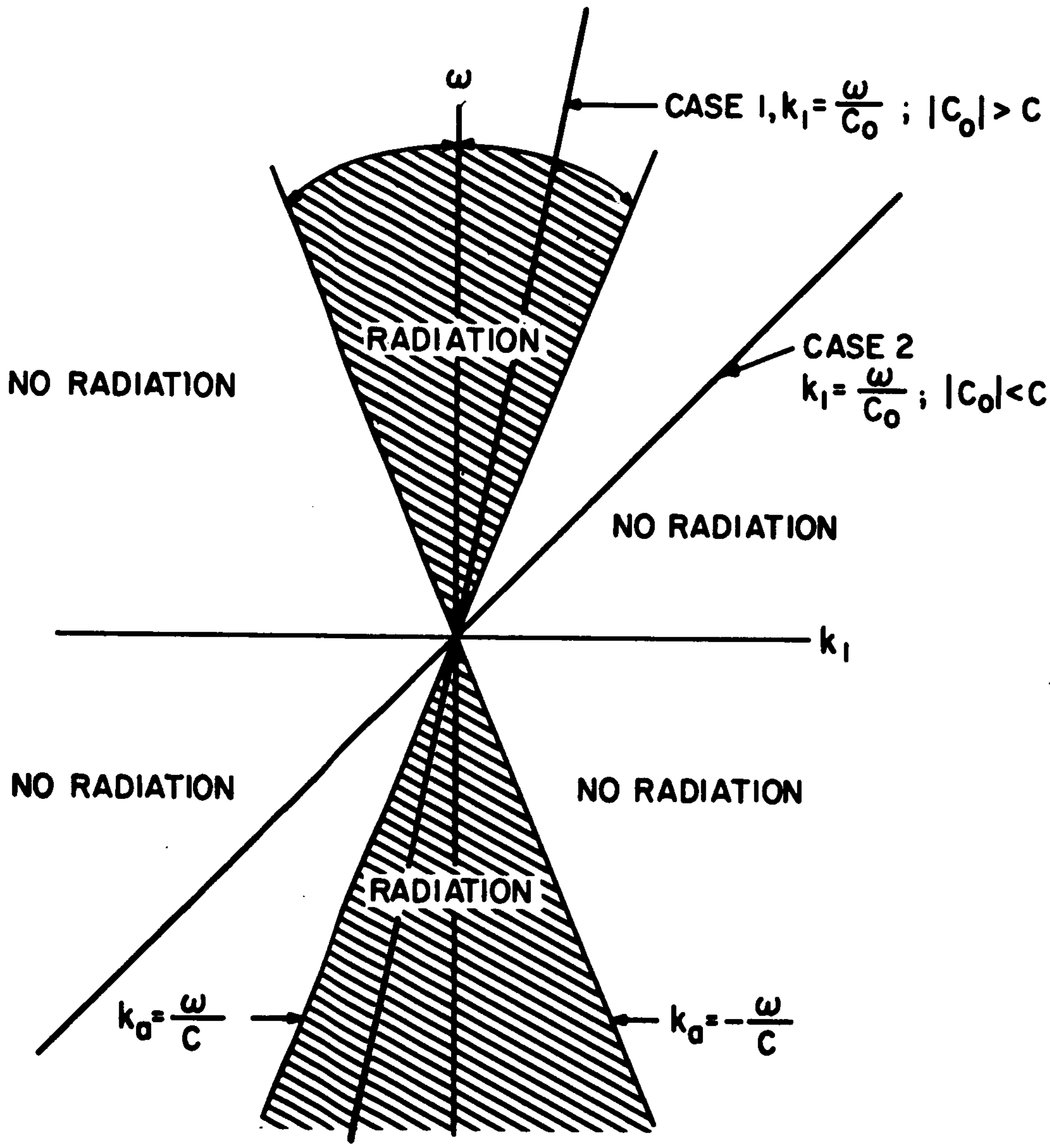

FIG. C.3. CASES OF RADIATION AND NO RADIATION FOR A SPATIALLY FROZEN ARBITRARY PATTERN, ILLUSTRATED IN THE k_1, ω PLANE.

be partial cancellation from the two end sources. For higher frequencies, the two end sources will radiate independently. This last remark is discussed more fully below when discrete line sources are considered in a stationary acoustic medium. However, the SBLE is regarded as a continuous line array, and a typical rotor wake impinging on it has a *local* convection velocity c_o along the *span* of the SBLE. Thus the preceding discussion of continuous line sources, or rather its related extension in Sec. C.2, where account is taken also of the moving-medium acoustics, is applied to determine the SBLE sweep; the criterion that is applied is in terms of the spanwise local velocity of the rotor wake along the SBLE.

Discrete Line Source

Now consider an array of equispaced coherent monopoles, spaced d apart (see Fig. C.4), where:

$$x_j = d_j \quad , \quad j = 0, \pm 1, \pm 2 \ldots \qquad \text{(C.28)}$$

In analogy with Eq. (C.1), consider one wavenumber k_o, one frequency ω_o and the corresponding phase velocity c_o. Thus, the source number j has the strength $q(x_j,t)$ given by

$$q(x_j,t) = Q_o \, e^{i(k_o x_j - \omega_o t)} \, \delta(x-d_j) \qquad \text{(C.29)}$$

The entire source strength can be written as

$$q(x,t) = Q_o \sum_{j=-\infty}^{+\infty} e^{i(k_o x - \omega_o t)} \, \delta(x-dj) \quad , \qquad \text{(C.30)}$$

and the phase velocity c_o, as before, is given by

$$c_o = \omega_o / k_o \quad . \qquad \text{(C.31)}$$

Eq. (C.12) is used to find the spatial Fourier transform of $q(x,t)$ of Eq. (C.30),

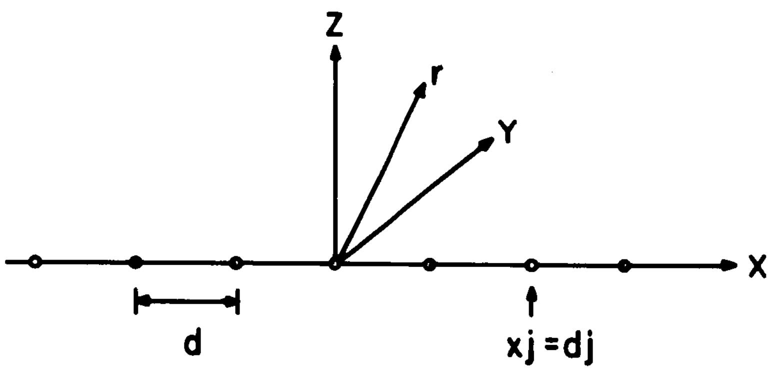

FIG. C.4. SKETCH OF AN ARRAY OF POINT SOURCES.

$$\tilde{q}(k_1,t) = \frac{Q_o}{2\pi} \int e^{-ik_1 x} e^{i(k_o x-\omega_o t)} \sum_{j=-\infty}^{+\infty} \delta(x-dj)\, dx \quad \text{(C.32)}$$

$$= \frac{Q_o}{2\pi} e^{-i\omega_o t} \sum_{j=-\infty}^{+\infty} e^{-i(k_1-k_o)dj} \quad \text{(C.33)}$$

$$= \frac{Q_o}{d} e^{-i\omega_o t} \sum_{m=-\infty}^{+\infty} \delta(k_o-k_1 - \frac{2\pi m}{d}) \quad \text{(C.34)}$$

$\tilde{q}(k_1,t)$ thus consists of an infinite string of Dirac delta functions equispaced along the wavenumber k_1, the spacing between two adjacent delta functions being $2\pi/d$. It is only the "fundamental mode" or harmonic at $k_1 = k_o$ (for $m = 0$ in Eq. C.34) that corresponds to the trace velocity c_o of Eq. (C.31). The remaining infinite harmonics correspond to infinite other velocities. The rule of radiation (Case 1) or no radiation (Case 2) is exactly the same as the one developed for the continuous array and illustrated in Fig. (C.2). If the fundamental mode or any harmonic(s) lie within the radiation span $(-k_{a_o}, k_{a_o})$, radiation will occur from the fundamental mode or from the harmonic(s) lying within the radiation span.

However, a more interesting and new feature of the discrete array is the classification based on a different criterion. That classification is as follows:

$$\text{Case A,} \quad \frac{2\pi}{d} > 2k_{a_o}, \quad \text{or } d < \frac{\lambda_{a_o}}{2} \quad \text{(C.35)}$$

$$\text{Case B,} \quad \frac{2\pi}{d} < 2k_{a_o}, \quad \text{or } d > \frac{\lambda_{a_o}}{2} \quad \text{(C.36)}$$

For Case A, the spacing $2\pi/d$ along wavenumber k_1 between harmonics is greater than the radiation span $2k_{a_o}$, since $k_{a_o} = 2\pi/\lambda_{a_o}$, where λ_{a_o} is the acoustic wavelength at frequency ω_o, the same condition is expressed by the statement that the array spacing d is smaller than half the acoustic wavelength. For

Case B, the opposite situations occur in the wavenumber and spatial descriptions.

The importance of these two cases is depicted in the next few figures. Figure C.5 describes Case A1 (the numbers 1 and 2 denote the older classification, 1 corresponds to radiation occurring, 2 corresponds to radiation not occurring). The radiation occurs from the fundamental mode at $k_1 = k_o$, but since $2\pi/d > 2k_{a_o}$, no other harmonic can radiate. Figure C.6 also describes Case A1, however, this time a harmonic, and *only one* harmonic radiates. Figure C.7 shows the Case A2, a situation one would hope to achieve. The fundamental mode at $k_1 = k_o$ lies just outside the radiation span, and no harmonic lies within the radiation span, hence no radiation occurs. Note that for this desired situation, the constraint of Eq. (C.8) (or equivalently of Eq. C.22) as well as the constraint of Eq. (C.35) applies.

Finally, Fig. C.8 shows Case B1. There *is no Case B2*. Radiation *must* occur through same mode(s), whether the phase velocity c_o is subsonic or supersonic. In other words, arranging for Case B, i.e., having array spacing d greater than half the wavelength, is basically a poor design.

Note that in contrast to the continuous line array for which the discussion related to Fig. C.2 for frequency ω_o could be generalized to discussion related to Fig. C.3 for all frequencies, the discussion of the discrete array presented above *cannot* be similarly generalized to all frequencies. This is because the array spacing d is in general fixed, whereas the radiation span $2k_{a_o}$ increases linearly with increasing ω_o. Thus, Case A for frequency ω_o is bound to merge into Case B at some higher frequency.

Aside from the re-definition in Sec. C.2 of the radiation span in wavenumber k_1, induced by consideration of moving-medium acoustics, the above discussion of a discrete array is applied to determine the number of stator blades, the spacing d corresponding to the circumferential spacing between two adjacent stator tips, and frequency ω_o corresponding to the blade passage frequency.

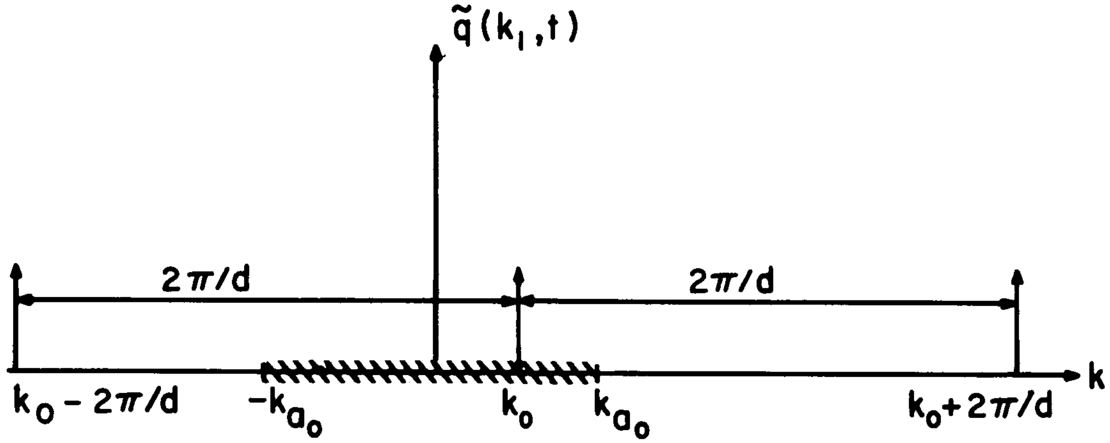

FIG. C.5. CASE A1 FOR A DISCRETE ARRAY; RADIATION FROM THE FUNDAMENTAL HARMONIC AT k_0.

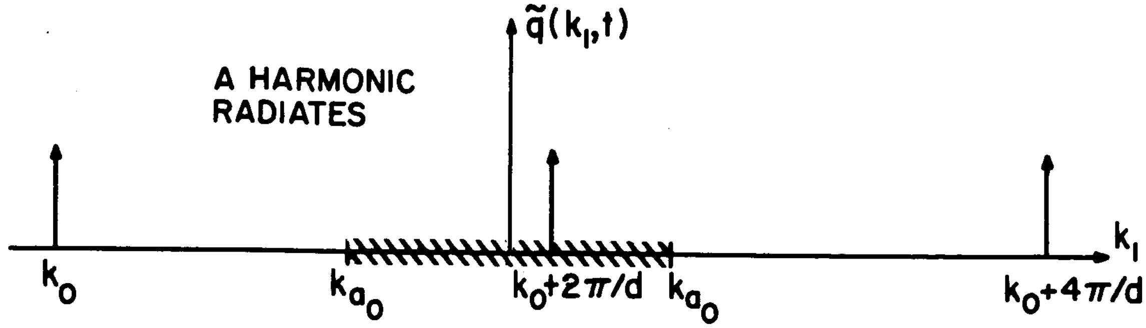

FIG. C.6. CASE A1; RADIATION FROM A HARMONIC OTHER THAN THE FUNDAMENTAL.

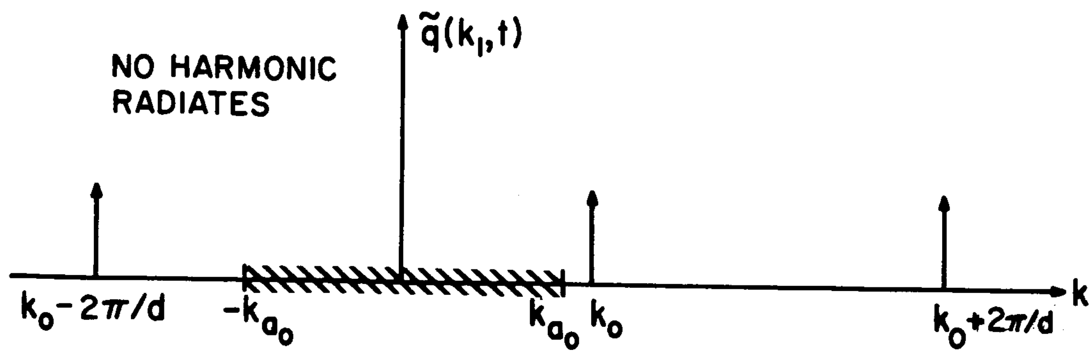

FIG. C.7. CASE A2; NO RADIATION.

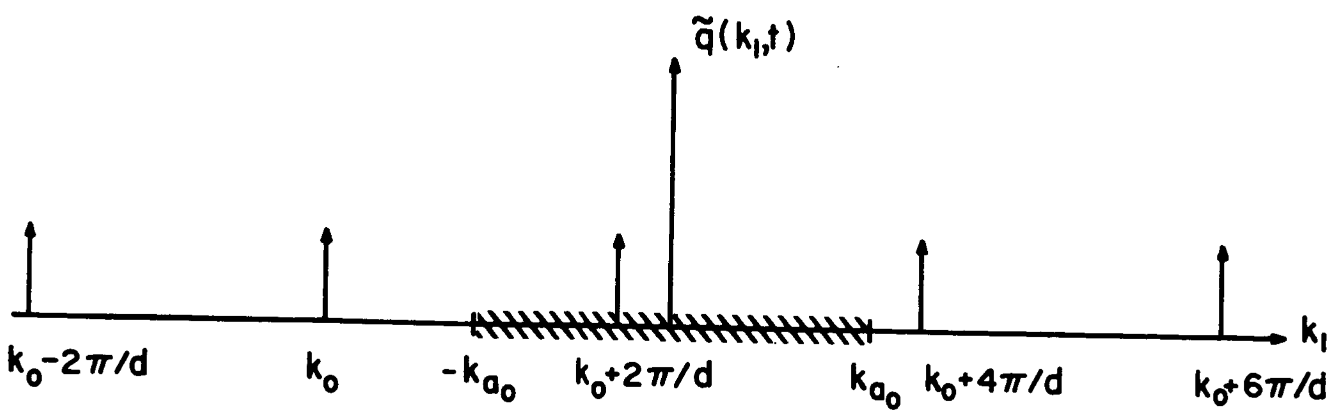

FIG. C.8. CASE B1; INEVITABLE RADIATION.

C.2 Acoustics of a Moving Medium

The only task that needs to be performed in this section is to investigate how the radiation span $(-k_{a_o}, +k_{a_o})$ along the wavenumber k_1 gets modified due to the fact that the acoustic medium is moving uniformly with subsonic velocity $\underline{u} = (u_1, u_2, u_3)$, where u_1, u_2, u_3 are the velocity components in the x, y and z directions.

Once again, consider the line monopole source of Fig. C.1, with Eqs. (C.1) through (C.5) still applicable. In addition to the radial coordinate r of Eq. (C.3), the corresponding radial vector $\underline{r}$ is defined as

$$\underline{r} = (y,z) \tag{C.37}$$

The far field pressure $P(x,\underline{r},t)$ now must satisfy the following field equation, (Morse and Ingard, 1964),

$$\nabla_p^2 + k_{a_o}^2 \left[1 + \frac{i}{\omega_o} \left(u_1 \frac{\partial}{\partial x} + u_2 \frac{\partial}{\partial y} + u_3 \frac{\partial}{\partial z}\right)\right]^2 p = 0 \tag{C.38}$$

For $u_1 = u_2 = u_3 = 0$, Eq. (C.38), reduces to the usual Helmholtz equation applicable for a stationary acoustic medium. In analogy with Eq. (C.11), a criterion is needed that the radial wavenumber k_r must satisfy for no radiation to occur to the far field (i.e., Case 2). However, in analogy with generalization of Eq. (C.3) to Eq. (C.37), a radial wavenumber vector $\underline{k_r}$ is defined as

$$\underline{k_r} = (k_2, k_3) , \tag{C.39}$$

where k_2 and k_3 are the wavenumber components of the radially outwards propagating wave.

Now the important phase aspect of the far field pressure $P(x,\underline{r},t)$ (for a given value of $\underline{r}$ in the farfield) is given by the correspondingly generalized version of Eq. (C.6)

$$P(x,\underline{r},t) = \text{constant} \times e^{i(k_o x - \underline{k_r} \cdot \underline{r} - \omega_o t)}, \tag{C.40}$$

where

$$\underline{k_r} \cdot \underline{r} = k_2 y + k_3 z \qquad \text{(C.41)}$$

The following definitions are required:

$$k_r = |\underline{k_r}| = (k_2^2 + k_3^2)^{1/2} \qquad \text{(C.42)}$$

$$u_r = |\underline{u_r}| = (u_2^2 + u_3^2)^{1/2} \qquad \text{(C.43)}$$

$$k_2 = k_r \sin\alpha_k \quad , \qquad \text{(C.44)}$$

$$k_3 = k_r \cos\alpha_k \quad , \qquad \text{(C.45)}$$

$$u_2 = u_r \sin\alpha_u \quad , \qquad \text{(C.46)}$$

$$u_3 = u_r \cos\alpha_u \quad , \qquad \text{(C.47)}$$

so that

$$\underline{k_r} \cdot \underline{u_r} = k_2 u_2 + k_3 u_3 = k_r u_r \cos\alpha \ , \qquad \text{(C.48)}$$

where

$$\alpha = (\alpha_k - \alpha_u) \quad . \qquad \text{(C.49)}$$

Thus, α is the angle between the radial wavenumber vector $\underline{k_r}$ (or the radial location vector (y,z) of observation in the far-field) and the radial flow vector $\underline{u_r}$.

Now, substituting Eq. (C.40) into Eq. (C.38) gives the following relation,

$$-k_r^2 - k_o^2 + k_{a_o}^2 \left[1 - \frac{1}{\omega_o}(u_1 k_o + u_r k_r \cos\alpha)\right]^2 = 0 \tag{C.50}$$

which can be rewritten as a quadratic equation in k_r as follows

$$Ak_r^2 + Bk_r + C = 0 \tag{C.51}$$

where

$$A = \frac{k_{a_o}^{\ 2}}{\omega_o^{\ 2}} u_r^2 \cos^2\alpha - 1 = m_r^2 \cos^2\alpha - 1 \tag{C.52}$$

$$B = 2 \frac{k_{a_o}^{\ 2}}{\omega_o^{\ 2}} u_1 k_o u_r \cos\alpha - 2 \frac{k_{a_o}^{\ 2}}{\omega_o} u_r \cos\alpha$$

$$= 2(m_1 m_r k_o \cos\alpha - k_{a_o} m_r \cos\alpha) \tag{C.53}$$

and

$$C = (-k_o^2 + k_{a_o}^{\ 2} - 2 \frac{k_{a_o}^{\ 2}}{\omega_o} u_1 k_o + \frac{k_{a_o}^{\ 2} u_1^2}{\omega_o^{\ 2}} k_o^{\ 2})$$

$$= (-k_o^2 + k_{a_o}^{\ 2} - 2k_{a_o} m_1 k_o + m_1^2 k_o^{\ 2}) \tag{C.54}$$

In the above equations appropriate Mach numbers are introduced by division of velocities by the sound speed $c = \omega_o/k_{a_o}$.

For the stationary acoustic medium, the condition on radial wavenumber magnitude k_r, for no radiation to occur (Case 2), was that k_r be imaginary (see Eq. C.11). In analogy with that requirement for no radiation to occur, it is required that k_r of Eq. (C.51) be complex (with positive imaginary part). That will happen if and only if

$$AC - B^2/4 > 0 \quad . \tag{C.55}$$

Now, the left hand side of Eq. (C.55) does not contain k_r, but is a quadratic form in k_o, the wavenumber of the source wave. Thus, Eq. (C.55) can be rewritten as

$$DK_o^2 + Ek_o + F > 0 \quad , \tag{C.56}$$

where

$$D = 1 - m_1^2 - m_r^2 \cos^2\alpha \tag{C.57}$$

$$E = 2k_{a_o} m_1 \tag{C.58}$$

$$F = -k_{a_o}^2 \tag{C.59}$$

The minimum value of D occurs for $\alpha = 0$ or π (i.e., when $\underline{k_r}$ and $\underline{u_r}$ are coincident or oppositely directed. This minimum value D_{minm} is given by

$$D_{minm} = 1 - m_1^2 - m_r^2 = 1 - m^2 > 0 \quad ,$$

where m is total flow Mach number. Since D_{minm}, and therefore D is always positive, the left hand side of Eq. (C.56) is positive for large $|k_o|$ (i.e., for $k_o \to \pm\infty$), being dominated by the first term Dk_o^2. This behavior, incidently, is consistent with the inequality expressed by Eq. (C.56). Recalling that the inequality of Eq. (C.56) is the condition on k_o for no radiation to occur (i.e., Case 2), the radiation will, in fact, take place for a range of wavenumbers k_o of relatively small magnitude. This range, the radiation span along axial wavenumber k_1, is determined by the two *real* roots $k_{a_{o+}}$ and $k_{a_{o-}}$ of the quadratic form of Eq. (C.56)

$$k_{a_{o\pm}} = k_{a_o} \frac{-m_1 \pm (1-m_r^2\cos^2\alpha)^{1/2}}{(1-m_1^2-m_r^2\cos^2\alpha)} \tag{C.60}$$

In analogy with Fig. C.2, this radiation span is shown as a shaded strip in Fig. C.9. The center O' of the span is shifted to the left by the amount $k_{a_o} m_1/D$ (with D given by Eq. (C.57) from the origin O (k_1=0). This shift resulting from first (common) term on the right hand side of Eq. (C.60), is interpreted as a Galilean shift. The equal intervals ($k_{a_{o-}}$, O') and O', $k_{a_{o+}}$), resulting from the second terms on the right hand side of Eq. (C.60) are interpreted as Lorentz half-spans.

Also shown in Fig. C.9 is $\tilde{q}(k_1,t)$ for a phase wave whose phase velocity c_o is supersonic in the fixed coordinate system (or equivalently whose k_o is less than k_{a_o}), yet since k_o lies outside the radiation span, the particular phase wave illustrated will not radiate to the farfield.

Reformulation of the condition of no radiation in terms of Mach numbers can be done along exactly similar lines as done in Eqs. (C.19), (C.20) and (C.21). Thus, the upper and lower permissible Mach numbers m_u and m_ℓ are given by

$$m_\ell = \frac{(1-m_1^2-m_r^2\cos^2\alpha)}{-m_1-(1-m_r^2\cos^2\alpha)^{1/2}} = m_1-(1-m_r^2\cos^2\alpha)^{1/2} \quad , \tag{C.61}$$

$$m_u = \frac{(1-m_1^2-m_r^2\cos^2\alpha)}{-m_1+(1-m_r^2\cos^2\alpha)^{1/2}} = m_1+(1-m_r^2\cos^2\alpha)^{1/2} \quad , \tag{C.62}$$

and for no radiation to occur, the following must be satisfied:

$$m_\ell < m_o < m_u \quad . \tag{C.63}$$

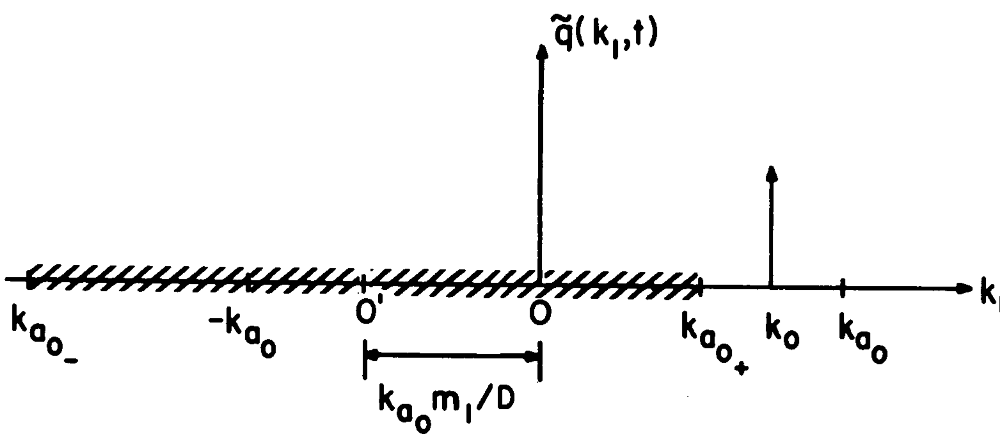

FIG. C.9. SKETCH OF RADIATION SPAN ALONG WAVENUMBER k_1 FOR A MOVING ACOUSTIC MEDIUM.

Extension similar to that from Figs. C.2 to C.3 can also be easily performed for the present case; as a result of the medium motion, the acoustic "cones" of radiation in the ω-k_1 plane will be asymmetrical about the ω axis.

Finally, the entire discussion of discrete arrays in Sec. C.2 can be applied here with the newly defined radiation span.

C.3 An Estimate Of Overall Power Radiated From The Stator

Figure C.10 shows the wake velocity deficits as viewed in time at one SBLE near the tip. There are f_r such deficits per second, where f_r = 8600 Hz is the rotor blade passage frequency. Each individual wake deficit, v(t) has an approximately Gaussian shape around its peak deficit value v_o, thus

$$v(t) \approx v_o \, e^{-t^2/2T^2} \quad . \tag{C.64}$$

where the "standard deviation" T, and the maximum deficit v_o are estimated to be:

$$T \approx 9.6 \times 10^{-6} \text{ sec.} \tag{C.65}$$

$$v_o \approx 44 \text{ m/sec (144 ft/sec)} \tag{C.66}$$

The maximum deficit, v_o corresponds to 10^o change in angle of attack. The time interval τ between consecutive deficits is given by

$$\tau = \frac{1}{f_r} \approx 1.16 \times 10^{-4} \text{ sec.} \tag{C.67}$$

Note that τ is about an order of magnitude greater than T, in other words the wake deficits are narrow in time when compared to their rate of arrival.

The above data regarding the wake velocity deficits was developed from Kemp and Sears (Ref. 18). The description of the wake velocity deficit in a spatial coordinate, x, can be obtained by assuming that the wakes arrive at the SBLE tips as (locally) frozen spatial patterns, being convected along with the local gas speed V, where

$$V = (m_c{}^2 + m_a{}^2)^{1/2} \, c \approx 195 \text{ m/s (641 ft/sec)} \tag{C.68}$$

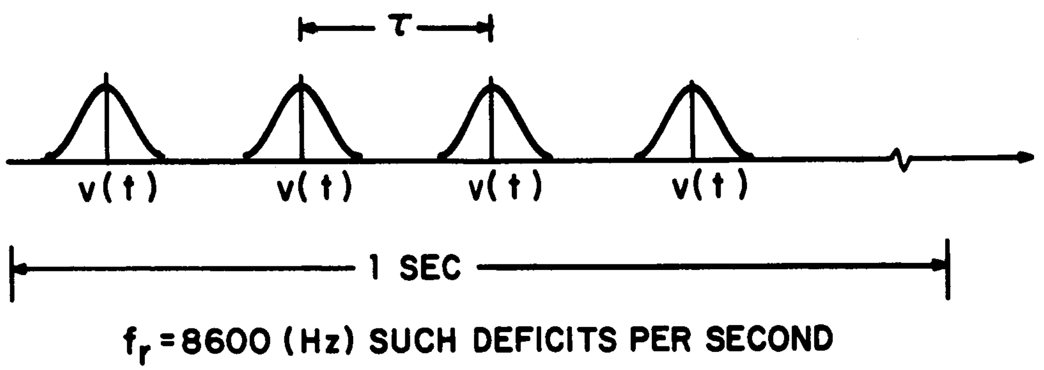

FIG. C.10. SKETCH OF TIME HISTORY OF WAKE VELOCITY DEFICITS AS THEY IMPINGE ON A SINGLE SBLE TIP.

m_c and m_a being given by Eqs. 21 and 22 . Thus, the spatial picture of a wake velocity deficit is obtained by the transformation,

$$x = Ut \quad . \qquad (C.69)$$

For estimating the overall acoustic power radiated from the stator it is convenient, as shown below, to integrate the results in the time domain. However, in order to get a qualitative understanding of the situation in the frequency domain we discuss briefly the Fourier transform $\tilde{v}(\omega)$ of $v(t)$ of Eq. (C.64).

$$\tilde{v}(\omega) = \frac{1}{2\pi} \int v(t) e^{i\omega t}\, dt \qquad (C.70)$$

$$= \frac{T v_o}{(2\pi)^{1/2}} \; e^{-\omega^2 T^2/2} \qquad (C.71)$$

The Fourier transform $\tilde{v}'(\omega)$ of the sequence of pulses of Fig. C.10 may then be written as

$$\tilde{v}'(\omega) = \frac{1}{2\pi} \int v'(t) e^{i\omega t}\, dt$$

$$= \frac{1}{2\pi} \int \sum_{j=-\infty}^{+\infty} v(t-\tau j)\, e^{i\omega t}\, dt \qquad (C.72)$$

$$= \tilde{v}(\omega)\, \omega_r \sum_{n=-\infty}^{+\infty} \delta(\omega - n\omega_r) \; , \qquad (C.73)$$

where ω_o is the blade passage frequency in radians/sec (see Eqs. 17 and 18),

$$\omega_o = 2\pi f_r = \frac{2\pi}{\tau} = \Omega B \ . \qquad \text{(C.74)}$$

Thus, as expected, the frequency content of the rotor wake velocity deficits $v'(t)$ consists of the various rotor harmonics n. Since $\tilde{v}(\omega)$ does not decay appreciably with increasing frequency (the "standard deviation" of $\tilde{v}(\omega)$ is 1/T) the higher rotor harmonics at $n = \pm 2, \pm 3$, etc. have nearly the same strength or amplitude as the fundamental harmonic at $n = \pm 1$.

Now, reverting back to the time domain analysis, the fluctuating lift $\ell(t)$ generated at the leading edge of a SBLE tip from impingement of one wake deficit $v(t)$ is given by

$$\ell(t) = \int_0^{\infty} v(t')\, h(t-t')\, dt' \quad , \qquad \text{(C.75)}$$

where $h(t)$ is the unit impulse response function derived from Küssner's function [Bisplinghoff *et al.*, Ref. 19]. Since the essential uncancelled fluctuating lift is restricted to a relatively small segment of the SBLE span near the tip, use of Küssner's function, valid for low aspect ratio, is readily justified for the present calculation. Since Küssner's function gives the lift due to a sharp-edged gust (i.e., due to a gust that is a unit step function), the unit impulse response function $h(t)$ is obtained by differentiating the Küssner's function. $h(t)$, so obtained, is given by

$$h(t) = C_L \left[\frac{0.13}{2\tau_b} e^{-0.13t/\tau_b} + \frac{1}{2\tau_b} e^{-t/\tau_b} \right] , \qquad \text{(C.76)}$$

where τ_b is the time taken by the gust to travel the (swept) semichord b.

$$\tau_b = b/U \approx 1.33 \times 10^{-4} \text{ sec.} \qquad (C.77)$$

The above estimate of τ_b is based on b ≈0.034 m (0.11 ft), and U of Eq. C.68. The lift coefficient C_L is given by

$$C_L \approx 2\pi\rho U b \frac{\lambda_r}{4} , \qquad (C.78)$$

where ρ is the medium density (2.4×10^{-3} lb-sec²/ft⁴ ≈1.24 Kg/m³) and λ_r is the acoustic wavelength at blade passage frequency f_r (Eq. 26). Note that in Eq. C.78, $\lambda_r/4$ denotes a rough estimate of the SBLE span near the tip from which the uncancelled fluctuating lift is estimated to radiate. Now, this choice of $\lambda_r/4$ is suitable (only) for the rotor fundamental harmonic at frequency ω_r. For the higher rotor harmonics of Eq. C.73, correspondingly smaller spanwise length scales would be more appropriate. However, in the time domain analysis that is being pursued, the choice of $\lambda_r/4$ in Eq. C.78 is taken to apply to all the rotor harmonics, therefore the resulting estimate of the overall (i.e., frequency-integrated) radiated power is liable to be conservative.

Substituting Eqs. (C.64) and (C.76) into Eq. (C.75), enables calculation of fluctuating lift $\ell(t)$ at a single SBLE tip due to the impingement of a single wake velocity deficit v(t). Since the minimum time constant τ_b of h(t) is much larger than the time constant or "standard" deviation" T of v(t) [compare Eqs. (C.65) and (C.77)], for evaluating $\ell(t)$ from Eq. (C.75), one can justifiably approximate v(t) of Eq. (C.64) as follows,

$$v(t) \approx v_0 \, (2\pi)^{1/2} \, T\delta(t) . \qquad (C.79)$$

The constant $(2\pi)^{1/2}$ T in Eq. (C.79) is introduced so as to make the total "area" (in other words, the integral $\int v(t)\,dt$ the same for Eqs. (C.64) and (C.79). From Eq. (C.70) and (C.71), note that this area is equal to $2\pi\tilde{v}(\omega)|_{\omega=0}$. Substituting Eq. (C.79) into Eq. (C.75), gives

$$\ell(t) = v_0(2\pi)^{1/2}\ T\ h(t)\ . \tag{C.80}$$

From the point of view of generation of *steady* lift, the stator blade chord is expected to be oriented parallel to the flow velocity U at its leading edge, so that a zero *mean* angle of attack is ensured. Hence, the wake-deficit-induced fluctuating lift of Eq. C.80 is oriented normal to the flow velocity U. The acoustic intensity I(t) radiated by this "transverse" dipole (i.e., the direction of fluctuating lift is normal to flow) is given by [Lighthill, Ref. 15; Morse and Ingard, Ref. 17],

$$I(t) = [2\dot{\ell}(t)]^2\ \frac{1}{12\rho\pi c^3}\ G_2(m)\quad , \tag{C.81}$$

where $\dot{\ell}(t) = d/dt\ \ell(t)$ and $G_2(m)$ is a function of the flow Mach number $m = U/c$,

$$G_2(m) = \frac{3}{4}\left[\frac{2}{m^2(1-m^2)} - \frac{1}{m^3}\ \ell n\ \frac{1+m}{1-m}\right]. \tag{C.82}$$

The factor 2 appearing with $\dot{\ell}(t)$ in Eq. C.81 accounts for the baffling effect due to the presence of the duct wall (assumed to be acoustically rigid) enclosing the SBLE tip.

The radiated acoustic energy E, associated with the intensity I(t) of Eq. C.81 is given by

$$E = \int_0^\infty I(t)\ dt. \tag{C.83}$$

From Eqs. C.76, C.80 and C.81, we note that the only time dependent factor of I(t) involves h(t) of Eq. C.76, hence, the integral to be evaluated is

$$\int_0^\infty \dot{h}(t)^2 dt = C_L^2 \frac{0.133}{\tau_b^3} , \tag{C.84}$$

thus, substituting Eqs. C.80, C.81 and C.84 into Eq. C.83 we get

$$E = \frac{2}{3} \frac{G_2(m)}{\rho c^3} (v_0 T C_L)^2 \frac{0.133}{\tau_b^3} \tag{C.85}$$

Now, E is the acoustic energy radiated from a single SBLE tip due to impingement of a single wake velocity deficit v(t). Hence, the acoustic power radiated from a single SBLE tip is Ef_r, where f_r is the rate of impingement of wake deficits on the SBLE tip.

Next, assume that the V individual SBLE tips radiate more or less incoherently (an assumption particularly valid for higher rotor harmonics n of Eq. C.73). Hence, the power radiated from the V stator tip sources is Ef_rV.

Finally, even though the calculation for the power radiated from the stator leading edge sources at the hub is not carried out separately, because of closer circumferential spacing between these hub sources, the total power radiated from the stator hub is likely to be considerably less than that from the stator tip. The total power Π radiated from the stator is conservatively estimated to be given by

$$\Pi = 2Ef_rV \tag{C.86}$$

Substituting in Eqs. (C.85) and (C.86) the numerical values quoted for various parameters (with V = 59) gives

$$\Pi = 130.5 \text{ dB re } 10^{-12} \text{ watt} . \qquad (C.87)$$

APPENDIX D

NOTES ON EMPIRICAL CALCULATION OF FAN NOISE LEVELS

APPENDIX D: NOTES ON EMPIRICAL CALCULATION OF FAN NOISE LEVELS

As mentioned in Section 7, all components of the rotor and stator noise spectrum could not be calculated from basic considerations. The previous Appendix gives a noise level calculation for the residual stator noise sources. In the interest of determining what reduction in levels the swept rotor might be expected to cause, Burdsall's empirical correlation (Ref. 19), was exercised for both the actual fan model and a "full scale" counterpart. The parameters required in Burdsall's routine are given in Table D-1. Figure D-1 summarizes the narrow band power levels and spectra for the various components, (SPL arbitrarily computed at 150 ft., 60° from rotor axis) showing the predominance of MPT'S. Of course, the details of the MPT spectrum vary from fan to fan due to their origin in manufacturing tolerances. Fig. D-2 shows a typical comparison of Burdsall's prediction with measured data, indicating a fairly large fluctuation in harmonic levels around the mean line of the prediction. In Fig. D-1, it is clear that according to this scheme, elimination of MPT's would reduce the tone levels considerably. However, note that in Fig. D-1, the line is an envelope of discrete frequency levels at various multiples of rotation rate while the broadband spectrum is continous. Thus, integration into constant percentage bandwidths, and into overall levels will lead to the MPT and broadband levels being very nearly identical.

As a final point, it is interesting to note that the power level of the BPF tone (non-MPT noise) is ~10 dB above the predicted level for the swept stator as described in Appendix C.

TABLE D-1 INPUT PARAMETERS FOR EMPIRICAL NOISE PREDICTION

SYMBOL	DESCRIPTION	UNITS	MODEL FAN	FULL SCALE	BROADBAND	DISCRETE TONE	COMBINATION TONE
DIAT	fan tip diameter	inches	20.0	89.0	X	X	X
DIAH	fan hub diameter	inches	9.5	42.0			X
B	number of blades	----	28.0	28.0			X
NV	number of vanes	----	39.0	59.0			
BPR	bypass ratio	----	8.0	8.0	X		
GAP	rotor/stator space	inches	3.94	17.6			
CHORD	blade tip chord	inches	3.15	14.0			
DDDXT	fan tip dia. gradient	----	-0.222	-0.222			X
DDDXH	fan hub dia. gradient	----	0.444	0.444			X
RS	blade suction surface radius of curvature	inches	12.0 (avg.)	54.0			X
SIGPHI = σ_ϕ	standard deviation of blade tip metal angle	radians	0.015	0.015			X
DL	inlet duct length	feet	1.5	6.7		X	
FFR	radius to observer	feet	150.0	150.0	X	X	
RPM	fan speed	rpm	18450	4130.0			
SPAF	specific airflow rate	$lb/sec/ft^2$	32.8	32.0			
XMXTIP	tip axial Mach number	----	0.62	0.62			X
PR	fan pressure ratio	----	1.6	1.6		X	
DF	diffusion factor (avg)	----	0.4	0.4	X		
TT2	ambient inlet temp-temperature	°F	46	46.0			
PT2	ambient inlet pressure	in. Hg	29.92	29.92			

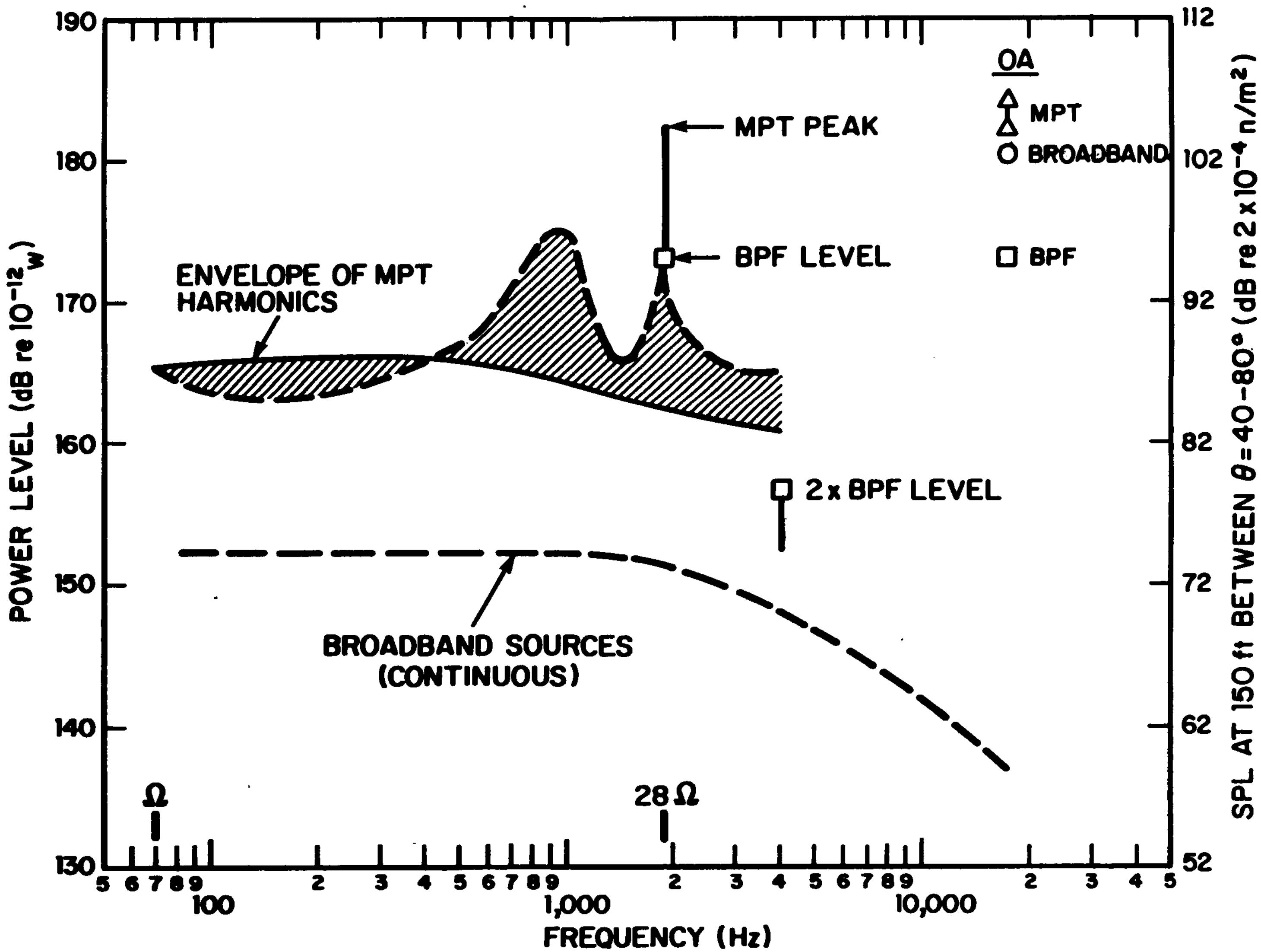

FIG. D-1. NARROWBAND LEVELS FOR FULL SCALE FAN

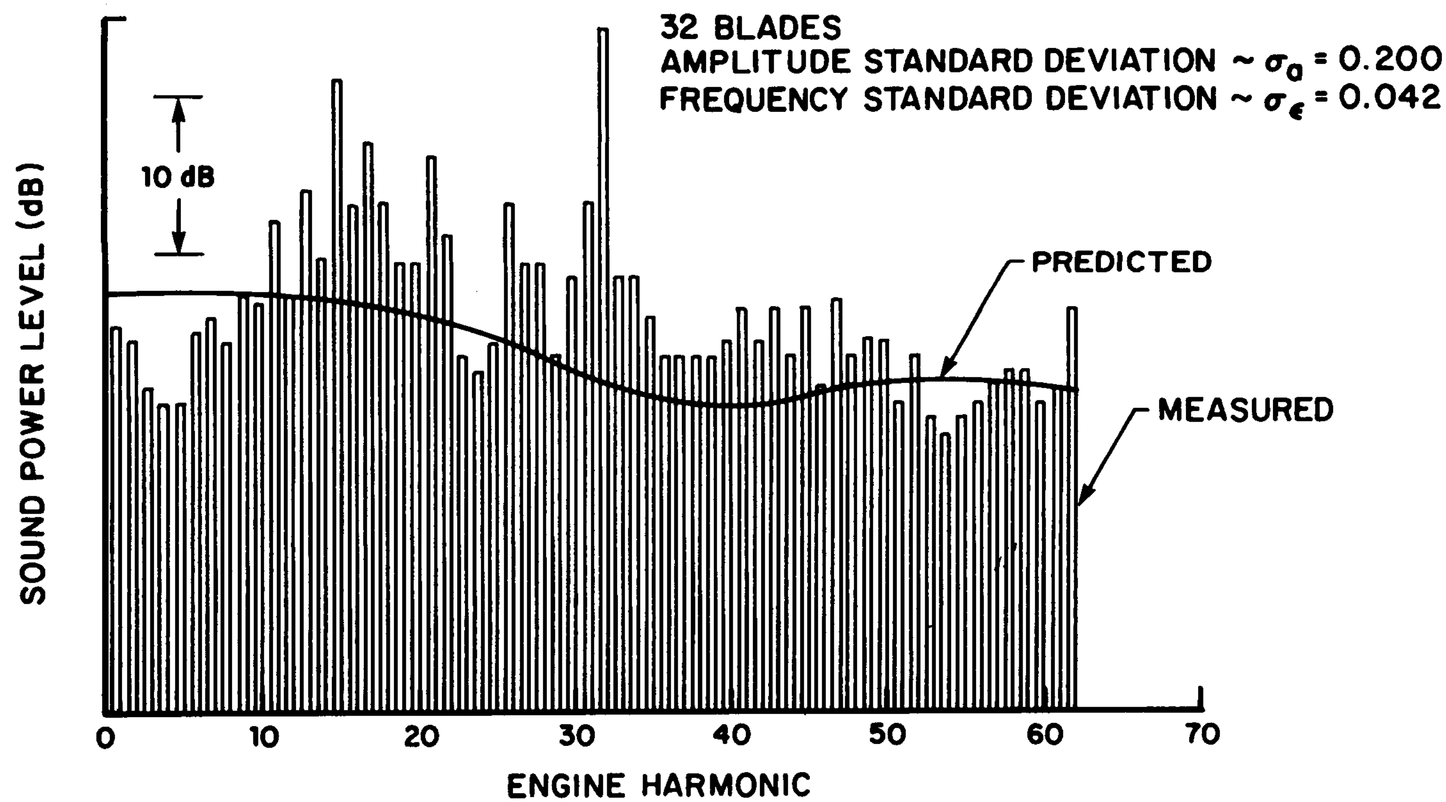

FIG. D-2 COMPARISON OF MEASURED AND PREDICTED MPT SPECTRA (BURDSALL *et al.*).

APPENDIX E

ALGORITHM FOR DERIVATION OF STATOR LEADING EDGE TRACE VELOCITY IN STATOR FIXED COORDINATES

APPENDIX E. ALGORITHM FOR DERIVATION OF STATOR LEADING EDGE TRACE VELOCITY IN STATOR FIXED COORDINATES

The geometry of a rotor wake as it reaches the stator is given in Fig. E-1. Refer to Fig. 9b in the text for 3-dimensional representation. The following four steps give the rotor wake shape and local trace velocity for both an unswept stator (or at the inlet plane of a swept stator), and for swept stators. Aerodynamic reaction on the rotor path by the stator is not taken into account.

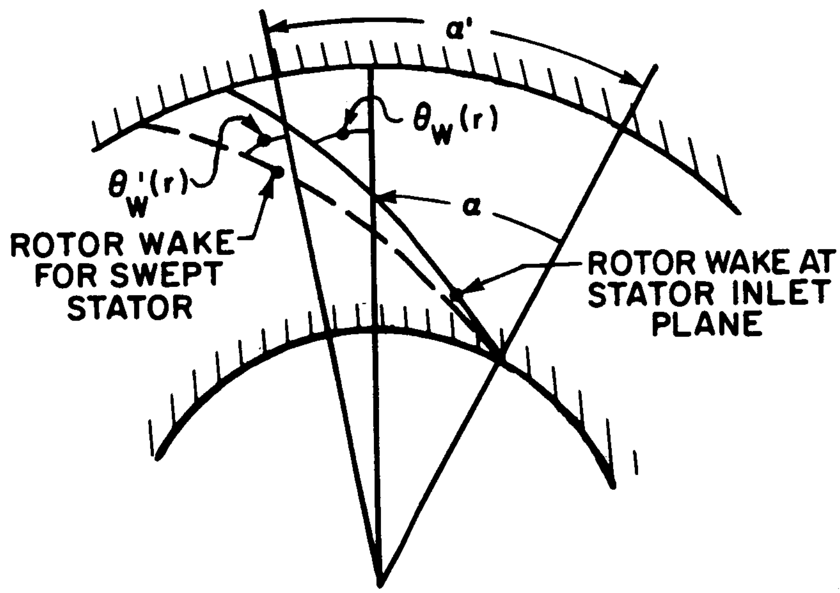

FIG. E-1. GEOMETRY FOR CALCULATION OF ROTOR WAKE SHAPE AND TRACE SPEED ON STATOR VANES.

1) Unswept, Unskewed Stator

The skew of the rotor wake at stator plane is $\alpha(r)$. The local angle between the wake and the radial direction may be derived from:

$$\tan \theta_W = r \, {}^{\delta\alpha}/\delta r \quad .$$

The trace velocity in the radial and axial directions is respectively

$$V_{T_{B_R}}(r) = (wr)/\tan{}_w(r)$$

and

$$V_{T_{B_x}} = 0$$

where:

$V_{T_{B_{R,x}}}$ = the trace velocity in blade fixed coordinates for radial and axial directions respectively.

2) Add Sweep μ_B

The rotor wake in the conical surface of the swept leading edge is changed, as follows.

$$V_{T_{B_R}}(r) = \frac{wr}{\tan\theta'_w(r)} \qquad \text{where} \quad \tan\theta'_w = r\,\frac{\delta\alpha'}{\delta r}$$

and

$$V'_{T_{B_x}}(r) = V_{T_{B_R}} \tan\mu_B(r) \qquad \text{where} \quad \mu_B(r) = \text{local blade sweep angle.}$$

$$\alpha'(r) = \alpha(r) + \Delta x \frac{\delta\alpha(m)}{\delta x} ,$$

where Δx is the downstream displacement of the leading edge caused by sweep.

$$\tan\theta'_w(r) = r\frac{\delta\left[\alpha(r) + \Delta x \frac{\delta\alpha(r)}{\delta x}\right]}{\delta r}$$

$$= r \frac{\delta\alpha(r)}{\delta r} + r \Delta x \frac{\delta^2\alpha(r)}{\delta x \delta r} + r \frac{\delta \Delta x}{\delta r} \frac{\delta\alpha(r)}{\delta x}$$

$$= \tan\theta_w + \Delta x \frac{\delta \tan\theta w}{\delta x} + r \frac{\delta\alpha(r)}{\delta x} \tan\mu_B$$

$$\tan\theta'_w(r) = \tan\theta_w + r \frac{\delta\alpha(r)}{\delta x} \tan\mu_B .$$

3) Trace Velocity for Swept Stator in Stator-Fixed Coordinates

The radial component of trace velocity is

$$V_{T_{B_R}}(r) = \frac{wr}{\tan\theta^*_w + r\frac{\delta\alpha(r)}{\delta x} \tan\mu_B} ,$$

where $\tan\theta^*_w (r,x) = \tan\theta_w + \Delta x \frac{\delta \tan_w}{\delta x}$.

The axial component is:

$$V_{T_{B_x}}(r) = \frac{wr \tan\theta_B}{\tan\theta^*_w + r\frac{\delta\alpha(r)}{\delta x} \tan\mu_B} ,$$

where θ_w^* is determined from cross-plots of the wake path in the r,α plane at various axial locations, and $\delta\alpha/\delta r$ = the local wake helix pitch angle determined from wake crossplots in the meridional plane.

4) Transformation of Trace Velocity Amplitude From Stator-Fixed Coordinates to Gas-Fixed Coordinates

$$V_{T_{B_{R,x}}} \longrightarrow \left| V_{T_G} \right|$$

$$\left| V_{T_G} \right| = \left[\left(V_{T_{B_x}} - V_{B_x} \right)^2 + V_{T_{B_R}}^2 + V_{G_c}^2 \right]^{1/2}$$

where $V_{G_{x,c}}$ is the gas velocity in the axial and circumferential directions, respectively.

REFERENCES

1. Goldstein, A.W., Glaser, F.W., and Coats, J.W. (1973). "Acoustic Properties of a Supersonic Fan," NASA TN D-7096.

2. Morfey, C.L. and Fisher, M.S. (1970). "Shock-Wave Radiation from a Supersonic Ducted Rotor," *J. Roy. Aeron. Soc.* 74: 579-585.

3. Philpot, M.G. (1970). "Buzz-Saw Noise Generated by a High Duty Transonic Compressor," *ASME* Paper 70-GT-54.

4. Sofrin, T.G. and Pickett, G.F. (1970). "Multiple Pure Tone Noise Generated by Fans at Supersonic Tip Speed," presented at the International Symposium of Fluid Mechanics and Design of Turbomachinery, Pennsylvania State University.

5. Hawkings, D. (1971). "Multiple Tone Generation by Transonic Compressors," *J. Sound Vib.* 17(2): 241-250.

6. Kurosaka, M. (1971). "A Note on Multiple Pure Tone Noise," *J. Sound Vib.* 19(4): 453-462.

7. Kantola, R.A. and Kurosaka, M. (1972). "Theoretical and Experimental Investigations of Multiple Pure Tone Noise," *J. Aircraft* 9(11).

8. Jones, R.I. (1947). "Wing Plan Forms for High Speed Flight," *NACA Tech* 863.

9. Bliss, D.B., "method of and Apparatus for Preventing Leading Edge Shocks and Shock-Related Noise in Transonic and Supersonic Blades and the Like," *U.S. Patent* 3,989,406.

10. Filotas, L.T. (1969). "Theory of Airfoil Response in a Gusty Atmosphere, Part 1 - Aerodynamic Transfer Function," UTIAS Report No. 139.

11. Tyler, J.M. and Sofrin, T.G. (1962). "Axial Flow Compressor Noise Studies," *SAE Trans.* 70, pp. 309-322.

12. Widnall, S.E. (1971). "Helicopter Noise Due to Blade-Vortex Interaction," *JASA* 50(1).

13. Bliss, D.B., Chandiramani, K.L. and Piersol, A.G., "Data Analysis and Noise Prediction for the QF-1B Experimental Fan Stage," NASA CR-135066 (BBN Report No. 3338), (1976).

14. Howell, A.R., "Fluid Dynamics of Axial Compressors," *IME,* Vol. 153 (1945).

15. Lighthill, J., "The Fourth Fairey Lecture, The Propagation of Sound Through Moving Fluids," *J. Sound and Vib.,* 24, pp. 471-492, 1972.

16. Lakshminarayana, B. and Raj (1974). "Compressor and Fan Rotor Wake Characteristics," paper for Second Interagency Symposium of University Research in Transportation, North Carolina State University, 6-74.

17. Morse, P.M. and Ingard, K.U., *Theoretical Acoustics,* McGraw-Hill Inc., Chapter 11, Eqs. 11.1.4, 11.2.26 and 11.2.27, (1969).

18. Kemp, N.H. and Sears, W.R., "The Unsteady Forces Due to Viscous Wakes in Turbomachines," *J. Aeron. Soc.,* 22, pp. 478-483, (1955).

19. Bisplinghoff, R.L., *et al.,* "Aeroelasticity," Addison-Wesley, Fig. 5-21, Eq. 5.383, (1955).

20. Burdsall, E.A. and Urban, R.H. (1971). "Fan-Compressor Noise: Prediction Research, and Reduction Studies," FAA Report 71-7 FAA-RD-71-73.

LIST OF SYMBOLS

A	=	axial
A_{in}	=	inlet area (to rotor passage)
A_{min}	=	geometric throat area
A_s	=	area to choke the flow
$a_0\ t/\lambda$	=	normalized distance
b	=	blade semichord
B	=	number of blades
c	=	chord length; sound speed
c_0	=	phase or trace velocity; sound speed
CG	=	center of gravity
C_L	=	lift coefficient
D	=	diffusion factor
DCA	=	double circular area (blade profile)
d	=	distance from blade section c.g. to pressure surface; circumferential spacing between adjacent stator tips
$d\ell$	=	swept leading edge element
E	=	acoustic energy (radiated from a single SBLE tip)
f	=	Mach factor ($= 1/M_{W_{1L}}$); frequency
f_r	=	blade passage frequency of rotor blade

LIST OF SYMBOLS *(Cont.)*

ΔF_j	=	centrifugal force at center of a blade volume element located at j
$G_2(m)$	=	function of flow Mach number
h	=	unit impulse response function
I	=	acoustic intensity
j	=	source number
k	=	wavenumber; constant
k_r	=	radial wavenumber
L	=	harmonic
ℓ	=	distance from section c.g. to leading edge; fluctuating lift
LCF	=	low cycle fatigue
LE	=	leading edge
L_{mn}	=	rotor/stator interaction harmonic
m	=	circumferential mode number; component of Mach number; function in deviation angle formula
M	=	Mach number; moment
M_w	=	relative flow Mach number component
M_{w_1}	=	relative inlet Mach number
M_{w_1}'	=	Mach number required for a subsonic edge to achieve sonic (= M_{w_1})
$M_{w_{1L}}$	=	component of Mach number which is always normal to the leading edge (= 1 for sonic LE; < 1 for subsonic LE

$M_{w_{1L}}'$	=	Mach number required to make a subsonic LE a sonic LE
ΔM_{ij}	=	moment of j force about c.g. of section i
N	=	rotation rate
n	=	shape parameter for polynomial blade forms; harmonic number
P	=	total pressure; static pressur
P or p	=	far field acoustic pressure
P	=	location of leading edge point
P/P	=	pressure ratio
$\hat{P}$	=	static pressure after normal shock
PNL	=	Perceived Noise Level
q	=	source strength
A	=	monopole source strength per unit length
R	=	distance from origin
R_c	=	radius of curvature of streamline
r	=	radial distance
s	=	circumferential blade spacing
SAP	=	Structural Analysis Program
SCF	=	Stress Concentration Factor
SBLE	=	Stator Blade Leading Edge
SR	=	sweep reversal

LIST OF SYMBOLS *(Cont.)*

t	=	thickness; time
$t(x)$	=	thickness distribution
T	=	standard deviation (time)
TE	=	trailing edge
U or u	=	air velocity; wheel speed
v	=	velocity
v_0	=	peak velocity defect
V	=	number of stator vanes; velocity
ΔV_j	=	volume element of a blade
w	=	mass flow rate; velocity; inlet relative velocity
$\bar{W}$	=	average velocity
W_{as}	=	specific mass flow
w/w	=	flow deceleration rate
w	=	relative velocity
Δx	=	downstream displacement of SBLE caused by sweep
x	=	linear distance
z, z_L	=	axial coordinate of leading edge

LIST OF SYMBOLS *(Cont.)*

GREEK

α	=	angle of attack; angle between radial wave vector k_r and radial flow vector u_r; local Mach angle; wake displacement angle from radial
α_3	=	stator inlet angle
β	=	relative flow angle; exit angles of flow
γ	=	setting angle; ratio of specific heats
δ	=	flow deviation angles; Dirac delta function
δ_3	=	stator deviation angle
ε	=	slope of the relative flow velocity; slope between lines connecting section LE and CG and a line connecting LE with lower surfaces coordinate at mid-chord ($\varepsilon_{w_1} = \sin^{-1} V_r/w_1$)
ε_j	=	centerline-projected displacement of the c.g.'s of an airfoil section at r_j relative to one at r_1
λ	=	acoustic wavelength
λ	=	acoustic wavelength at blade passage frequency
η	=	polytropic state efficiency
θ	=	circumferential angle
θ_w	=	angle between radius and rotor wake centerline, unswept stator
θ_w'	=	angle between radius and rotor wake centerline, swept stator

LIST OF SYMBOLS *(Cont.)*

Θ_L	=	angular abscissa of leading edge point
μ	=	Mach cone angle; radial order of acoustic modes
μ_B	=	stator sweep angle
μ''	=	projection of the Mach cone angle on the w-r plane
ν	=	hub-to-tip ratio; lateral sweep angle; section thickness ratio (t_{max}/c); relative thickness
Π	=	acoustic power
ρ	=	density
σ	=	sweep angle; stress; cascade solidity
τ	=	shear stress; LE and TE thickness factors; time interval between successive events
τ_b	=	time for a gust to travel the swept semi-chord (b)
ϕ	=	local camber angle; angle between leading and trailing edge along the unwrapped conical surface
Φ	=	mean camber angle
ω	=	radian frequency; wheel rotation speed
ω_r	=	radian frequency of blade passages
Ω	=	shaft rotation frequency

LIST OF SYMBOLS *(Cont.)*

SUBSCRIPTS

A	=	axial; along blade leading edge
a	=	acoustic
ax	=	axial
B	=	blade-fixed coordinates
c	=	circumferential
crit	=	critical
cg	=	center of gravity
D	=	defect
G	=	gas-fixed coordinates
g	=	geometric
i	=	component parallel to blade array
i, j	=	indices of spatial coordinates
L	=	normal to leading edge; leading edge
ℓ	=	lower
M	=	mainstream
m	=	meridional component
minm	=	minimum
O	=	trace speed
R	=	radial

LIST OF SYMBOLS *(Cont.)*

r	=	radial; component normal to blade array
T	=	tangential; wake trace
t	=	tip
u	=	upper; tangential
w	=	tangential
x	=	chordwise distance from LE; direction normal to z-axis
y	=	Cartesian coordinate normal to z-axis
z	=	axial
∞	=	freestream relative
1,2,3	=	x, y, and z directions
1	=	rotor inlet station
2	=	rotor exit station
3	=	stator inlet station
4	=	stator exit station